



MAX-PLANCK-GESELLSCHAFT

Max-Planck-Institut
für Polymerforschung

Max Planck Institute
for Polymer Research



Conjugated Porous Polymers for Heterogeneous Visible Light Photocatalysis

Dissertation

Zur Erlangung des Grades
„Doktor der Naturwissenschaften“
im Promotionsfach Chemie

dem Fachbereich Chemie, Pharmazie und Geowissenschaften
der Johannes Gutenberg-Universität Mainz.

Zi Jun Wang

Geboren in Yuncheng, China

Mainz, December 2015



Dekan:

1. Gutachter:

2. Gutachter:

Tag der mündlichen Prüfung:

Affidavit

I hereby confirm that I have completed the present dissertation independently and without inadmissible external support. I have not used any sources or tools other than those indicated and have identified literal and analogous quotations.

Furthermore, I confirm that this thesis has not yet been submitted as part of another examination process neither in identical nor in similar form.

Place, date:

Signature:

Zusammenfassung

Konjugierte poröse Polymere (CPP) verbinden in idealer Weise die Eigenschaften eines photoaktiven Polymergrundgerüsts mit reichem Gehalt an π -Elektronen mit einer porösen spezifischen Oberfläche. Daher sind diese Materialien auf großes Interesse in der Wissenschaft gestoßen. Tatsächlich werden CPPs für eine Reihe von traditionellen Anwendungen wie Gasadsorption, Filtration, Katalyse und Lichtkonversion angewendet. In dieser Dissertation wurde eine neue Anwendungsmöglichkeit der CPPs auf ihrer hervorragenden Lichtadsorptionseigenschaft und hoher Porosität hervorgehend, nämlich die metallfreie heterogene Photokatalyse unter Bestrahlung mit sichtbarem Licht, dargestellt. Wichtige Aspekte wie Porosität, Morphologie, Bandstrukturen, chemische Komposition etc., die die photokatalytische Aktivität der CPPs beeinflussen, wurden in dieser Arbeit untersucht und weiterentwickelt. Zusätzlich wurde gezeigt, dass die Valenz- und Leitungsbandniveaus der CPPs mittels einer molekularen Strukturierungsmethode optimiert und die anschließende photooxidative Kupplungsreaktion von Benzylaminen unter Bestrahlung von sichtbarem Licht verbessert werden kann. Zur Porositätskontrolle wurde eine Porenmodifikationsmethode entwickelt, wodurch die Mikroporen in die Makroporen eingebaut und hierarchische Porenstrukturen erzeugt werden konnten. Neben der Porositäts- und internen Oberflächenkontrolle wurde außerdem die chemische Zusammensetzung von CPP-basierenden Photokatalysatoren auch durch Einlagerung des Akzeptoranteils in der Polymerhauptkette variiert. Dies führte zu deutlich erhöhter photokatalytischer Effizienz bei der photoinduzierten Dehalogenierung von α -Bromacetophenonen. Abgesehen von der Anwendung als Photokatalysator organische Reaktionen wurden die CPPs auch als effektive heterogene Photoinitiatoren bei der freien radikalischen Polymerisation von Methylmethacrylat mit Hilfe einer 23 W haushaltsüblichen Fluoreszenzlampe erzielt. Abschließend wurden die CPPs mit immobilisierten Palladiumnanokristallen synthetisiert und als heterogene Photokatalysatoren für die photoinduzierte Suzuki-Miyaura-kreuzkupplungsreaktion erfolgreich verwendet.

Abstract

Conjugated porous polymers (CPP) conveniently combine photoactive π -electron polymer backbone with high interfacial surface area and have drawn tremendous interest from material scientists. Indeed, CPPs have been employed for many applications such as gas adsorption and light harvesting. In this work, we demonstrate that the excellent visible light absorptivity and highly porous nature of the CPPs make them promising candidates as metal free heterogeneous visible light photocatalysts for various organic transformations. A comprehensive study of this new class of materials on different aspects such as porosity, morphology, valence and conduction band positions, chemical composition etc., which effectively influenced their photocatalytic activity, is discussed in this work. First, we present that the valence and conduction band levels of the conjugated microporous (CMP) photocatalysts can be fine-tuned by molecular structural control method in order to optimize the photocatalytic efficiency for the photooxidative coupling of benzylamine and its derivatives under visible light irradiation. Next, we introduce macroporosity as well as microporosity and prepare CPPs with hierarchical porous structures via high internal phase emulsion polymerization technique and micropore engineering method. In addition to porosity and surface area control, another aspect, the chemical composition control of the CPP-based photocatalysts is also shown via incorporating electron acceptor-moiety into the only electron donor-containing polymer backbone structure. Significantly enhanced photocatalytic efficiencies for the photoreductive dehalogenation of α -bromo acetophenone and its derivatives are demonstrated. Apart from being used as visible light photocatalysts for organic chemical reactions, we also present that the conjugated porous polymers can act as effective heterogeneous visible light macromolecular photoinitiator for the free radical polymerization of methyl methacrylate under a 23 W household fluorescent lightbulb. Last, hybrid CPP photocatalyst with immobilized palladium nanocrystals has been synthesized and employed as heterogeneous visible light photocatalyst for the efficient photoinduced Suzuki-Miyaura cross-coupling reactions.

Acknowledgments

Table of Contents

List of Figures	x
List of Tables	xvii
List of Acronyms	xix
1 Introduction	1
2 Aim of the Work.....	3
3 Theoretical Background	4
3.1 Catalysis	4
3.1.1 Fundamentals of Catalysis	4
3.1.2 Visible Light Photocatalysis	6
3.1.2.1 Visible Light Homogeneous Photocatalysis	7
3.1.2.2 Visible Light Heterogeneous Photocatalysis.....	9
3.2 Conjugated Polymers	12
3.2.1 Synthesis of Conjugated Polymers	14
3.2.1.1 Suzuki-Miyaura Coupling.....	15
3.2.1.2 Sonogashira-Hagihara Coupling	16
3.2.2 Conjugated Porous Polymers	17
3.2.3 Applications of Conjugated Porous Polymers	18
3.2.3.1 Heterogeneous Catalysis	18
3.2.3.2 Gas Adsorption.....	19
3.2.3.3 Chemical Encapsulation	20
3.2.3.4 Light Emission	20

3.3	Emulsion Polymerization	21
3.3.1	Colloids and their Stability	21
3.3.2	High Internal Phase Emulsion (HIPE)	23
4	Characterization Techniques	25
4.1	UV/Vis Diffuse Reflectance Spectroscopy	25
4.2	Brunauer, Emmett and Teller (BET) Surface Area Analysis	25
4.3	Electron Paramagnetic Resonance	27
4.4	Cyclic Voltammetry	28
4.5	Scanning Electron Microscopy	29
5	Results and Discussion	30
5.1	Molecular Structural Control of Conjugated Porous Polymers	30
5.1.1	Molecular Structural Design of Conjugated Microporous Poly(benzooxadiazole) Networks for Enhanced Photocatalytic Activity with Visible Light	31
5.1.1.1	Introduction	31
5.1.1.2	Synthesis and Characterization of Conjugated Microporous Polymers	32
5.1.1.3	Photooxidative Coupling of Benzylamine and its Derivatives	45
5.1.1.4	Conclusion	50
5.1.2	Conjugated Microporous Poly(Benzochalcogenadiazole)s for Photocatalytic Oxidative Coupling of Amines under Visible Light	51
5.1.2.1	Synthesis and Characterization of Conjugated Microporous Polymers	51
5.1.2.2	Photooxidative Coupling of Benzylamine and its Derivatives	61
5.1.2.3	Conclusion	68
5.2	Surface Area Control of Conjugated Porous Polymer Photocatalysts	69
5.2.1	Introduction	69
5.2.2	Synthesis of Conjugated Porous Polymers with Different Surface Areas	70

5.2.3	Characterization of Conjugated Porous Polymers with Different Surface Areas...	72
5.2.4	Selective Photo-oxidation of Organic Sulfides.....	84
5.2.5	Conclusion	88
5.3	Chemical Composition Control of Conjugated Porous Polymer Photocatalysts	89
5.3.1	Introduction.....	89
5.3.2	Synthesis and Characterization of B ₂ -FL ₃ and B ₂ -FL ₂ -BBT	89
5.3.3	Photoreductive Dehalogenation of Haloketones using B ₂ -FL ₃ and B ₂ -FL ₂ -BBT... ..	97
5.3.4	Conclusion	105
5.4	Conjugated Porous PolyHIPE as Visible Light Photoinitiator.....	106
5.4.1	Introduction.....	106
5.4.2	Synthesis and Characterization of B-(Boc-CB) ₂ -BO.....	107
5.4.3	Photoinitiation of Free Radical Polymerization of Methyl Methacrylate.....	112
5.4.4	Conclusion	117
5.5	Hybrid Conjugated Porous Polymer with Pd Nanocrystals	118
5.5.1	Introduction.....	118
5.5.2	Synthesis and Characterization of Hybrid Photocatalyst Pd@B-BO ₃	119
5.5.3	Photocatalytic Suzuki Cross-coupling at Room Temperature by Pd@B-BO ₃	123
5.5.4	Conclusion	128
6	Experimental Details and Supplemental Information	129
6.1	Molecular Structural Control of Conjugated Porous Polymers	129
6.1.1	Molecular Structural Design of Conjugated Microporous Poly(benzooxadiazole) Networks for Enhanced Photocatalytic Activity with Visible Light.....	129
6.1.1.1	Materials.....	129
6.1.1.2	Synthesis of B-BO-B.....	129
6.1.1.3	General Procedure for the Light-Promoted Electron Transfer from Tetramethylphenylenediamine (TMPD) to Dioxygen.....	130

6.1.1.4	NMR spectra of B-BO-B.....	130
6.1.2	Conjugated Microporous Poly(Benzochalcogenadiazole)s for Photocatalytic Oxidative Coupling of Amines under Visible Light	131
6.1.2.1	Materials.....	131
6.1.2.2	Synthesis of B-BO, B-BT and B-BS via Sonogashira coupling	131
6.1.2.3	Photocatalytic Oxidative Coupling of Benzylamines	132
6.1.2.4	Light on-off Experiment.....	132
6.1.2.5	Monitoring the photocatalytic oxidative coupling of benzylamine using B-BT as photocatalyst	132
6.2	Surface Area Control of Conjugated Porous Polymer Photocatalysts	133
6.2.1	Preparation of Conjugated Porous Polymers by HIPE Polymerization.....	133
6.2.1.1	Materials.....	133
6.2.1.2	Monomer Synthesis.....	134
6.2.1.3	Synthesis of Boc-NPh ₂	134
6.2.1.4	Synthesis of Boc-CB.....	134
6.2.1.5	General Procedure for Conjugated Porous Polymer Synthesis via HIPE Polymerization	138
6.2.2	General Experimental Procedures in the Continuous Flow System	138
6.2.3	Density function theory (DFT) calculations	138
6.2.4	Additional SEM Images of PolyHIPEs.....	143
6.3	Chemical Composition Control of Conjugated Porous Polymers.....	149
6.3.1	Materials	149
6.3.2	Procedure for the Sonogashira Cross-Coupling Reaction via High Internal Phase Emulsion (HIPE) Polymerization	149
6.3.3	Synthesis of the Short Linear Polymer B-FL2-BBT-L.....	150
6.3.4	General Procedure for the Photodehalogenation Reaction of α -Bromo acetophenone Derivatives.....	150

6.3.5	Dehalogenation Reaction of α -Bromo-acetophenone using the Linear Polymer as Photocatalyst.....	151
6.3.6	Apparent Quantum Yield (AQY) Estimation	151
6.3.7	Repeating Experiments of Dehalogenation of 2-Bromoacetophenone.....	153
6.4	Conjugated Porous Polymer as Free Radical Photoinitiator	154
6.4.1	Materials	154
6.4.2	Synthesis of Boc-CB.....	154
6.4.3	Synthesis of B-(Boc-CB) ₂ -BO	154
6.4.4	Photopolymerization of MMA with B-(BOC-CB) ₂ -BO.....	155
6.4.5	Supplementary Characterization Information.....	155
6.5	Hybrid Conjugated Porous Polymer with Pd Nanocrystals	158
6.5.1	Materials	158
6.5.2	General procedure for synthesis of end-capped B-BO ₃ by Sonogashira cross-coupling reaction	158
6.5.3	Synthesis of Pd@B-BO ₃	158
6.5.4	General Procedure for the Suzuki Coupling Reaction by Pd@B-BO ₃	158
6.5.5	Repeating Experiments	159
6.5.6	Additional SEM and TEM images of Pd@B-BO ₃	159
6.5.7	Photocatalytic Reaction Set-up.....	161
7	Conclusions	162
8	References	164
9	List of Related Publications.....	173

List of Figures

Figure 3.1 Potential energy diagram comparing uncatalyzed reaction route with a catalyzed route.	4
Figure 3.2 Solar Spectrum. Courtesy of Charles Chandler.....	7
Figure 3.3 Ruthenium and iridium complexes.....	8
Figure 3.4 Selected organic dyes as photoredox catalysts.....	8
Figure 3.5 The oxidation of benzyl alcohols on TiO ₂ under visible light.....	10
Figure 3.6 Selective aerobic oxidation of alkyl aromatics.....	10
Figure 3.7 Surface plasmonic metal (Au, Ag or Cu) NPs for visible light induced reactions. Adapted from Lang et al. ⁶¹ Copyright (2014) Royal Society of Chemistry.	11
Figure 3.8 Hydroxylation of benzene with H ₂ O ₂	12
Figure 3.9 (a) Trans-polyacetylene (b) cis-polyacetylene (c) poly(para-phenylene) and (d) poly(para-phenylene vinylene).	13
Figure 3.10 Range of conductivities covered by doped polyacetylene in a comparison with other materials. Adapted from The Physics of Polymers. ¹¹⁰ Copyright (2007) Springer.	14
Figure 3.11 Reaction scheme of Suzuki-Miyaura coupling.....	15
Figure 3.12 The mechanism of the Suzuki cross-coupling reaction. Adapted from Strategic Applications of Named Reactions in Organic Synthesis. Copyright(2005) Elsevier.	16
Figure 3.13 Reaction scheme of Sonogashira-Hagihara coupling.....	17
Figure 3.14 Reaction mechanism of Sonogashira-Hagihara coupling. Adapted from Strategic Applications of Named Reactions in Organic Synthesis. Copyright(2005) Elsevier.	17
Figure 3.15 Illustration of interaction potential between two particles as a function of distance according to DLVO theory. Adapted from Napper. ¹⁶⁴ Copyright (1970) American Chemical Society.....	22
Figure 3.16 Schematic illustration of HIPE formation and polyHIPE synthesis within a water in oil HIPE (an aqueous internal phase dispersed within a hydrophobic external phase).	24
Figure 3.17 Scanning electron microscopy (SEM) image of typical porous polyHIPE structure. Adapted from Sergienko et al. ¹⁷⁴ Copyright (2002) Wiley VCH.	24
Figure 4.1 IUPAC classification of sorption isotherms. Adapted from Sing et al. ¹⁷⁸ Copyright (1985) Blackwell Science Ltd.....	26

Figure 4.2 Energy levels for an electron spin ($M_s = +1/2$ or $-1/2$) in an applied magnetic field B. Adapted from Electron Paramagnetic Resonance. ¹⁷⁹ Copyright (1964) Academic Press.	28
Figure 4.3 Voltammogram with key parameters. Adapted from Electroanalytical Methods. ¹⁸⁰ Copyright (2010) Springer.	29
Figure 5.1 Geometry design principle of valence and conduction band position modification of conjugated microporous poly(benzooxadiazole) networks by altering the substitution position on the 3-D center.	33
Figure 5.2 Solid State $^{13}\text{C}/\text{MAS}$ NMR of B-BO-1,3,5.	34
Figure 5.3 Solid State $^{13}\text{C}/\text{MAS}$ NMR of B-BO-1,2,4.	34
Figure 5.4 Solid State $^{13}\text{C}/\text{MAS}$ NMR of B-BO-1,2,4,5.	35
Figure 5.5 N_2 gas sorption isotherms.	36
Figure 5.6 Pore size distribution of the CMPs.	36
Figure 5.7 TGA curves of the three CMPs.	37
Figure 5.8 FTIR spectra of B-BO-1,3,5.	38
Figure 5.9 FTIR spectra of B-BO-1,2,4.	38
Figure 5.10 FTIR spectra of B-BO-1,2,4,5.	39
Figure 5.11 SEM images of B-BO-1,3,5 (a), B-BO-1,2,4 (b), B-BO-1,2,4,5 (c) and TEM images of B-BO-1,3,5 (d), B-BO-1,2,4 (e), B-BO-1,2,4,5 (f).	40
Figure 5.12 Photographs of the CMPs.	41
Figure 5.13 (a) UV/Vis DR spectra. (b) Valence band (VB) and Conduction band (VB) positions of the CMPs and redox potentials of some substrates such as benzylamine (BA) and molecular oxygen into superoxide used in the photocatalytic reaction determined by CV.	41
Figure 5.14 Cyclic voltammograms.	42
Figure 5.15 EPR spectra for of CPPs taken in dark and under light irradiation.	43
Figure 5.16 UV/Vis spectra and photograph of the cationic radical of TMPD (100 mM in 3 mL CH_3CN) after photo-induced oxidation by CMPs (2 mg/ml) in after 1 h under blue LED in air. Insert: (i) B-BO-1,3,5; (ii) B-BO-1,2,4; (iii) B-BO-1,2,4,5.	44
Figure 5.17 ESR spectra of $\text{DMPO-O}_2^{\bullet-}$, and (d) $\text{TEMPO-O}_2^{\bullet-}$ adducts for different CMPs under light and in dark.	45
Figure 5.18 ^1H NMR spectra of the photooxidative coupling of benzyl amine using a 23 W household energy saving fluorescent light bulb over 24 hours.	48

Figure 5.19 UV/Vis spectra of B-BO-B before and after the 3-hour-long photooxidative coupling of benzyl amine (synthesis and experimental details are described in chapter 5.1).	49
Figure 5.20 Repeating experiments of the photooxidative coupling of benzyl amine by B-BO-1,3,5 under a 23 W household energy saving fluorescent light bulb at room temperature.	49
Figure 5.21 Synthetic route and representative structures of the designed conjugated porous poly(benzochalcogenadiazole)s.	52
Figure 5.22 Solid state ¹³ C/MAS NMR spectra of B-BO, B-BT and B-BS. Adapted from the diploma thesis of Kim Garth.	53
Figure 5.23 Nitrogen gas sorption isotherm and pore size distribution of the polymer series.	54
Figure 5.24 Thermogravimetric analysis (TGA) of the three polymers.	55
Figure 5.25 FTIR spectra of B-BO, B-BT and B-BS.	55
Figure 5.26 SEM images of (a) B-BO, (b) B-BT, (c) B-BS, and TEM images of (d) B-BO, (e) B-BT, (f) B-BS.	56
Figure 5.27 (a) UV/Vis DR spectra. (b) Valence band (VB) and Conduction band (VB) positions and (c) EPR spectra of B-BO, B-BT and B-BS under light irradiation.	57
Figure 5.28 Pictures of CMP B-BO, B-BT and B-BS.	58
Figure 5.29 Cyclic voltammograms.	59
Figure 5.30 EPR spectra taken in dark.	60
Figure 5.31 EPR spectra taken under light.	60
Figure 5.32 Light on-off experiment. Adapted from the diploma thesis of Kim Garth.	62
Figure 5.33 Control experiments of the photocatalytic oxidative coupling of benzylamine with different scavengers.	63
Figure 5.34 Proposed reaction mechanism of the photocatalytic oxidative coupling of benzylamine.	65
Figure 5.35 Repeating experiment of photocatalytic oxidative coupling of benzylamine using B-BT as catalyst.	66
Figure 5.36 FT-IR spectra for B-BT before and after reactions.	67
Figure 5.37 Idealized structures and surface area control via micropore engineering and of π -conjugated microporous polymers. Conditions: (i) Suzuki coupling in HIPE. (ii) 250 °C, 12 h, vacuum.	71
Figure 5.38 Thermogravimetric analysis of poly(HIPE)s with Boc groups.	72

Figure 5.39 Thermogravimetric analysis of poly(HIPE)s without Boc groups.	73
Figure 5.40 FTIR spectra of B-(BOC-NPh ₂) ₃ and B-(NPh ₂) ₃	73
Figure 5.41 FTIR spectra of B-(BOC-CB) ₃ and B-CB ₃	74
Figure 5.42 FTIR spectra of B-(BOC-CB) ₂ -BT and B-CB ₂ BT.....	74
Figure 5.43 Solid state ¹³ C CP/MAS NMR spectrum of B-(NPh ₂) ₃ and B-(Boc-NPh ₂) ₃	75
Figure 5.44 Solid state ¹³ C CP/MAS NMR spectrum of B-CB ₃ and B-(Boc-CB) ₃	75
Figure 5.45 Solid state ¹³ C CP/MAS NMR spectrum of B-CB ₂ -BT and B-(Boc-CB) ₂ -BT.....	76
Figure 5.46 N ₂ Sorption Isotherms and Pore Size Distributions of poly(HIPE)s with Boc groups.	78
Figure 5.47 N ₂ Sorption Isotherms and Pore Size Distributions of poly(HIPE)s after removal of Boc groups.	79
Figure 5.48 SEM images of the conjugated polyHIPEs before and after removal of Boc group. (a) B-(Boc-NPh ₂) ₃ , (b) B-(NPh ₂) ₃ , (c) B-(Boc-CB) ₃ , (d) B-CB ₃ , (e) B-(Boc-CB) ₂ -BT, (f) B-CB ₂ -BT.	80
Figure 5.49 (a) UV/Vis DR spectra of B-(Boc-NPh ₂) ₃ , B-(Boc-CB) ₃ , and B-(Boc-CB) ₂ -BT containing Boc group. (b) DRS UV/Vis spectra of B-(NPh ₂) ₃ , B-CB ₃ , and B-(CB) ₂ -BT. (c) Illustrated setup of the glass column photoreactor in a continuous flow system.....	82
Figure 5.50 Fluorescence spectra of poly(HIPE)s with Boc groups.....	83
Figure 5.51 Fluorescence spectra of poly(HIPE)s after removal of Boc groups.....	83
Figure 5.52 ¹ H NMR spectrum of thioanisole before and after photooxidation reaction.....	85
Figure 5.53 Synthetic route and idealized structure of B ₂ -FL ₂ -BBT and B ₂ -FL ₃ . Reaction conditions: (i) Pd(PPh ₃) ₄ , CuI, K ₂ CO ₃ , span 80, toluene/H ₂ O (v/v: 1/9), 80 °C, overnight.	91
Figure 5.54 Solid state ¹³ C/MAS NMR spectrum of B ₂ -FL ₂ -BBT and B ₂ -FL ₃	92
Figure 5.55 TGA of of B ₂ -FL ₂ -BBT and B ₂ -FL ₃	93
Figure 5.56 N ₂ sorption isotherms of (a) B ₂ -FL ₂ -BBT and (b) B ₂ -FL ₃	94
Figure 5.57 Pore size Distributions of B ₂ -FL ₂ -BBT and B ₂ -FL ₃	94
Figure 5.58 FT-IR spectra of B ₂ -FL ₂ -BBT and B ₂ -FL ₃	95
Figure 5.59 SEM images of B ₂ -FL ₂ -BBT (a) and B ₂ -FL ₃ (b).....	96
Figure 5.60 (a) UV/Vis DRS spectra of B ₂ -FL ₂ -BBT and B ₂ -FL ₃	96
Figure 5.61 Electron paramagnetic resonance (EPR) spectra of B ₂ -FL ₂ -BBT and B ₂ -FL ₃ under light irradiation.....	97

Figure 5.62 ^1H NMR spectra of the reaction mixture before light irradiation and the reaction components taken separately in DMF- <i>d</i> . $\delta = 7.35$ ppm (s, 1H, trichloroethylene), 4.98 ppm (s, 2H, C(O)-CH ₂ -Br, starting material).	98
Figure 5.63 ^1H NMR spectrum of the reaction mixture after light irradiation $\delta = 7.35$ ppm (s, 1H, trichloroethylene), 2.80 ppm (s, 3H, C(O)-CH ₃ , product).	99
Figure 5.64 Repeating experiment of the dehalogenation of 2-bromoacetophenone using B ₂ -FL ₂ -BBT as photocatalyst.	101
Figure 5.65 N ₂ sorption isotherms and pore size distribution of B ₂ -FL ₂ -BBT after the reductive dehalogenation reaction.	102
Figure 5.66 Proposed mechanism of the visible light-driven dehalogenation reaction using the conjugated porous polymers as heterogeneous photocatalyst.	103
Figure 5.67 Structure of linear polymer used as photocatalyst.	104
Figure 5.68 ^1H NMR spectrum of the reaction mixture using linear polymer after light irradiation. $\delta = 7.35$ ppm (s, 1H, trichloroethylene), 2.80 ppm (s, 3H, C(O)-CH ₃ , product).	104
Figure 5.69 UV/vis spectra of the linear polymer before and after the photo dehalogenation reaction.	105
Figure 5.70 Synthetic route and idealized structure of B-(Boc-CB) ₂ -BO using palladium catalyzed Suzuki-Miyaura cross-coupling reaction via high internal phase emulsion (HIPE) polymerization. Reaction conditions: Pd(PPh ₃) ₄ , K ₂ CO ₃ , Span [®] 80, H ₂ O/toluene, 80 °C, 12 h.	107
Figure 5.71 (a) and (b) SEM images of B-(Boc-CB) ₂ -BO, the insert is a photograph of the monolithic polymer.	108
Figure 5.72 (a) DRS UV/Vis, and (b) photoluminescence spectra.	109
Figure 5.73 N ₂ sorption isotherms of BET surface area measurement.	109
Figure 5.74 Pore size distribution of BET measurement.	110
Figure 5.75 Solid state ^{13}C NMR of B-(BOC-CB) ₂ -BO.	111
Figure 5.76 Thermogravimetry analysis (TGA) of B(BOC-CB) ₂ BO.	111
Figure 5.77 FTIR spectrum of conjugated poly(HIPE) B-(Boc-CB) ₂ -BO.	112
Figure 5.78 Polymerization of methyl methacrylate (MMA).	113
Figure 5.79 Photopolymerization of methyl methacrylate using B-(Boc-CB) ₂ -BO as heterogeneous photoinitiator at room temperature under visible light.	113

Figure 5.80 Suggested mechanism of the photoinitiation using conjugated porous polyHIPE under visible light.	115
Figure 5.81 Additional repeating experiments of the photopolymerization of methyl methacrylate in 50 wt% THF solution in the presence of Et ₃ N at room temperature with visible light.	116
Figure 5.82 SEM image of B-(Boc-CB) ₂ -BO after the photoinitiation under visible light.	116
Figure 5.83 (a) Polymer backbone structure of B-BO ₃ . (b) TEM image of B-BO ₃ immobilized with Pd NPs with sizes between 5 and 10 nm.	120
Figure 5.84 N ₂ sorption isotherms.	120
Figure 5.85 Pore size distribution of (a) B-BO ₃ .and (b) Pd@ B-BO ₃	121
Figure 5.86 (a) UV/vis DR spectra of Pd@B-BO ₃ and B-BO ₃ . (d) VB (HOMO) and CB (LUMO) band positions of Pd@B-BO ₃ and B-BO ₃ (vs SCE) measured by CV.	121
Figure 5.87 Electron paramagnetic resonance (EPR) spectra of B-BO ₃ and Pd@B-BO ₃ in dark (dash line) and under light irradiation (straight line).	122
Figure 5.88 Solid-State ¹³ C Magic Angle Spinning Nuclear Magnetic Resonance (MAS-NMR) of B-BO ₃	123
Figure 5.89 Suggested reaction mechanism of the photocatalytic Suzuki coupling via the light-induced heterojunction at the interface of B-BO ₃ and Pd NPs.	125
Figure 5.90 Repeating experiment of the photocatalytic Suzuki coupling of iodobenzene and phenylboronic acid. The lost weight percentage of Pd after the repeating cycles is also displayed.	128
Figure 5.91 TEM image of a used Pd@B-BO ₃ sample after the catalytic reactions.	128
Figure 6.1 ¹ H NMR and ¹³ C NMR spectrum of B-BO-B.	131
Figure 6.2 ¹ H NMR spectrum of the crude mixture of the photo-oxidation of benzylamine with B-BT as photocatalyst. Reaction time 2 h, conversion ~55%.	133
Figure 6.3 ¹ H NMR spectrum of Boc-NPh ₂	135
Figure 6.4 ¹³ C NMR spectrum of Boc-NPh ₂	135
Figure 6.5 ¹ H NMR spectrum of Boc-CB.	136
Figure 6.6 ¹³ C NMR spectrum of Boc-CB.	136
Figure 6.7 FTIR spectrum of BOC-NPh ₂	137
Figure 6.8 FTIR spectrum of BOC-CB.	137
Figure 6.9 HOMO-LUMO band structures of the star-shaped repeating units.	141

Figure 6.10 HOMO-LUMO band structures of the idealized ring structures.....	143
Figure 6.11 SEM images of B-(Boc-NPh ₂) ₃	143
Figure 6.12 SEM images of B-(NPh ₂) ₃	144
Figure 6.13 SEM images of B-(BOC-CB) ₃	145
Figure 6.14 SEM images of B-CB ₃	146
Figure 6.15 SEM images of B-(BOC-CB) ₂ -BT.....	147
Figure 6.16 SEM images of B-CB ₂ -BT.....	148
Figure 6.17 ¹ H-NMR spectrum for estimation of the apparent quantum yield (AQY) of B ₂ -FL ₂ -BBT after a reaction time of 3 h. δ = 7.35 ppm (s, 1H, trichloroethylene), 4.98 ppm (s, 2H, C(O)-CH ₂ -Br, starting material), 2.80 ppm (s, 3H, C(O)-CH ₃ , product).....	152
Figure 6.18 ¹ H NMR spectrum of the linear polymer B ₂ -FL ₂ -BBT-L.....	153
Figure 6.19 Simple set-up of the dehalogenation of haloketones a 23 W household energy saving light bulb.....	153
Figure 6.20 ¹ H NMR spectrum of BOC-CB.....	155
Figure 6.21 ¹³ C NMR spectrum of BOC-CB.....	156
Figure 6.22 A simple photoinitiation set-up using a 23 W household energy saving light bulb.....	156
Figure 6.23 SEM image of B-(Boc-CB) ₂ BO.....	157
Figure 6.24 SEM image of B-(Boc-CB) ₂ -BO.....	157
Figure 6.25 SEM image of B-BO ₃	159
Figure 6.26 SEM image of Pd@B-BO ₃	160
Figure 6.27 TEM images of B-BO ₃	160
Figure 6.28 The photocatalytic reaction set-up. A water bath was used to avoid the photo-heating effect by monitoring the temperature during the reaction.....	161

List of Tables

Table 3.1 Selected examples of industrial processes based on heterogeneous catalysis.	5
Table 5.1 Porosity data of the CMPs.	35
Table 5.2 Oxidative coupling of benzylamines using the CMPs as photocatalyst. ^a	46
Table 5.3 Screening experiments of the oxidative coupling of benzylamines using B-BO-1,3,5 as photocatalyst. ^a	50
Table 5.4 Porosity data of the polymer networks.	53
Table 5.5 Photooxidative coupling of benzyl amine and its derivatives by the different poly(benzochalcogenadiazole)s under visible light irradiation. ^a	58
Table 5.6 Screening and control experiments of the oxidative coupling of benzyl amine and its derivatives using B-BT as photocatalyst. ^a	63
Table 5.7 Surface area and pore size characterizations of various poly(HIPE)s.	77
Table 5.8 Photocatalytic oxidation of thioanisole using π -conjugated polyHIPEs as heterogeneous photocatalysts under visible light: (a) thioanisole, (b) methyl phenyl sulfoxide and (c) methyl phenyl sulfone, and the optical and electronic properties.	84
Table 5.9 Repeating experiments of the selective photooxidation of thiolanisole.	87
Table 5.10 Selective oxidation of various sulfides using B-(Boc-CB) ₂ -BT as photocatalyst under visible light irradiation.*	87
Table 5.11 Surface area and pore size distribution data of the polymers.	96
Table 5.12 Visible light driven photoreductive dehalogenation of haloketones using the conjugated porous polymers as heterogeneous photocatalyst under irradiation of a 23 W household fluorescent light bulb.	100
Table 5.13 Visible light initiated free radical polymerization using B-(Boc-CB) ₂ -BO as photoinitiator at room temperature.	114
Table 5.14 Porosity data of B-BO ₃ and Pd@B-BO ₃	121
Table 5.15 Screening and mechanism study of the photocatalytic Suzuki coupling reaction using Pd@B-BO ₃ . ^a	124
Table 5.16 Scope of the photocatalytic Suzuki coupling reaction with various substituents using Pd@B-BO ₃ as photocatalyst. ^a	127

Table 6.1 HOMO-LUMO levels of the polymers calculated with Gaussian 09 using the density function theory RB3LYP/6311G method. 138

List of Acronyms

Atm	atmospheric pressure
AQY	apparent quantum yield
B	magnetic field
BBT	benzobisthiadiazole
BO	benzoxadiazole
BOC	tert-butylcarboxylate
BT	benzothiadiazole
BTF	benzotrifluoride
CB	conduction band
CMP	conjugated microporous polymer
C ₃ N ₄	carbonnitride
CPP	conjugated porous polymer
CV	cyclic voltammetry
3D	threedimensional
DFT	density functional theory
DMF	dimethylformamide
DOE	the department of energy
DRS	diffuse reflectance spectroscopy
E _a	activation energy
E _f	Fermi level
E _{p/2}	midpointpotential
E _{p,a}	anodicpeakpotential
E _{p,c}	cathodicpeakpotential
EPR	electron paramagnetic resonance spectroscopy

ESR	electron spin resonance
FTIR	fourier transform infrared
ΔG	Gibbs free energy
h	planck constant
h^+	positively charged hole
HIPE	high internal phase emulsion
HOMO	highest occupied molecular orbital
ICP	inductively coupled plasma
ISC	intersystem crossing
LED	light emitting diode
LUMO	lowest unoccupied molecular orbital
μ_B	Bohr magneton
MLCT	metal to ligand charge transfer
MMA	methyl methacrylate
NbBA	niobium hydroxide grafted with benzyl alcohol
NbMBA	niobium hydroxide grafted with 4-methoxybenzyl alcohol
NIR	near infrared
NMR	nuclear magnetic resonance
NP	nanoparticleP
P	steric factor
P_0	the saturated pressure of adsorbate gas
PDT	photodynamic therapy
PL	photoluminescence
R	gas constant
SCE	saturated calomel electrode

SEM	scanning electron microscopy
SP	surface plasmon
SPR	surface plasmon resonance
T	absolute temperature
TGA	thermalgravimetric analysis
THF	tetrahydrofuran
TON	turnover number
TPE	tetrakisphenylethene
UV	ultraviolet
V_T	potential energy of total interaction
V_A	potential energy of attractive interaction
V_a	the volume of gas adsorbed at STP
V_R	potential energy of repulsive interaction
V_m	energy barrier
V_B	valence band
Z	collision frequency

1 Introduction

Catalysis is one of the most important phenomena in chemistry and catalysts are the workhorses of the chemical industry, where approximately 85-90% of the products are made in catalytic processes. Catalysts enable chemical transformations to be carried out under industrially feasible conditions by offering energetically favorable alternative mechanisms to the non-catalytic reactions. The earliest example of catalysis is perhaps the use of yeast to trigger fermentation, during which sugar from grains or grapes is converted into ethyl alcohol. In fact, the origin of brewing can be dated back to the Sumerian cuneiform tablets and Egyptian hieroglyphics from more than 5000 years ago.¹ Since then, catalysts have penetrated into all aspects of our daily life and have become indispensable, for instance, in the production of transportation fuels in oil refineries all around the world and abatement of pollution in the end of pipes (e.g. automotive and industrial exhaust).

Compared to the more established thermal catalysis, photocatalysis, particularly visible light photocatalysis is an emerging field and still in its infancy in terms of industrial applications. However, the appreciation and use of sunlight were never new to life on Earth and mankind. Photosynthesis supports mankind with food to eat and oxygen to breathe. In the 14th century BC Egyptian Pharaoh Akhenaten rejected many old gods and introduced a monotheistic religion based on the sun-god Aton. Also, in the Christian genesis God said, “let there be light,” after he had created the earth and heaven. As one of the earliest examples of active use of photochemistry, it was reported that Egyptian physicians had been curing skin cancer by smearing bergamot oil onto the tumor and exposing the patient to sunlight. The oil-photosensitized formation of very reactive singlet oxygen is also utilized in modern medicine and termed photodynamic therapy (PDT) in cancer treatment. The “holy grail” of photocatalysis, which is the splitting of water into hydrogen and oxygen, was already discussed by Jules Verne in his book *The Mysterious Island* (1875): “Yes, my friends, I believe that water will one day be employed as fuel, that hydrogen and oxygen which constitute it will furnish an inexhaustible source of heat and light. Water will be the coal of the future.” Thanks to the research efforts from numerous groups in the past decades, visible light water splitting has gradually transformed from science fiction to scientific reality.²⁻¹¹ Apart from water splitting, a plethora of different organic transformations have also

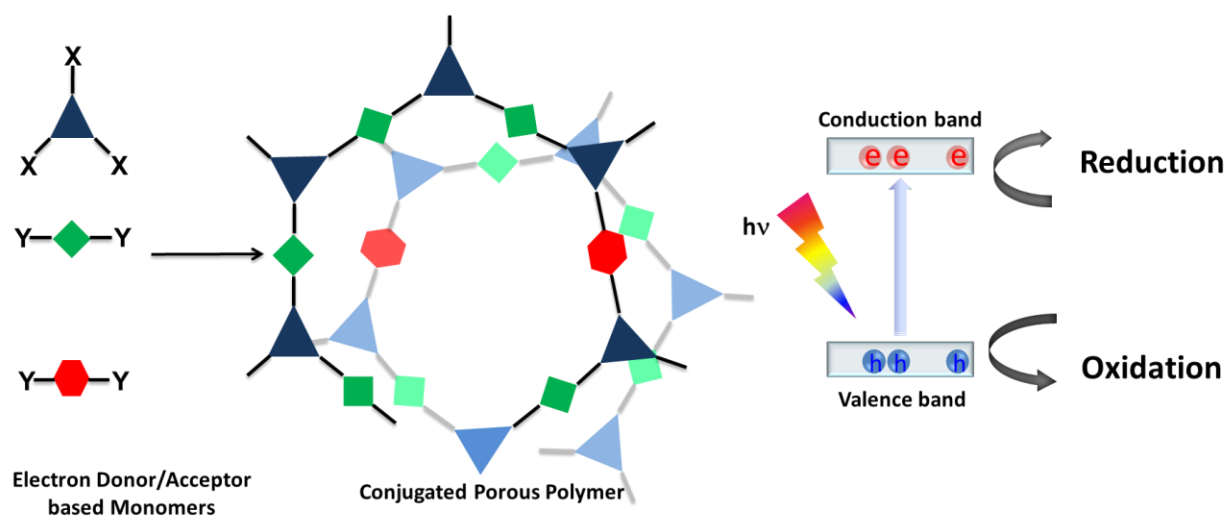
been realized by visible light photocatalysis, such as photocatalytic reduction of Cr^{6+} ,¹² photodegradation of dyes,¹³ photooxidation of benzene to phenol,¹⁴ photoreductive dehalogenation of phenacyl bromides,¹⁵ reduction of nitrobenzenes to anilines,¹⁶ reduction of hydrazides and hydrazines,¹⁷ radical cyclization reactions,^{18,19} aerobic oxidative hydroxylation of arylboronic acids,²⁰ oxidative conversion of thiobenzanilides to benzothiazoles,²¹ photoredox aza-Henry reaction,²² just to name a few.

Although exalted for their efficiencies, there are some intrinsic drawbacks associated with the homogeneous systems, such as high cost, toxicity of these rare metals, as well as limited availability and post-reaction purification steps for catalyst removal. The above-mentioned disadvantages have led material scientists to pursue the further development of stable, recyclable, reusable and transition metal-free photocatalysts for organic synthesis. Furthermore, heterogeneous catalysts can be easily integrated into continuous chemical processes, which are generally more efficient than batch processes and provide higher throughput per unit volume and unit time.

Conjugated microporous polymers were first reported by Cooper et al. in 2007, where various poly(aryleneethylene) networks with microporosity and surface areas as high as $834 \text{ m}^2/\text{g}$ were synthesized using palladium-catalyzed Sonogashira-Hagihara cross-coupling.²³ Since then, much attention has been dedicated to the synthesis and design of conjugated microporous polymers for a variety of interesting applications such as gas adsorption and storage,²⁴⁻³² light emitting,³³⁻³⁵ light harvesting,³⁶ energy storage,³⁷⁻³⁹ encapsulation of dyes and solvents,⁴⁰⁻⁴² chemical sensors,⁴³⁻⁴⁵ and heterogeneous catalysis.⁴⁶⁻⁵⁰ Conveniently combining low bandgap (i.e. visible light absorption) with microporosity as well as high interfacial surface area, conjugated microporous polymers (CMPs) are promising candidates as heterogeneous visible light photocatalysis.

2 Aim of the Work

In this work, the possibility of using conjugated porous polymers (CPP) as heterogeneous visible light photocatalyst is comprehensively explored. From the material science perspective, several critical parameters of the CPP photocatalysts could be independently varied, controlled and investigated in order to achieve enhanced photocatalytic efficiencies for targeted catalytic reactions. First, the valence and conduction band levels of the semiconducting CPP photocatalysts are of vital importance since the energy levels of the excited electron-hole pairs directly influence the type and reaction rate of accessible photoredox reactions. Second, as heterogeneous catalytic reactions usually occur at the interface between the catalyst and the reaction medium, higher surface areas of the CPP photocatalysts should in principle lead to enhanced photocatalytic efficiency. Next important parameter is the bandgap which dictates the light absorption range of the CPP photocatalysts and the lower the bandgap, the more visible light the corresponding photocatalyst can absorb. On the other hand, from the perspective of photocatalysis, a variety of photocatalytic reactions such as selective photooxidation of organic sulfides, photoreductive dehalogenation reactions, aerobic oxidative hydroxylation of arylboronic acids, photooxidative coupling of benzyl amines, photoinitiation of free radical polymerization as well as photoinduced Suzuki coupling reactions were closely examined by using CPPs as heterogeneous visible light photocatalysts to demonstrate their efficacy and versatility.



3 Theoretical Background

3.1 Catalysis

3.1.1 Fundamentals of Catalysis

A catalyst accelerates a chemical reaction by orders of magnitude, enabling them to be carried out under the most favorable thermodynamic regime and at much lower temperature and pressures. It does so by forming bonds with the reacting molecules, and by allowing them to react to form a product, which then detaches from the catalyst, and leaves it unaltered such that it is available for the next reaction.

According to reaction rate theories, the difference between an uncatalyzed and catalytic reaction can be described in the form of a potential energy diagram (Figure 3.1).

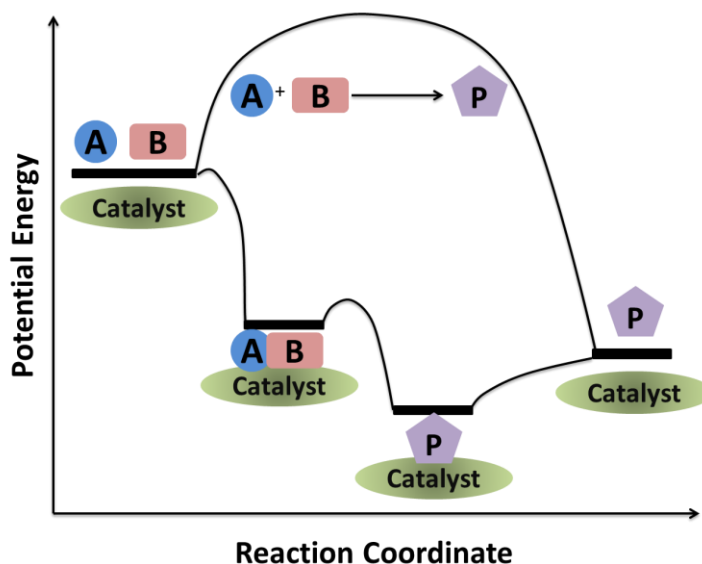


Figure 3.1 Potential energy diagram comparing uncatalyzed reaction route with a catalyzed route.

For the non catalytic reaction, the figure is simply the familiar way to visualize the Arrhenius equation, the reaction proceeds when A and B collide with sufficient energy to overcome the activation barrier. The change in Gibbs free energy between the reactants, A and B and the product P is ΔG . The catalytic reaction starts by the bonding of the reactant A and B to the catalyst, in a spontaneous reaction. The formation of the complex is exothermic and free energy

is lowered. While they are bound to the catalyst, A reacts with B. This step is associated with an activation energy, however, it is significantly lower than that of the uncatalyzed reaction. Finally, the product P separates from the catalyst. Because the activation energy of the catalytic route is significantly lower than that of the uncatalyzed route, the rate of the catalyzed reaction is much higher. The overall change in Gibbs free energy for the catalytic reaction equals that of the uncatalyzed reaction. Hence, the catalyst does not affect the equilibrium constant for the overall reaction. A catalyst changes the kinetics but not the thermodynamics. Furthermore, the catalyst accelerates both the forward and the reverse reaction to the same extent.

According to collision theory, the rate constant k is given by the following equation:

$$k = P \times Z \times e^{-\frac{E_a}{RT}}$$

where P is a steric factor, Z is the collision frequency, R is the gas constant, and T is the absolute temperature. In the presence of the catalyst, the activation energy E_a becomes much lower. In addition, a catalyst must not be consumed during the reaction. Turnover number (TON) is defined as the ratio of concentration of a product formed divided by the catalyst concentration. Only when TON is greater than one, the reaction is catalytic.

In homogeneous catalysis, both the catalyst and the reactants are in the same phase, i.e. all in the gas phase or more commonly, in the liquid phase. In heterogeneous catalysis, solid catalysts catalyze reactions in gas or liquid phase and catalytic reactions occur at the interface. Roughly 85-90% of all industrial chemical products are made in catalytic processes and overwhelming majority of these processes are based on heterogeneous catalysis (Table 3.1).

Table 3.1 Selected examples of industrial processes based on heterogeneous catalysis.

Reaction	Catalyst
Catalytic cracking of crude oil	Zeolites
Hydrotreating of crude oil	Co-Mo, Ni-Mo
Polymerization of ethylene, propylene	Cr, $TiCl_x/MgCl_2$
Ethylene epoxidation to ethylene oxide	Ag
Steam reforming of methane to $CO+H_2$	Ni
Ammonia synthesis	Fe

3.1.2 Visible Light Photocatalysis

Sunlight, a unique natural resource, is an ideal reagent for environmentally friendly, green chemical synthesis. It is non-toxic, waste-free and renewable. In 1912, pioneering chemist Giacomo Ciamician challenged his fellow contemporary scientists to imagine a chemical industry that could synthesize chemicals as plants do, by using sunlight as a clean, cheap and renewable resource. In a now-famous article named “The photochemistry of the future”, he envisioned a sustainable future chemical industry by writing “On the arid lands there will spring up industrial colonies without smoke and without smokestacks; forests of glass tubes will extend over the plains and glass buildings will rise everywhere; inside of these will take place the photochemical process that hitherto have been guarded secret of the plants, but that will have been mastered by human industry which will know how to make them bear even more abundant fruit than nature, for nature is not in a hurry and mankind is. And if in a distant future the supply of coal becomes completely exhausted, civilization will not be checked by that, for life and civilization will continue as long as the sun shines! If our black and nervous civilization, based on coal, shall be followed by a quieter civilization based on utilization of solar energy, that will not be harmful to progress and to human happiness.”⁵¹

The terms “photokatalyse” and “photokatalytisch” appeared probably the first time in the text book *Photochemie*, published by Plotnikov in 1910.⁵² Although a relatively old concept, no general agreement exists on the definition of the term photocatalysis. According to IUPAC (International Union of Pure and Applied Chemistry) photocatalysis is defined as “change in the rate of a chemical reaction or its initiation under the action of ultraviolet, visible, or infrared radiation in the presence of a substance-the photocatalyst-that absorbs light and is involved in the chemical transformation of the reaction partners”.⁵³ Reactions fulfilling this definition is called photocatalytic. This often includes photosensitization, “a process by which a photochemical alteration occurs in one molecular entity as a result of initial absorption of radiation by another molecular entity called photosensitizer”.

Visible light photons account for about 44% of the total solar energy reaching earth compared to 3% from ultraviolet (UV) irradiation (Figure 3.2). Compared to ultraviolet light, the use of visible light does not require special reaction vessels and can typically afford higher selectivity of the desired products. One major challenge that hindered the progress in the field of

visible light photocatalysis is the fact that most organic molecules do not absorb in the visible light range of the solar spectrum. Over the past years, the field has witnessed a resurging interest in the discovery and development of new visible light responsive photocatalysts, ranging from transition-metal based complexes, modified titania, organic dyes to metal-free graphitic C_3N_4 .⁵⁴⁻

64

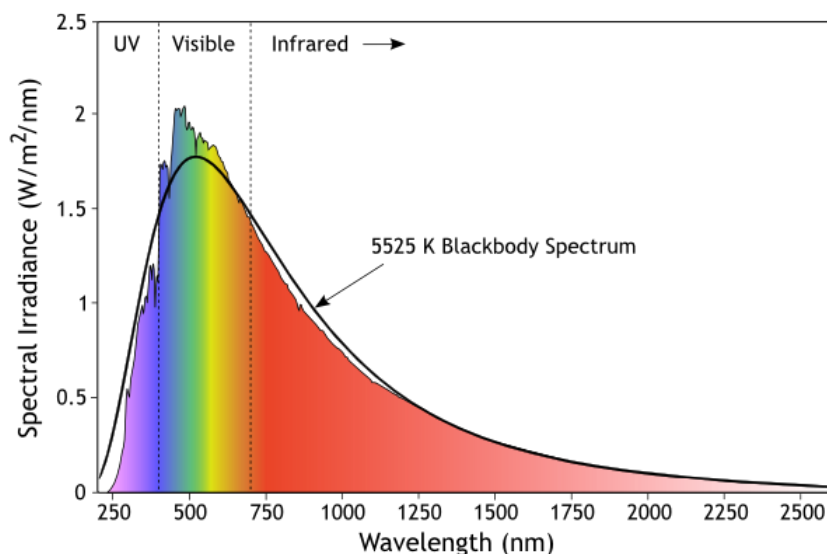


Figure 3.2 Solar Spectrum. Courtesy of Charles Chandler. Copyright SCS-INC.US

3.1.2.1 Visible Light Homogeneous Photocatalysis

In visible light homogeneous photocatalysis, the photocatalysts are soluble in the liquid phase and the catalytic reactions happen in solution. Two major categories of visible light homogeneous photocatalysts are transition-metal based complexes (e.g. Ru^{2+} or Ir^{3+})^{59,60} (Figure 3.3) and organic dye molecules (e.g. eosin or rhodamine B)^{65,66} (Figure 3.4) have been intensely investigated in the last two decades. The transition-metal based photocatalysts are commonly believed to have strong visible light absorption, long excited state lifetime and excellent stability under photolytic conditions. On the other hand, organic dye photocatalysts provide a metal-free, purely organic alternative to avoid the use of expensive and potentially toxic ruthenium and iridium salts. Visible light homogeneous photocatalytic reactions occur under extremely mild conditions, without most reactions proceeding at room temperature. The irradiation source is typically a commercial household light bulb. In addition, these catalysts are highly efficient and can be employed at very low loadings, with 1 mol% or less usually.

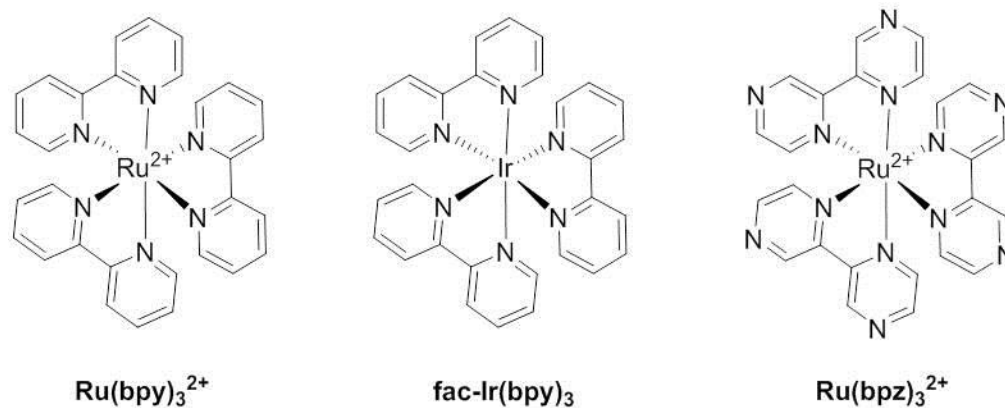


Figure 3.3 Ruthenium and iridium complexes.

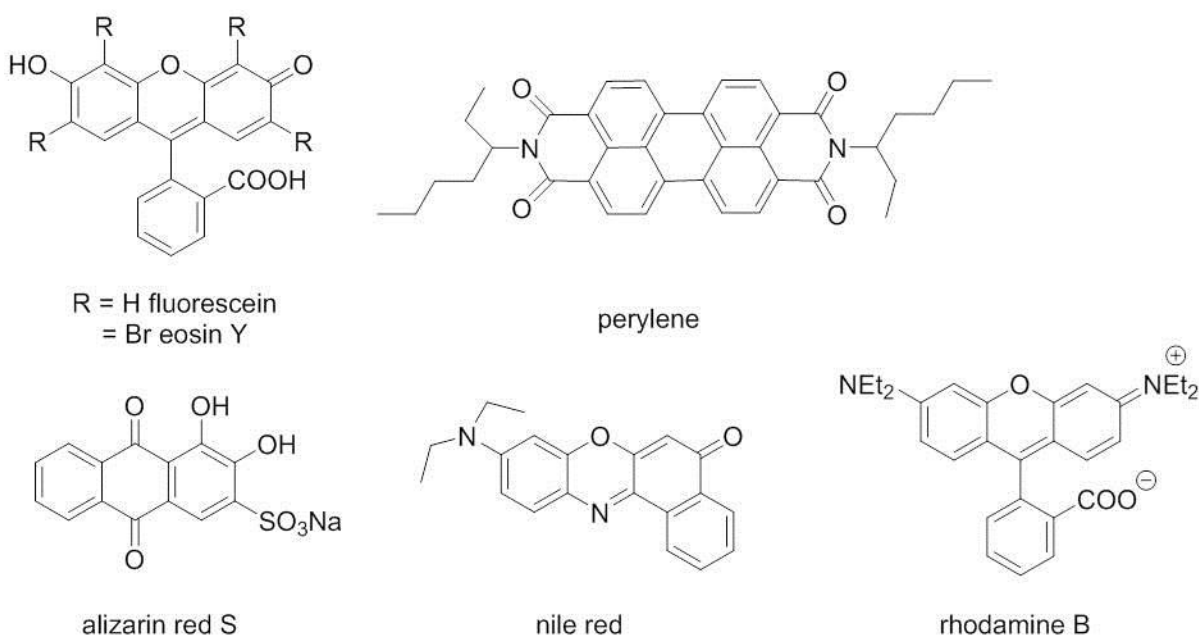


Figure 3.4 Selected organic dyes as photoredox catalysts.

Most visible light homogeneous photocatalysts, both metal-based and metal-free, share similar activation mechanisms. Take the prototypical photoredox catalyst $\text{Ru}(\text{bpy})_3^{2+}$ as an example, upon absorption of a photon in the visible region, an electron in one of the photocatalyst's metal-centered t_{2g} orbitals is excited to a ligand-centered π^* orbital,^{67,68} which is termed a metal to ligand charge transfer (MLCT) and results in the formation of Ru(III) oxidation state and a reduced state of the ligand framework.⁶⁹ The singlet MLCT state undergoes rapid intersystem crossing (ISC) to give the lowest-energy triplet state, which is the long-lived photoexcited species that engages in single-electron transfer and its long lifetime derives from

the fact that decay to the singlet ground state is spin-forbidden. The photoexcited species are both more oxidizing and more reducing than the ground-state species. For instance, the half-reaction $\text{Ru}(\text{bpy})_3^{3+} + \text{e}^- \rightarrow * \text{Ru}(\text{bpy})_3^{2+}$ is described by the reduction potential $E_{1/2}^{\text{III}/* \text{II}} = -0.81$ V vs the saturated calomel electrode (SCE),⁷⁰ which signifies that the excited-state $* \text{Ru}(\text{bpy})_3^{2+}$ is a much stronger electron donor than ground-state $\text{Ru}(\text{bpy})_3^{2+}$. Similarly, the $\text{Ru}(\text{bpy})_3^+$ is a much stronger oxidant than the ground state $\text{Ru}(\text{bpy})_3^{2+}$ ($E_{1/2}^{\text{II}/\text{I}} = -1.33$ V vs SCE). Upon excitation by light, photocatalyst $\text{Ru}(\text{bpy})_3^{2+}$ generates a higher-energy electron from the π^* orbital and serves as a reductant. At the same time, the photoexcitation reveals a lower-energy hole in the t_{2g} orbital, which can accept an electron and the photocatalyst acts as an oxidant.

3.1.2.2 Visible Light Heterogeneous Photocatalysis

In visible light heterogeneous photocatalysis, the catalysts are insoluble in solution and catalytic reactions presumably proceed at the interface between the solid and liquid phase. From a material science perspective, there are two major established categories of visible light heterogeneous photocatalysts, metal-oxide based photocatalysts and metal-free photocatalysts with graphitic carbon nitride photocatalysts being the most established.

Metal-oxide based photocatalysts, such as TiO_2 , Nb_2O_5 and ZnO , are typical large bandgap semiconductors. Since it is more appealing to use visible light photocatalysis for organic transformations, there have been many reports where surface complexes were formed by the interaction of TiO_2 with colourless carboxyl-group-containing molecules, such as ethylenediaminetetraacetic acid,⁷¹ trans-ferulic acid,⁷² or phenolic hydroxyl group,⁷³ to enhance the visible light absorption of the photocatalysts and to initiate photocatalytic reactions under visible light irradiation. In this case, metal oxides serve as platform for visible light induced organic reactions via forming surface complexation with substrates. Traditionally, the excitation of an electron from the valence band (VB) to the conduction band (CB) of a semiconductor metal oxide can only be achieved by UV irradiation due to its large bandgap. However, heteroatoms (X = O, S or N) in the substrates are electron rich atoms that can be easily activated and electrons from the heteroatoms can be injected into the CB of the metal oxide under visible light irradiation.⁷⁴⁻⁷⁸ For example, the oxidation of benzyl alcohols to corresponding carbonyl compounds with O_2 was achieved on anatase TiO_2 under visible light irradiation (Figure 3.5).⁷⁹ Excellent conversions and selectivities were achieved for a series of substituted benzyl alcohols.

Apart from anatase TiO₂, rutile TiO₂ nanorods have also been successful in the aerobic oxidation of benzyl alcohols to benzaldehydes with high selectivity of 99% under visible light.⁸⁰

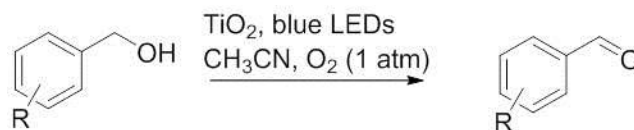


Figure 3.5 The oxidation of benzyl alcohols on TiO₂ under visible light.

Another effective method for the preparation of visible light responsive photocatalysts is to graft organic substrates on the surface of niobium hydroxide. It was reported that aromatic alkanes can be oxidized by O₂ in benzotrifluoride (BTF) using niobium hydroxide grafted with benzyl alcohol (NbBA) or 4-methoxybenzyl alcohol (NbMBA) as an efficient visible light photocatalyst (Figure 3.6).⁸¹ The resulted photocatalysts led to high conversions of the substrates and high selectivity for the corresponding aldehydes or ketones.

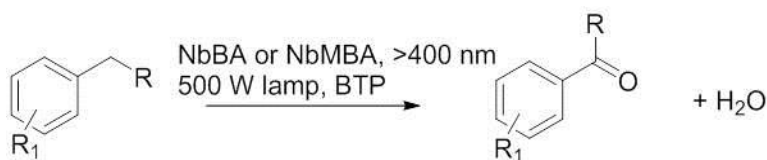


Figure 3.6 Selective aerobic oxidation of alkyl aromatics.

Although a plethora of studies regarding visible light induced organic reactions on the surface of metal oxides have been reported, the substrates that can form surface complexations and then undergo organic transformations are limited. Another method to accommodate a broader range of substrates takes advantage of the surface plasmon resonance (SPR) effect. SPR is the collective oscillation of electrons in a solid or liquid, which is stimulated when the frequency of the incident light photons matches the natural frequency of surface electrons oscillating against the restoring force of positive nuclei. The absorbance spectra surface plasmon bands of Au, Ag and Cu nanoparticles (NPs) show maxima at around 530, 400 and 580 nm, respectively, due to the localized SPR effect.⁸²

Upon visible light irradiation, electrons below the Fermi level (E_f) of the plasmonic NPs are excited to the surface plasmon (SP) states and leave positively charged holes (h^+) below E_f (Figure 3.7). The SP state electrons are then injected into the CB of the metal oxide and

transferred to electron acceptors such as O_2 . In the meantime, h^+ is quenched by organic substrate to complete the photocatalytic cycle.

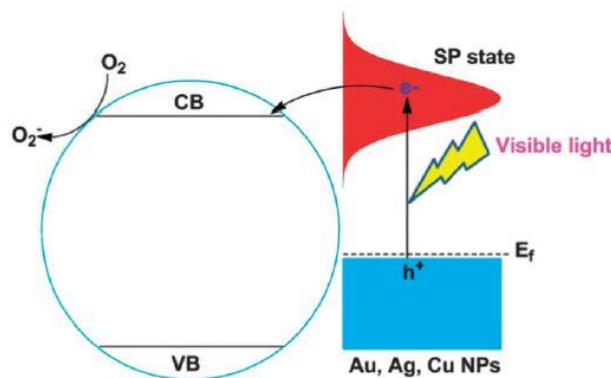


Figure 3.7 Surface plasmonic metal (Au, Ag or Cu) NPs for visible light induced reactions. Adapted from Lang et al.⁶¹ Copyright (2014) Royal Society of Chemistry.

As an example, it has been reported that Au/CeO₂ can be prepared by photochemical deposition of H₄AuCl₄ on CeO₂ in the presence of citric acid as the reducing agent. With 530 nm LED irradiation, aromatic alcohols can be selectively oxidized into corresponding aldehydes with O₂ in water.⁸³ In addition, Au/CeO₂ can also be prepared by multistep photodeposition method, which leads to larger Au NPs than those prepared by the single-step method. These catalysts were used for the selective oxidation of 4-aminobenzyl alcohol to 4-aminobenzaldehyde under visible light.⁸⁴

In short, various plasmonic photocatalysts have been shown to be efficient photocatalysts in driving versatile selective organic transformations under visible light irradiation.⁸⁵⁻⁹¹ Nonetheless, the preparation of these photocatalysts require the use of expensive noble metals, such as Au and Ag, which makes them economically uncompetitive when compared with other earth-abundant materials and metal free visible light photocatalysts, such as g-C₃N₄.

Polymeric graphitic carbon nitride (g-C₃N₄) is a graphene-like layered material which comprises C, N and H impurities. Due to its medium range bandgap and high structural stability, g-C₃N₄ has been widely used as a metal-free visible light photocatalyst for various redox reactions, such as oxidation of aromatic and aliphatic alcohols,^{92,93} oxidation of primary benzylic amines and secondary benzylic amines to corresponding imines,⁹² oxidation of sulfides to sulfoxides,⁹⁴ and C-C bond formation with N-aryltetrahydroisoquinolines.⁹⁵ Additionally, g-

C₃N₄ was also employed as support material for transition metals for the more challenging sp² C-H activation of benzene (Figure 3.8).¹⁴ Specifically, Fe-g-C₃N₄ supported on ordered mesoporous silica SBA-15 achieved higher photocatalytic activity than bulk g-C₃N₄ thanks to the enhanced surface area.

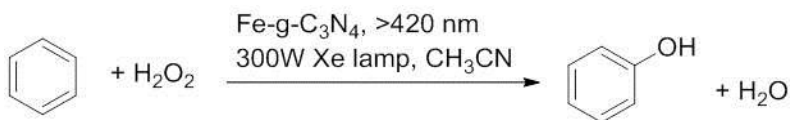


Figure 3.8 Hydroxylation of benzene with H₂O₂.

Graphitic carbon nitride is an intriguing metal-free visible light photocatalyst that possesses excellent chemical stability and tunable electronic structure. Tremendous amount of efforts have been invested in the design and preparation of various g-C₃N₄ based catalytic systems to tackle environmental and energy challenges in the past decade, the details of which are excellently summarized in several recent review articles.⁹⁶⁻⁹⁸

3.2 Conjugated Polymers

Conjugate comes from the Latin word *conjugatus*, meaning to join or unite. A conjugated polymer is a carbon based macromolecule through which the valence π electrons are delocalized. The conjugation refers to the resonance interaction between the π bonds resulting in delocalized π electron states. Figure 3.9 illustrates some examples of linear conjugated polymers. For example, the ground state structure of polyacetylene is composed of alternating single and double bonds. In 1977, Shirakawa, Heeger and MacDiarmid found that films of polyacetylene increase their conductivity tremendously when they are exposed to iodine vapor, from the lower end of the semiconducting range up to metal range. Figure 3.10 shows that the iodine dopant induced changes in comparison with other materials, which encompass an enormous range of 17 orders of magnitude. The development of conjugated polymers by Heeger, MacDiarmid, and Shirakawa was recognized with the 2000 Nobel Prize in Chemistry.

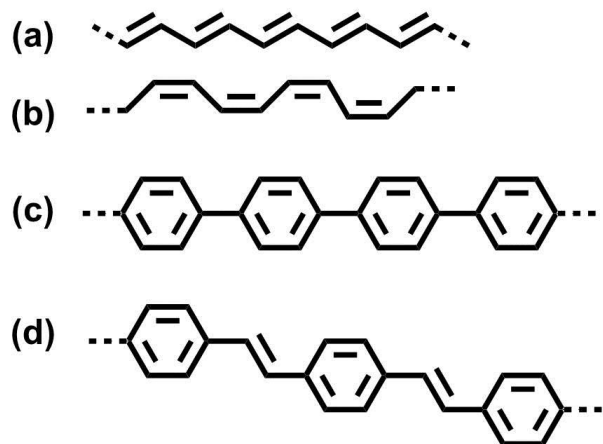


Figure 3.9 (a) Trans-polyacetylene (b) cis-polyacetylene (c) poly(para-phenylene) and (d) poly(para-phenylene vinylene).

Owing to their high conductivity and intriguing optoelectronic properties, conjugated polymers have attracted widespread attention over the last three decades. The electronic and optical properties of conjugated polymers, combined with their mechanical properties and intrinsic processing advantages, make them particularly attractive materials for the electronics industry. Their applications include light emitting devices,⁹⁹⁻¹⁰¹ nonlinear optical devices,^{102,103} photovoltaic devices,^{104,105} plastic field effect transistors^{106,107} and electromagnetic shielding.^{108,109}

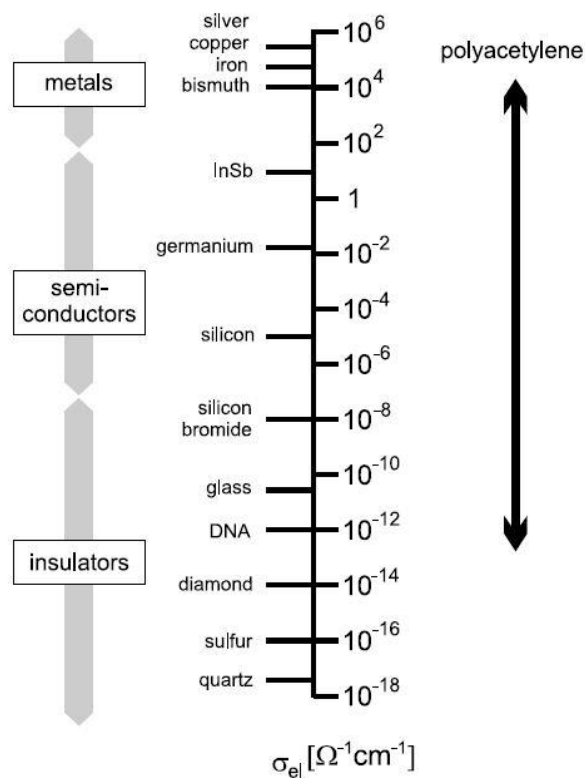


Figure 3.10 Range of conductivities covered by doped polyacetylene in a comparison with other materials. Adapted from The Physics of Polymers.¹¹⁰ Copyright (2007) Springer.

Different from traditional polymers (e.g. polyethylene, polypropylene, poly(ethylene terephthalate) or polystyrene), which are colorless and have no mobile charges, conjugated polymers are semiconductors that can interact with light. The bandgaps of conjugated polymers are in the range of 1.5 eV to 3 eV, i.e. in the range of visible light and near infrared, similar to inorganic semiconductors.

3.2.1 Synthesis of Conjugated Polymers

Conjugated polymers possess high conductivity and unique electrochemical properties,¹¹¹⁻¹¹⁴ which are strongly influenced by the type of the conjugation system, the maximum effective conjugation length, stereoregularity, regioregularity, and the characteristics of the substituents in the polymers. Oxidative polymerization has been widely utilized for the synthesis of π -conjugated polymers containing heteroaromatic rings. For example, polypyrroles that bear the nitrogen-containing heteroaromatic rings have been prepared by electrochemical oxidative reactions of the corresponding monomers.¹¹⁵ However, the electrochemical

polymerization methods do have some disadvantages. For example, the polymerization can be adversely affected by the bulkiness of the substituents of the monomers and are likely to result in structurally irregular polymers with crosslinked bonds. To circumvent these problems, the transition-metal-catalyzed cross-coupling reactions have been generally applied and well-defined polymers with good regioregularity have been synthesized.¹¹⁶⁻¹¹⁸ Some examples of common transition-metal-catalyzed cross-coupling reactions include Kumada-Tamao-Corriu coupling, Negishi coupling, Migita-Kosugi-Stille coupling, Suzuki-Miyaura coupling, Sonogashira-Hagihara coupling and etc. (The pioneering work of Heck, Suzuki, and Negishi on Pd-catalyzed cross-coupling reaction in organic synthesis was recognized with the 2010 Nobel Prize in Chemistry.) The focus will be placed on the Suzuki-Miyaura coupling and Sonogashira-Hagihara coupling in the following section since they are main methods used in this thesis.

3.2.1.1 Suzuki-Miyaura Coupling

Suzuki-Miyaura cross-coupling reaction protocol was developed by Suzuki and Miyaura at Hokkaido University, Japan in 1979.^{119,120} The coupling reaction uses organoboron reagents with the help of a base as an activator under palladium catalysis (Figure 3.11). Its wide applicability can be attributed to several intrinsic advantages: (1) the stability of organoboronic acids to water, air and heat; (2) the high functional group tolerance of organoboron compounds; and (3) a lower toxicity of the boron-containing by-products produced by the reactions. In general, most cross-coupling reactions are believed to go through three major steps: oxidative addition, transmetalation, and reductive elimination in a catalytic cycle.

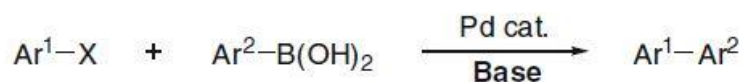


Figure 3.11 Reaction scheme of Suzuki-Miyaura coupling.

The mechanism of the Suzuki cross-coupling is analogous to the catalytic cycle for the other cross-coupling reactions (Figure 3.12) and has four steps: (1) oxidative addition of an organic halide to the Pd(0)-species to form Pd(II); (2) exchange of the anion attached to the palladium for the anion of the base (metathesis); (3) transmetalation between Pd(II) and the alkylborate complex; and (4) reductive elimination to form the C-C bond and regeneration of Pd(0). The rate determining step of the catalytic cycle is believed to be the oxidative addition

step. The role of the base is to activate the boron-containing reagent and the reaction does not occur without the base. The base is postulated to serve one of two possible roles: (1) reaction with organoboron reagent to form a trialkoxyboronate which then attacks the palladium halide complex, or (2) by conversion of the palladium halide to a palladium oxo complex that reacts with the neutral organoboron reagent.¹²¹ However, the exact mechanism is still debatable.

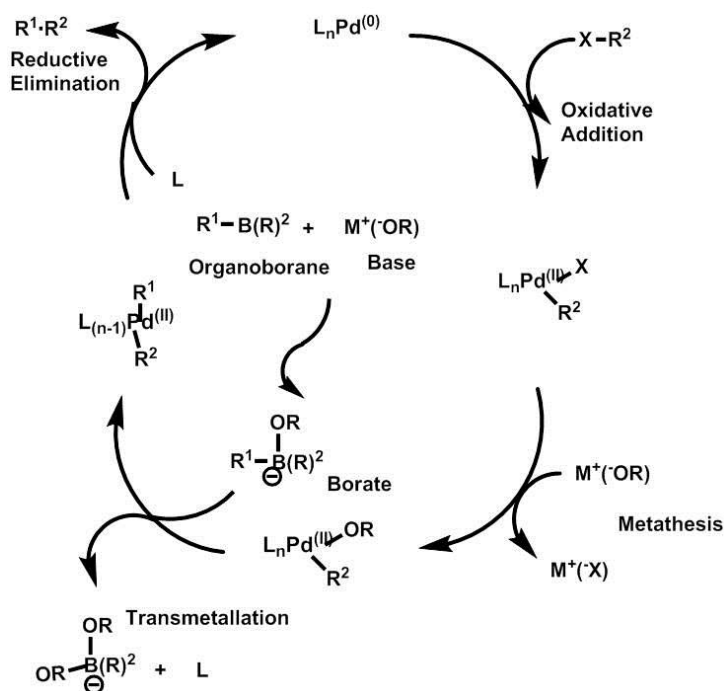


Figure 3.12 The mechanism of the Suzuki cross-coupling reaction. Adapted from *Strategic Applications of Named Reactions in Organic Synthesis*.¹²² Copyright (2005) Elsevier.

3.2.1.2 Sonogashira-Hagihara Coupling

Sonogashira and Hagihara reported on the cross-coupling reactions of acetylene gas or the terminal alkynes with aryl or alkenyl halides in the presence of palladium catalysts and copper(I) salts in 1975.¹²³ They showed that with the addition of copper (I) salts as co-catalyst, product yields can be improved. It was found that copper (I) salts and amines are necessary additives to generate alkynylcopper species from terminal alkynes, which is an important intermediate for smooth transmetalation to Pd.¹²⁴⁻¹²⁶ Several advantages of this reaction (Figure 3.13) are: (1) the coupling can be conducted at mild reaction conditions; (2) the solvents and reagents do not have to be rigorously dried; (3) the coupling is stereospecific and the stereochemical information of the substrates is preserved.

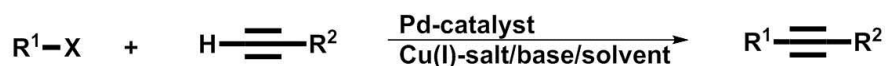


Figure 3.13 Reaction scheme of Sonogashira-Hagihara coupling.

Similar to Suzuki-Miyaura cross-coupling reaction, the mechanism of the Sonogashira cross-coupling (Figure 3.14) follows the general oxidative addition-reductive elimination pathway.¹²⁷⁻¹²⁹ However, the structure of the catalytically active species and the exact role of the copper (I) catalyst is still not clear. First, a coordinatively unsaturated Pd(0) species is generated from a Pd(II) complex by reduction with the alkyne substrate or with an added phosphine ligand. The Pd(0) subsequently undergoes oxidative addition with the aryl or vinyl halide followed by transmetalation by the copper(I)-acetylide. At the end, the coupled product is formed by reductive elimination and the catalyst is regenerated to complete the catalytic cycle.

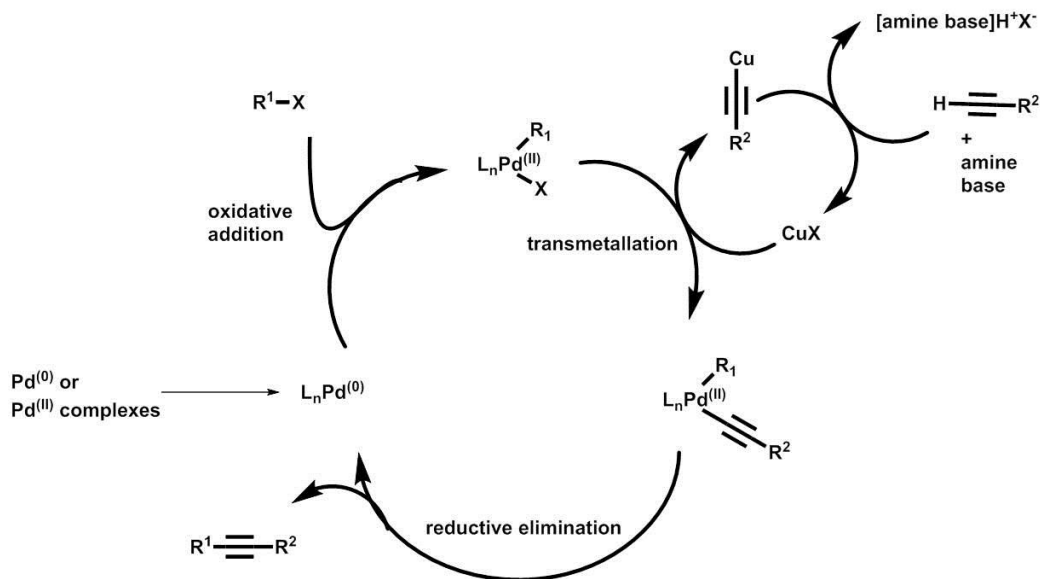


Figure 3.14 Reaction mechanism of Sonogashira-Hagihara coupling. Adapted from *Strategic Applications of Named Reactions in Organic Synthesis*.¹²² Copyright (2005) Elsevier.

3.2.2 Conjugated Porous Polymers

Conjugated porous polymers (CPPs) are a class of amorphous three-dimensional (3D) networks that are linked in a p-conjugated fashion. These structures are unique and are not available in other non-conjugated porous materials. The first conjugated microporous polymer was discovered by Cooper in 2007,²³ many material scientists have contributed to the rapid

growth of this field since then. Although a relatively young field, the development of CPPs has benefited greatly from a diverse pool of building blocks⁴⁶ and the wide availability of different reaction types. From a synthetic perspective, typical synthetic protocols employed for the preparation of CPPs include Suzuki cross-coupling reaction,^{130,131} Yamamoto reaction,^{132,133} Sonogashira-Hagihara reaction,^{134,135} oxidative coupling,^{136,137} Schiff-base reaction,^{138,139} cyclotrimerization,^{140,141} phenazine ring fusion reaction^{142,143} and Friedel-Crafts arylation.^{144,145}

Depending on the targeted applications, the chemical structure and physical morphology of CPPs can be controlled by various methods. For example, it was found recently that the morphology of a phenylethynylene CPP changed from spherical to tubular and platelet when the reaction solvent was changed from toluene to p-xylene and mesitylene.¹⁴⁶ The variation in macroscopic morphology resulted in different organic solvent adsorption efficiency with the platelet morphology being the best.

Furthermore, recent studies reported that the pore size and pore volume of the CPPs can be precisely controlled varying the linker length.¹⁴⁷ It was found that CPP with different linkers exhibited BET surface area of 512 up to 1018 m²g⁻¹ and the pore volumes of 0.16 to 0.38 cm³g⁻¹. In addition, good structural control has also been achieved by using linkers with different geometries.¹⁴⁸ Apart from two-component systems, systems with three reactive units have also been developed using a statistical copolymerization scheme for good control of porosity.¹⁴⁷ Several recent reviews on CPPs provide excellent overview of the synthesis and property controls for this new type of material.^{46,149}

3.2.3 Applications of Conjugated Porous Polymers

3.2.3.1 Heterogeneous Catalysis

Heterogeneous catalysis is also an important application of conjugated porous polymers, which have the capability of integrating various functionalities in their skeletons. The first examples of CPP-based catalytic systems employed metalloporphyrin functional units as active sites and displayed high catalytic activity with high conversions and turnover numbers.^{47,48} Chiral CPPs based on 1,10-binaphthyl were also developed and after complexation with titanium ions, the catalysts exhibits good activity and modest enantioselectivity for asymmetric diethylzinc addition to aldehydes.⁴⁹

The first reported CPPs for heterogeneous visible light photocatalysis were a benzothiadiazole based system with surface area up to $660 \text{ m}^2 \text{ g}^{-1}$ and achieved high conversion of 96% for the oxidation of terpinene upon irradiation at 420 nm.¹⁵⁰ After post-synthesis modification using thiol-yne chemistry, hydrophobic CPP photocatalysts became water-dispersible and were used for photoinduced singlet oxygen generation, which transformed furoic acid to 5-hydroxy-2(5H)-furanone with 90% conversion in aqueous solution upon visible light irradiation.¹⁵¹ Since then, various different structures, novel synthetic methodologies and challenging photoredox catalytic reactions have been reported using CPP as efficient heterogeneous visible light photocatalysts. For example, conjugated microporous polyHIPEs were prepared via high internal phase emulsion polymerization technique and were studied in a continuous flow reaction setup to achieve complete conversion of alpha-terpinene into ascaridole.¹⁵² Except for the generation of singlet oxygen, CPP photocatalysts were found to be effective in the photodegradation of organic dyes,^{153,154} visible light driven hydrogen evolution,¹⁵⁵ water splitting,¹⁵⁶ oxidative hydroxylation of arylboronic acids, aza-Henry reactions¹⁵⁷, and photooxidative coupling of benzylamines.¹⁵⁸

3.2.3.2 Gas Adsorption

Conjugated porous polymers (CPPs) are a unique type of materials that combine π -conjugation with high surface area (i.e. porosity) and their structures can be synthetically controlled at the molecular level. Various recent studies have demonstrated their potential for a range of challenging energy and environmental issues, such as gas adsorption, heterogeneous catalysis, light emitting, light harvesting and electric energy storage. Only selected representative examples are briefly mentioned below. Excellent recent reviews offer a more comprehensive summary of the current field.^{46,149} The Department of Energy (DOE) target for hydrogen storage by 2015 is set at 9 wt% at 81 kg m^{-3} in the range of 253-323 K and at a pressure of 100 atm. CPPs with microporosity and high surface areas ($>3000 \text{ m}^2 \text{ g}^{-1}$) are of high interest for this type of application.

Apart from hydrogen, the adsorption of carbon dioxide, a type of greenhouse gas, and methane have also been investigated with CPPs. According to the DOE, the target value for methane storage is 180 cm^3 (STP) at 35 bar and 298 K. Xiang et al reported that COP-1 showed a CH_4 uptake capacity of 29 mg g^{-1} at 298 K and 18 bar, whereas the capacity increased to 39 mg

g^{-1} for Li@COP-1 after loading Li ions.¹⁵⁹ However, the uptake capacity is still relatively low compared to the reported 187 mg g^{-1} for COFs¹⁶⁰ and 220 mg g^{-1} for MOFs.¹⁶¹

3.2.3.3 Chemical Encapsulation

Other than small molecules like gases, the pores of CPPs are also accessible to larger organic molecules such as organic solvents and dyes. Wang et al. synthesized a porphyrin-based porous polymer PCPF-1 via Yamamoto reaction.⁴¹ The polymer is highly hydrophobic with a contact angle of 135° , and has a BET surface area of $1333 \text{ m}^2 \text{ g}^{-1}$ and a pore volume of $9.86 \text{ cm}^3 \text{ g}^{-1}$. It was found that the PCPF-1 polymer (1 g) can adsorb 14.7 g of n-pentane, 1.67 g of n-hexane, 22.5 g of cyclohexane and 20.5 g of gasoline, respectively, which shows great potential for the recovery of oil from water.

Similarly, amines are important chemicals but can cause severe environmental pollution and health damage if spilled. Liu et al. Prepared a series of metalloporphyrin-based CPP superabsorbents with BET surface areas of 1140, 1247 and $1080 \text{ m}^2 \text{ g}^{-1}$ in $\text{ZnP}_1\text{-CMP}$, $\text{CuP}_1\text{-CMP}$ and $\text{CoP}_1\text{-CMP}$, respectively.¹⁶² The authors found that the uptake capacities depend on the metal center species and $\text{CuP}_1\text{-CMP}$ is nearly as effective as $\text{ZnP}_1\text{-CMP}$, while $\text{CoP}_1\text{-CMP}$ is relatively less efficient. The differences in effectiveness was attributed to the different electron densities formed around different metal centers.

3.2.3.4 Light Emission

The conjugated skeletons in CPP systems afford them unique visible light absorption and highly efficient luminescence. Xu et al reported a highly luminescent CPP with tetrakisphenylethene (TPE) as a building block.³³ The authors found that an interweaving CPP architecture promoted π conjugation and exciton migration, which led to improved luminescence activity. The resulting CPP particles grew larger in size, showed increased surface area and exhibited a red-shifted electronic absorption band when reaction time is elongated. The crosslinked CPP polymers exhibited fluorescence quantum yield of as high as 40% compared to the 0.65% of linear polymer under otherwise identical conditions. In addition, the CPP polymer displayed high luminescence in various solvents, such as methanol, dichloromethane, THF, chloroform and water, whereas the linear polymer counterpart was found to be nonemissive in dichloromethane, chloroform and THF.

A more recent study by Xu et al. reported a core-shell strategy to achieve color-tunable light emission.³⁴ A one-pot two-stage synthetic protocol was employed. A blue luminescent PP-CMP core was first prepared and then a yellow luminescent TPE-CMP shell was added on the exterior surface of the core. Similarly, an inverse core-shell CPP architecture with a TPE-CMP core and PP-CMP shell was also prepared. Both systems exhibited redshifts in absorption band compared to the PP-CMP. The authors attributed this finding to the better π conjugated afforded by the core-shell design. Furthermore, it was found that the emission wavelength of the core-shell CPPs shift to longer wavelength when the shell becomes thicker. As a result, changing the shell thickness continuously can tune the emission from deep blue, near white to green. Similar to the previous reports, the CPP polymer showed much higher fluorescence quantum yield than their linear counterparts and maintained high luminescence in various solvents, including dichloromethane, chloroform, hexane, DMF, THF, benzene, and water.

3.3 Emulsion Polymerization

3.3.1 Colloids and their Stability

A colloid is a heterophase mixture containing at least two immiscible components, dispersed phase and continuous phase. Familiar examples of colloidal systems include fog, mist and smokes (dispersions of fine liquid droplets or solid particles in a gas - aerosols); milk (a dispersion of fine droplets of fat in an aqueous phase - emulsions); paint, muds and slurries (dispersions of fine solid particles in a liquid medium – sols or colloidal suspensions); jellies (dispersions of macromolecules in liquid - gels); opal and ruby stained glass (dispersions of solid silica particles in a solid matrix or of gold particles in glass – solid dispersions). The stability of colloids depends on the balance of the attractive and repulsive forces between individual particles.

To maintain colloid stability, repulsive forces between particles have to be introduced to counter-balance the attractive force (e.g. van der Waals forces). There are two major types of stabilization methods, electrostatic stabilization and steric stabilization. Electrostatic stabilization is achieved with charged surfactants or stabilizers and is based on the coulomb repulsion of two similarly charged surfaces. The colloid stability is determined by the combination of van der

Waals attraction and electrostatic repulsion, which is known as DLVO (Derjaguin and Landau, Verwey and Overbeek) theory^{163,164}:

$$V_T = V_A + V_R$$

where V_T is the potential energy of the total interaction, V_A the attractive interaction and V_R the repulsive interaction (Figure 3.15). When two charged particles approach each other, there exists an energy barrier (V_m) that has to be overcome. Without sufficient energy, the particles stay separated from each other and the colloidal dispersion is stable. With sufficient energy, the attractive forces dominate, draw the particles together and irreversible coagulation (primary minimum) occurs.

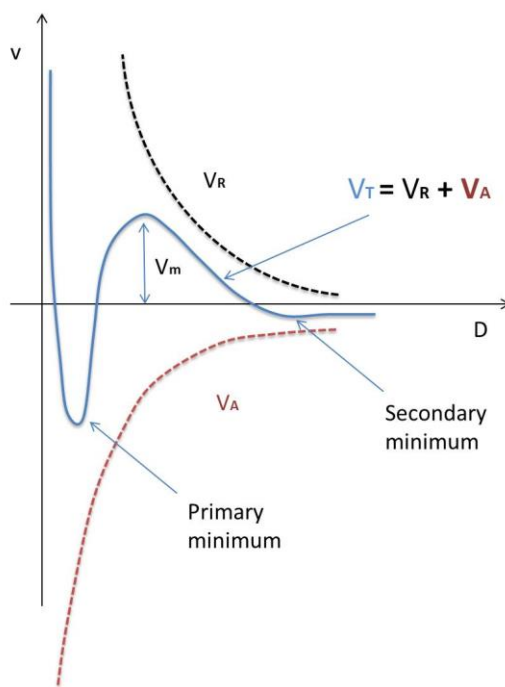


Figure 3.15 Illustration of interaction potential between two particles as a function of distance according to DLVO theory. Adapted from Napper.¹⁶⁵ Copyright (1970) American Chemical Society.

Steric stabilization takes advantage of the steric hindrance effect provided by the non-ionic polymers that are adsorbed on the surface of the particles.¹⁶⁶ The polymers usually consist of one section with high affinity for the dispersed phase and another section that ensures solubility in the continuous phase. When all colloidal particles are well-dispersed in the continuous phase, the polymer surfactant achieves its maximum entropy. It is energetically

unfavorable for two colloidal particles to approach and interact with each other since it reduces the freedom of the polymer surfactant in the continuous phase. The system is stable when the steric repulsive forces are larger than the van der Waals attractive forces.

3.3.2 High Internal Phase Emulsion (HIPE)

PolyHIPEs are porous emulsion-templated polymer polymers synthesized by high internal phase emulsions (HIPEs).¹⁶⁷ HIPEs are highly viscous emulsions in which the “internal” phase consists of more than 74% of the volume and is dispersed within a continuous “external” phase.¹⁶⁸⁻¹⁷⁰ One familiar example of HIPE in everyday life is mayonnaise, where the internal phase is vegetable oil dispersed in the continuous phase, vinegar, and the lecithin in egg yolk functions as the surfactant. Sorbitan monooleate (Span 80®) is the most commonly used emulsifier for water-in-oil stabilization. The formation of a typical water-in-oil HIPE and the synthesis of a typical polyHIPE are illustrated in Figure 3.16. The structures of the original HIPE and the resulting polyHIPE are usually very different because droplet coalescence and/or Ostwald ripening can occur during polymerization. Ruptures or interconnects are formed at the thinnest points of the external phase surrounding the internal phase. After removing the internal phase, a highly porous structure with interconnected cells is obtained. Figure 3.17 shows a typical polyHIPE porous structure with interconnecting holes. PolyHIPEs have been investigated for a myriad of applications, such as supports for separation membranes,^{171,172} tissue engineering scaffolds¹⁷³ and templates for the synthesis of porous ceramics.¹⁷⁴

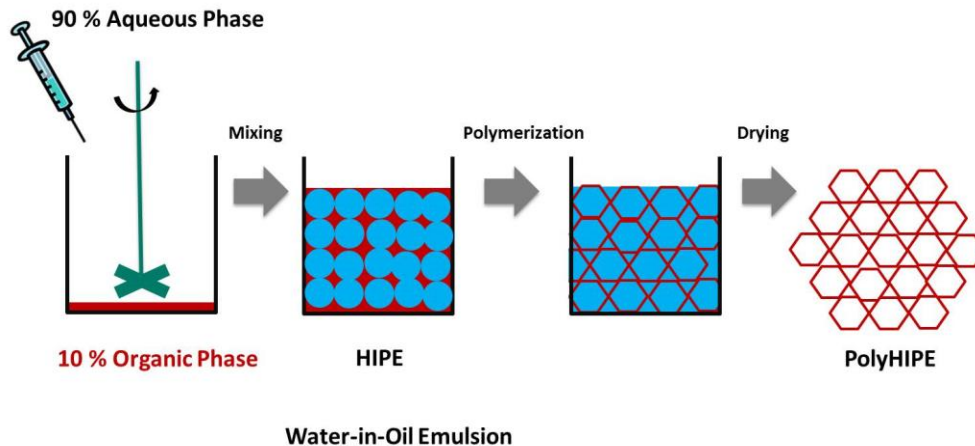


Figure 3.16 Schematic illustration of HIPE formation and polyHIPE synthesis within a water in oil HIPE (an aqueous internal phase dispersed within a hydrophobic external phase).

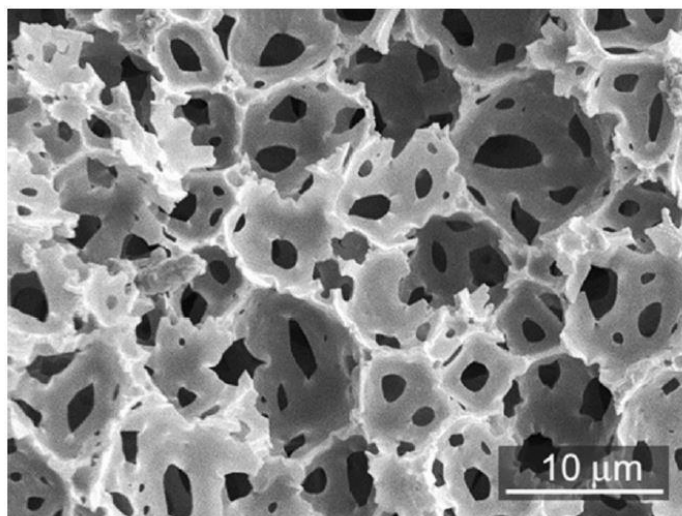


Figure 3.17 Scanning electron microscopy (SEM) image of typical porous polyHIPE structure. Adapted from Sergienko et al.¹⁷⁵ Copyright (2002) Wiley VCH.

4 Characterization Techniques

4.1 UV/Vis Diffuse Reflectance Spectroscopy

Diffuse reflectance spectroscopy (DRS) is very closely related to UV/Vis spectroscopy.^{176,177} Since light cannot penetrate opaque samples (e.g. powder samples) and is reflected. DRS measures the relative change in the amount of reflected light off of a surface, whereas the UV/Vis spectroscopy measures the relative change of the transmitted light as it passes through a solution or a thin film. There are two kinds of reflectance, specular and diffuse. Specular reflectance refers to the part of the incident beam reflected at the same angle as the angle of incident light. For example, mirrors typically produce specular reflectance when used as samples. The incident light scattered in different directions is called “diffuse reflection”. Powders produce diffuse reflectance when used as samples. Most samples produce a combination of both.

4.2 Brunauer, Emmett and Teller (BET) Surface Area Analysis

Based on the literature survey by Brunauer et al.,¹⁷⁸ a classification of six sorption isotherms was published by IUPAC in 1985 (Figure 4.1).¹⁷⁹ Type I isotherms are obtained when adsorption is limited to only a few molecular layers and is often obtained on microporous materials. Type II isotherms are usually obtained in case of non-porous or macroporous materials. Point B is the inflection point of the isotherm, which indicates that monolayer coverage is complete and multilayer adsorption begins. Type IV isotherms are commonly observed for mesoporous materials. The hysteresis loop is associated with the occurrence of pore condensation. In type V isotherms, the initial part of the sorption isotherms is similar to type III, which is convex to the P/P_0 axis, indicating weak attractive interactions between the adsorbent and the adsorbate. Type VI isotherm represents stepwise multilayer adsorption on a uniform, non-porous surface.

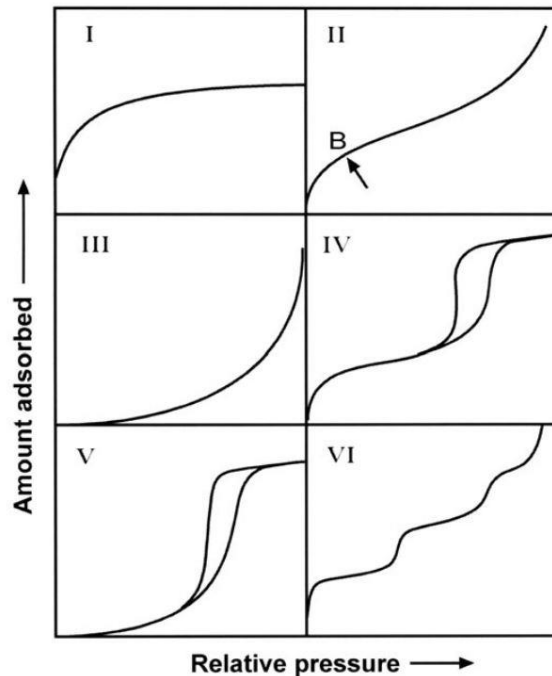


Figure 4.1 IUPAC classification of sorption isotherms. Adapted from Sing et al.¹⁷⁹ Copyright (1985) Blackwell Science Ltd.

The Langmuir equation is more applicable to chemisorption, where a chemisorbed monolayer is formed. In 1938, Brunauer, Emmett and Teller extended Langmuir's kinetic theory to multilayer adsorption and arrived at **Error! Reference source not found.**, where P is the partial vapour pressure of the adsorbate gas in equilibrium with the surface at 77.4 K, P_0 is the saturated pressure of adsorbate gas, V_a is the volume of gas adsorbed at STP, V_m is the volume of gas adsorbed at STP to produce an monolayer on the sample surface, C is a dimensionless constant related to the enthalpy of adsorption of the adsorbate gas on the sample. The BET theory assumes that molecules in the uppermost layer of the adsorbed stacks are in dynamic equilibrium with the vapour phase. Due to the dynamic feature of the equilibrium, the actual location of the surface sites covered by one, two or more layers may vary but the number of molecules in each layer remains constant:

$$\frac{1}{[V_a(\frac{P_0}{P} - 1)]} = \frac{C - 1}{V_m} \times \frac{P}{P_0} + \frac{1}{V_m C}$$

4.3 Electron Paramagnetic Resonance

Electron paramagnetic resonance spectroscopy (EPR), also called electron spin resonance (ESR), is a technique to study chemical species with unpaired electrons. In many ways, basic EPR theory and methods are similar to those of nuclear magnetic resonance (NMR). EPR spectroscopy has been applied to study kinetics and mechanisms of highly reactive radical intermediates in various fields ranging from organic radicals to paramagnetic metal clusters in biological enzymes. EPR analyses the interaction between an external magnetic field and the unpaired electrons and is usually performed using microwaves in the 3 – 400 GHz range. Due to the short relaxation times of electron spins, the experiments are often performed at low temperatures (e.g. 10 K). For a single unpaired electron, there are two possible energy states, which is called Zeeman splitting shown in the following equations:

$$E_{+\frac{1}{2}} = \frac{1}{2}g\mu_B B$$

$$E_{-\frac{1}{2}} = -\frac{1}{2}g\mu_B B$$

where μ_B , the Bohr magneton, is the magnetic moment for one unit of quantum mechanical angular momentum, g is the g -factor and B is the magnetic field. In the presence of external magnetic field (Figure 4.2), the difference between the two energy states can be written as:

$$\Delta E = h\nu = g\mu_B B$$

As the intensity of the applied magnetic field increase, the energy difference between the energy levels widens until it matches with the microwave radiation and results in the absorption of energy.

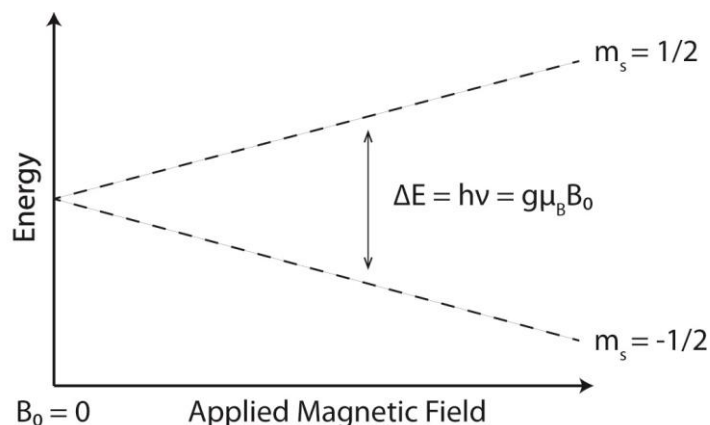


Figure 4.2 Energy levels for an electron spin ($M_s = +1/2$ or $-1/2$) in an applied magnetic field B . Adapted from *Electron Paramagnetic Resonance*.¹⁸⁰ Copyright (1964) Academic Press.

4.4 Cyclic Voltammetry

Cyclic voltammetry (CV) is an electrochemical technique that measures the current that develops in an electrochemical cell when the voltage is in excess of what's predicted by the Nernst equation. In CV measurements, the potential of the working electrode is changed in a cyclic manner and the resulting current is recorded. The most common experimental configuration consists of an electrochemical cell that has three electrode, counter electrode, reference electrode and working electrode, all of which are immersed in solution and connected to a potentiostat. Commonly used reference electrodes are aqueous Ag/AgCl or calomel half cells, while a non-reactive electrode, such as platinum, is usually used as the counter electrode. Preparation of the samples, electrolytic solutions, and the measuring cell is essential for successful measurements. Trace amounts of impurities in the electrolyte solution can considerably impair the quality of the cyclic voltammograms. Typical characteristic parameters can be extracted from a representative cyclic voltammogram shown in Figure 4.3. $E_{p,a}$ and $E_{p,c}$ are the anodic and cathodic peak potentials and the midpoint potential $E_{p/2}$ is calculated from $\frac{1}{2}(E_{p,c} + E_{p,a})$.

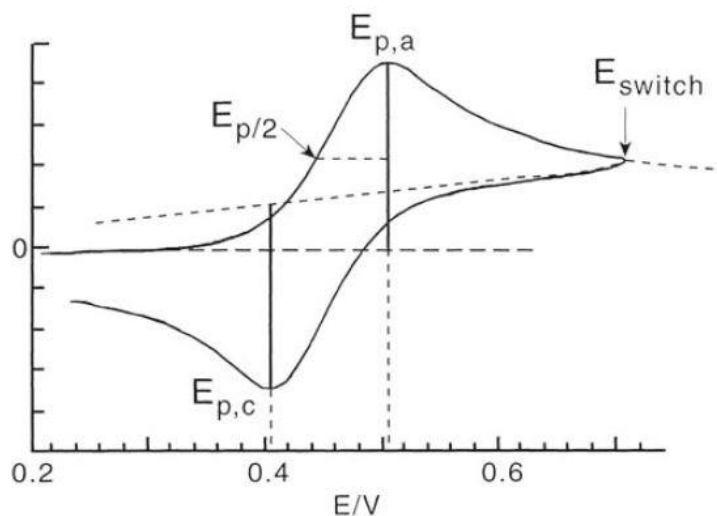


Figure 4.3 Voltammogram with key parameters. Adapted from *Electroanalytical Methods*.¹⁸¹ Copyright (2010) Springer.

4.5 Scanning Electron Microscopy

Scanning electron microscopy (SEM) makes it possible to resolve surface structures from several micrometers to a few nanometers. The two major components of an SEM are the electron column and the control console. The electron column consists of an electron gun and electron lenses, which direct the paths of electron movements. The electrons are generated by the electron gun and accelerated to an energy of 0.1-30k eV. The electron beam moves in a grid fashion. Two pairs of electromagnetic scan coils are needed to sweep the beam across the sample. The first pair deflects the beam off the optical axis of the microscope and the second pair bends the beam back to the pivot point of the scan. The detector collects the scattered electrons and creates an image. SEM imaging technique provided the possibility to visualize the surface micro- and nano-morphology of the polymeric structures presented in this work.

5 Results and Discussion

The following chapter is divided into five main sections. In chapter 5.1, a bottom-up design approach at the molecular level was applied. Specifically in chapter 5.1.1, conjugated microporous polymer (CMP) photocatalysts with different geometry design were prepared and their photocatalytic efficiencies were compared using the photooxidative coupling of benzylamines as a model reaction. Similarly in chapter 5.1.2, CMP photocatalysts with different chalcogen elements in the acceptor moiety were synthesized and compared. Starting from chapter 5.2 to 5.4, the focus of the projects shifted from micropores (< 2 nm) to macropores (> 50 nm) using the high internal phase emulsion (HIPE) polymerization technique. In particular, good surface area control was demonstrated in chapter 5.2, whereas in chapter 5.3 conjugated hierarchically porous polymer (CPP) photocatalysts with different chemical compositions were synthesized and compared. In chapter 5.4, CPP photocatalyst was used for the first time as a macromolecular visible light photoinitiator for the free radical polymerization of methyl methacrylate. Lastly, a hybrid CMP photocatalyst with immobilized Pd nanocrystals was prepared and employed as heterogeneous visible light photocatalyst for visible light induced Suzuki-Miyaura cross-coupling reaction in chapter 5.5.

5.1 Molecular Structural Control of Conjugated Porous Polymers

This chapter is based on the published articles “Molecular Structural Design of Conjugated Microporous Poly(Benzooxadiazole) Networks for Enhanced Photocatalytic Activity with Visible Light”, *Adv. Mater.*, 2015, DOI: 10.1002/adma.201502735 and “Conjugated Microporous Poly(Benzochalcogenadiazole)s for Photocatalytic Oxidative Coupling of Amines under Visible Light”, *ChemSusChem*, 2015, **8**, 3459-3464 with copyright (2015) from Wiley VCH.

5.1.1 Molecular Structural Design of Conjugated Microporous Poly(benzooxadiazole) Networks for Enhanced Photocatalytic Activity with Visible Light

5.1.1.1 Introduction

This chapter takes a bottom-up design approach at the molecular level to investigate the influence individual parameters have on the effective photocatalytic efficiencies of the conjugated porous polymer photocatalysts. In this section of the chapter, a simple structural design principle and band position alignment of conjugated porous polymers for enhanced photocatalytic efficiency is presented. It is demonstrated that the valence and conduction band positions of the polymer networks can be fine-justified via merely altering the substitution positions on the centered phenyl unit, in order to match the required redox potential of the catalytic reactions under visible light.

Many molecular inorganic, transition metal-based complexes or organic dye compounds (see chapter 3.1) that absorb significantly in the visible spectrum were intensely studied to harvest solar energy and catalyze organic photochemical reactions.^{58,60,65,75,77,182-195} For the above mentioned transition metal-based homogeneous organometallic complexes, the redox potential can be easily adjusted by modifying the metal center and surrounding ligands, in order to meet the specific activation energies of the organic reactions.¹⁹⁰ Similarly, the effective valence (VB) and conduction band (CB) positions of inorganic heterogeneous metal photocatalytic systems can also be modified by the formation of hybrid or heterostructures with selected metals to achieve enhanced photoactivity.^{12,196,197}

Motivated by the band position tuning methods for transition metal-based and other inorganic systems, a simple structural design principle of conjugated microporous polymers as pure organic, heterogeneous photocatalytic systems to allow the fine alignment of the valence and conduction band levels for enhanced catalytic activity is presented here. Figure 5.1 shows that by merely altering the substitution positions on the centered phenyl unit, which functions as the 3-D center of the polymer network, the VB and CB positions can be aligned to optimally bracket the redox potentials of individual catalytic reactions, without changing the electron donor and acceptor moieties in the polymer network backbone. Under light irradiation, the photogenerated electrons and holes function as the reductive and oxidative sides of the organic

polymer-based photocatalyst, respectively. The enhanced photocatalytic activity of the CMPs was demonstrated in the oxidative coupling of amines under irradiation of a 23 W household energy saving fluorescent light bulb.

5.1.1.2 Synthesis and Characterization of Conjugated Microporous Polymers

The chemical structures of the synthesized CMPs are displayed in Figure 5.1. Taking a phenyl unit as the 3-D center, a well-known electron acceptor, benzoxadiazole (BO) unit was connected via a triple bond to the phenyl unit on its 1,3,5-, 1,2,4- and 1,2,4,5-positions, forming the microporous polymer networks B-BO-1,3,5 B-BO-1,2,4 and B-BO-1,2,4,5, respectively. The synthetic details and characterization data are described in Section 6.1. The resulting polymers are insoluble in all common organic solvents tested. Solid state $^{13}\text{C}/\text{MAS}$ NMR spectroscopy showed similar signals for all three CMPs between 80 and 160 ppm, which can be assigned to the aromatic carbons (Figure 5.2-Figure 5.4).

Structural Design Principle

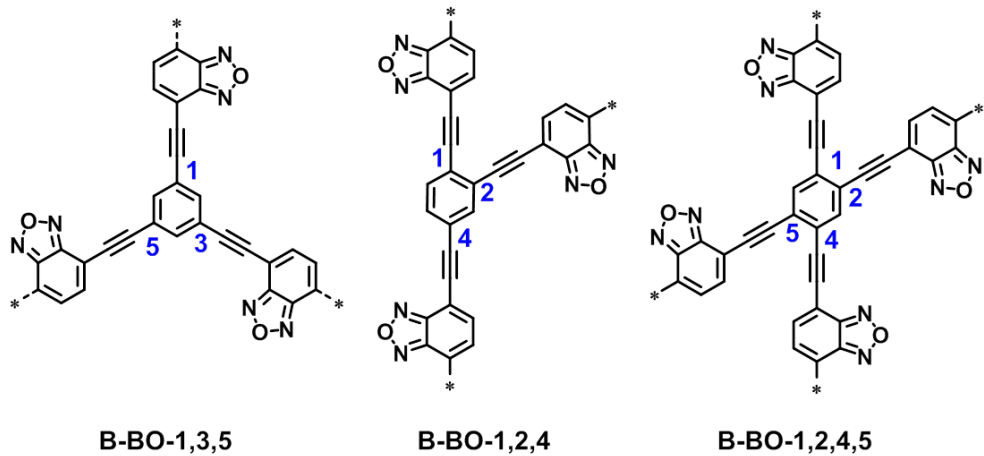
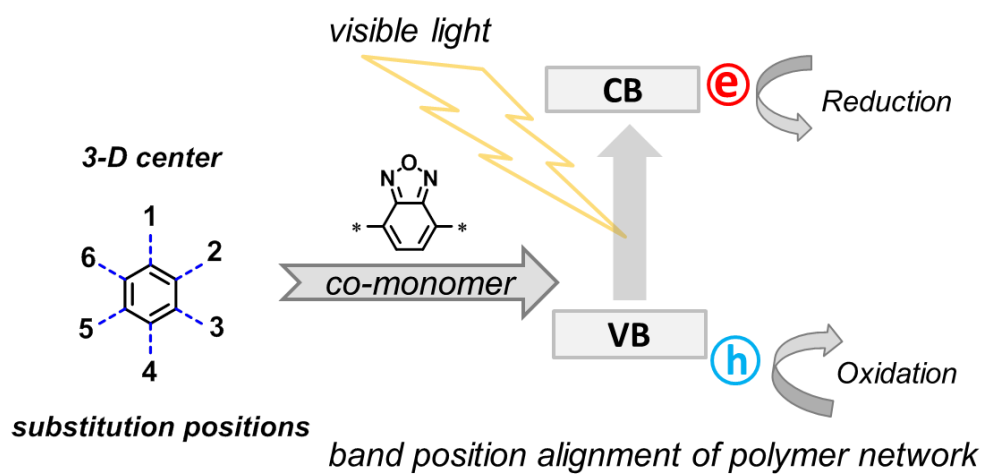
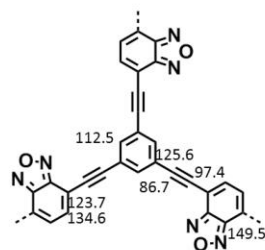


Figure 5.1 Geometry design principle of valence and conduction band position modification of conjugated microporous poly(benzooxadiazole) networks by altering the substitution position on the 3-D center.

Weng_140805/2
13C CP-MAS NMR 10kHz
Sample: ZW010 CMP
CP 1 ms



B-BO-1

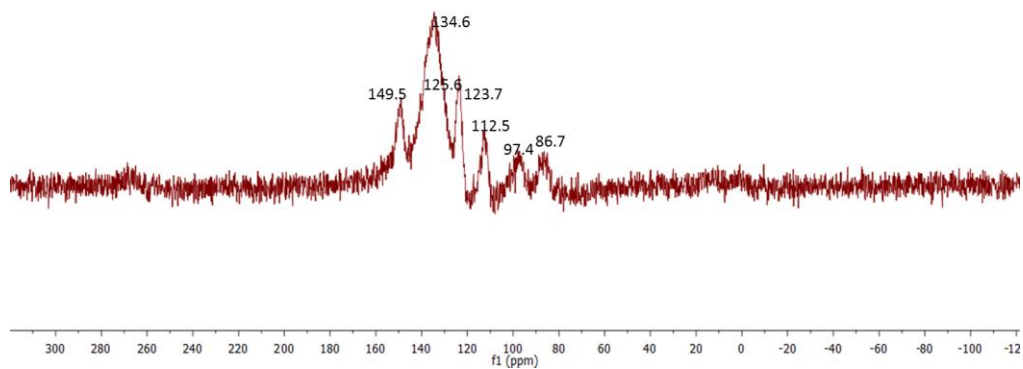
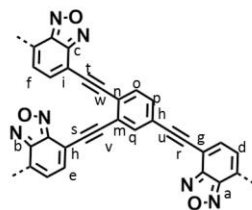


Figure 5.2 Solid-State ^{13}C /MAS NMR Spectrum of B-BO-1,3,5.

Weng_140812/6
13C CP-MAS NMR 10kHz
Sample: ZW011
cp 1ms



B-BO-2

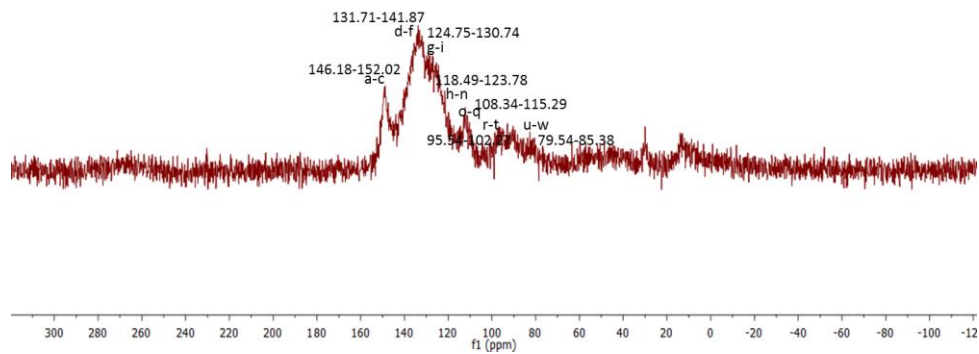
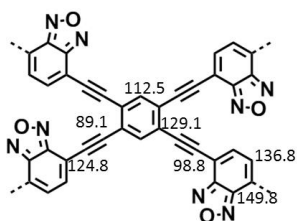


Figure 5.3 Solid-State ^{13}C /MAS NMR Spectrum of B-BO-1,2,4.

Wang_140813/3
 13C CP-MAS NMR 10kHz
 Sample: ZW012
 cp 1ms



B-BO-3

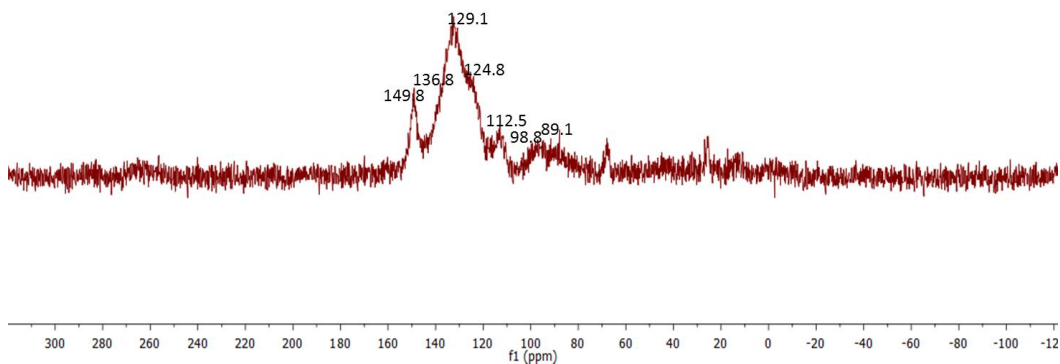


Figure 5.4 Solid-State $^{13}\text{C}/\text{MAS}$ NMR Spectrum of B-BO-1,2,4,5.

The Brunauer-Emmett-Teller (BET) surface areas of B-BO-1,3,5, B-BO-1,2,4 and B-BO-1,2,4,5 were measured to be 474 m^2/g , 475 m^2/g and 378 m^2/g , with pore volumes of 0.31 cm^3/g , 0.37 cm^3/g and 0.20 cm^3/g , respectively. Similar pore diameters of round 1.5 nm were determined for all three polymers (Table 5.1, Figure 5.5 and Figure 5.6).

Table 5.1 Porosity data of the CMPs.

CMP	S_{BET} (m^2/g)	Pore Size (nm)	Pore Volume (cm^3/g)
B-BO-1,3,5	474	1.5	0.31
B-BO-1,2,4	475	1.5	0.37
B-BO-1,2,4,5	378	1.5	0.20

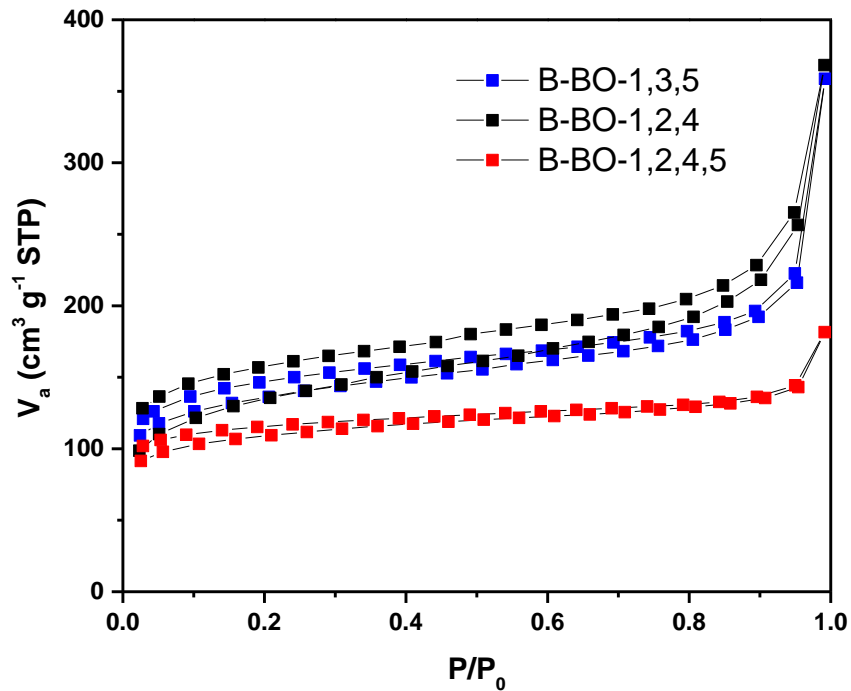


Figure 5.5 N₂ gas sorption isotherms.

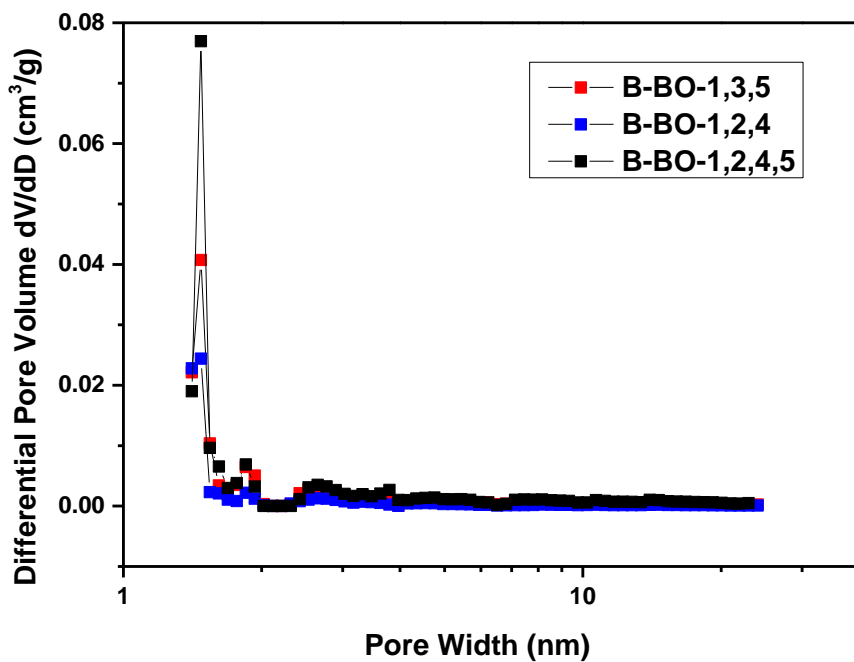


Figure 5.6 Pore size distribution of the CMPs.

Thermal gravimetric analysis (TGA) measurements showed a high thermal stability of B-BO-1,3,5 and B-BO-1,2,4 up to ca. 350 °C, while B-BO-1,2,4,5 showed a lower thermal stability

up to ca. 200 °C (Figure 5.7). The FTIR spectra of the polymers are displayed in (Figure 5.8- Figure 5.10). The signal at 1620 cm^{-1} can be assigned to the C=N stretching mode of the BO unit of the polymer networks. Signals between 1370 and 1440 cm^{-1} indicate the skeleton vibration of the aromatic rings in the polymers. A C=C stretching mode at 1600 cm^{-1} was observed. All networks showed the typical C≡C stretching mode at about 2200 cm^{-1} .

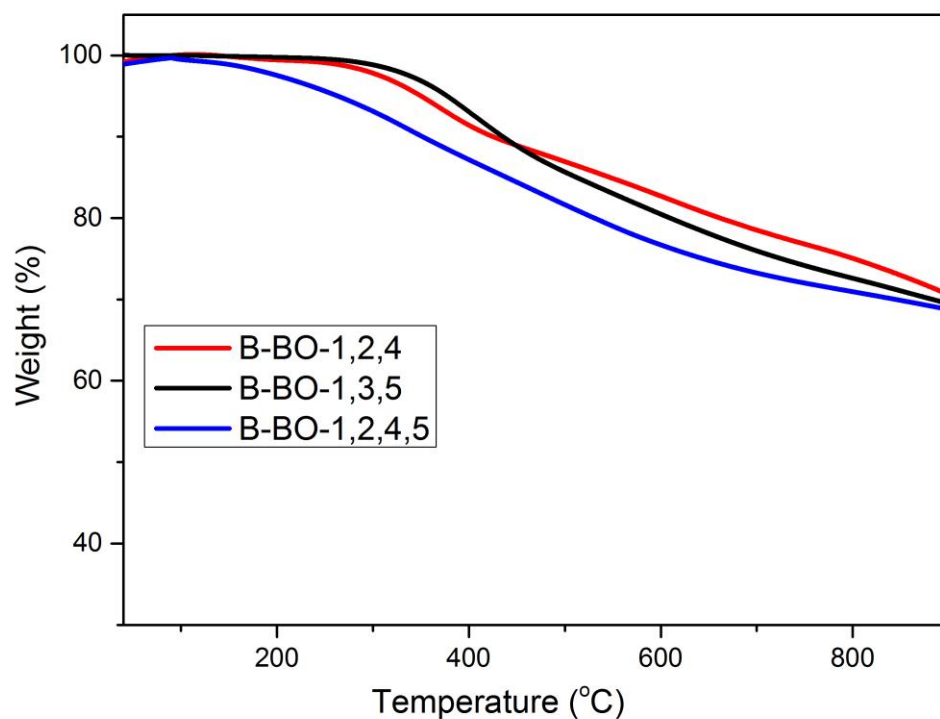


Figure 5.7 TGA curves of the three CMPs.

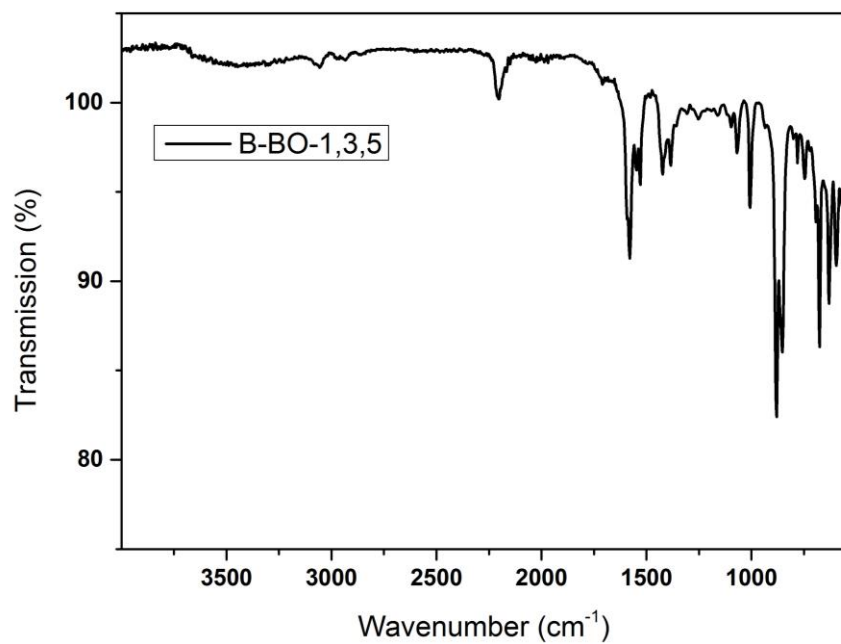


Figure 5.8 FTIR spectra of B-BO-1,3,5.

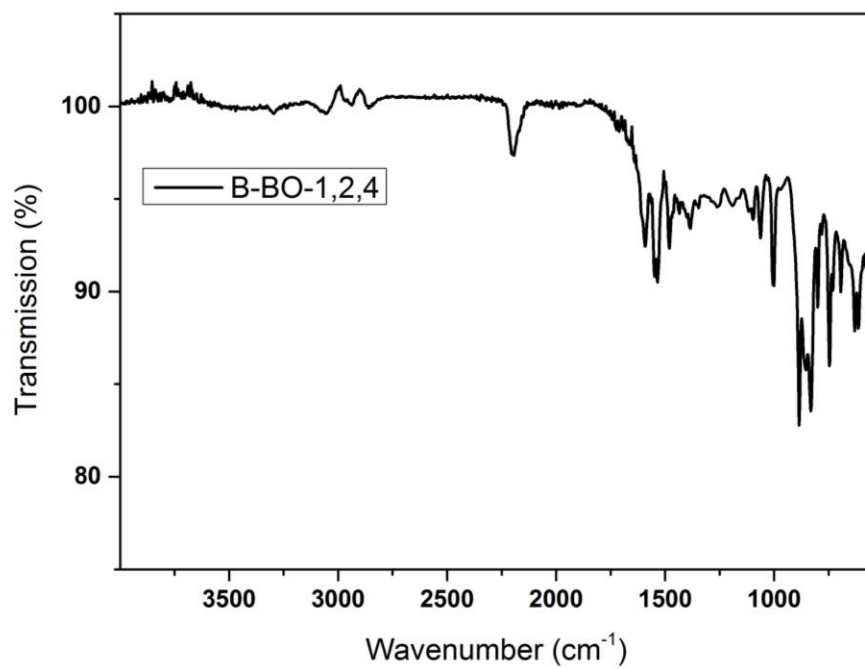


Figure 5.9 FTIR spectra of B-BO-1,2,4.

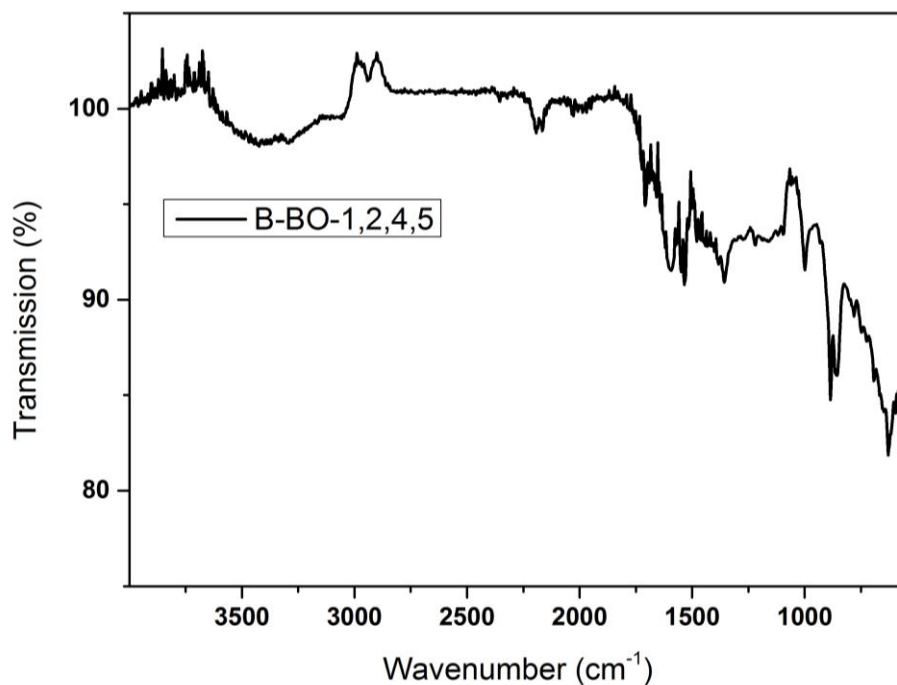


Figure 5.10 FTIR spectra of B-BO-1,2,4,5.

The SEM and TEM images of the three CMPs illustrated different morphologies at sub-micron scale (Figure 5.11). In particular, B-BO-1,3,5 appeared as fiber-like structures with a diameter of less than 100 nm (Figure 5.11a and d), whereas a porous flake-like shape was observed for CMP B-BO-1,2,4 (Figure 5.11b and e) and B-BO-1,2,4,5 showed a fused irregular particle-like structure (Figure 5.11c and f). This formation mechanism could stem from the steric effect inside the polymer network due to different substitution positions of their 3-D center.

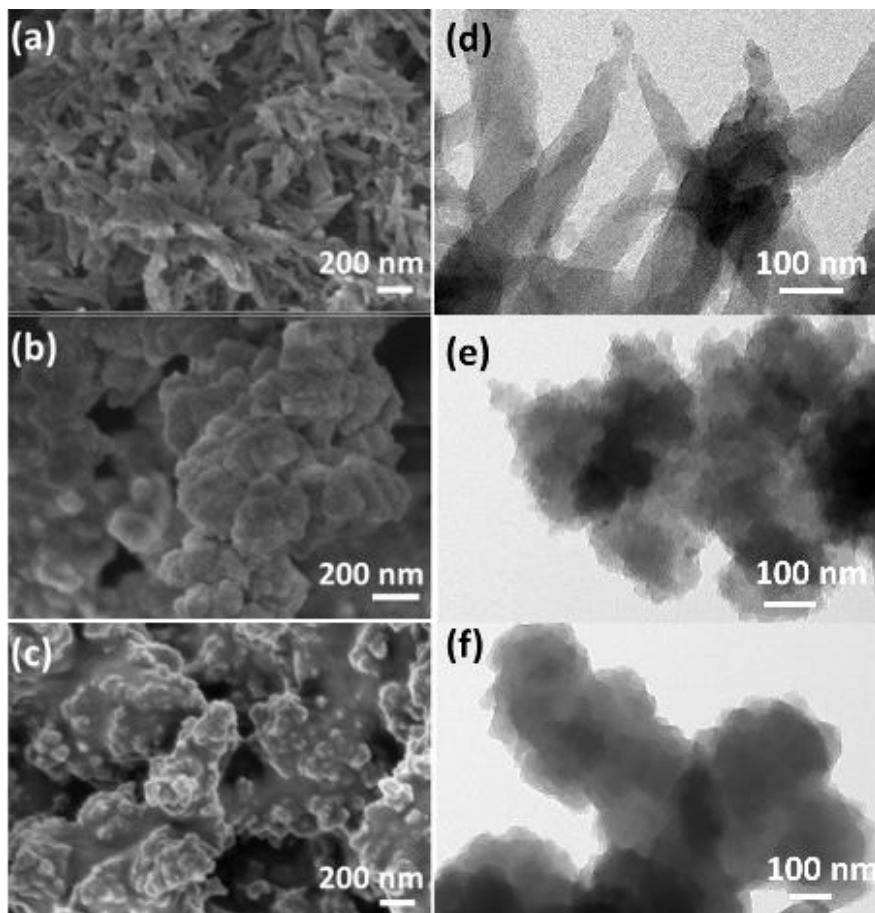


Figure 5.11 SEM images of B-BO-1,3,5 (a), B-BO-1,2,4 (b), B-BO-1,2,4,5 (c) and TEM images of B-BO-1,3,5 (d), B-BO-1,2,4 (e), B-BO-1,2,4,5 (f).

In Figure 5.13a, the UV/Vis diffuse reflectance (DR) spectra of the CMPs are displayed. B-BO-1,3,5 showed a broad absorption range until 800 nm, while B-BO-1,2,4 and B-BO-1,2,4,5 absorb significantly up to the near infrared region, indicating a decreasing optical band gap within the CMP series. This also corresponds to the color change in the CMP series, from yellowish, brown to almost black for B-BO-1,3,5, B-BO-1,2,4 and B-BO-1,2,4,5, respectively (Figure 5.12).

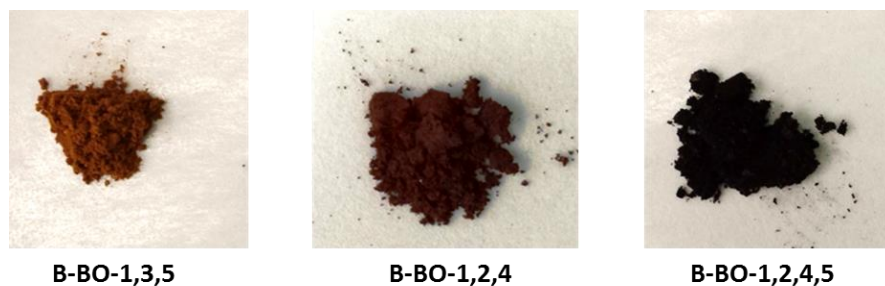


Figure 5.12 Photographs of the CMPs.

Cyclic voltammetry (CV) measurements revealed lowering potentials during the reductive and oxidative cycles within the polymer series (Figure 5.13b and Figure 5.14), implying different VB and CB positions of the polymer series. B-BO-1,3,5 exhibited VB and CB at +1.55 V and -1.19 V. In comparison, the VB and CB positions of B-BO-1,2,4 and B-BO-1,2,4,5 were determined to be at +1.45 V/-1.13 V and +1.14 V/-0.89 V, respectively. This is comparable to the redox potentials of established organometallic photocatalysts such as $[\text{Ru}(\text{bpy})_3]^{3+}$ (+1.29 V) and $[\text{Ru}(\text{bpy})_3]^{2+}$ (-0.81 V).⁵⁹

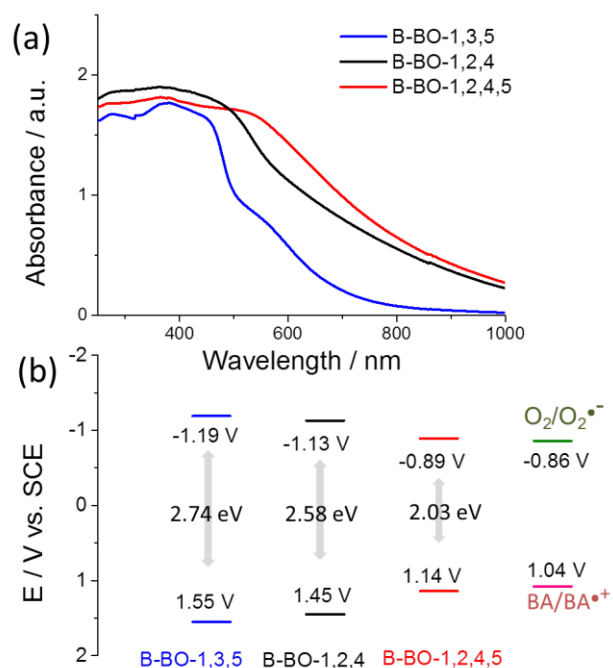


Figure 5.13 (a) UV/Vis DR spectra. (b) Valence band (VB) and Conduction band (CB) positions of the CMPs and redox potentials of some substrates such as benzylamine (BA) and molecular oxygen into superoxide used in the photocatalytic reaction determined by CV.

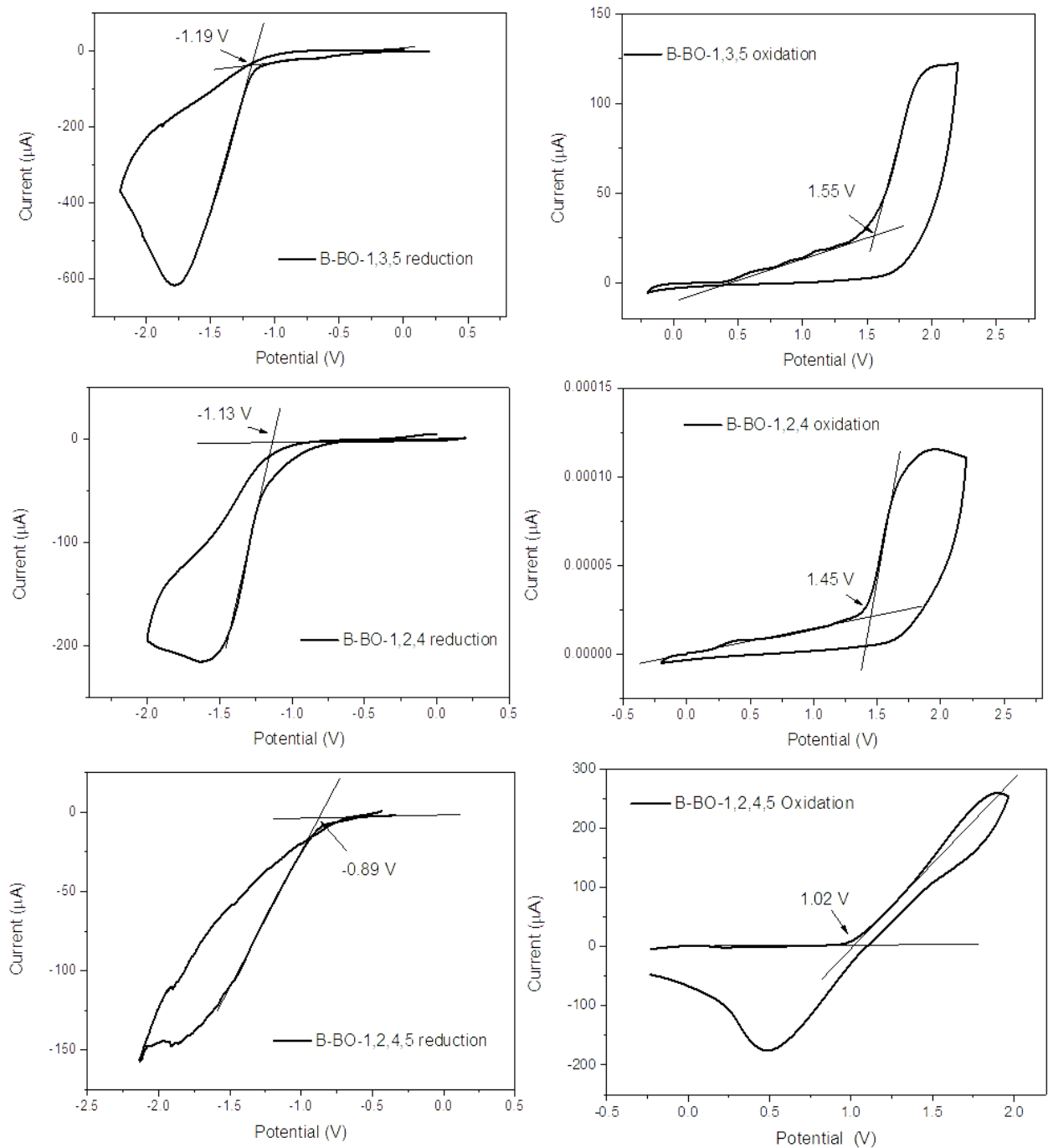


Figure 5.14 Cyclic voltammograms.

The electron paramagnetic resonance (EPR) spectra showed a large increase in the intensity B-BO-1,3,5 under light irradiation, whereas B-BO-1,2,4 and B-BO-1,2,4,5 barely exhibited an enhanced signal (Figure 5.15). This probably indicates that longer living electron-

hole pairs were generated in B-BO-1,3,5 under light irradiation compared to those of other CMPs.

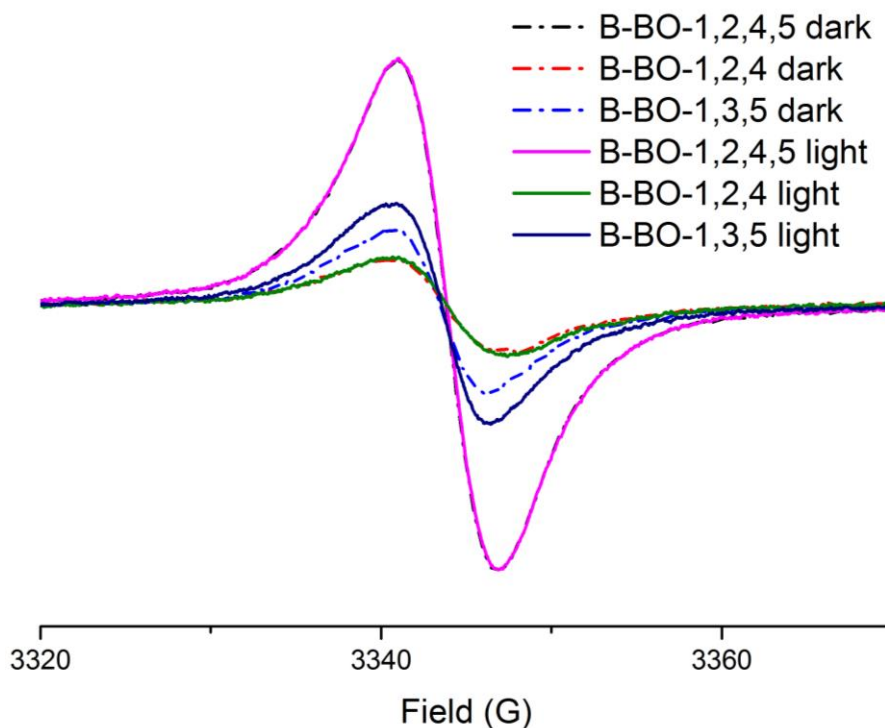


Figure 5.15 EPR spectra for of CPPs taken in dark and under light irradiation.

It was previously shown that conjugated macromolecular systems could mediate the electron transfer from *N,N,N',N'*-tetramethyl-phenylenediamine (TMPD) ($E_{oxi.} = 0.12$ V vs. SCE) to molecular oxygen, resulting in blue-colored cationic radical and the activated oxygen species superoxide ($O_2^{\bullet-}$) ($E_{red.} = 0.86$ V vs. SCE) under light irradiation, using the photogenerated hole inside the conjugated system as the oxidative side and the photoexcited electron as reductive side.¹⁹⁸ As shown in Figure 5.16a, the intensity variations in UV/Vis absorption spectra of the resulting blue-color species verified the superior photooxidative activity of B-BO-1,3,5 compared to B-BO-1,2,4 and B-BO-1,2,4,5, which results from the highest oxidation potential of 1.55 V and reduction potential of -1.19 V of B-BO-1,3,5 (Figure 5.13b).

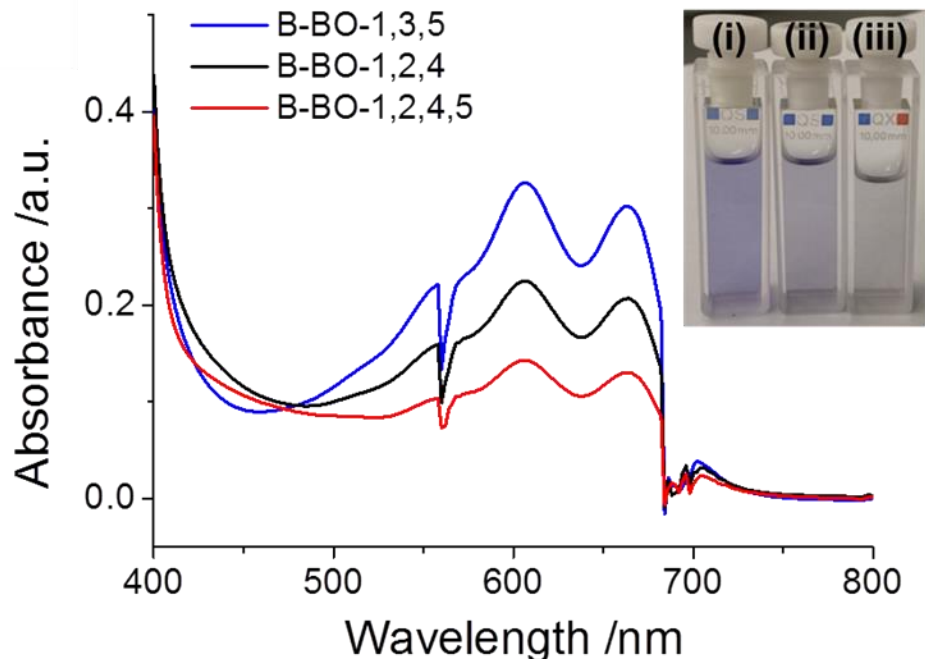


Figure 5.16 UV/Vis spectra and photograph of the cationic radical of TMPD (100 mM in 3 mL CH₃CN) after photo-induced oxidation by CMPs (2 mg/ml) in after 1 h under blue LED in air. Insert: (i) B-BO-1,3,5; (ii) B-BO-1,2,4; (iii) B-BO-1,2,4,5

Previously, we reported that CMPs could generate singlet oxygen species (¹O₂) under light irradiation, using triplet electrons in the excited state.¹⁹⁹ Here, spin trap EPR experiments were conducted using 5,5-dimethyl-1-pyrroline N-oxide (DMPO) and 2,2,6,6-tetramethylpiperidinyloxyl (TEMPO) as superoxide and singlet oxygen trapping agents, respectively. As shown in Figure 5.17c and d, both active oxygen species O₂^{•-} and ¹O₂ could be determined, with B-BO-1,3,5 generating the most intense signals among the three polymers.

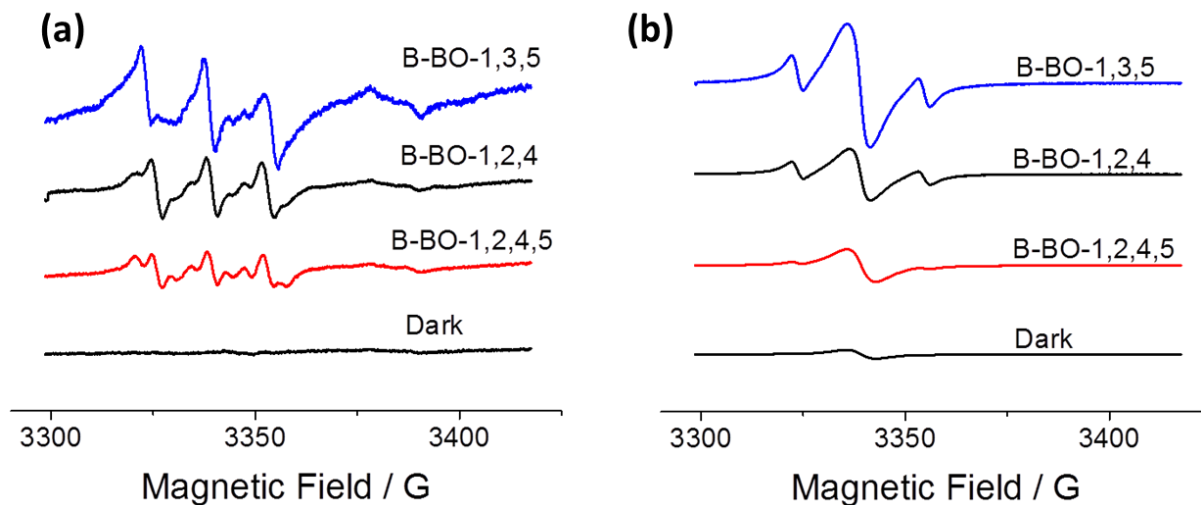
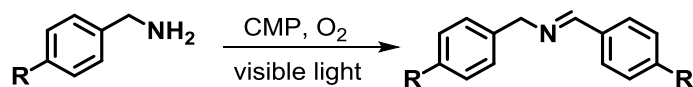


Figure 5.17 ESR spectra of DMPO–O₂[•], and (d) TEMPO–¹O₂ adducts for different CMPs under light and in dark.

5.1.1.3 Photooxidative Coupling of Benzylamine and its Derivatives

To further determine the feasibility of CMPs and confirm the superior catalytic activity of B-BO-1,3,5 in visible light-promoted photocatalytic chemical transformation reactions, the oxidative coupling reaction of benzylamines was chosen as a model reaction. The three CMPs were employed under exact same reaction condition to catalyze the photooxidative coupling of benzylamine and its derivatives bearing electron-donating (–OCH₃) and electron-withdrawing (–F) moieties (Table 5.2, entries 1-3). As expected, the reactions catalyzed with B-BO-1,3,5 achieved significantly higher conversions (entry 1) than the other two CMPs in all three cases. This further demonstrates that 3-D network structure with 1,3,5-substitution on the center phenyl unit delivers the highest reduction and oxidation potentials and therefore the most efficient photocatalyst. Terao et al. reported structurally defined conjugated polymers and demonstrated that significantly higher charge mobility can be attained by simply changing the configuration of poly(phenylene–ethynylene) from linear (*para*, via 1,4-positions) to zigzag (*meta*, via 1,3-positions) chain through the phenyl unit.²⁰⁰ This could explain the superior photocatalytic performance of B-BO-1,3,5.

Table 5.2 Oxidative coupling of benzylamines using the CMPs as photocatalyst.^a



Entry	CMP	O ₂	Light	Additive	Conversion (%) ^b		
					R = H	R = F	R = OCH ₃
1	B-BO-1,3,5	+	+	-	48	28	15
2	B-BO-1,2,4	+	+	-	17	8	6
3	B-BO-1,2,4,5	+	+	-	13	5	4
4 ^c	-	+	+	-	<5	-	-
5 ^d	B-BO-1,3,5	+	-	-	<1	-	-
6 ^e	B-BO-1,3,5	-	+	-	<1	-	-
7 ^f	B-BO-1,3,5	+	+	hole scavenger	14	-	-
8 ^g	B-BO-1,3,5	+	+	superoxide scavenger	5	-	-
9 ^h	B-BO-1,3,5	+	+	singlet oxygen scavenger	24	-	-
10 ⁱ	B-BO-B	+	+	-	68	-	-

^aAll experiments were conducted with 1 mmol of substrate, 6 mg of CMP in 3 mL CH₃CN under the irradiation of blue LED (460 nm, 1.2 W/cm²) for 3 h (1 atm O₂, room temperature); ^b Conversion determined by ¹H NMR and GCMS; ^c Without B-BO-1,3,5, under light, 1 atm O₂; ^d With B-BO-1,3,5, no light, 1 atm O₂; ^e With B-BO-1,3,5, under light, no O₂; ^f KI as hole scavenger. ^g benzoquinone (BQ) as superoxide scavenger; ^h NaN₃ as singlet oxygen scavenger; ⁱ B-BO-B as homogeneous catalyst, concentration: 2 mg/ml in CH₃CN, blue LED, 3 h.

To further investigate the reaction mechanism and the specific roles of the photo-generated electron-hole pairs during oxidative coupling reaction of benzylamines, we extended

the study by conducting control experiments and adding different hole and electron scavengers into the reaction mixture (Table 5.2). From entries 4-6, it could be concluded that all three components, B-BO-1,3,5 as photocatalyst, light and oxygen, are indispensable for achieving high conversion. By adding KI, i.e. a hole scavenger, a reduced conversion of 14% was obtained (entry 7). By adding benzoquinone as superoxide scavenger, a conversion of only 5% was found (entry 8). Using sodium azide as singlet oxygen scavenger led to a conversion of 24% (entry 9). All these results indicate that both activated oxygen species (e.g. superoxide and singlet oxygen) took part in the oxidative coupling reaction of benzylamine, with superoxide playing a more significant role. In Figure 5.18, the peak at ca. 10 ppm could be assigned to benzaldehyde, which only appeared after reaching the full conversion of the catalytic reaction. This indicates that benzaldehyde is probably not an active intermediate, but an over-oxidized side product after the reaction. During the monitoring experiment (Figure 5.18), we did not observe any evidence of benzaldehyde as a possible intermediate after the elimination of water and ammonia from hydroperoxy (phenyl)methanamine, we thus propose that it could form directly the imine species after elimination of H_2O_2 ,²⁰¹ which then reacts with an additional benzylamine molecule, forming N-benzyl-1-phenylmethanediamine as intermediate. Interestingly, after reaching the full conversion of the catalytic reaction, benzaldehyde was determined (Figure 5.18). This indicates that benzaldehyde is probably not an active intermediate, but an over-oxidized side product after the reaction. After elimination of ammonia from the intermediate N-benzyl-1-phenylmethanediamine, the final product is obtained. Both photogenerated electrons and holes actively participate in the photooxidative coupling of amines. The reductive (-1.19 V) and oxidative (1.55 V) potentials of B-BO-1,3,5 are sufficiently high to reduce molecular oxygen into its active species and oxidize benzylamine into its cationic radical form ($E_{\text{oxi.}} = +1.08 \text{ V}$) (Figure 5.13b). In comparison, the lower reductive (-0.89 V) and oxidative (1.14 V) potentials of B-BO-1,2,4,5 are rather insufficient for both redox processes.

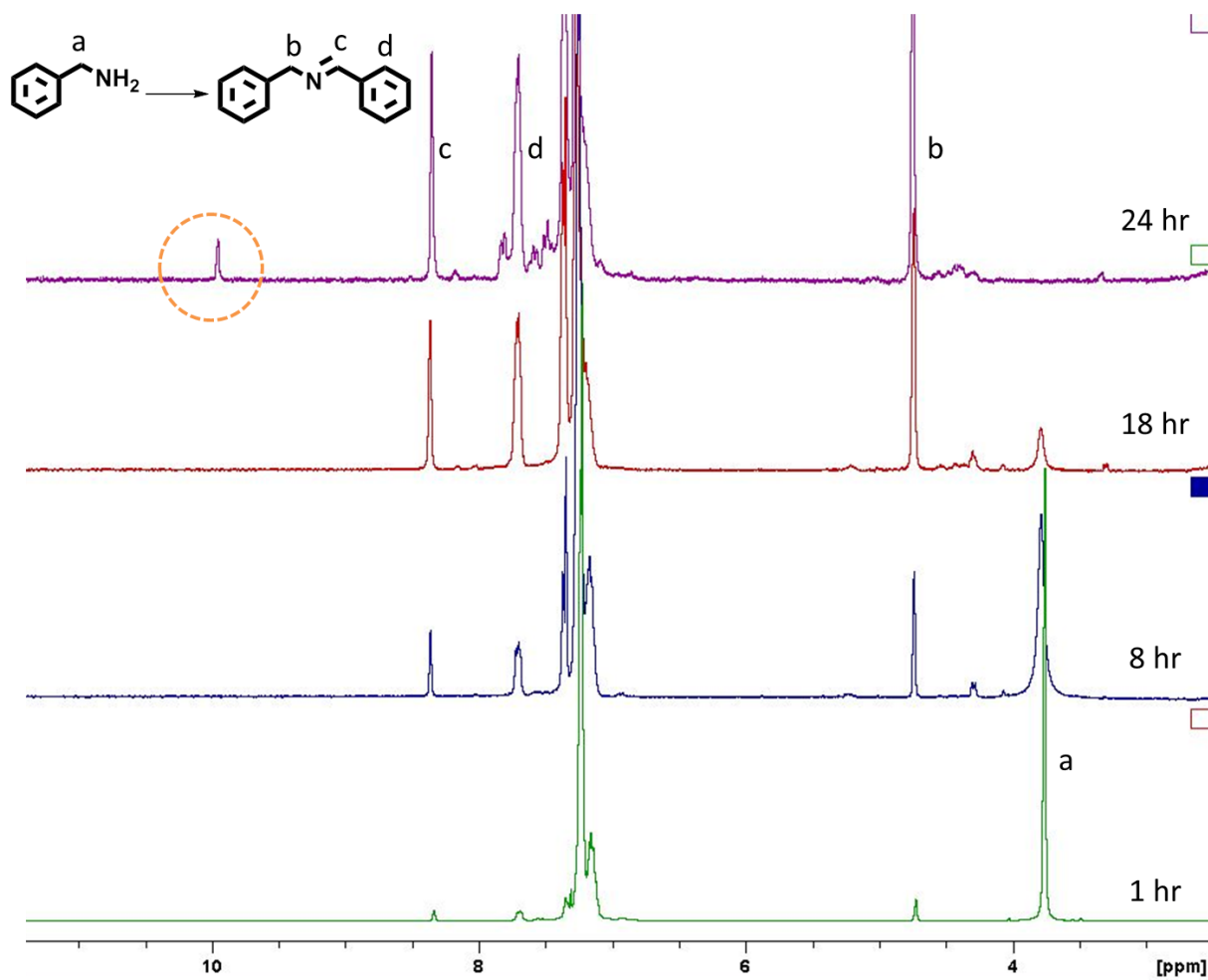


Figure 5.18 ^1H NMR spectra of the photooxidative coupling of benzyl amine using a 23 W household energy saving fluorescent light bulb over 24 hours.

A small molecule, 4,7-bis(phenylethynyl)benzo[*c*][1,2,5]-oxadiazole (B-BO-B) as a soluble and homogeneous analogue was employed for the same photocatalytic reaction (entry 10). A higher conversion of 68% under the same reaction condition was recorded. However, after the reaction, a clear decrease of the absorption maximum by ca. 30%, the so-called photo-bleaching effect was observed (Figure 5.19). In comparison, the heterogeneous counterpart B-BO-1,3,5 could be used for another 5 repeating cycles without significantly losing its catalytic efficiency (Figure 5.20).

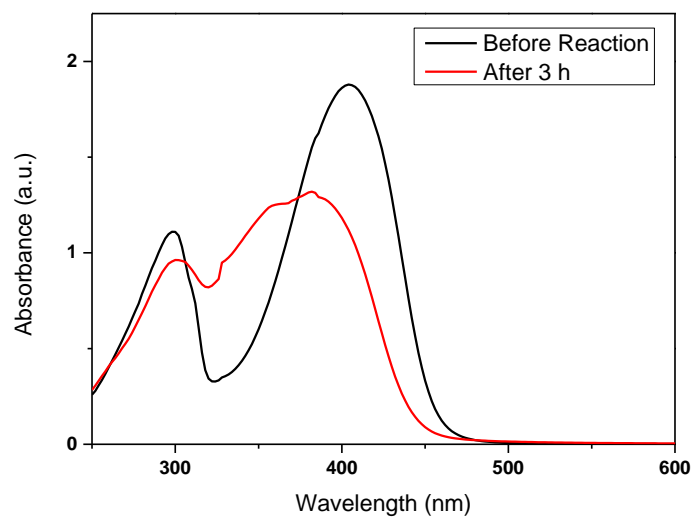


Figure 5.19 UV/Vis spectra of B-BO-B before and after the 3-hour-long photooxidative coupling of benzyl amine (synthesis and experimental details are described in chapter 5.1).

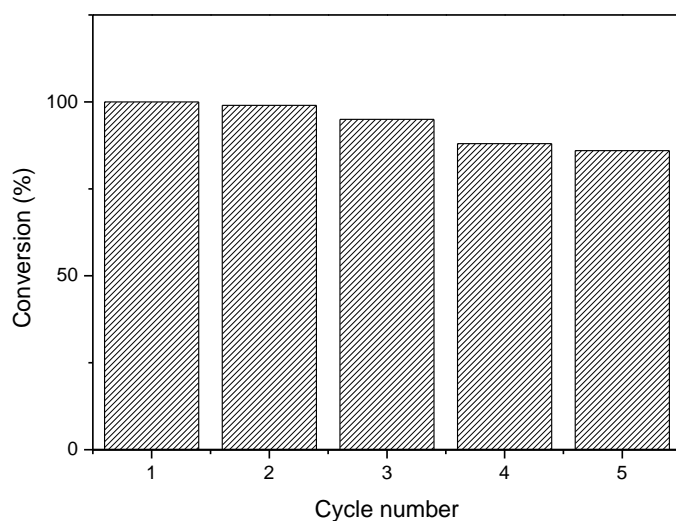
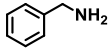
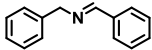
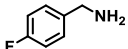
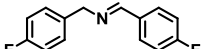
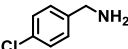
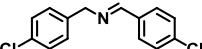
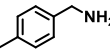
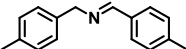
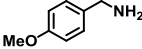
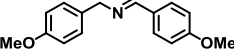
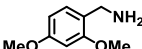
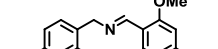
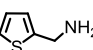
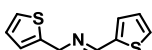


Figure 5.20 Repeating experiments of the photooxidative coupling of benzyl amine by B-BO-1,3,5 under a 23 W household energy saving fluorescent light bulb at room temperature.

A number of benzylamine derivatives were also investigated to demonstrate the general applicability of B-BO-1,3,5 as photocatalysts (Table 5.3). To note, a 23 W household energy saving fluorescent light bulb was used as a low-cost light source. It could be determined that

electron withdrawing groups such as F or Cl led to higher conversions (entry 12 and 13) than the electron donating groups such as methyl (entry 14), methoxy (entry 15 and 16). The reason could be the stabilized cationic radical by the methyl and especially methoxy groups, which decelerated the formation of the final product. However, this effect was not observed with the thiophene unit (entry 17).

Table 5.3 Screening experiments of the oxidative coupling of benzylamines using B-BO-1,3,5 as photocatalyst.^a

Entry	Substrate	Product	Conversion (%) ^b
11			>99
12			97
13			82
14			60
15			22
16			8
17			83

^a) Reaction condition: B-BO-1,3,5 (6 mg), substrate (1 mmol), 1 atm O₂, 3 mL CH₃CN, 23 W energy saving fluorescent light bulb, 24 h, water bath, room temperature. ^b) Conversion data were obtained by ¹H NMR.

5.1.1.4 Conclusion

In summary, this section of the chapter presents a simple structural design principle of conjugated microporous polymers as pure organic, heterogeneous photocatalytic systems to allow the fine justification of the photoredox potential for enhanced catalytic activity. Via merely altering the substitution positions on the centered phenyl unit, which functions as the 3-D center

of a series of poly(benzooxadiazole) networks, the resulted valence and conduction band positions of the polymers can be optimally aligned to bracket the required reductive and oxidative potentials of the catalytic reactions, without changing the electron donor and acceptor moieties in the polymer network backbone. It was shown that the photocatalyst designed with the 1,3,5-substitution positions of the centered phenyl ring demonstrated the superior photocatalytic activity in the oxidative coupling of amines.

5.1.2 Conjugated Microporous Poly(Benzochalcogenadiazole)s for Photocatalytic Oxidative Coupling of Amines under Visible Light

While the above section introduces a geometric design method, this section of the chapter studies the impact of various chalcogen elements in the acceptor moiety on the effective photocatalytic efficiency. Enhanced photocatalytic efficiency was observed by simply altering the chalcogene moieties in the electron accepting benzochalcogenadiazole unit of the polymer backbone structure.

Specifically, this section reports a molecular design strategy to fine-tune the valence and conduction band levels of a series of conjugated microporous poly(benzochalcogenadiazole) networks by altering the chalcogene moieties in the acceptor, i.e. benzochalcogenadiazole unit of the polymer backbone structure. We show that the porous polymer based on the sulphur-containing benzothiadiazole unit exhibits the optimal VB and CB band levels, the largest band gap and could generate most long-lived electron-hole pairs under visible light irradiation. Enhanced photocatalytic efficiency was demonstrated with the photooxidative coupling reaction of benzylamines under visible light irradiation. Furthermore, a detailed study of the photocatalytic reaction mechanism is discussed.

5.1.2.1 Synthesis and Characterization of Conjugated Microporous Polymers

Some findings shown in the following section were results obtained through a cooperation project and have been partially published in the diploma thesis of Kim Garth, 2015, Max Planck Institute for Polymer Research. Specifically, I prepared the CMP polymers and characterized the polymers with BET, EPR, UV-Vis, SEM, TEM, CV as well as catalyst recycle and control experiments with scavengers. Kim Garth synthesized polymer samples for the solid state ^{13}C NMR measurements, TGA and FTIR measurements. In addition, she conducted

photocatalytic experiments to compare the photocatalytic efficiencies of three CMP photocatalysts for the photooxidative coupling of benzylamine and its derivatives as well as the light on-off experiment.

A series of poly(benzochalcogenadiazole) networks was synthesized via Sonogashira cross-coupling reaction using 1,3,5-triethynylbenzene as the crosslinker and a series of 4,7-dibromo-2,1,3-benzoxadiazole (Br-BO), 4,7-Dibromo-2,1,3-benzothiadiazole (Br-BT) and 4,7-Dibromo-2,1,3-benzoselenadiazole (Br-BS) as comonomer unit for the polymers B-BO, B-BT and B-BS respectively. The synthetic route and representative structures of the polymers are displayed in Figure 5.21.

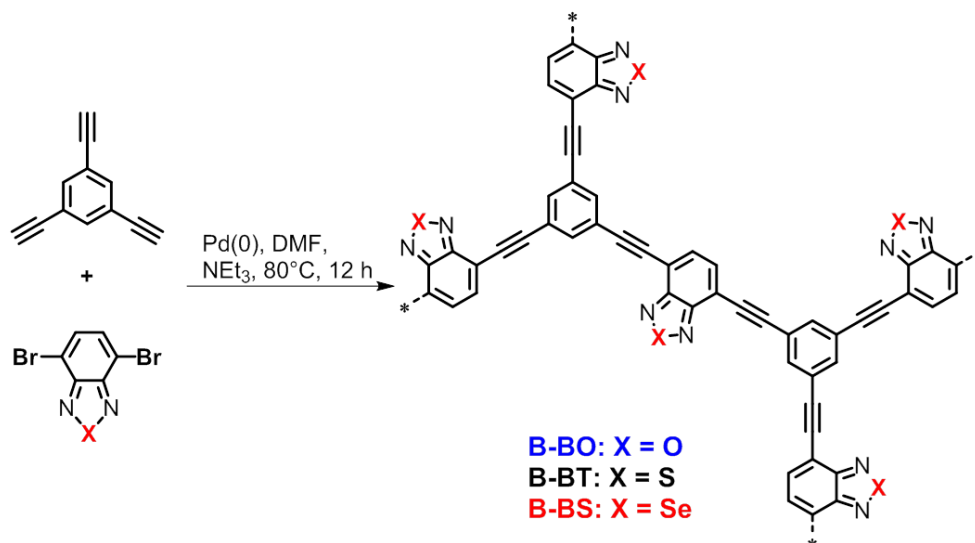


Figure 5.21 Synthetic route and representative structures of the designed conjugated porous poly(benzochalcogenadiazole)s.

All three polymer networks are insoluble in all common organic solvents tested. Solid state $^{13}\text{C}/\text{MAS}$ NMR spectra (Figure 5.22) showed characteristic signals between 110 and 160 ppm, which can be assigned to the aromatic carbons of the BO, BT and BS units and the centered phenyl rings. The chemical shifts between 70 and 100 ppm can be assigned to the *sp* carbons of the triple bonds.

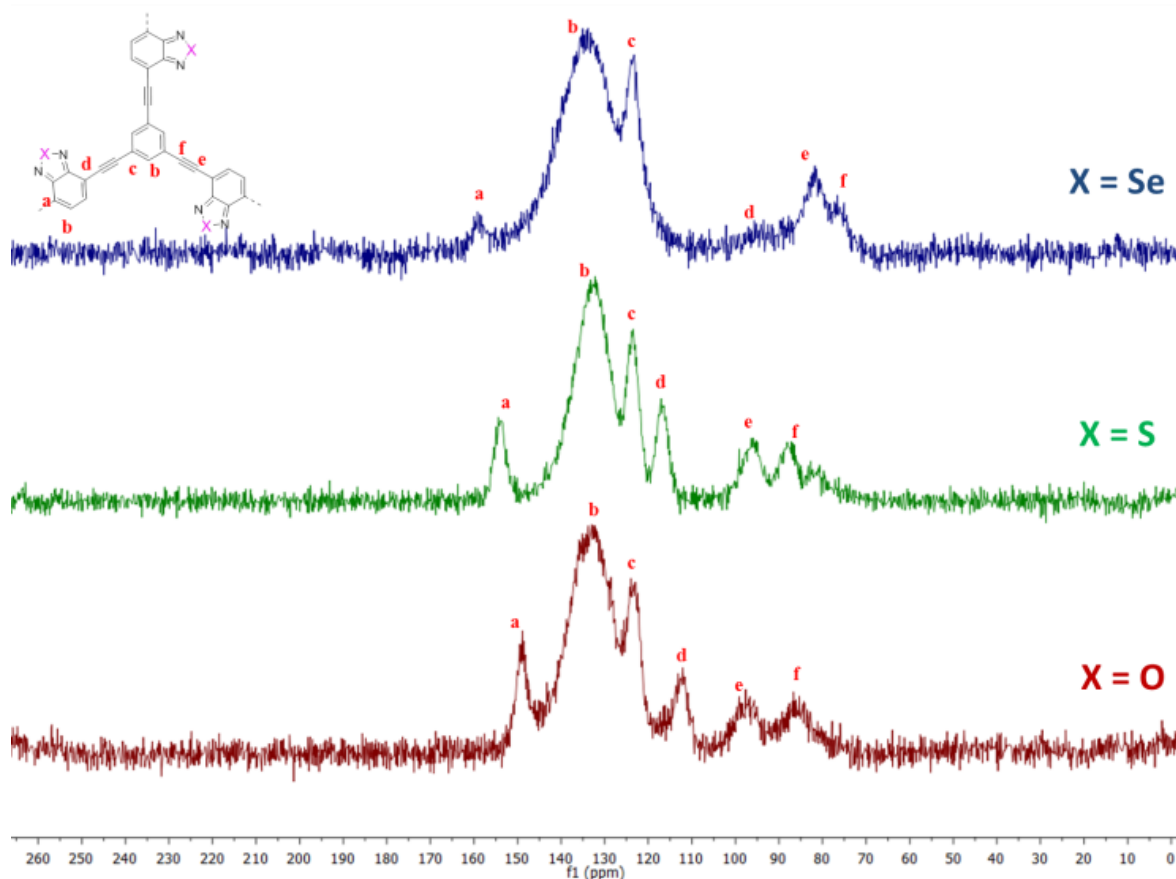


Figure 5.22 Solid-state ^{13}C /MAS NMR spectra of B-BO, B-BT and B-BS. Adapted from the diploma thesis of Kim Garth.

The Brunauer-Emmett-Teller (BET) surface areas of the polymers were measured to be $474\text{ m}^2/\text{g}$ for B-BO, $689\text{ m}^2/\text{g}$ for B-BT and $433\text{ m}^2/\text{g}$ for B-BS with pore volumes of $0.31\text{ cm}^3/\text{g}$, $0.38\text{ m}^3/\text{g}$ and $0.39\text{ m}^3/\text{g}$, respectively (Table 5.4). A similar pore size of 1.5 nm was determined for all three polymers (Figure 5.23).

Table 5.4 Porosity data of the polymer networks.

Polymer	S_{BET} (m^2/g)	Pore volume (cm^3/g)	Pore size (nm)
B-BO	474	0.31	1.5
B-BT	689	0.38	1.5
B-BS	433	0.39	1.5

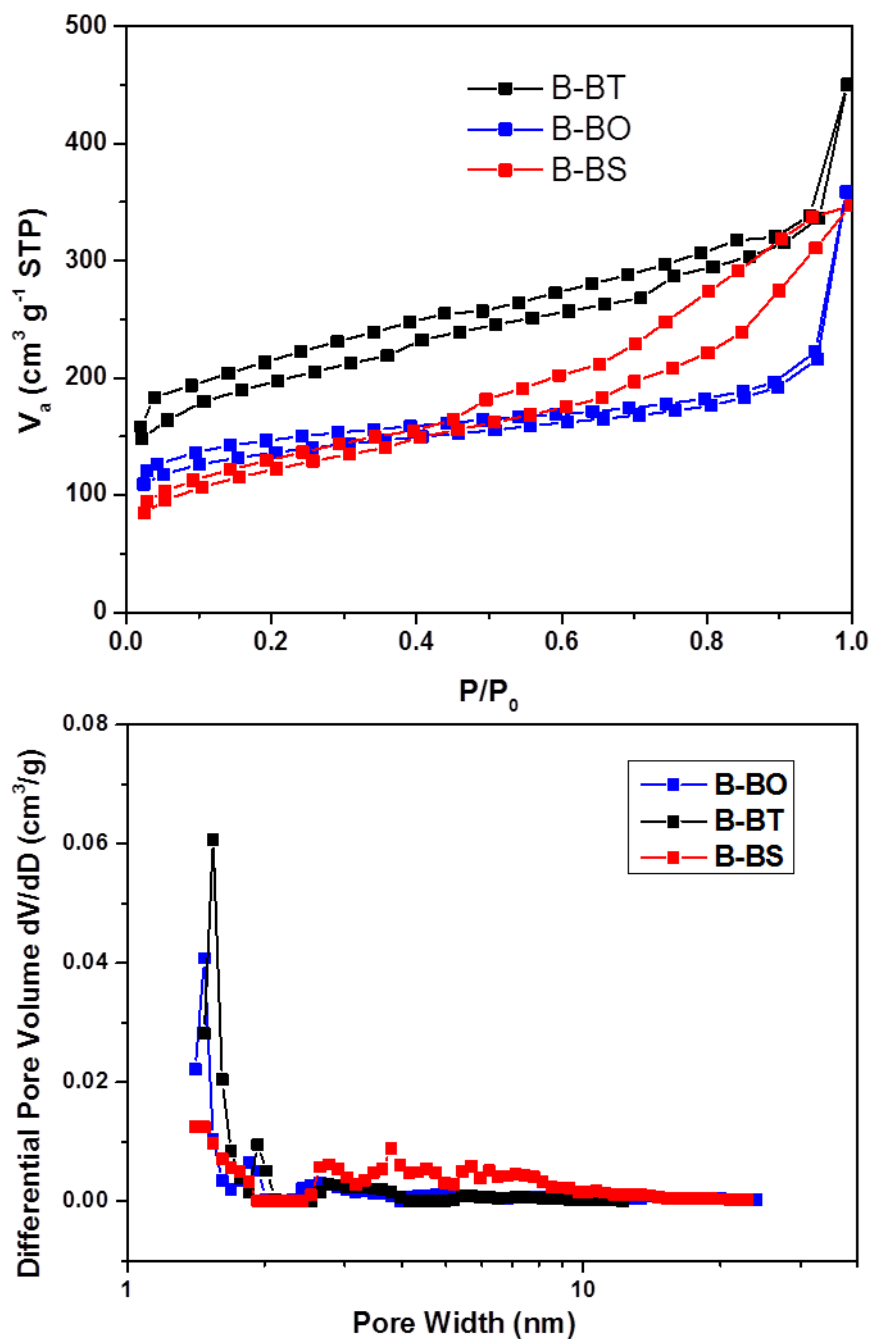


Figure 5.23 Nitrogen gas sorption isotherm and pore size distribution of the polymer series.

Thermal gravimetric analysis (TGA) measurements showed that the polymer networks remained intact up to 380 °C under nitrogen (Figure 5.24). To note, the relatively high residual weight of B-BS (about 80%) after heating to 1000 °C indicates a carbonized material with high selenium content.

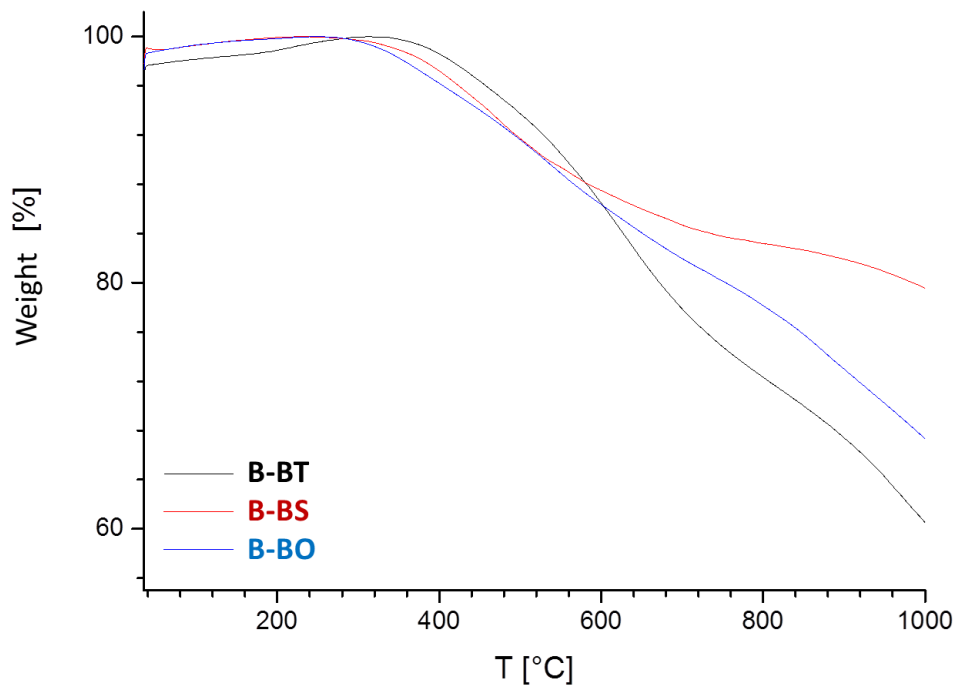


Figure 5.24 Thermogravimetric analysis (TGA) of the three polymers.

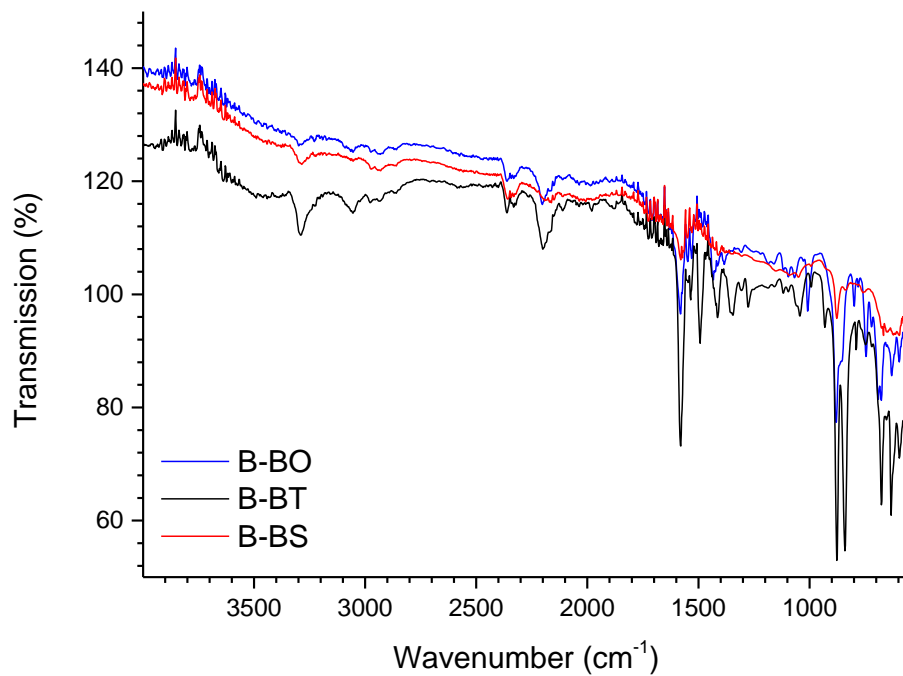


Figure 5.25 FTIR spectra of B-BO, B-BT and B-BS.

The SEM and TEM images of the three polymers illustrated different morphological structures at the micrometer scale (Figure 5.26). Specifically, B-BO showed a fiber-like structure with a diameter of less than 100 nm, B-BT showed a flake-like structure, while particle-like structure was observed for B-BS.

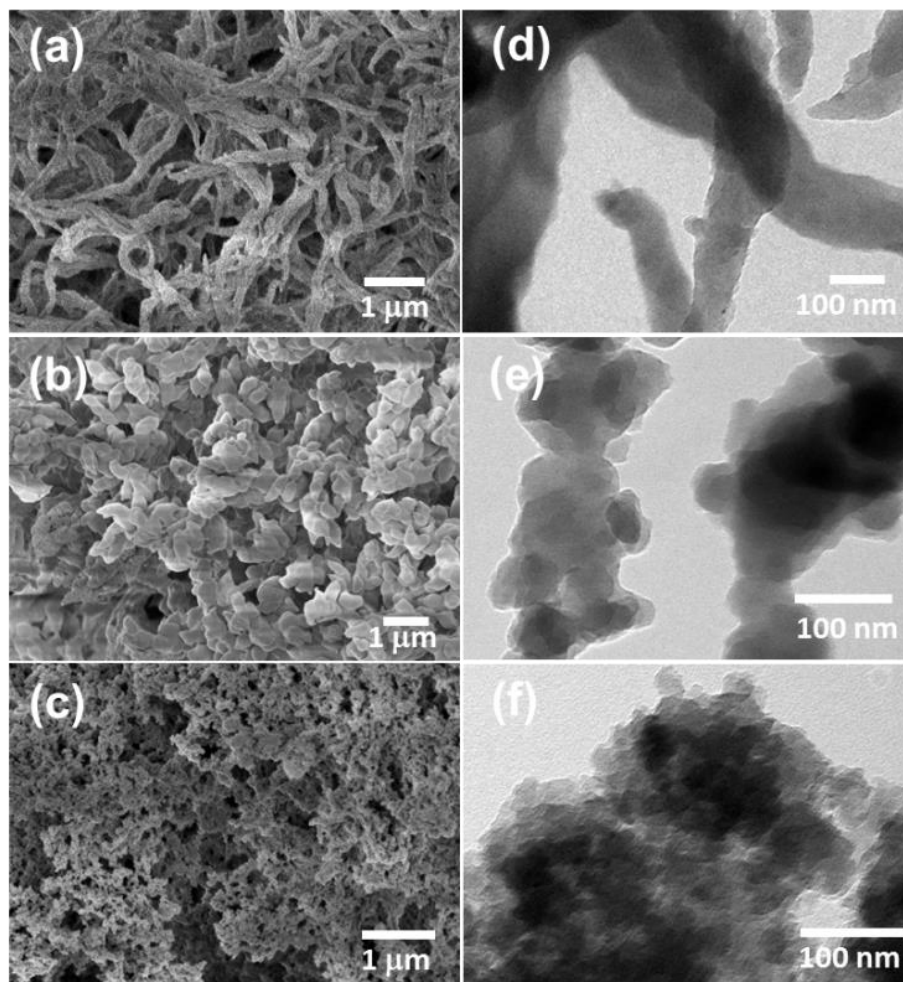


Figure 5.26 SEM images of (a) B-BO, (b) B-BT, (c) B-BS, and TEM images of (d) B-BO, (e) B-BT, (f) B-BS.

As illustrated in Figure 5.27a, the UV/Vis DR spectra of B-BO and B-BT show similar absorption range with maximal absorption between 300 and 500 nm and gradually levelling off until ca. 800 nm, whereas the absorption spectrum of B-BS is much broader ranging up to the near infrared (NIR) region. Indeed, both B-BT and B-BO have a yellowish color, while the color of B-BS is rather black (Figure 5.28).

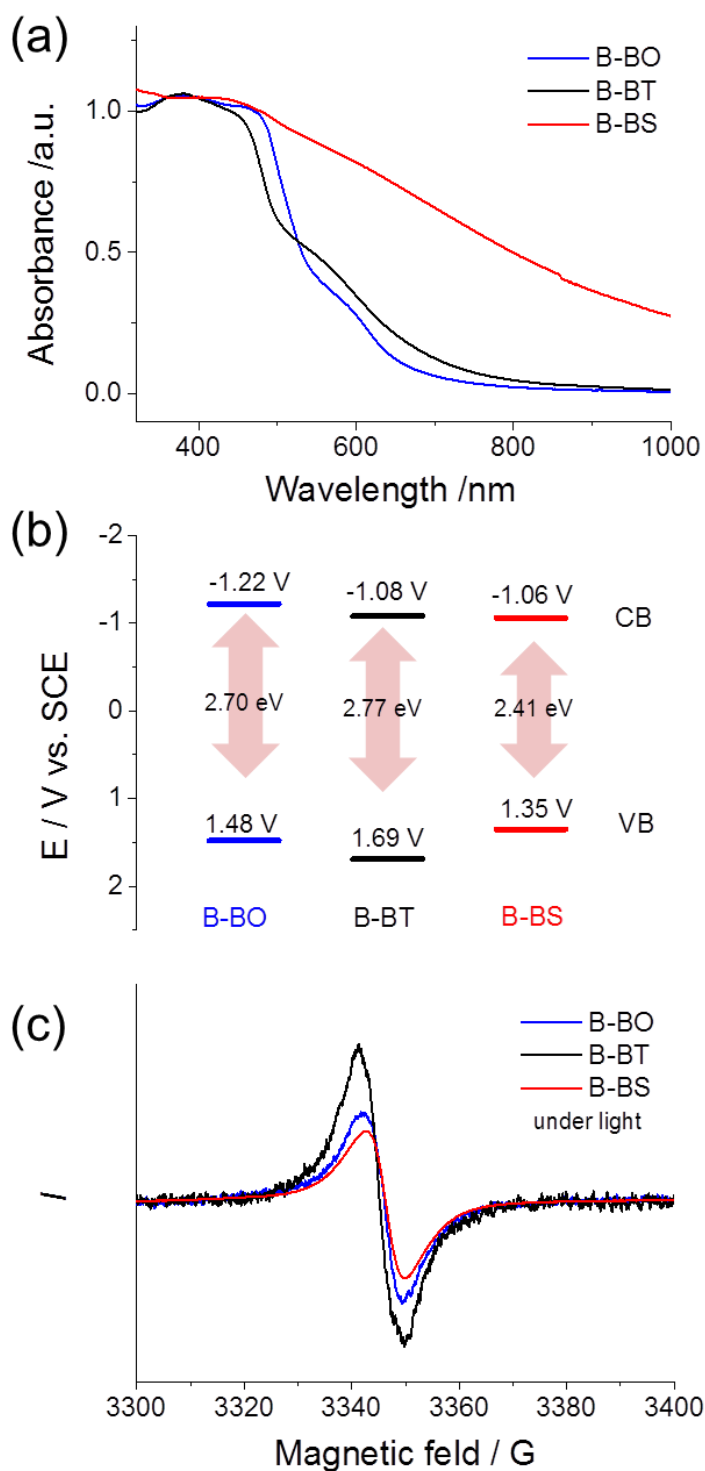


Figure 5.27 (a) UV/Vis DR spectra. (b) Valence band (VB) and Conduction band (VB) positions and (c) EPR spectra of B-BO, B-BT and B-BS under light irradiation.

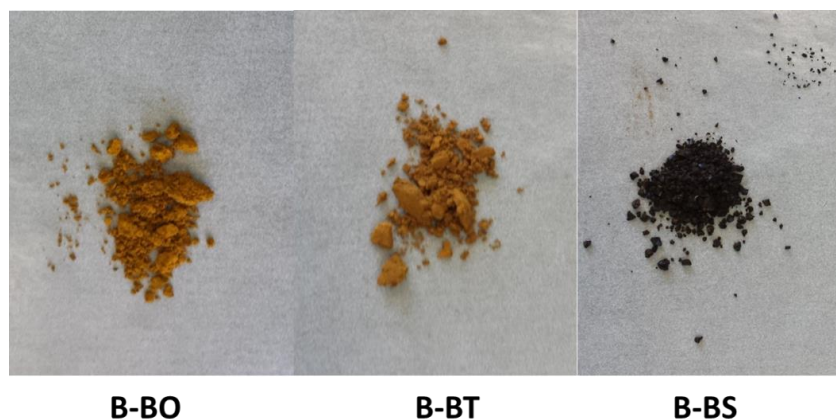
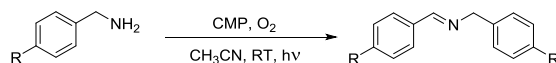


Figure 5.28 Pictures of CMP B-BO, B-BT and B-BS.

Table 5.5 Photooxidative coupling of benzyl amine and its derivatives by the different poly(benzochalcogenadiazole)s under visible light irradiation.^a



Entry	Polymer	Conversion (%)		
		R = H	R = F	R = OCH ₃
1	B-BO	48	20	7
2	B-BT	74	50	12
3	B-BS	8	3	2

Reaction conditions: 1 mmol substrate, 3 mg CMP, 3 mL CH₃CN, blue LED, 3h, 1 atm O₂, RT.

Cyclic voltammetry (CV) measurements revealed different oxidation and reduction onset potentials of the three polymers. (Figure 5.27b and Figure 5.29) implying different VB and CB positions of the polymer series. B-BO exhibited VB and CB at +1.48 V and -1.22 V versus SCE, respectively. In comparison, the VB and CB positions of B-BT are slightly lower at 1.68 V and -1.08 V, respectively. B-BS presented the narrowest band gap with VB and CB at 1.35 V and -1.06 V vs. SCE, respectively. It is noteworthy that these values are comparable to the redox potentials of well-established organometallic photocatalysts such as [Ru(bpy)₃]³⁺ (+1.29 V versus SCE) and [Ru(bpy)₃]²⁺ (-0.81 V versus SCE),⁶⁰ which indicates rather promising photocatalytic capabilities of the conjugated polymers.

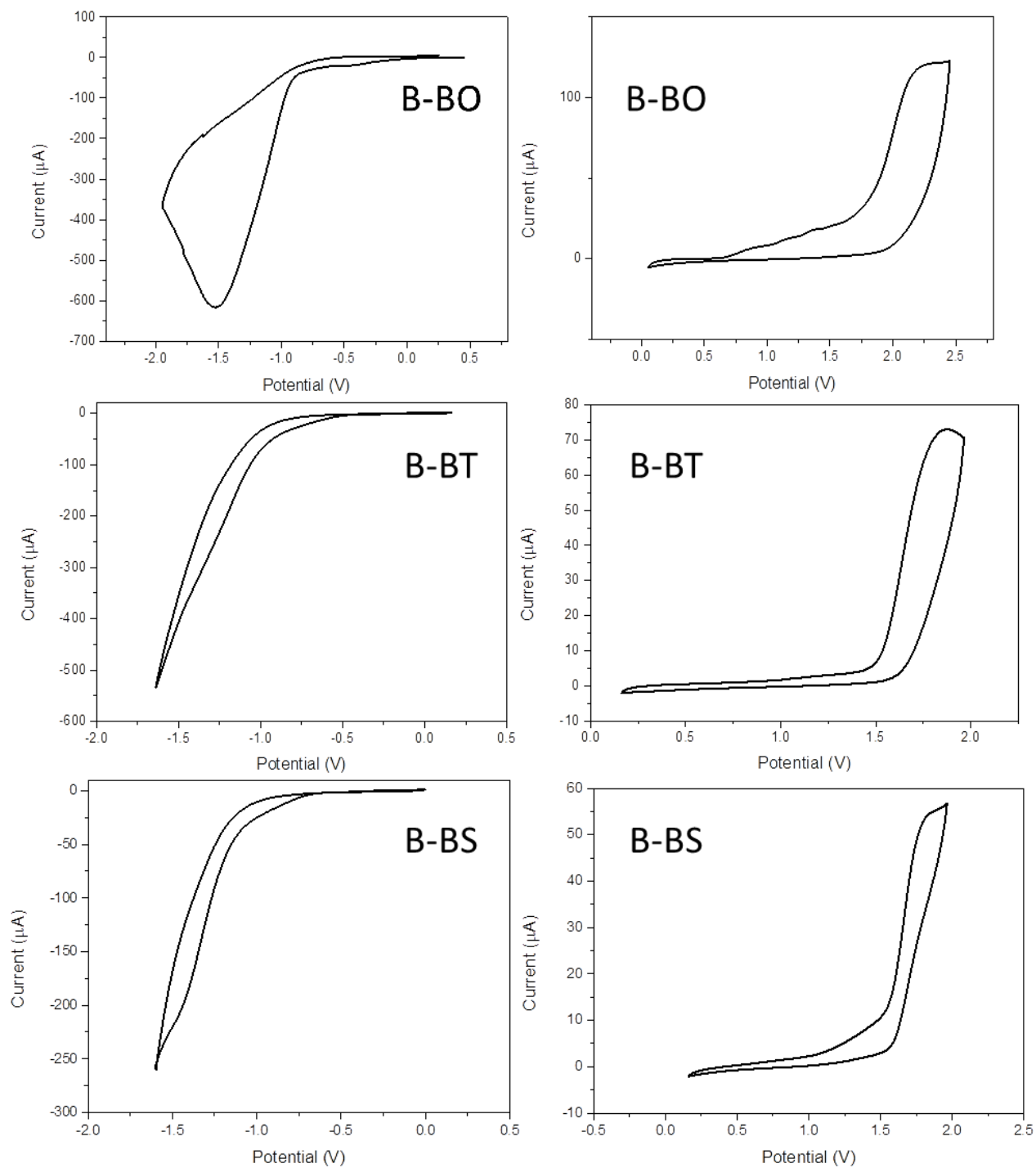


Figure 5.29 Cyclic voltammograms of CMPs B-BO, B-BT and B-BS.

The electron paramagnetic resonance (EPR) spectra showed the largest increase in signal intensity for B-BT under light irradiation compared to in dark. B-BO exhibited a moderately enhanced signal and B-BS the least (Figure 5.30-Figure 5.31). Comparing the three polymers, it

can be inferred from the significantly more intense EPR signal of BT (Figure 5.27c) that more long-lived electron-hole pairs could be generated in B-BT under light irradiation than in either B-BO or B-BS.

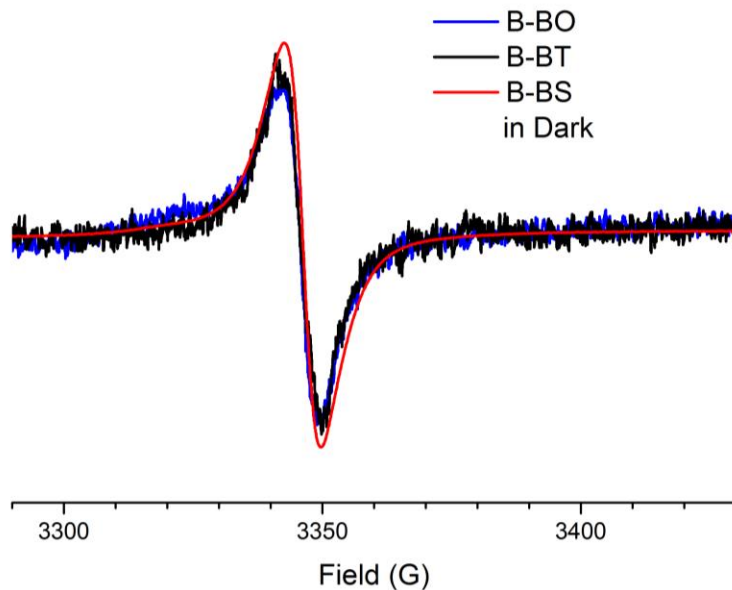


Figure 5.30 EPR spectra taken in dark for CMPs B-BO, B-BT and B-BS.

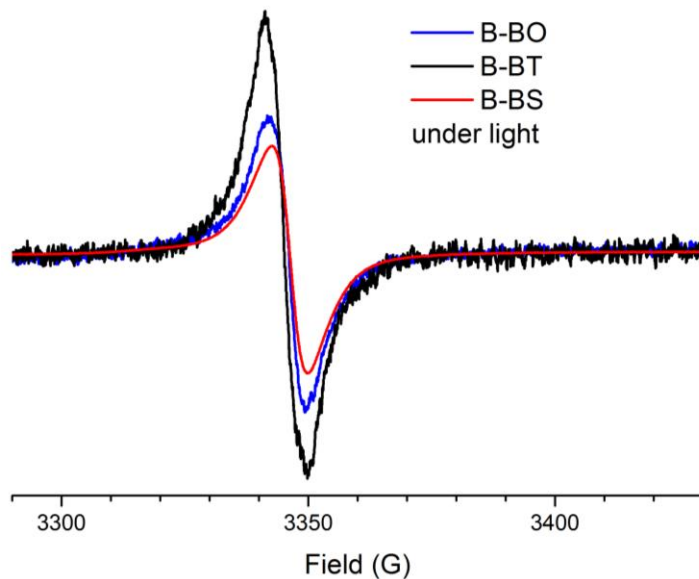


Figure 5.31 EPR spectra taken under light for CMPs B-BO, B-BT and B-BS.

5.1.2.2 Photooxidative Coupling of Benzylamine and its Derivatives

Similar as the first section, this section also investigated and compared the photocatalytic efficiencies of three conjugated polymers B-BO, B-BT and B-BS using the oxidative coupling of benzyl amine as a model reaction. First, benzylamine and its two derivatives with electron-withdrawing group (-F) and with electron-donating group (-OCH₃) were studied. As listed in Table 5.5, in all cases, reactions catalyzed by B-BT (entry 2) achieved significantly higher conversions compared to those catalyzed by B-BO and B-BS (entries 1 and 3) under the exact same reaction conditions.

Although the surface area of heterogeneous photocatalysts is generally believed to be an important parameter,^{199,202} in this case, we would argue that the higher BET surface area of B-BT(689 m²/g) could not by itself fully account for the remarkable increase in photocatalytic efficiencies and only play a minor role. More importantly, it is rather the optimal alignment of the VB and CB positions (+1.69 V/-1.08 V versus SCE for B-BT and +1.48 V/-1.22 V versus SCE for B-BO) and thus the favorable redox potentials that led to the superior catalytic efficiencies of B-BT and B-BO.

Previous studies showed that both photogenerated holes and electrons play significant roles in the redox reaction cycle. In the case of the oxidative coupling of amines, the active oxygen species, superoxide radical anion (O₂^{•-}, $E_{red.} = -0.86$ V) acts as the terminal oxidant.^{203,204} To shed further light on the reaction mechanism, we conducted several control experiments as shown in Table 5.6. Only traces of the final product were detected for entries 4 (without light) and 5 (without B-BT as catalyst). Entry 6 showed that only 7% conversion was obtained in 3 hours without O₂, thus confirming the vital role of oxygen in the reaction cycle. In addition, a kinetic study with intermittent light irradiation was conducted to further demonstrate the importance of light in this photocatalytic reaction (Figure 5.32). Light was turned on and off every hour. Conversions were only observed to increase under irradiation conditions, confirming that the reaction does not proceed in dark.

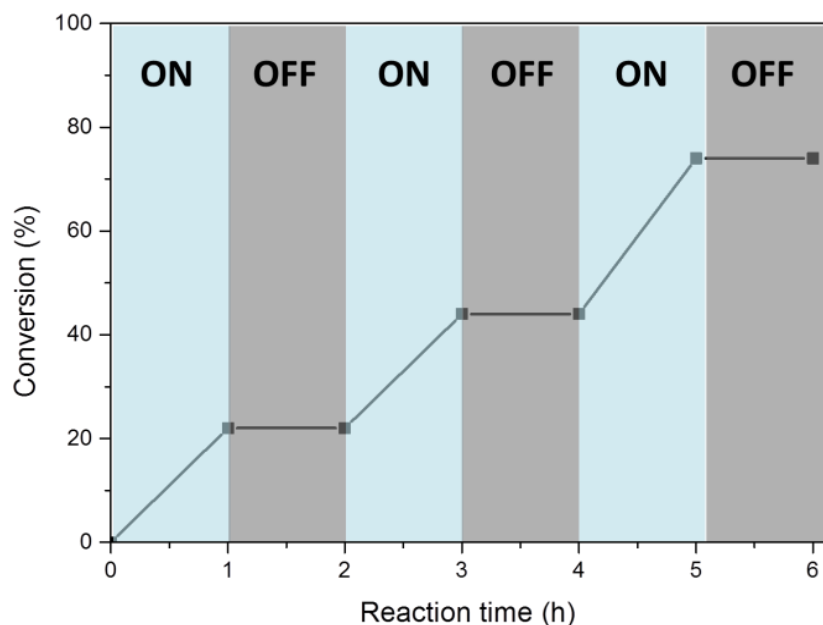


Figure 5.32 Light on-off experiment. Adapted from the diploma thesis of Kim Garth.

Table 5.6 and Figure 5.33 show the effects of adding various scavengers on the photocatalytic efficiencies of the photocatalysts. By adding KI, i.e. a hole scavenger, a reduced conversion of 26% was obtained (entry 7). By adding benzoquinone as superoxide radical scavenger, a conversion of only 12% was found (entry 8). Recent reports showed that conjugated macromolecular systems could generate another active oxygen species, singlet oxygen under visible light irradiation, using triplet electrons in the excited state.¹⁹⁹ We then carried out the reaction under standard conditions with the addition of sodium azide as singlet oxygen scavenger and a conversion of 35% was observed (entry 9). All these results indicate that both activated oxygen species (e.g. superoxide and singlet oxygen) took part in the oxidative coupling reaction of benzylamine, with superoxide playing a more dominant role. Interestingly, by using isopropanol as a hydroxyl radical ($\bullet\text{OH}$) scavenger, a reduced conversion of 50% was obtained (entry 10). We speculate that $\bullet\text{OH}$ could be generated from H_2O_2 , which could be obtained as a side product during the oxidative coupling reaction of benzylamine,²⁰¹ and plays a minor role in the catalytic process. Based on the observations from the screening and control experiments, we propose a modified reaction mechanism similar to the literature.^{201,203,204} As illustrated in Figure 5.34 under light irradiation, benzylamine is oxidized by the photogenerated hole of the polymer and then forms its cationic radical intermediate, which reacts with both photogenerated active oxygen species, $\text{O}_2^{\bullet-}$ and $^1\text{O}_2$ to form the intermediate hydroperoxy (phenyl)methanamine.

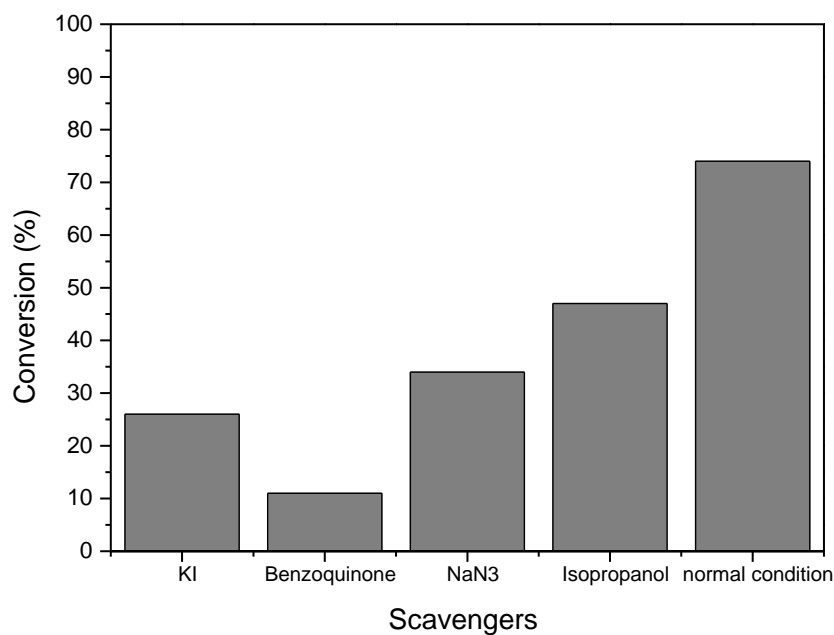
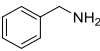
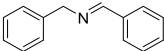
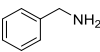
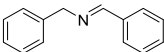
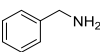
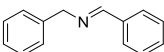
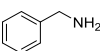
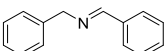
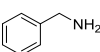
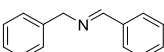
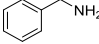
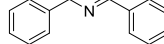
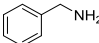
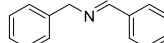
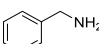
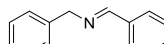
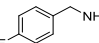
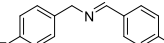
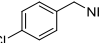
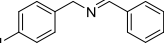
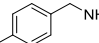
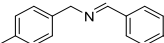
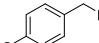
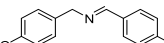
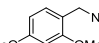
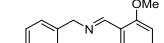
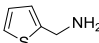
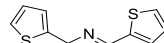


Figure 5.33 Control experiments of the photocatalytic oxidative coupling of benzylamine with different scavengers.

Table 5.6 Screening and control experiments of the oxidative coupling of benzyl amine and its derivatives using B-BT as photocatalyst.^a

Entry	Substrate	Product	Conv. (%)	E_{oxi} (V) ^b
4 ^c			trace	1.08
5 ^d			trace	1.08
6 ^e			7	1.08
7 ^f			26	1.08
8 ^g			10	1.08

9 ^h			35	1.08
10 ⁱ			50	1.08
11			74	1.08
12			50	0.99
13			43	0.90
14			55	0.97
15			12	0.93
16			5	1.03
17			10	0.87

^{a)} Standard reaction condition: 3 mg B-BT, 1 mmol substrate, 3 mL CH₃CN, 1 atm O₂, RT, blue LED irradiation at 460 nm, 3 h. Conversion data obtained by ¹H NMR ^{b)} E_{oxi.}= oxidation onset potential of benzylamine and its derivatives measured by cyclic voltammetry. ^{c)} In dark, 24 h. ^{d)} no B-BT, but under irradiation, 24 h. ^{e)} no O₂, with B-BT, under light, 3 h. ^{f)} KI as hole scavenger. ^{g)} benzoquinone as superoxide scavenger. ^{h)} NaN₃ as singlet oxygen scavenger. ⁱ⁾ isopropanol as •OH scavenger.

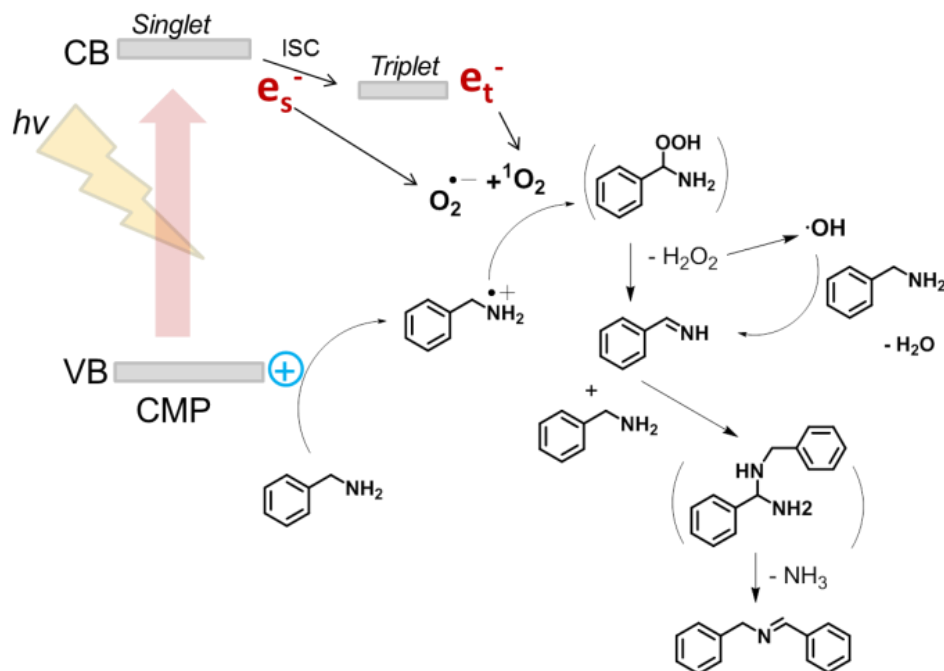


Figure 5.34 Proposed reaction mechanism of the photocatalytic oxidative coupling of benzylamine.

After elimination of H_2O_2 , an imine species is formed, which further reacts with an additional benzylamine molecule, forming N-benzyl-1-phenylmethanediamine as intermediate. GC-MS analysis was performed to verify the role of benzylimine as intermediate in the catalytic reaction. However, only trace amount can be observed by GC. This could be caused by the high activity of the imine intermediate. After elimination of ammonia from N-benzyl-1-phenylmethanediamine, the final product is obtained. In this process, the obtained $\cdot\text{OH}$ could also extract a proton from the oxidized benzylamine cationic radical and thus form the imine species. Both photogenerated electrons and holes actively participate in the photooxidative coupling of amines.

The reduction and oxidation potentials of all three photocatalysts are sufficiently high enough to reduce molecular oxygen into radical anion superoxide ($E_{red.} = -0.86 \text{ V}$) and oxidize benzylamine into its cationic radical form ($E_{oxi.} = +1.08 \text{ V}$) (Table 5.6). It is probably the interplay of the higher overpotential afforded by the lowest-lying oxidation potential of B-BT ($\text{VB} = 1.69 \text{ V}$ versus SCE) and the most photogenerated electron-hole pairs (Figure 5.27c) that played the decisive role, leading to its superior catalytic efficiency (Table 5.5). However, the system is still yet to be fully-understood and to some degree, a combination of different

parameters, such as porosity, stability of the photogenerated electron-hole pairs and the redox potentials can all influence the effective photocatalytic efficiency.

Repeating experiment was also carried out using B-BT as photocatalyst and benzylamine as substrate. It was shown that the polymer could be used for another 5 repeating cycles without significant change in its catalytic efficiency (Figure 5.35). No clear change of the FTIR spectra of the polymer before after the catalytic reaction appeared (Figure 5.36).

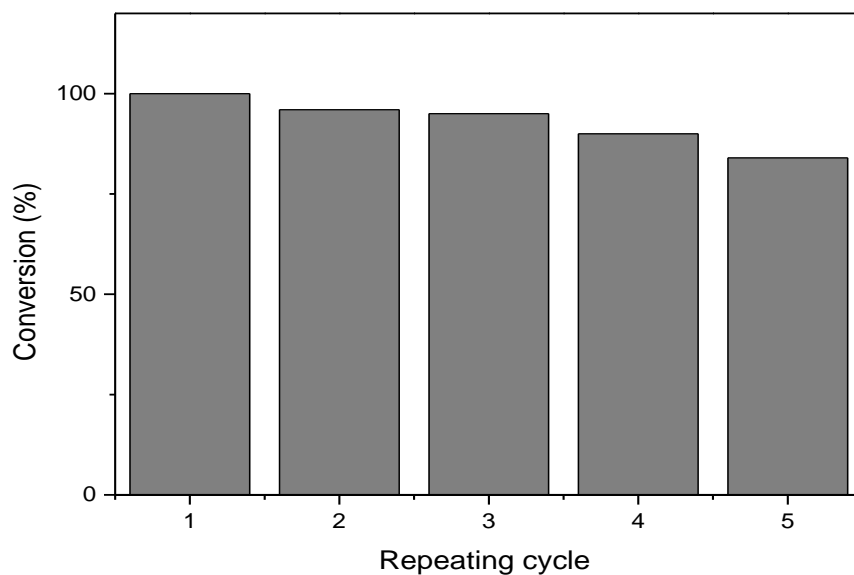


Figure 5.35 Repeating experiment of photocatalytic oxidative coupling of benzylamine using B-BT as catalyst.

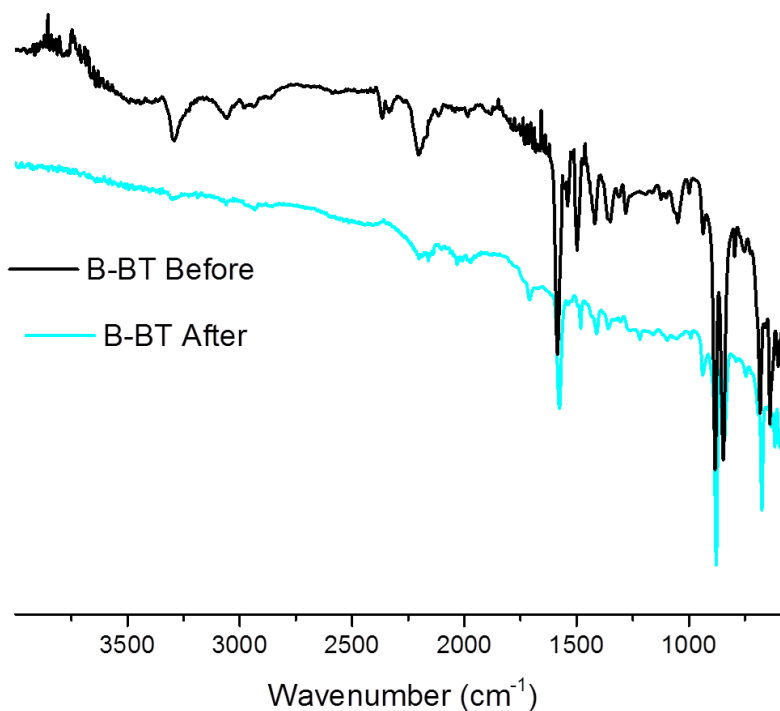


Figure 5.36 FT-IR spectra for B-BT before and after reactions.

To further demonstrate the general applicability of B-BT, extensive investigation of photooxidative coupling of a series of benzylamine derivatives were performed. The conversion data are listed in Table 5.6. Generally, substrates with electron-withdrawing functionalities (entries 8 and 11) were found to react faster than those with electron-donating groups (entries 9 and 12). It was observed that electron withdrawing groups such as F or Cl led to higher conversions (entries 12 and 13) than the electron donating groups such as methyl or methoxy groups (entries 14 - 16). This could be attributed to the stabilized cationic radical by the methyl and especially methoxy groups, which decelerate the formation of the final product. This could explain the low conversion of dimethoxy benzylamine (entry 16). Similar stabilizing effect could be observed with thiophen-2-ylmethanamine (entry 17).

The oxidation onset potentials of benzylamine and its derivatives were measured and also listed in Table 5.6. It could be observed that the oxidation potential of the substrate were not proportional to the conversion of the oxidative coupling reaction. The reason might not lie at the electron transfer step from the benzylamines to the photocatalyst (hole), but on the nucleophilic addition step (the reaction between imine and amine). The lower charged density on the -NH_2

group of the benzylamine derivative with electron-withdrawing groups such as fluoro or chloro groups are better reactants than the ones with electron-donating groups such as methoxy group.

5.1.2.3 Conclusion

In summary, this chapter demonstrates a simple molecular design protocol for fine-tuning the valence and conduction band levels of conjugated microporous polymers based on poly(benzochalcogenadiazole)s as pure organic, heterogeneous visible light photocatalysts. Enhanced photocatalytic efficiency was observed by altering the chalcogen moieties in the electron accepting benzochalcogenadiazole unit of the polymer backbone structure. It was shown that benzothiadiazole-containing photocatalyst demonstrated superior photocatalytic activity in the oxidative coupling of amines. This design strategy and enhanced efficiency could be extended to a wider range of conjugated microporous polymeric photocatalysts for photoredox catalytic reactions in general.

5.2 Surface Area Control of Conjugated Porous Polymer Photocatalysts

This chapter is based on the published article “Highly Porous Conjugated Polymers for Selective Oxidation of Organic Sulfides under Visible Light”, *Chem. Comm.*, 2014, **50**, 8177-8180 with copyright (2014) from Royal Society of Chemistry.

5.2.1 Introduction

In heterogeneous photocatalysis, it is generally believed that the catalytic reactions occur at the interface between the phases and higher interfacial surface area would generally lead to enhanced catalytic efficiency. Thus, it is of high interest to investigate independently the influence of enlarged surface area of the conjugated porous polymer photocatalysts on their photocatalytic efficiencies while keeping other parameters constant. In the following chapter, π -conjugated microporous polymers with hierarchical pore structures were synthesized as efficient heterogeneous photocatalysts for highly selective oxidation of organic sulfides into sulfoxides under visible light. The polymers were prepared via the high internal phase emulsion polymerization (polyHIPE) technique and the surface areas could be increased up to eight times by micropore surface engineering via incorporation of the thermally cleavable *tert*-butyl carboxylate (Boc) functional group as spacer into the polymer network.

High internal phase emulsion polymerization (polyHIPE) is a relatively new technique for the preparation of highly porous materials with versatile applications such as tissue engineering scaffolds,²⁰⁵ enzyme immobilization,^{206,207} gas storage,²⁰⁸ and separation media.²⁰⁹ Giving the micrometer-sized pore structures, which is highly suitable for mass transfer, polyHIPEs are also used as catalyst support.²¹⁰ Only a few reports on the synthesis of photocatalysts by HIPE polymerization were published.^{211,212} Recently, the synthesis of the first examples of fully π -conjugated polyHIPEs was reported, these materials showed surface areas of 35-50 m²g⁻¹ and could be used as highly efficient and reusable heterogeneous photosensitizer for the singlet oxygen generation under visible light.²¹² Combining the interconnected porosity of polyHIPEs and the π -conjugated framework throughout the polymer network, π -conjugated polyHIPEs hold great promise in metal-free heterogeneous photocatalysis with visible light. Because π -conjugated polyHIPEs act as photocatalysts with a stable inherent porous skeleton,

the use of additional support materials such as silica gels²¹³ and zeolites²¹⁴ can be eliminated. Classical polyHIPEs have rather low surface areas (up to 50 m²g⁻¹).^{215,216} It was later shown that the surface area of polyHIPEs can be tuned by varying the crosslinker content²¹⁷ or by hypercrosslinking the system²¹⁸ via chemical functionalization. Nonetheless, these methods are not suitable for π -conjugated polyHIPEs to be used as photocatalysts since the chemical composition of the π -conjugated polyHIPEs is of vital importance to their photochemical properties and photocatalytic performance.

Organic sulfides are key intermediates in pharmaceutical or other fine chemical industries.^{219,220} Selective oxidation of sulfides to the corresponding sulfoxides is traditionally achieved with stoichiometric amounts of organic or inorganic oxidants, which usually generates huge amount of toxic byproducts or heavy metal wastes.^{221,222} Recent developments of catalysts based on organometallic complexes have been attempted to alleviate this problem but they still generally require substantial amounts of additional oxidants, such as H₂O₂ at elevated temperatures,^{223,224} urea hydroperoxide,²²⁵ and isobutyraldehyde.⁴⁷ Thus, π -conjugated polyHIPEs have the clear advantage of serving as green, effective, chemoselective and recyclable photocatalysts that require only visible light and air. Not only can the π -conjugated polyHIPEs be easily removed and recycled after use, they can also be readily incorporated into continuous flow systems, which offer facile automation, precise control over reaction parameters and predictable scale-up.²¹²

5.2.2 Synthesis of Conjugated Porous Polymers with Different Surface Areas

This chapter reports on design and preparation of high surface area π -conjugated microporous polymers with hierarchical pore structures by the Suzuki-Miyaura cross-coupling reaction via high internal phase emulsion polymerization and micropore surface engineering. By incorporation and removal of cleavable *tert*-butyl carboxylate (Boc) functional group as spacer into the polymer network, the surface area can be increased up to eight time of their size, gaining extra hierarchical porosity (Figure 5.37). The porous polymers showed high photocatalytic activity for highly selective oxidation of organic sulfides into the desired mono-oxidized sulfoxides under visible light irradiation. Furthermore, the influence of surface area and energetic

level on the photocatalytic performance was investigated by introducing a well-studied electron acceptor, the benzothiadiazole (BT) unit into the polymer backbone.

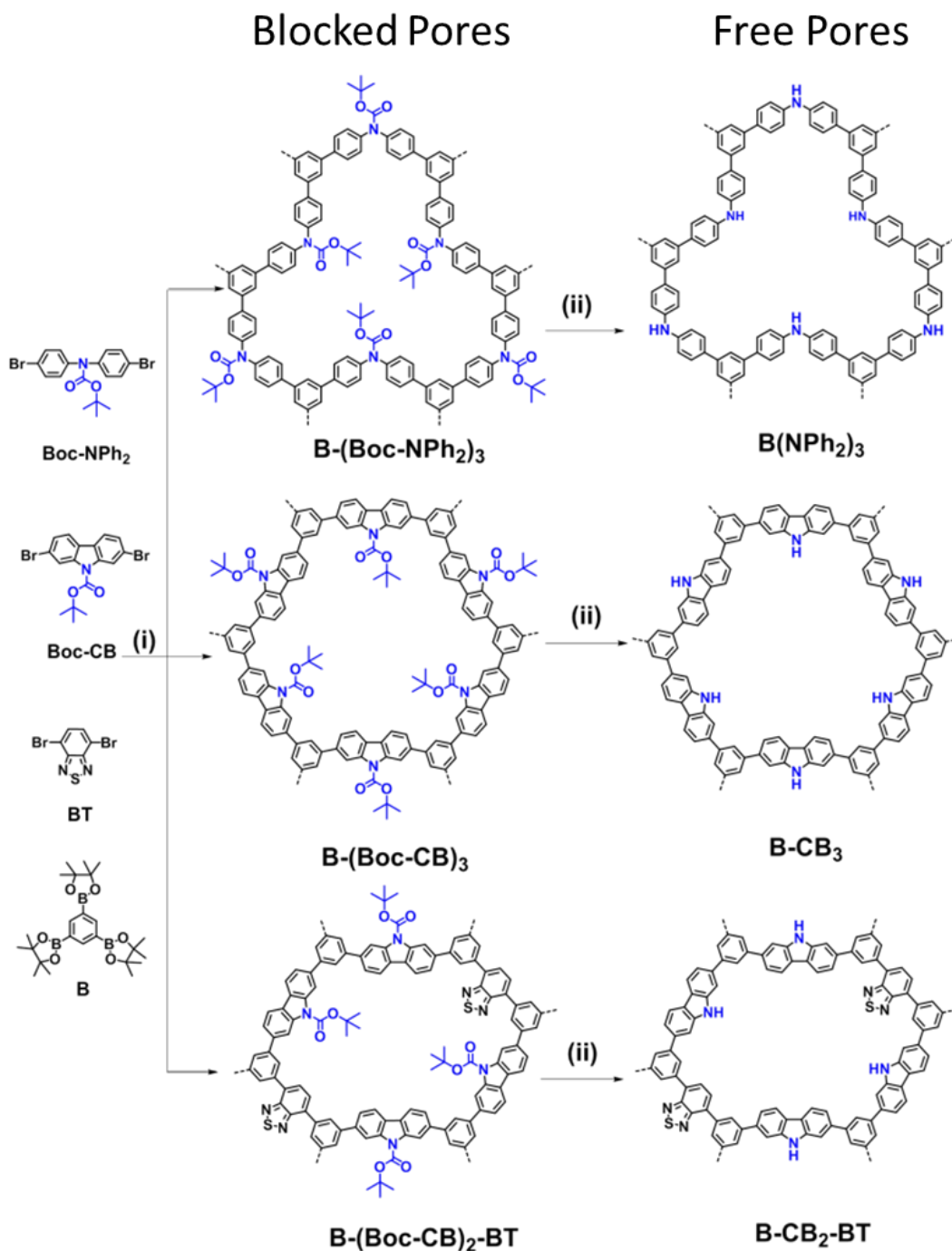


Figure 5.37 Idealized structures and surface area control via micropore engineering and of π -conjugated microporous polymers. Conditions: (i) Suzuki coupling in HIPE. (ii) 250 °C, 12 h, vacuum.

5.2.3 Characterization of Conjugated Porous Polymers with Different Surface Areas

All systems investigated here resulted after the reaction in monolithic solids, which were completely insoluble in all solvents investigated (Figure 5.37). The thermogravimetric analysis (TGA) of the Boc containing polymers showed a significant weight lost at 250 °C under N₂, indicating the thermal cleavage of the Boc group inside the porous polymers (Figure 5.38 and Figure 5.39). The FTIR spectra confirmed the disappearance of the typical signals for >C=O groups at 1750 cm⁻¹ (Figure 5.40). The solid-state ¹³C/MAS NMR spectra showed a significant decrease of chemical shifts at $\delta = 30$ and 80 and 155 ppm, which are assigned to the -CH₃, *quart.*-C and >C=O groups of the Boc moiety. The signals between 100 and 160 ppm remained, which are assigned to the aromatic rings in the polymer backbones (Figure 5.43-Figure 5.45). This indicates that under the thermal treatment the aromatic structure stays intact.

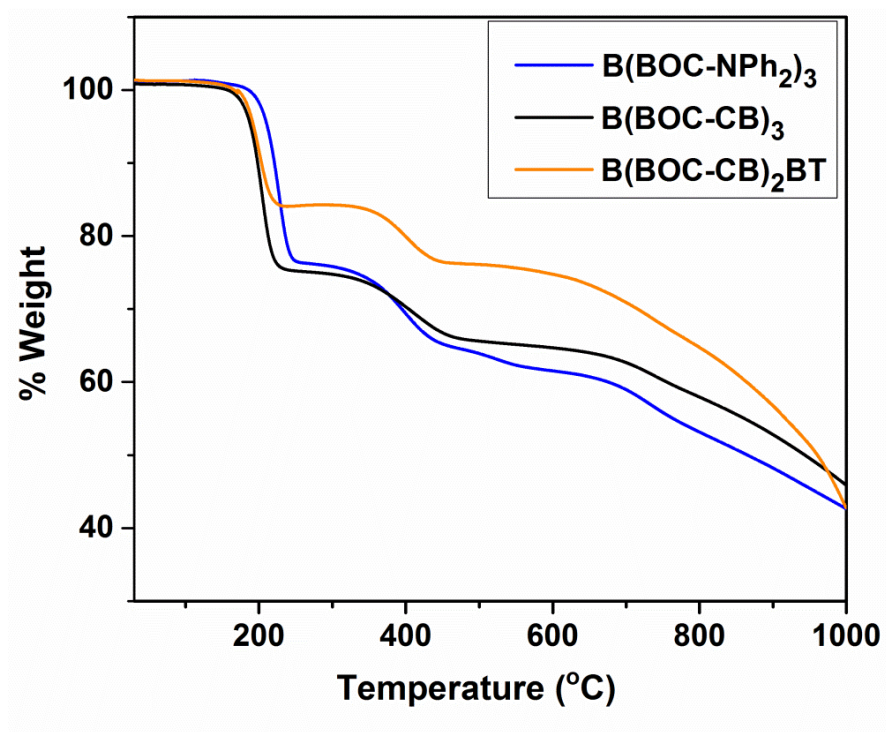


Figure 5.38 Thermogravimetric analysis of poly(HIPE)s with Boc groups.

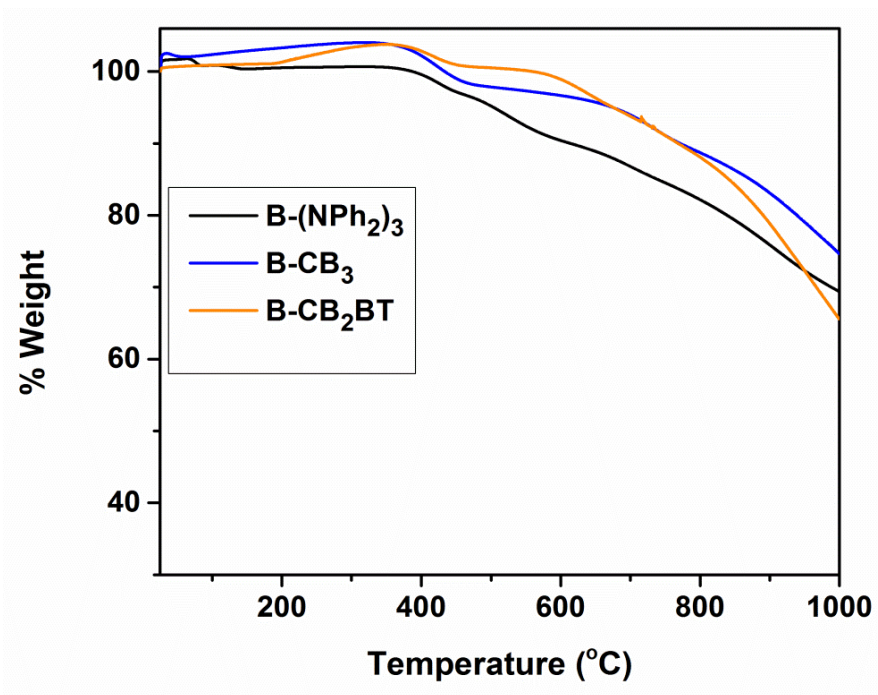


Figure 5.39 Thermogravimetric analysis of poly(HIPE)s without Boc groups.

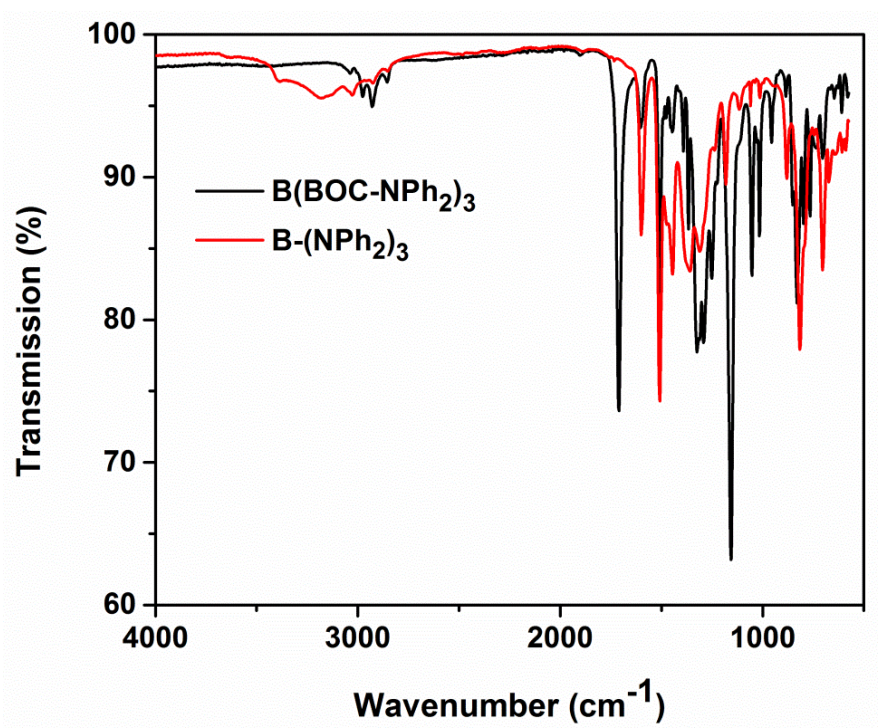


Figure 5.40 FTIR spectra of B-(BOC-NPh₂)₃ and B-(NPh₂)₃.

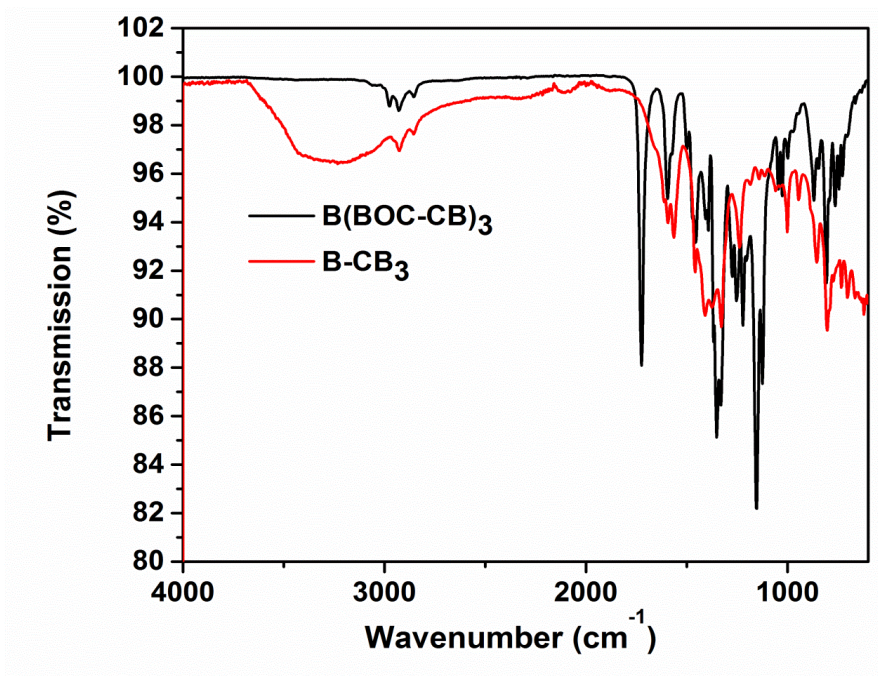


Figure 5.41 FTIR spectra of B-(BOC-CB)₃ and B-CB₃.

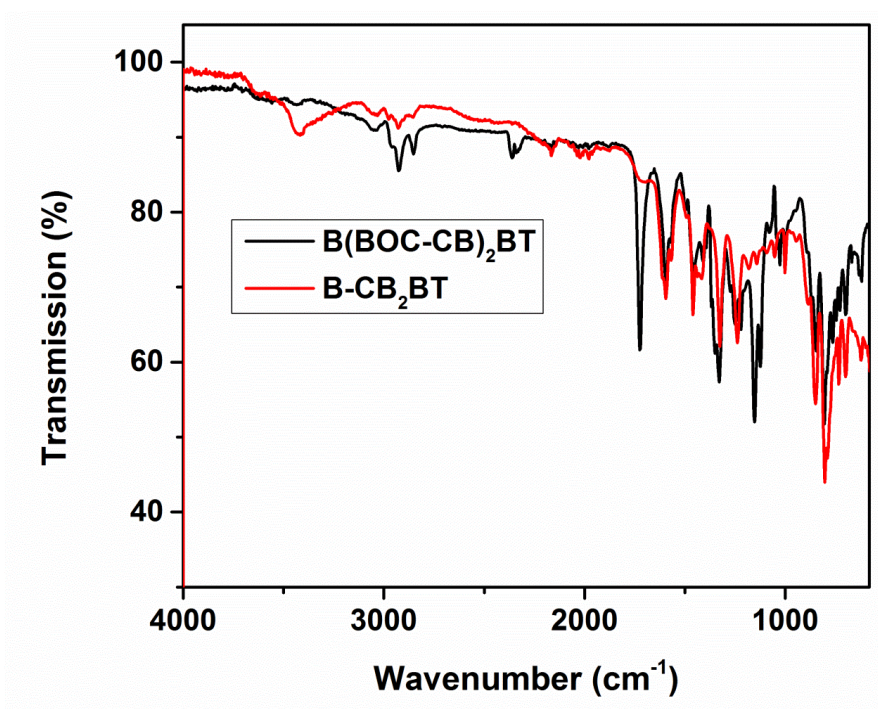


Figure 5.42 FTIR spectra of B-(BOC-CB)₂-BT and B-CB₂BT.

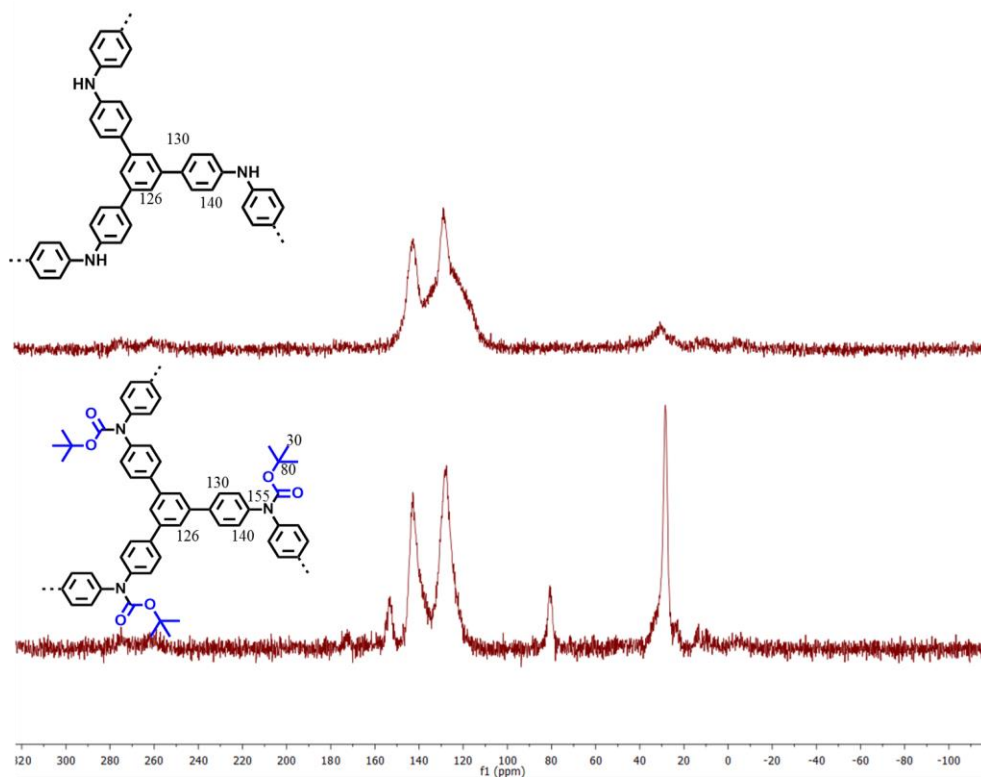


Figure 5.43 Solid state ^{13}C CP/MAS NMR spectrum of $\text{B}-(\text{NPh}_2)_3$ and $\text{B}-(\text{Boc-NPh}_2)_3$.

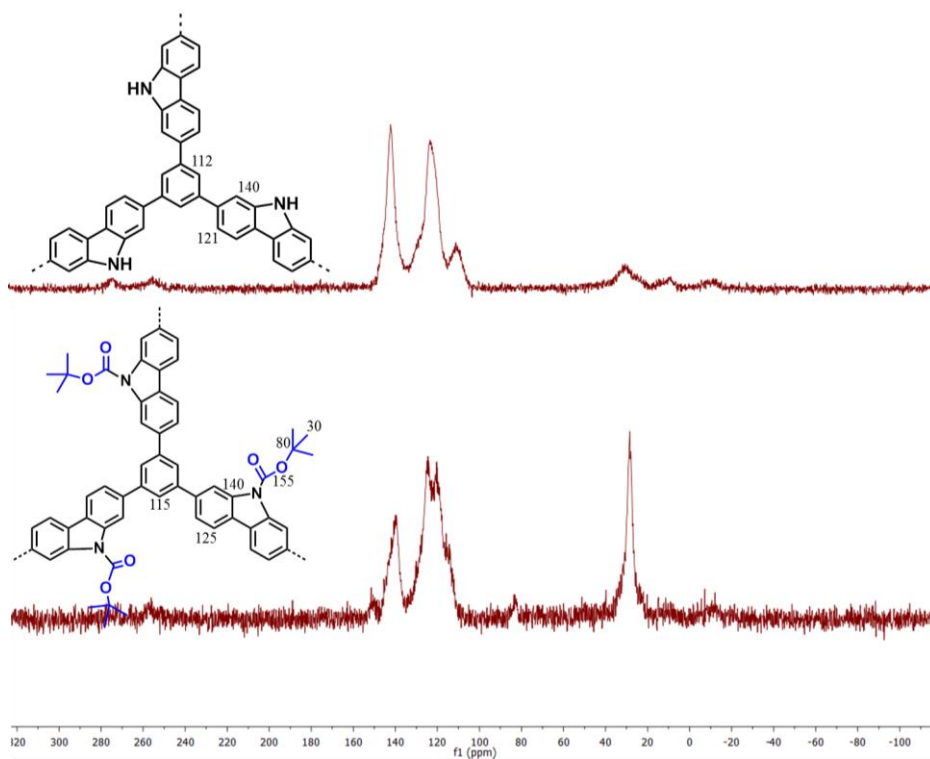


Figure 5.44 Solid state ^{13}C CP/MAS NMR spectrum of B-CB_3 and $\text{B}-(\text{Boc-CB})_3$.

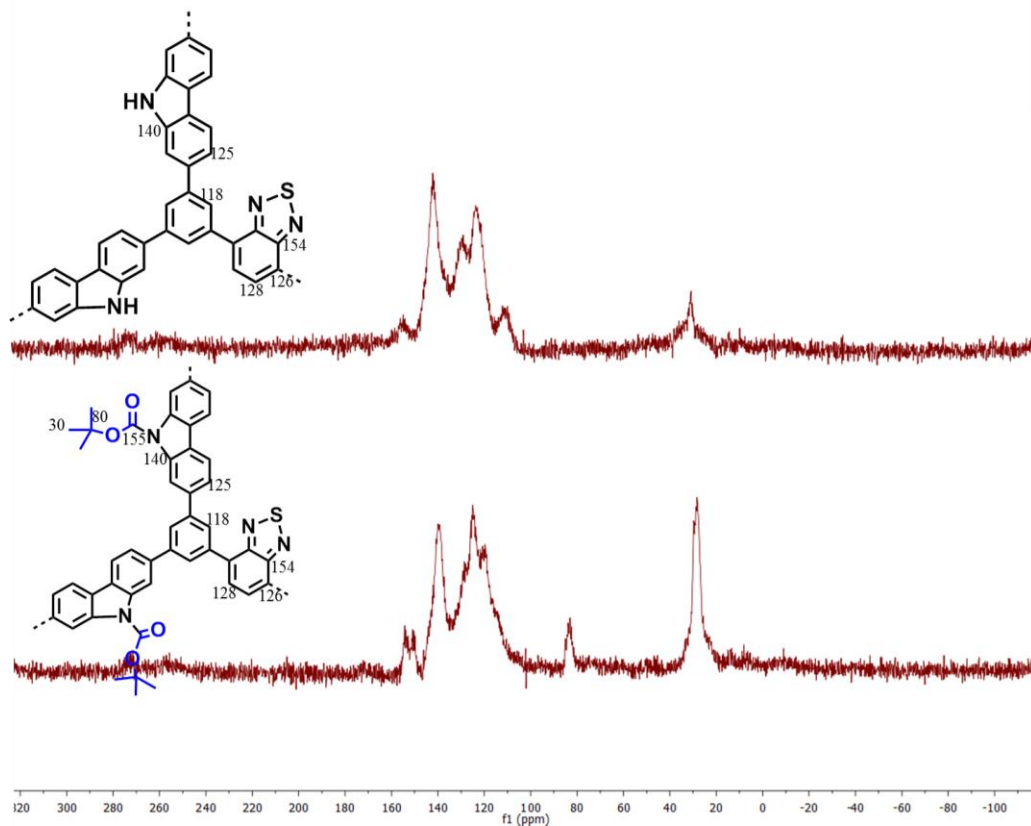


Figure 5.45 Solid state ^{13}C CP/MAS NMR spectrum of B-CB₂-BT and B-(Boc-CB)₂-BT.

The Brunauer-Emmett-Teller (BET) surface areas of all three polymers increased significantly after the removal of the Boc group. In particular, they range from $198\text{ m}^2\text{ g}^{-1}$ for B-(NPh₂)₃, $230\text{ m}^2\text{ g}^{-1}$ for B-CB₃ and $53\text{ m}^2\text{ g}^{-1}$ for B-CB₂-BT, exhibiting an increasing factor of 4, 8 and 2 times from B-(Boc-NPh₂)₃ with $45\text{ m}^2\text{ g}^{-1}$, B-(Boc-CB)₃ with $27\text{ m}^2\text{ g}^{-1}$, and B-(Boc-CB)₂-BT with $26\text{ m}^2\text{ g}^{-1}$, respectively (Figure 5.46 and Figure 5.47). Likewise, the total pore volumes of the porous polymers also increase, the micropore diameter exhibited ca. 1.5 nm via this micropore modification method. The data are listed in Table 5.7

Table 5.7 Surface area and pore size characterizations of various poly(HIPE)s.

PolyHIPE	Surface Area (m²/g)	Pore Diameter (nm)	Pore Volume (cm³/g)
B-(Boc-NPh₂)₃	45	1.5	0.066
B-(Boc-CB)₃	27	2.7	0.051
B-(Boc-CB)₂-BT	26	2.9	0.056
B-(NPh₂)₃	198	1.5	0.161
B-CB₃	229	1.5	0.169
B-CB₂-BT	53	1.5	0.065

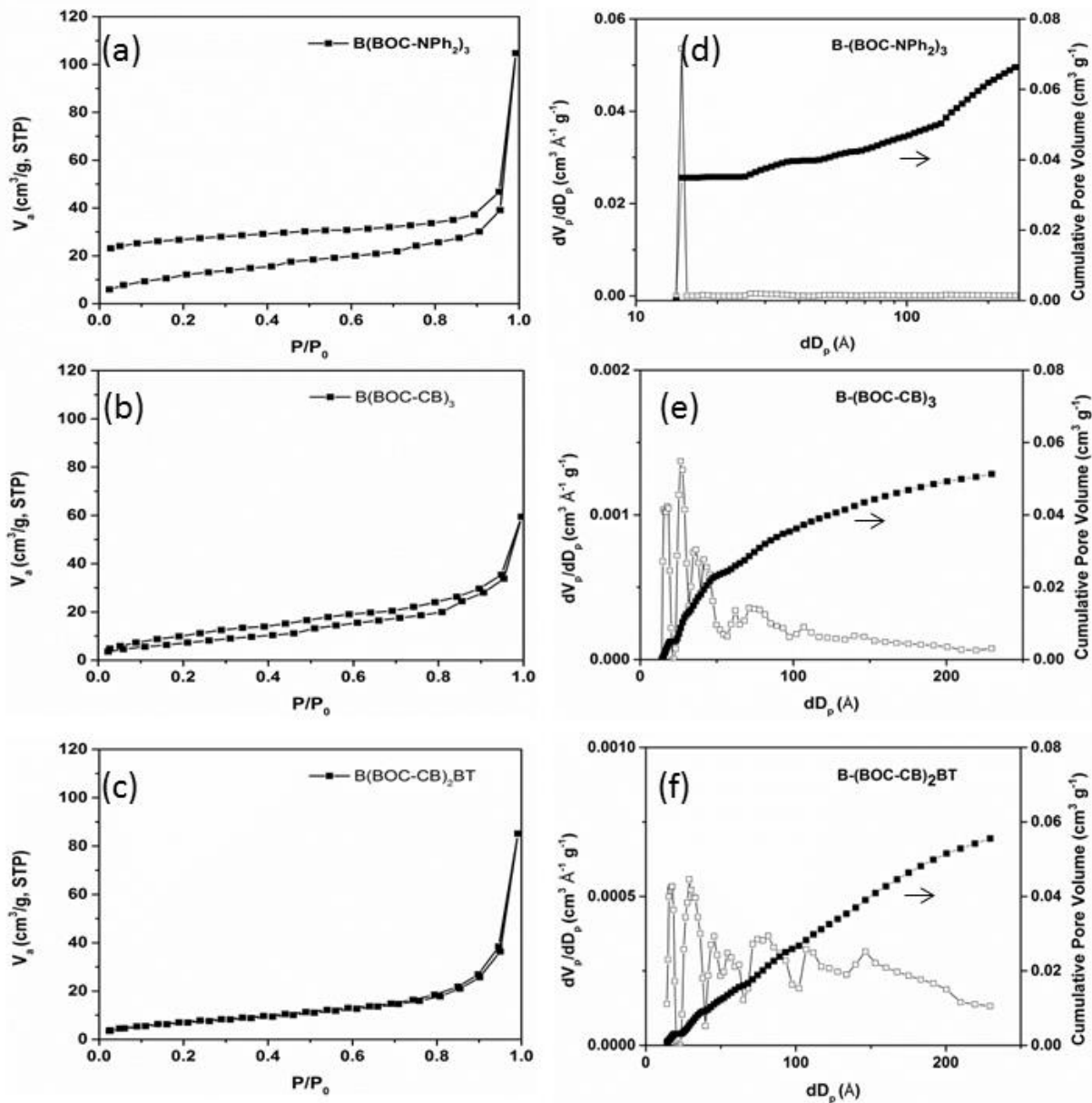


Figure 5.46 N_2 Sorption Isotherms and Pore Size Distributions of poly(HIPE)s with Boc groups.

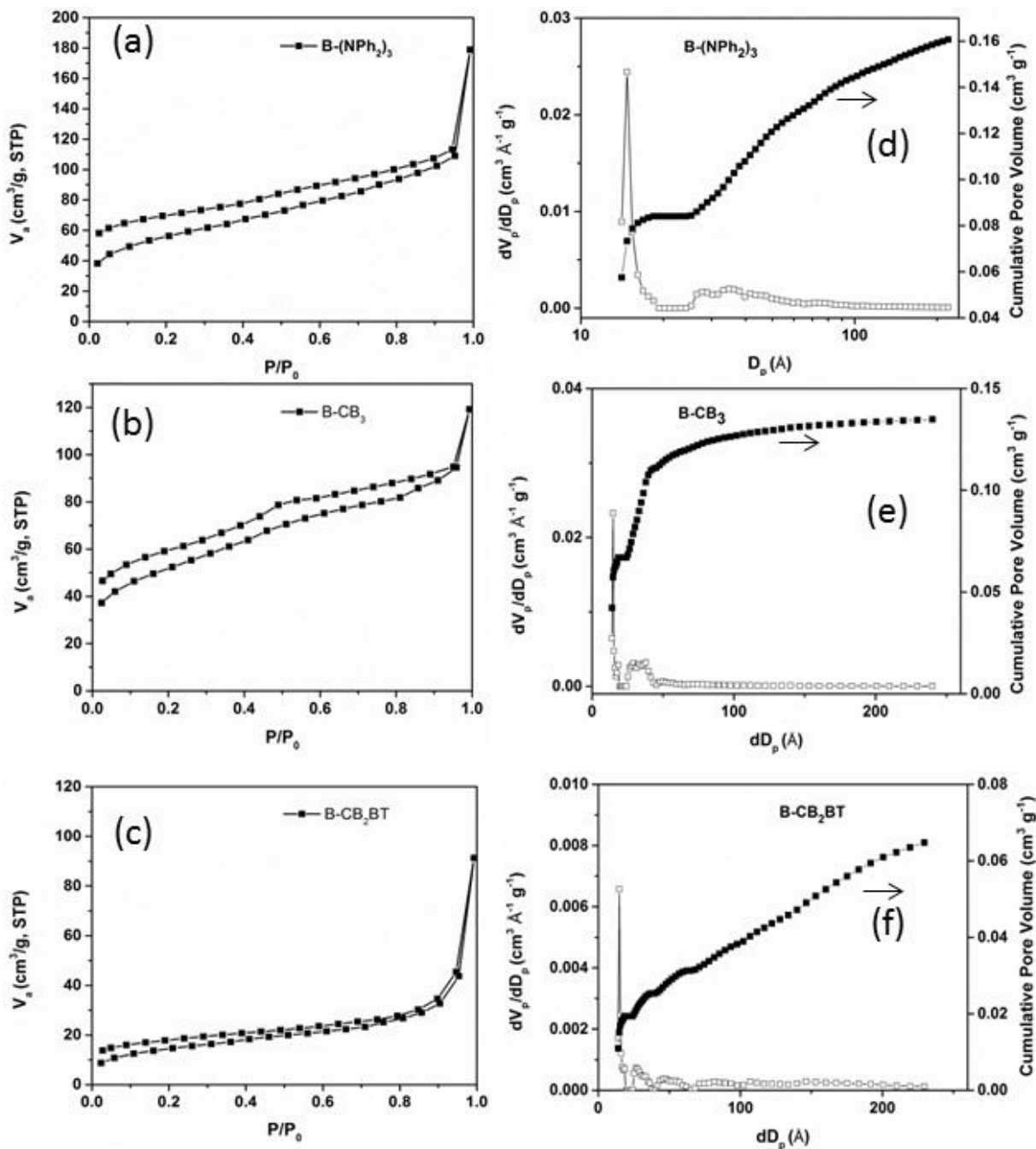


Figure 5.47 N_2 Sorption Isotherms and Pore Size Distributions of poly(HIPE)s after removal of Boc groups.

In Figure 5.48, SEM images of the two series of polyHIPEs are displayed. The polyHIPE series after the Boc cleavage appeared in very similar morphology as the series containing Boc, showing interconnected pore structures. The cavities of the polyHIPEs range from 10 μm to 20

μm in size whereas the interconnected pores have diameters of about $1\ \mu\text{m}$. To note is that the removal of Boc group via heat treatment did not affect the stability of the macrostructure, the porous skeleton remained intact. Only a huge amount of micropores ($d = \sim 1.5\ \text{nm}$) appeared after the Boc cleavage.

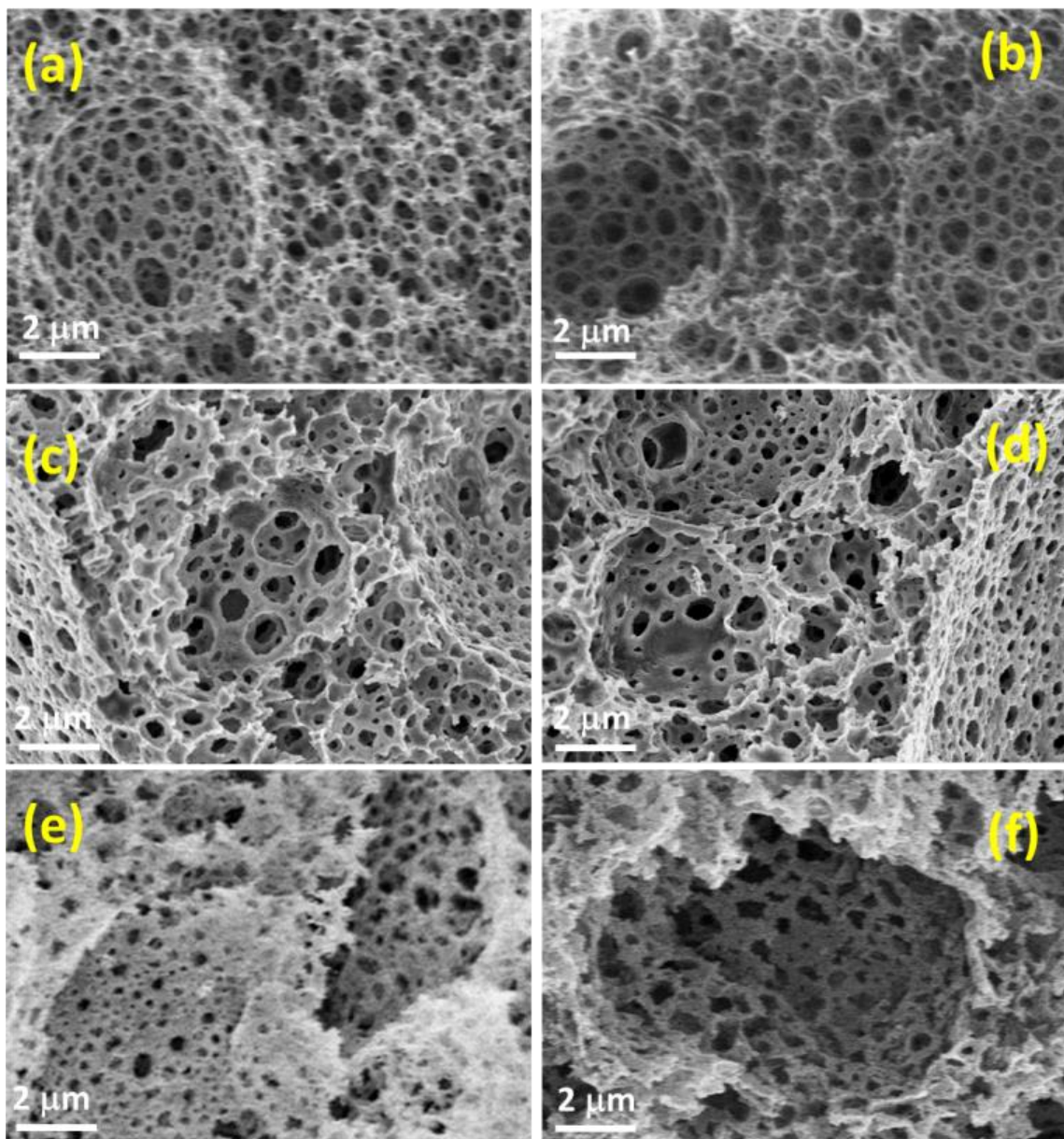


Figure 5.48 SEM images of the conjugated polyHIPEs before and after removal of Boc group. (a) B-(Boc-NPh₂)₃, (b) B-(NPh₂)₃, (c) B-(Boc-CB)₃, (d) B-CB₃, (e) B-(Boc-CB)₂-BT, (f) B-CB₂-BT.

The UV/Vis diffusive reflectance spectra (DRS) of the polymers were slightly bathochromically shifted after removing the Boc moiety (Figure 5.49b), compared to the ones containing Boc (Figure 5.49a). This shift could be caused by the thermal annealing effect of the conjugated polymer backbone, leading to more ordered π - π -stacking and therefore slightly lower energy levels. By introducing the strong electron acceptor BT unit into the polymer backbone, a bathochromic shift of ca. 55 nm occurred, indicating lower HOMO and LUMO levels and narrower band gaps. Similarly, the photoluminescence (PL) spectra of B-(Boc-CB)₂-BT and B-CB₂-BT are largely bathochromically shifted compared to B-(Boc-CB)₃ and B-CB₃ (Figure 5.50 and Figure 5.51). An extra fluorescence band at about 520 nm occurred for both BT containing polymers. This emerged large Stokes-shift reflects a stronger π - π^* -transition of the electrons under excitation. The NPh-based polymers B-(Boc-NPh₂)₃ and B-(NPh₂)₃ exhibited the largest optical HOMO-LUMO band gaps of 3.31 and 3.03 eV, followed by the B-(Boc-CB)₃ with 3.02 and B-CB₃ with 2.83 eV. The lowest band gaps were exhibited by B-(Boc-CB)₂-BT with 2.47 and B-CB₂-BT with 2.31, respectively (Table 5.8).

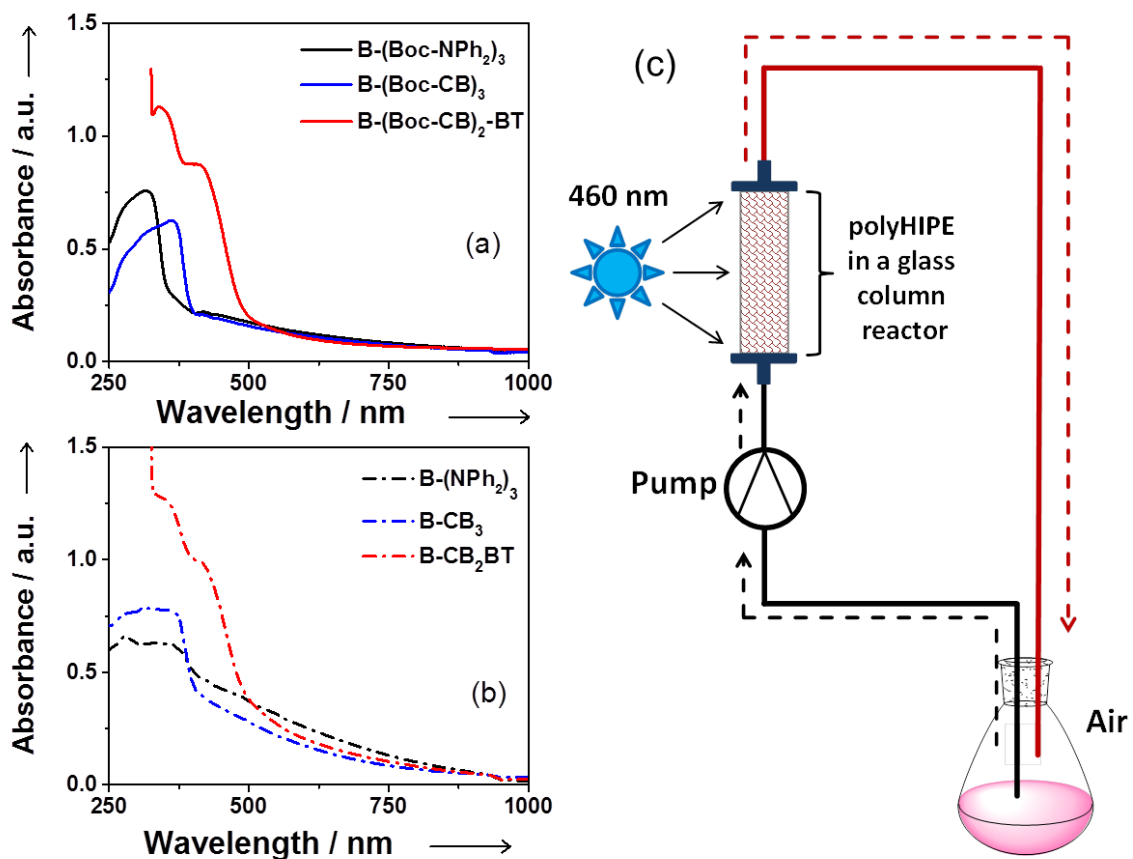


Figure 5.49 (a) UV/Vis DR spectra of B-(Boc-NPh₂)₃, B-(Boc-CB)₃, and B-(Boc-CB)₂-BT containing Boc group. (b) UV/Vis spectra of B-(NPh₂)₃, B-CB₃, and B-(CB)₂-BT. (c) Illustrated setup of the glass column photoreactor in a continuous flow system.

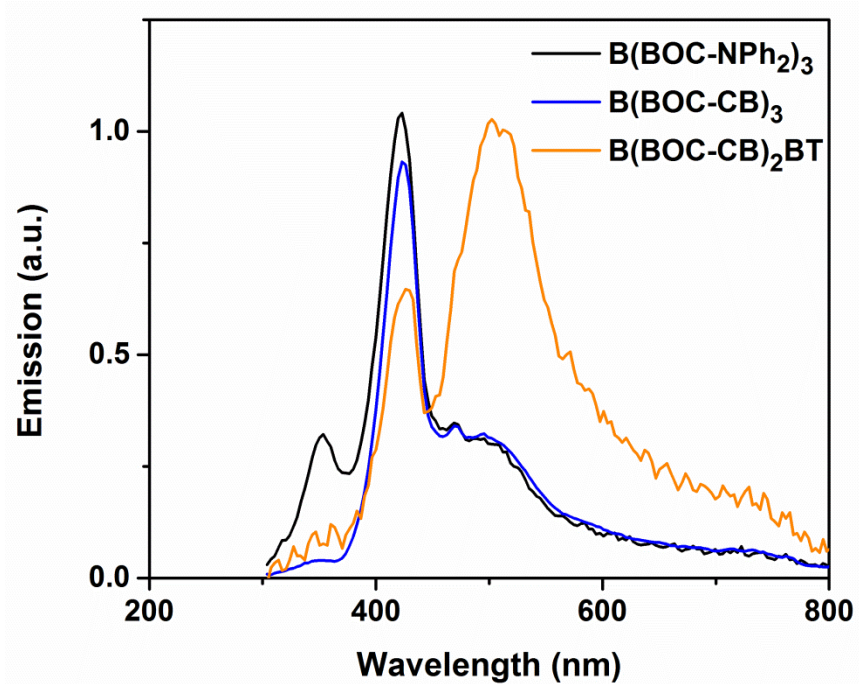


Figure 5.50 Fluorescence spectra of poly(HIPE)s with Boc groups.

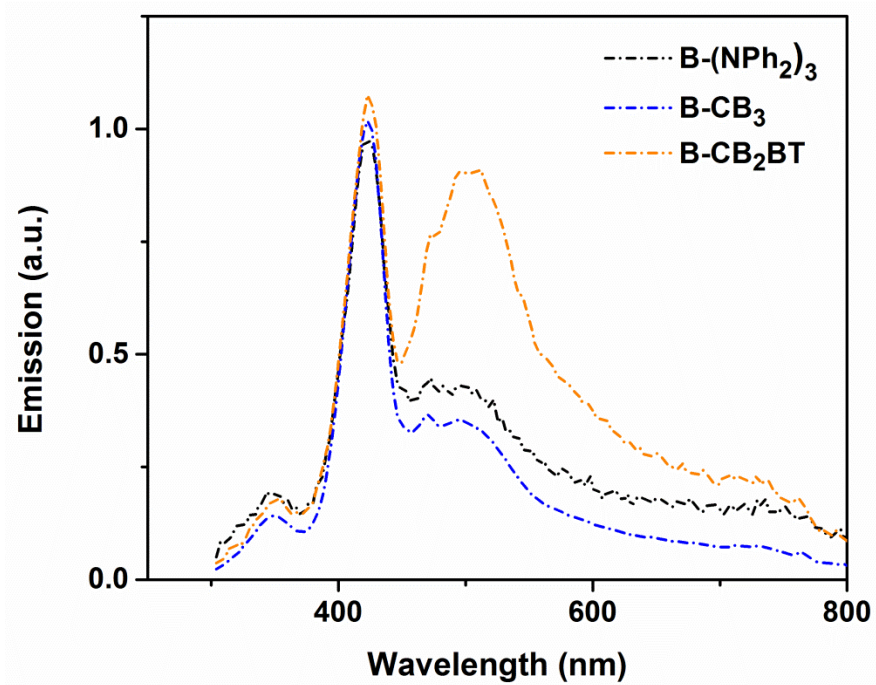


Figure 5.51 Fluorescence spectra of poly(HIPE)s after removal of Boc groups.

5.2.4 Selective Photo-oxidation of Organic Sulfides

To investigate the electronic properties, theoretical HOMO-LUMO levels of the repeating units was calculated. The data are listed in Table 5.8 and Table 6.1 and the electronic structures are displayed in Figure 6.9 and Figure 6.10 in chapter 6.2.

Table 5.8 Photocatalytic oxidation of thioanisole using π -conjugated polyHIPEs as heterogeneous photocatalysts under visible light: (a) thioanisole, (b) methyl phenyl sulfoxide and (c) methyl phenyl sulfone, and the optical and electronic properties.

Reaction scheme: Thioanisole (a) $\xrightarrow[\text{air, acetonitrile, RT, } h\nu (460 \text{ nm})]{\text{polyHIPEs}}$ Methyl phenyl sulfoxide (b) + Methyl phenyl sulfone (c)

Entry	PolyHIPEs	Time (h)	Conversion (%)	Selectivity (%)		Band Gap/opt. (eV)	HOMO/LUMO /theo.* (eV)
				b	c		
1	B-(Boc-NPh ₂) ₃	48	38	>99	<1	3.31	-5.95 / -1.26
2	B-(NPh ₂) ₃	48	33	>99	<1	3.03	-5.39 / -1.16
3	B-(Boc-CB) ₃	48	91	>99	<1	3.02	-5.65 / -1.65
4	B-CB ₃	48	93	>99	<1	2.83	-5.64 / -1.47
5	B-(Boc-CB) ₂ -BT	24	99	95	5	2.47	-5.76 / -3.10
6	B-CB ₂ -BT	24	98	99	<1	2.31	-5.69 / -3.07
blank 1	-	24	0	-	-	-	-
blank 2	B-(Boc-CB) ₂ -BT	24	0	-	-	-	-

Blank 1: no polymer, but with light irradiation. Blank 2: with B-(Boc-CB)₂-BT as photocatalyst, but no light irradiation. *: Calculated HOMO/LUMO levels of the ring-shaped repeating units.

Similar to the optical band gaps, the NPh-containing units exhibited the highest HOMO-LUMO gap, followed by the CB-based ones. And the BT-containing units showed clearly lower band gaps. Contrastingly, all repeating units exhibited similar HOMO level ranging from -5.40 to -5.90 eV. However, the LUMO levels of the BT-containing B-(Boc-CB)₂-BT and B-CB₂-BT of ca. -3.10 eV were significantly lower than the NPh- and CB-based polymers (-1.10 to -1.60 eV). A better electron transition can be expected.

The photocatalytic activity of the conjugated porous polymers as heterogeneous photocatalyst under visible light was investigated with the photooxidation of thioanisole at room temperature in continuous flow system as displayed in Figure 5.49c. The ^1H NMR spectra of thioanisole before and after the photooxidation reaction are shown in Figure 5.52. As shown in Table 5.8, an almost quantitative selectivity up to >99% of the photooxidation of thioanisole into the desired mono-oxidized product methyl phenyl sulfoxide was achieved. PolyHIPEs containing the CB moiety showed higher conversion than those with NPh_2 moieties, and the polymers containing a strong electron acceptor, BT unit, exhibited the best photocatalytic efficiency. This corresponds with the lower HOMO-LUMO band gaps, which, in particular, the low LUMO levels according to the theoretical calculation.

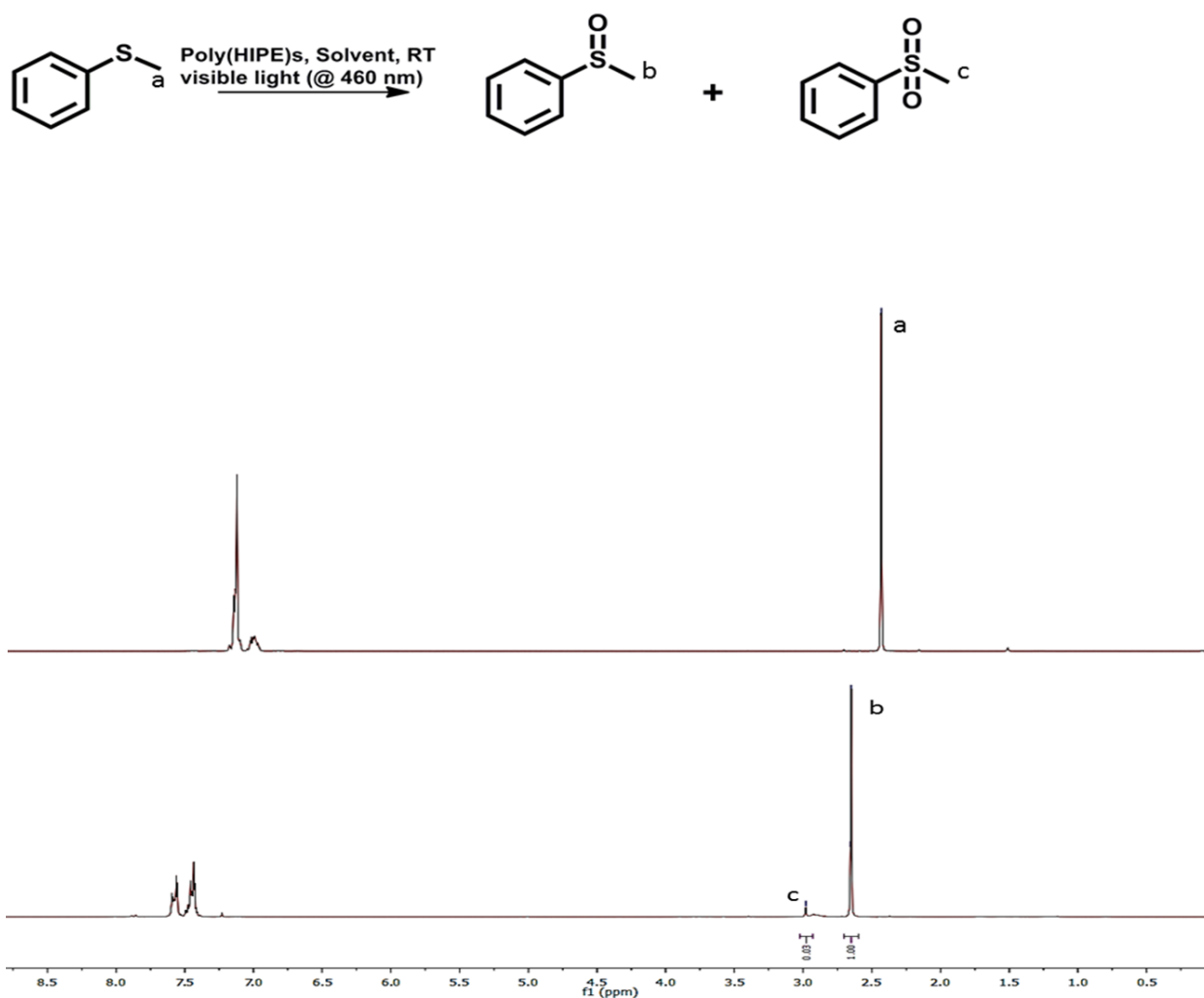


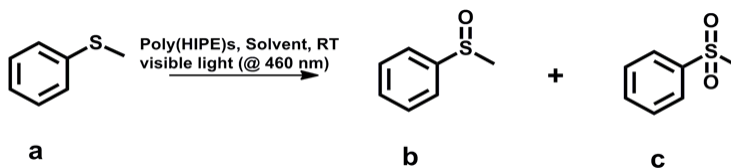
Figure 5.52 ^1H NMR spectra of thioanisole before and after photooxidation reaction.

To note, the series of the polyHIPEs without the Boc moieties, B-(NPh₂)₃, B-CB₃, and B-CB₂-BT, with higher BET surface areas did not distinguish themselves as more efficient photocatalysts than their counterparts with Boc. This can be attributed to the micropores, which after the removal of the Boc moieties were still too small ($d = 1.5$ nm) to allow efficient mass diffusion of the reactants. This finding further proves that in heterogeneous catalysis, it rather depends on the larger pores (> 1 μm) that play the vital role in providing accessible surface sites for interfacial reactions than the micropores (< 2 nm).^{92,226,227} B-(Boc-CB)₂-BT and B-CB₂-BT exhibited almost quantitative conversions within 24 h in acetonitrile (entries 5 and 6 in Table 5.8) with 95% and 99% selectivity, respectively. Likely, the reaction time (24 h) might be too long for B-(Boc-CB)₂-BT as active photocatalyst, an overoxidation of 5% occurred.

The photocatalytic experiment suggests that the π -electron features in the conjugated polymer backbone should play a more crucial role for the photocatalytic feasibility than surface area. This further proved a previous study on a series of conjugated porous polymers as photosensitizer, which showed that the polymers containing strong electron acceptor units such as BT could generate singlet oxygen in a more efficient manner.²¹² And most importantly, low LUMO levels are mandatory.

Furthermore, five additional repeating experiments of the photooxidation of thioanisole were carried out using B-(Boc-CB)₂-BT under the same reaction conditions (Table 5.9). The desired mono-oxidised product was obtained in an almost quantitative manner, demonstrating the stability and reusability of the polyHIPE. The oxidation of sulfides is likely mediated by photochemically generated singlet oxygen, which should be similar to a previous study.¹⁹⁹ Blank experiments were also carried out as control (Table 5.8). The same reaction was tested by using the polyHIPE as photocatalyst, but without light irradiation; or without the polyHIPE, but with light irradiation. No oxidized product was obtained in both experiments, indicating both components are indispensable.

Table 5.9 Repeating experiments of the selective photooxidation of thiolanisole.

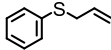
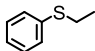


Entry	Time (h)	Conversion (%)	Selectivity (%)	
			b	c
1	24	>99	95	5
2	24	>99	94	6
3	24	>99	97	3
4	24	>99	99	1
5	24	97	>99	<1
6	24	98	>99	<1

Additionally, for the determination of the general applicability of the selective photooxidation of organic sulfides, a number of various thioanisole derivatives were examined under the same reaction conditions. B-(Boc-CB)₂-BT was used in all reactions due to its high photocatalytic activity. Table 5.10 shows the examples.

Table 5.10 Selective oxidation of various sulfides using B-(Boc-CB)₂-BT as photocatalyst under visible light irradiation.*

Entry	Time (h)	Conv. (%)	Selectivity (%)	
7	24	98	>99	<1
8	24	45	>99	<1
9	24	33	>99	<1
10	24	35	96	4
11	24	50	98	2

12		24	39	88	12
13		24	84	>99	<1

* Reaction condition: 10 mg of B-(Boc-CB)₂-BT, flow rate of sulfides in acetonitrile: 1 mL min⁻¹, RT, air.

We tested different phenyl sulfides bearing electron-withdrawing (entries 7 - 9) or electron-donating substituents (entries 10 and 11) on the phenyl ring as substrates for the oxidation reaction. All reactions exhibited high selectivity of the mono-oxidated sulfoxides. The conversion corresponded to the electro-withdrawing ability of the substituents (-Cl < -Br < -F). In case of the electron-donating substituents (entry 10 and 11), the conversion followed the opposite order of the electron affinity (-CH₃ < -OCH₃). Allyl phenyl sulfide with a considerable selectivity of 88% (entry 12) and ethyl phenyl sulfide (entry 13) with >99% were employed to demonstrate the chemoselectivity of the photooxidation reaction.

5.2.5 Conclusion

In conclusion, this chapter reports a novel method to synthesize high surface area conjugated porous polymers with unique electronic properties via high internal phase emulsion polymerization and micropore surface engineering. The *tert*-Butyl carboxylate (Boc) group was introduced as spacer into the micropores of the cross-linked polymer networks. The BET surface of the porous polymers can be increased by up to eight times their size. They exhibit hierarchical porosity with pore size ranging from micrometer to nanometers.

The photocatalytic activity of the conjugated porous polymers was demonstrated via photooxidation of organic sulfides into sulfoxides under visible light, achieving almost quantitative conversion and selectivity in the best cases. The influence of the surface area and electron feature on the photoactivity of the porous polymers was investigated. High surface areas did not play a crucial role with respect to the photocatalytic efficiency. Nanometer sized pores of ca. 1.5 nm are indeed insufficient for reactants to diffuse in. The more important factor was the electronic structure, i.e. donor and acceptor combination of the polymer backbone, with the best photocatalytic activity being shown by the polymer containing benzothiadiazole unit as a strong acceptor. This is in consonance with the lower optical HOMO-LUMO band gap values of the BT containing polymers, which was caused by the significantly low LUMO levels of the polymers.

Conjugated porous polyHIPEs are therefore a new class of visible light-driven heterogeneous catalyst systems. By incorporation of the insoluble polymers into a glass column reactor, further filtration and recovery processes are no more necessary.

5.3 Chemical Composition Control of Conjugated Porous Polymer Photocatalysts

This chapter is based on the published article “Conjugated Porous Poly-benzobisthiadiazole Network for Visible Light-Driven Photoredox Reaction”, *J. Mat. Chem. A*, 2014, **2**, 18720-18724 with copyright (2014) from Royal Society of Chemistry.

5.3.1 Introduction

Conjugated polymers are organic macromolecules through which the valence π electrons are delocalized. Their unique electronic and optical properties make them particularly attractive materials for the electronic industry. In fact, many of their potential applications include light emitting devices, photovoltaic devices and plastic field effect transistors. From the perspective of photocatalysis, it is interesting to investigate the effect of additional electron-withdrawing moieties in the conjugated backbone on the photocatalytic efficiency. In the following chapter, two conjugated porous polymers, poly-hexylfluorene (donor-only) and poly-benzobisthiadiazole (donor and acceptor) network was synthesized via high internal phase emulsion polymerization as highly active and stable heterogeneous photocatalysts. Under a household energy saving light bulb, dehalogenation of α -bromoacetophenones was performed in an almost quantitative manner at room temperature.

5.3.2 Synthesis and Characterization of B₂-FL₃ and B₂-FL₂-BBT

This chapter reports on the design and preparation of a conjugated porous polymer via Sonogashira cross-coupling reaction using high internal phase emulsion polymerization technique. A strong electron acceptor, benzobisthiadiazole (BBT) was incorporated into the porous polymer backbone, gaining broad absorption band and the desired energy level. The visible light-driven photocatalytic activity of the porous polymer was demonstrated with the reductive dehalogenation reaction of α -bromoacetophenones under a 23 W household energy saving fluorescent light bulb.

In Figure 5.53, the synthetic pathway of the conjugated porous polymer B₂-FL₂-BBT is displayed. As a comparison, another porous polymer only containing fluorene (B₂-FL₃) was synthesized for investigation of the photocatalytic performance of the dehalogenation reaction without the electron withdrawing BBT unit. The experimental synthetic details and polymer characterization data are described in Chapter 6.3. To note, for the Sonogashira coupling reaction, K₂CO₃ seems to be one of few bases which lead to stable high internal phase emulsion. By adding amines as base, in comparison, only unstable emulsions were formed, rapid phase separation occurred during the polymerization. The formed monolithic cross-linked polymers were insoluble in all common organic solvents tested. The solid state ¹³C/MAS NMR spectroscopy showed chemical shifts between $\delta = 15$ and 60 ppm that can be assigned to the alkyl groups of the fluorene units. The signals between 110 and 160 ppm can be assigned to the aromatic carbons in the polymer backbone (Figure 5.54).

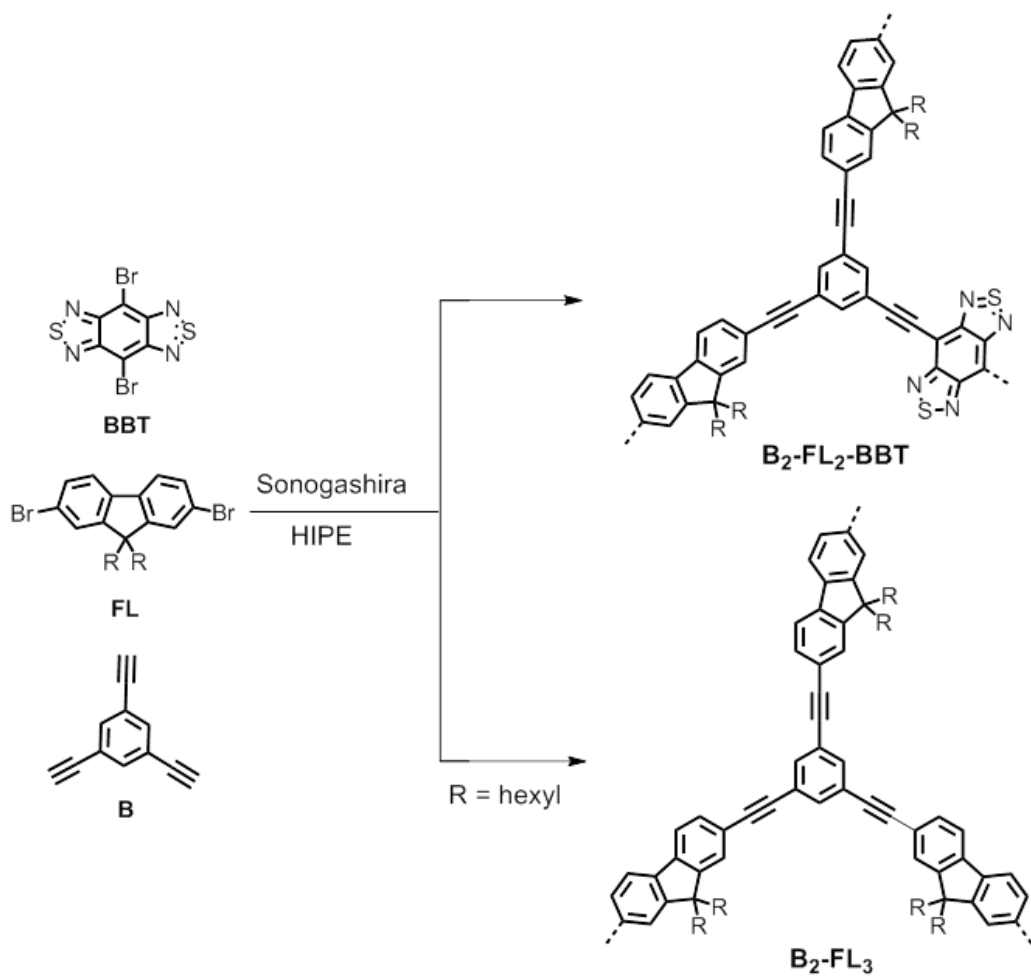


Figure 5.53 Synthetic route and idealized structure of $B_2\text{-FL}_2\text{-BBT}$ and $B_2\text{-FL}_3$. Reaction conditions: (i) $Pd(PPh_3)_4$, CuI , K_2CO_3 , span 80, toluene/ H_2O (v/v: 1/9), $80\text{ }^\circ\text{C}$, overnight.

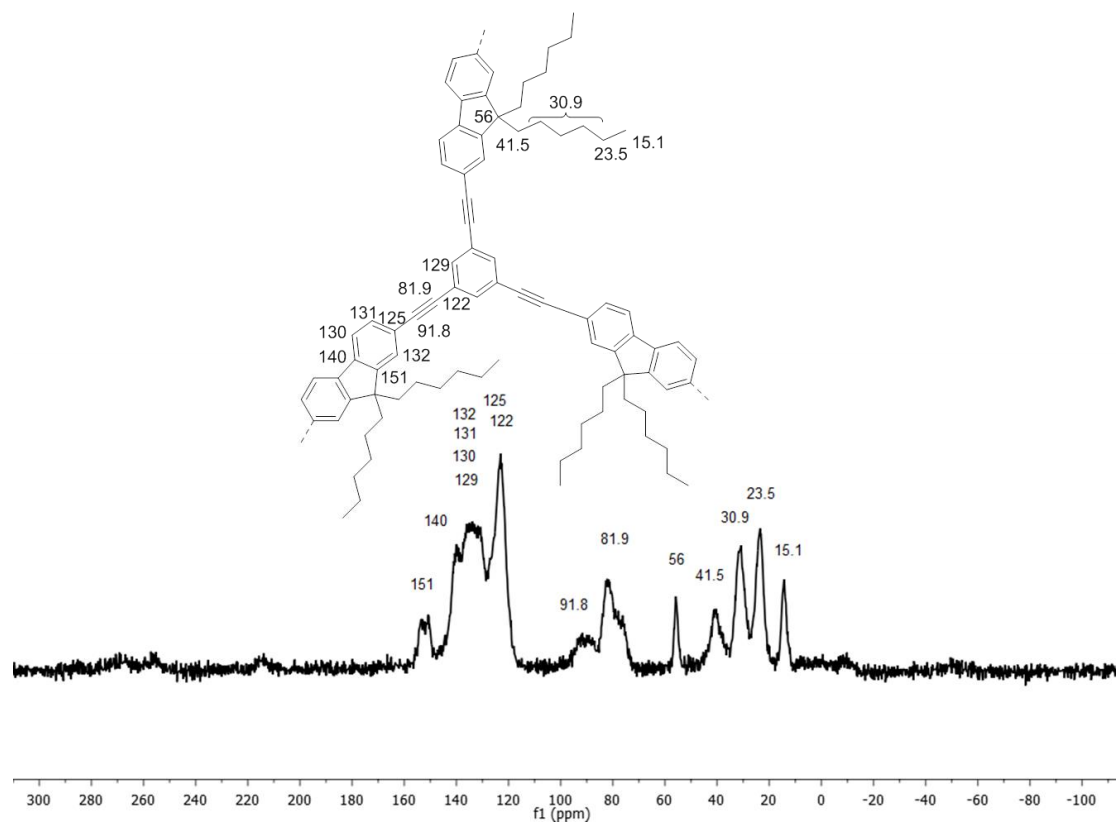
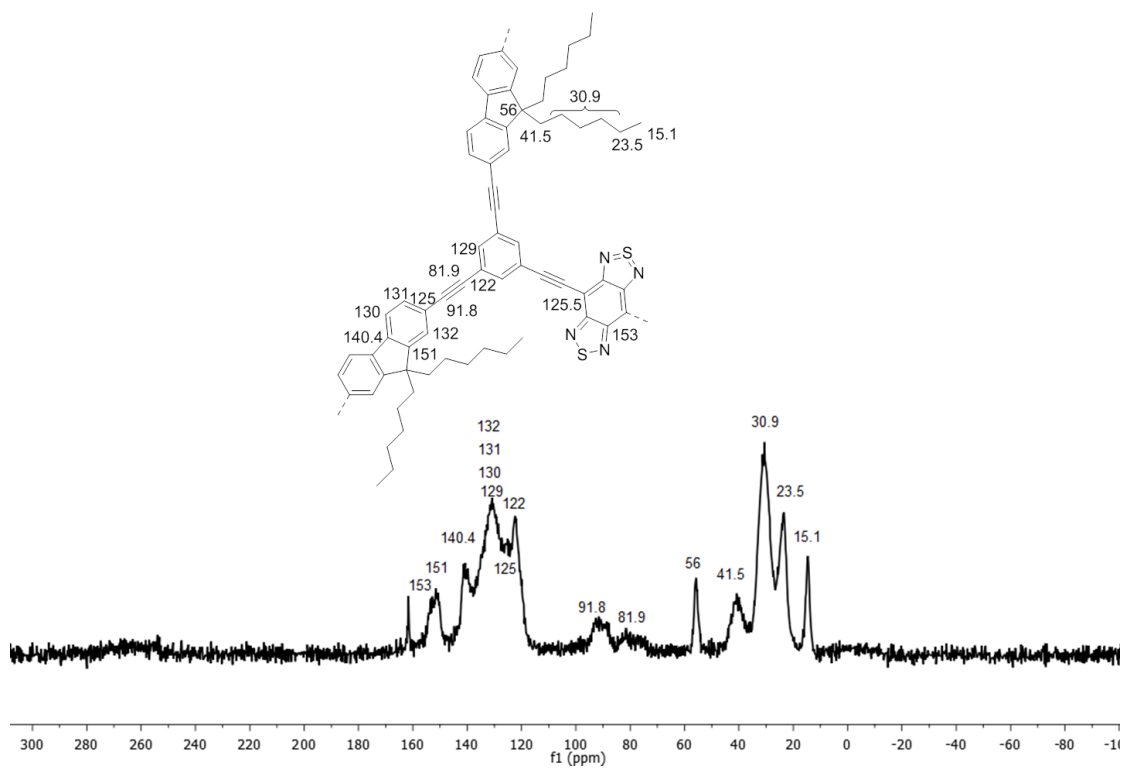


Figure 5.54 Solid state ¹³C/MAS NMR spectra of B₂-FL₂-BBT and B₂-FL₃.

From the elemental analysis, a BBT/fluorene ratio of approximately 1:3 inside the polymer B₂-FL₂-BBT was observed. This could be caused by the non-quantitative polymerization degree and different reactivities of both building blocks during the polymerization. Thermal gravimetric analysis (TGA) measurements showed that the conjugated network remained intact up to 450 °C and the weight loss at around 300 °C can be attributed to the alkyl groups (Figure 5.55). The Brunauer-Emmett-Teller (BET) surface areas of B₂-FL₂-BBT and B₂-FL₃ are around 23 and 17 m²g⁻¹ (Figure 5.56 and Table 5.11). Broad pore distributions from the meso to macropore range were observed for both polymers (Figure 5.57). This is similar to the previously reported surface area values and pore analyses of this class of conjugated porous polymers prepared using the HIPE technique.^{212,228} The broad pore size distribution could be caused by the alkyl side chains of the fluorene unit, which block the micropores and require larger space inside the porous polymers. As it was shown previously that micropores are too small to be effectively accessible by diffusion and no enhancement in catalytic efficiency was observed from higher surface area polymers with additional micropore volume, the hierarchically porous structure of the polymers could be advantageous for a higher efficiency of the catalytic reactions.²²⁹

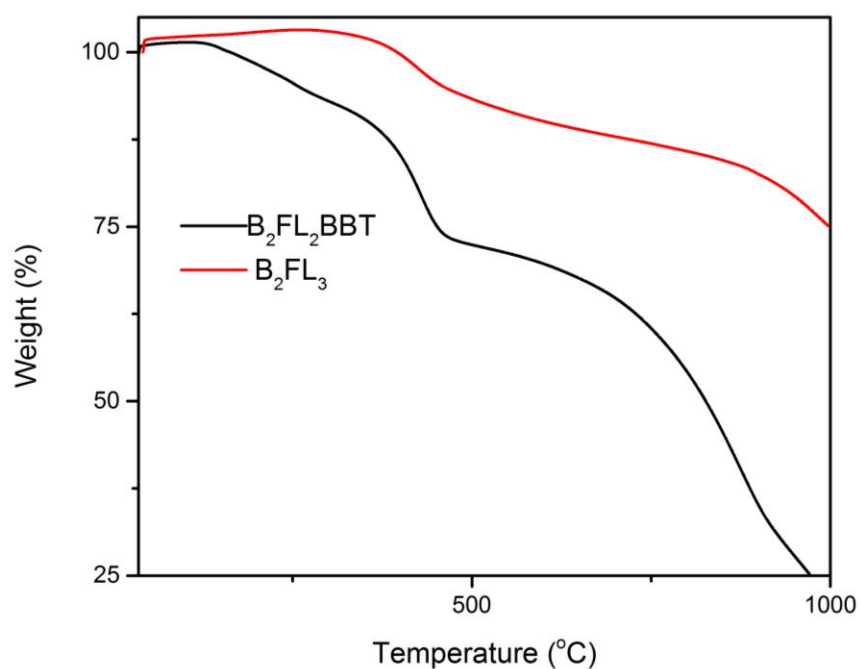


Figure 5.55 TGA of of B₂-FL₂-BBT and B₂-FL₃.

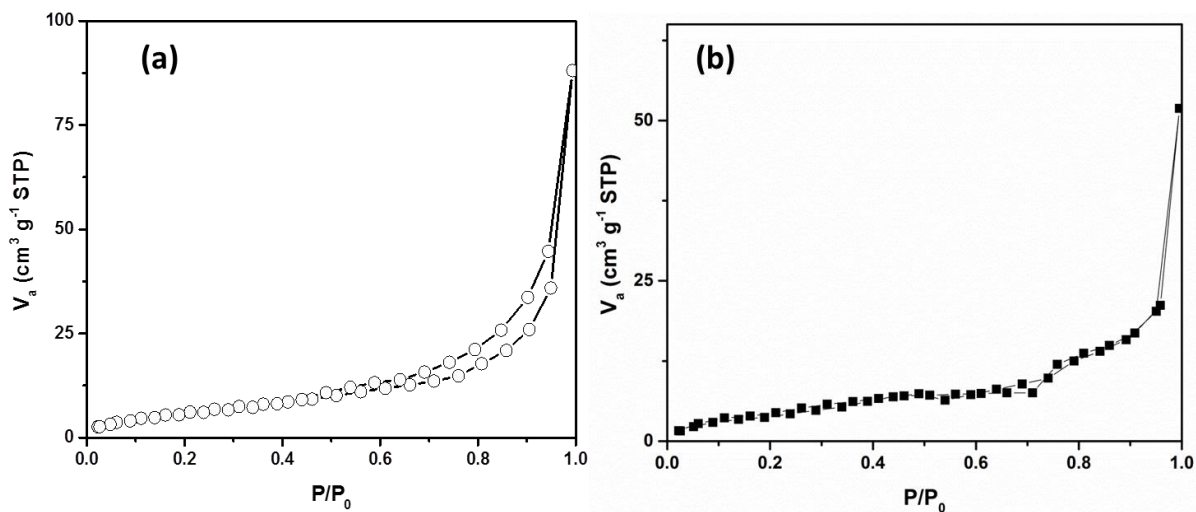


Figure 5.56 N₂ sorption isotherms of (a) B₂-FL₂-BBT and (b) B₂-FL₃.

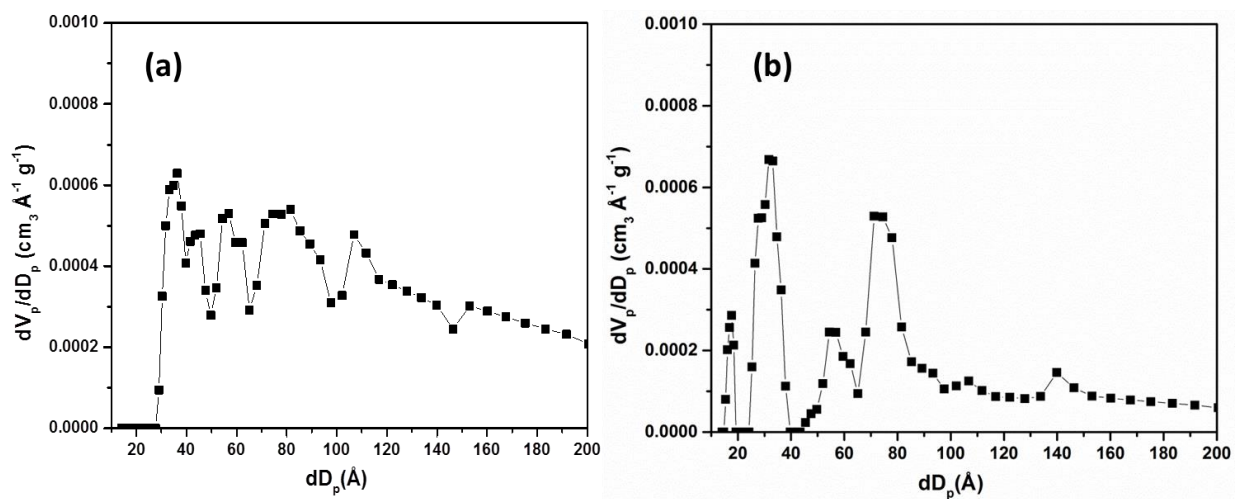


Figure 5.57 Pore size distributions of B₂-FL₂-BBT and B₂-FL₃.

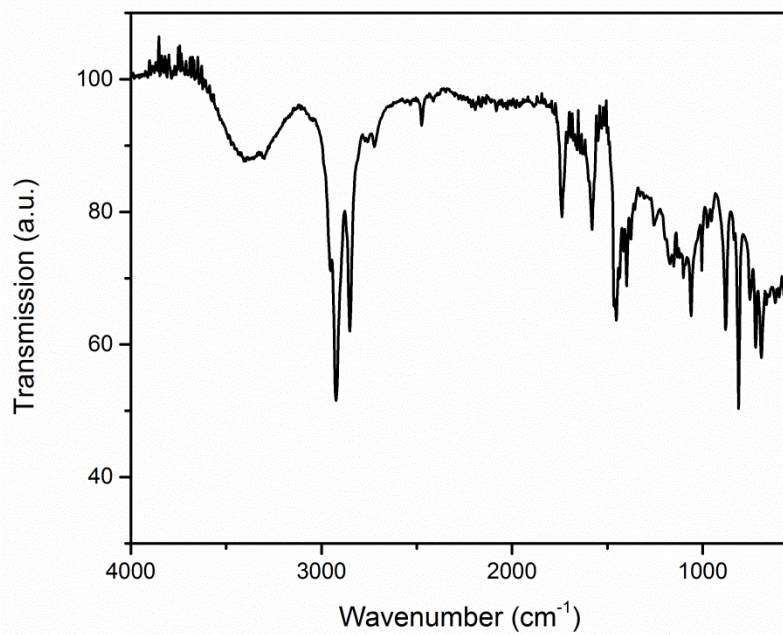
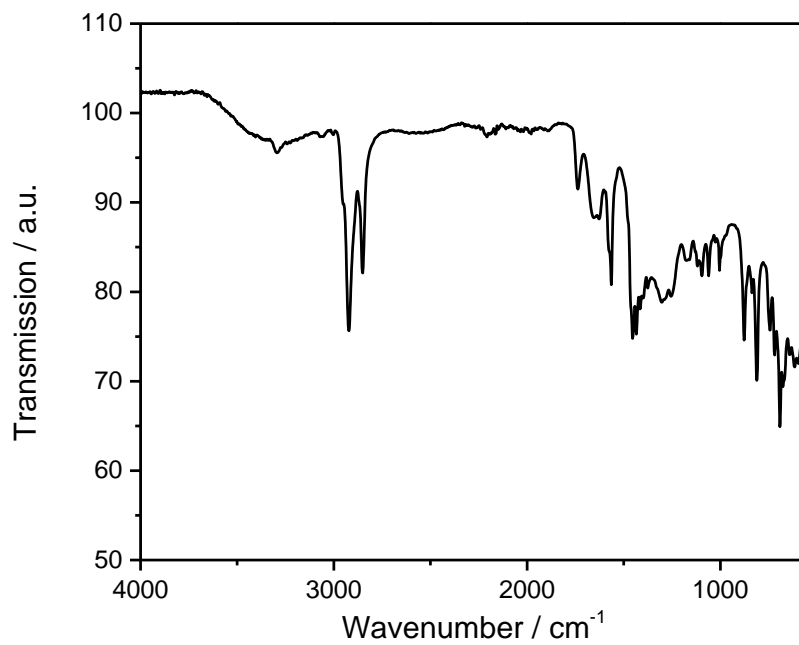


Figure 5.58 FT-IR spectra of B₂-FL₂-BBT and B₂-FL₃.

Table 5.11 Surface area and pore size distribution data of the polymers.

Polymer	S_{BET} [m^2/g]	Pore diameter [nm]	Pore volume [cm^3/g]
$\text{B}_2\text{-FL}_2\text{-BBT}$	23	3.6	0.06
^a $\text{B}_2\text{-FL}_2\text{-BBT}$	21	3.9	0.06
$\text{B}_2\text{-FL}_3$	17	3.2	0.03

^a: Measured after the reductive photodehalogenation.

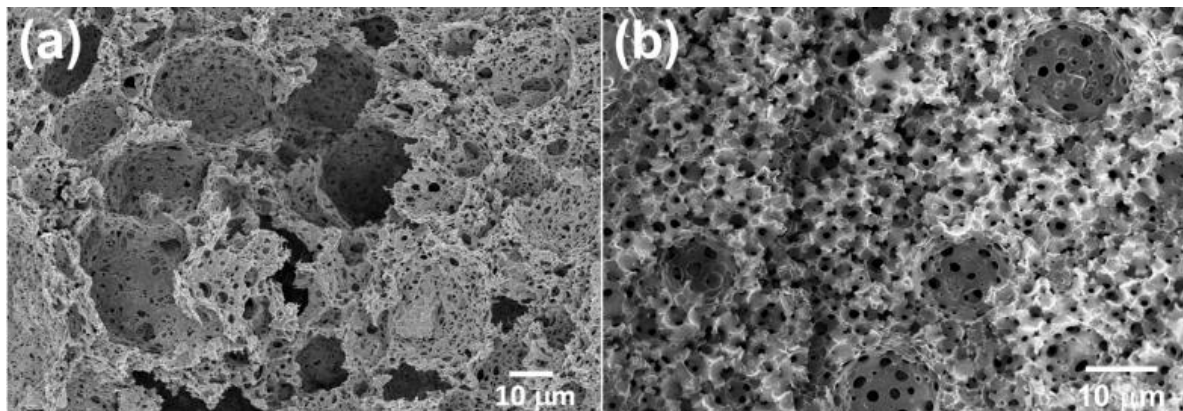


Figure 5.59 SEM images of $\text{B}_2\text{-FL}_2\text{-BBT}$ (a) and $\text{B}_2\text{-FL}_3$ (b).

SEM images (Figure 5.59) of two porous polymers illustrate the interconnected porous structures with cavities ranging from 10 to 20 μm in size, while the interconnected pores show diameters from 0.5 to 1 μm .

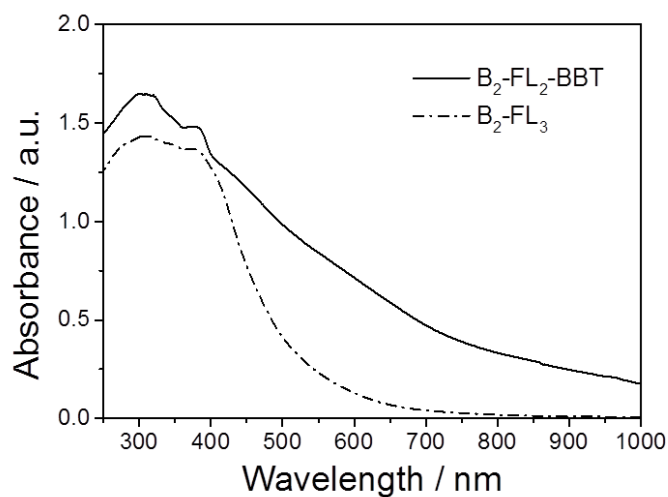


Figure 5.60 (a) UV/Vis spectra of $\text{B}_2\text{-FL}_2\text{-BBT}$ and $\text{B}_2\text{-FL}_3$.

The UV/Vis diffuse reflectance spectrum (Figure 5.60) of B₂-FL₂-BBT showed broad absorption band ranging from the visible and into the near infrared (NIR) region. An optical band gap of ca. 1.5 eV can be derived from the absorption edge. In comparison, the UV/Vis spectrum of B₂-FL₃ only containing fluorene showed a sharper absorption shoulder, exhibiting an optical band gap of ca. 2.40 eV. This is probably due to the strong electron withdrawing properties of the BBT unit, exhibiting lower HOMO-LUMO levels and the resulting band gap of the polymer. It is to note that that board shoulder of the spectra could partially due to light scattering effect, giving the broad pore size range inside the porous polymers. Interestingly, by incorporating the electron withdrawing BBT group into the polymer backbone, the electron paramagnetic resonance (EPR) spectrum of B₂-FL₂-BBT exhibited significantly higher intensity than B₂-FL₃ (Figure 5.61).

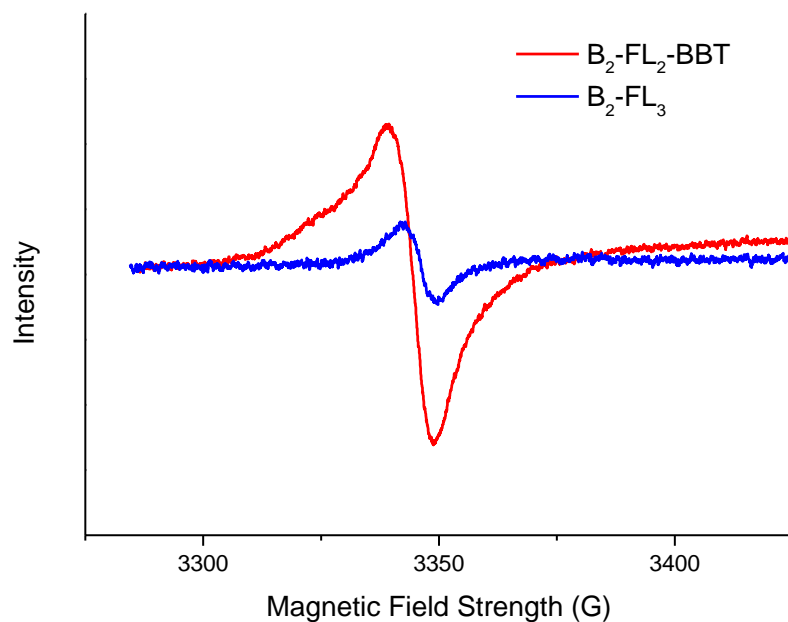


Figure 5.61 Electron paramagnetic resonance (EPR) spectra of B₂-FL₂-BBT and B₂-FL₃ under light irradiation.

5.3.3 Photoreductive Dehalogenation of Haloketones using B₂-FL₃ and B₂-FL₂-BBT

The photocatalytic activity of the conjugated porous polymers as heterogeneous photocatalyst under visible light was investigated with the photoreductive dehalogenation reaction of α -bromoacetophenones. A 23 W household energy saving light bulb was used as the

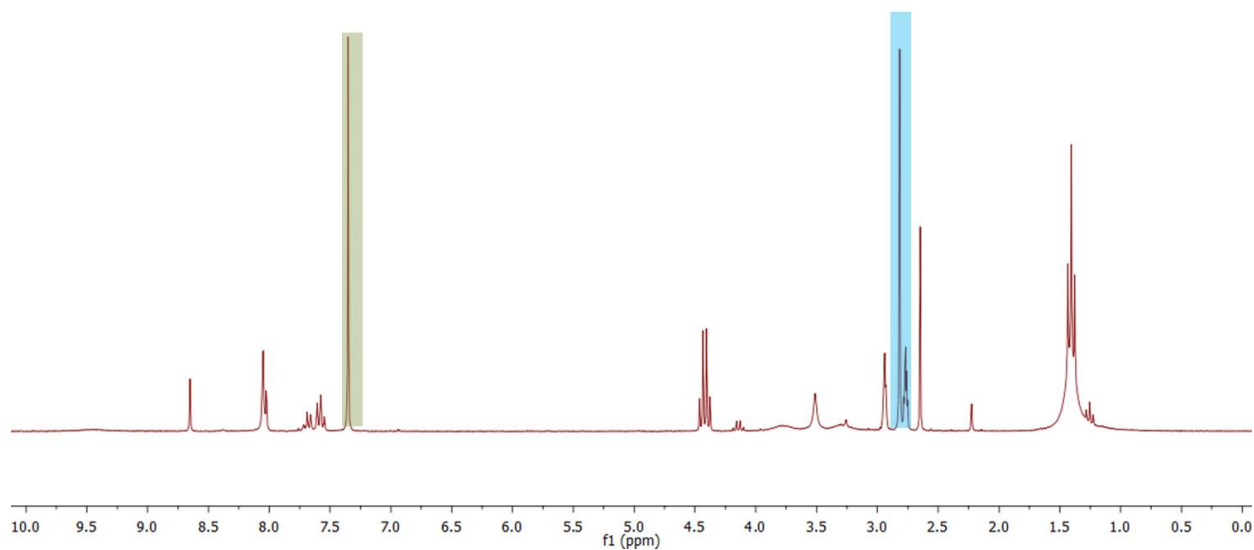


Figure 5.63 ^1H NMR spectrum of the reaction mixture after light irradiation $\delta = 7.35$ ppm (s, 1H, trichloroethylene), 2.80 ppm (s, 3H, C(O)-CH₃, product).

Various α -bromoacetophenone derivatives were investigated (Table 5.12). B₂-FL₂-BBT showed notably higher photocatalytic activity than B₂-FL₃ (entry 1 and 2), which proved the importance of incorporation of the electron withdrawing BBT unit. We further tested different phenones bearing electron-withdrawing (entries 3 - 6) or electron-donating substituents (entries 7 and 8) on the phenyl ring as substrates for the reaction. As shown in Table 5.12, almost quantitative conversion of the dehalogenation reaction was achieved in every case, demonstrating the general applicability of the conjugated porous polymer B₂-FL₂-BBT as a highly efficient photocatalyst.

Table 5.12 Visible light driven photoreductive dehalogenation of haloketones using the conjugated porous polymers as heterogeneous photocatalyst under irradiation of a 23 W household fluorescent light bulb.



Entry	Substrate	Product	t (h)	Conversion ^a (%)	Yield ^b (%)
1			4	>99	93
2 ^c			4	19	15
3			4	95	89
4			4	>99	95
5			4	>99	93
6			4	>99	97
7			5	>99	92
8			5	>99	90
9 ^d			4	<1	-
10 ^e			4	<1	-

^a: Conversion determined by ¹H-NMR using trichloroethylene as internal standard. ^b: Isolated yield by chromatography. ^c: Using B₂-FL₃ as photocatalyst. ^d: blank experiment without B₂-FL₂-BBT, but under light. ^e: blank experiment with B₂-FL₂-BBT, but in dark. Reaction conditions: 10 mg porous polymer, 0.2 mmol substrate, 0.4 mmol DIPEA, 0.22 mmol Hantzsch ester in 1 mL deuterated DMF under a 23 W household fluorescent light bulb at room temperature.

Five additional repeating experiments of the visible light induced dehalogenation of α -bromoacetophenone were carried out using B₂-FL₂-BBT under the same reaction conditions (Figure 5.64). The dehalogenated product was obtained in an almost quantitative manner, demonstrating the stability and reusability of B₂-FL₂-BBT as photocatalyst. Blank experiments were also carried out as control (entry 9 and 10). The same reaction with α -bromoacetophenone was tested by using B₂-FL₂-BBT as photocatalyst, but without light irradiation; or without B₂-FL₂-BBT but with light irradiation. The dehalogenated product, acetophenone was barely obtained in either experiment, indicating that both components are indispensable. After repeated use, the BET surface area and porosity of the photocatalyst B₂-FL₂-BBT exhibited no significant difference compared to those of the pristine.

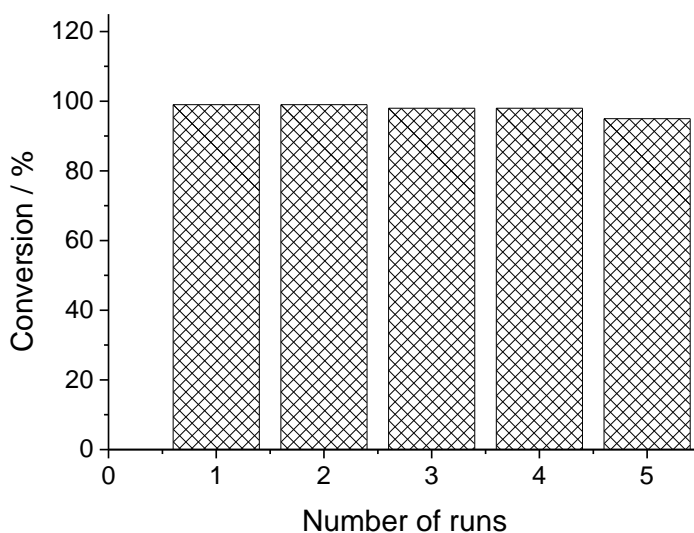


Figure 5.64 Repeating experiment of the dehalogenation of 2-bromoacetophenone using B₂-FL₂-BBT as photocatalyst.

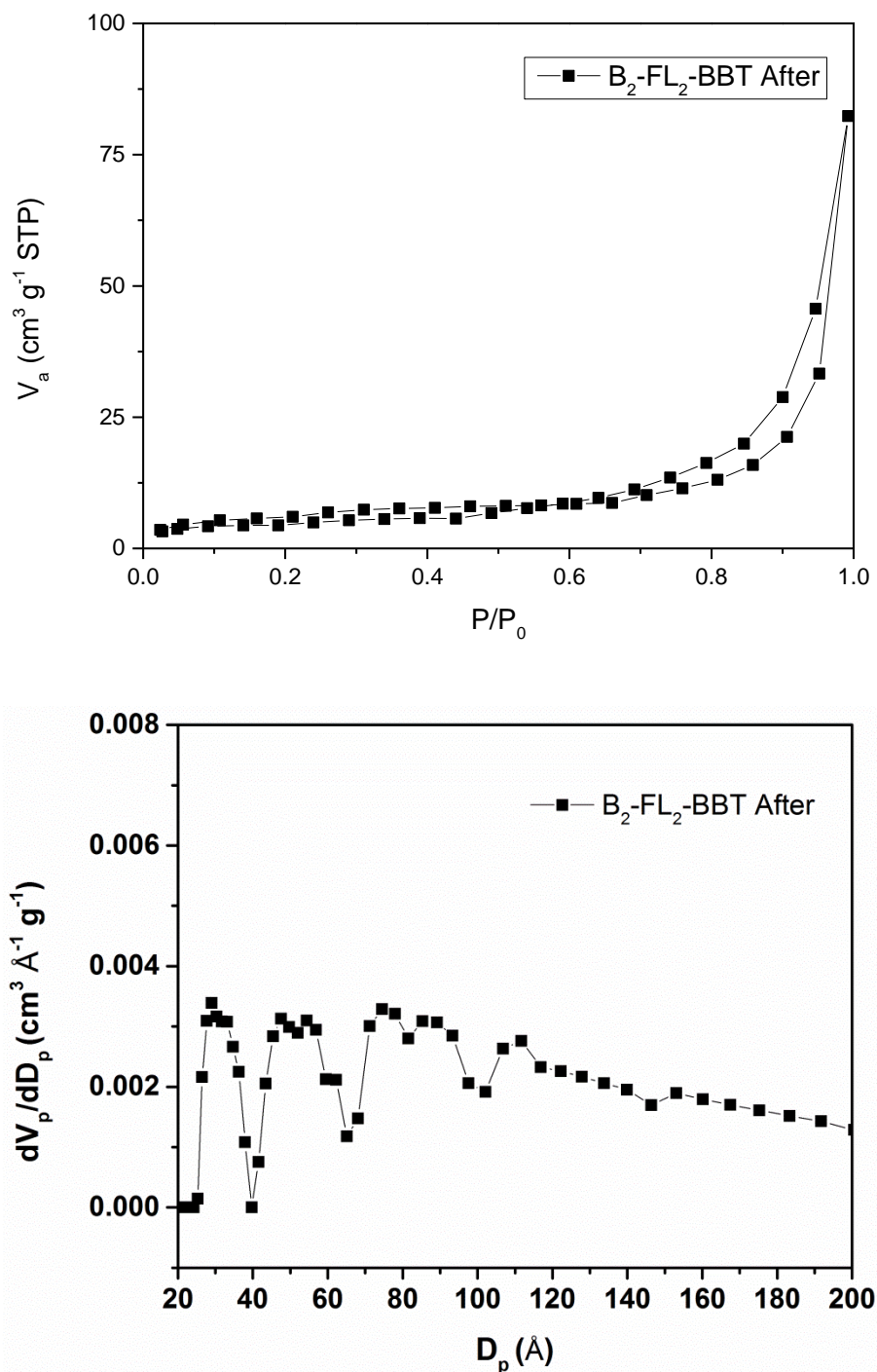


Figure 5.65 N_2 sorption isotherms and pore size distribution of $\text{B}_2\text{-FL}_2\text{-BBT}$ after the reductive dehalogenation reaction.

We propose a reaction mechanism as shown in Figure 5.66. Under visible light irradiation, the excited state of the conjugated porous polymer generates a hole via charge

separation, which oxidizes the amine DIPEA, leading to a radical anion inside the porous polymer. The radical anion reacts with α -bromoacetophenone, generating the phenone radical, as the Br leaving group cleaves off. Hydrogen radical is then subsequently donated by the sacrificial hydrogen donor Hantzsch ester to produce the final product. The dehydrogenated Hantzsch ester radical reacts with DIPEA radical cation, ammonium bromide and pyridine ester are obtained as side products.

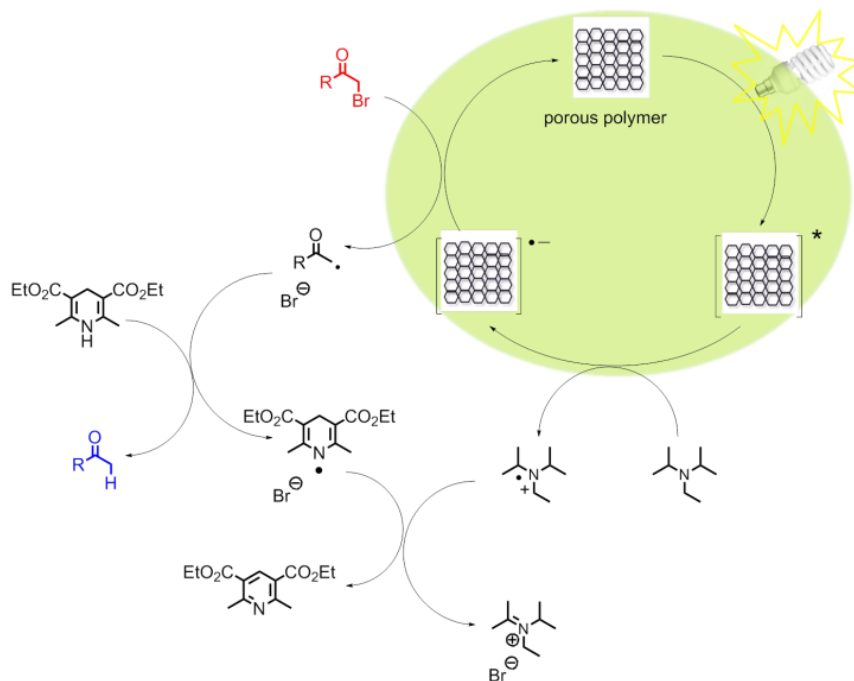


Figure 5.66 Proposed mechanism of the visible light-driven dehalogenation reaction using the conjugated porous polymers as heterogeneous photocatalyst.

Inductively coupled plasma (ICP) spectroscopy was performed to determine the metal catalyst traces after the Sonogashira coupling reaction. For both B_2 -FL₂-BBT and B_2 -FL₃, traces of Pd (15 and 25 ppm) and Cu (~20 ppm) were determined. To prove the origin of the photocatalytic activity, a short-chain linear polymer consisting of similar structure was prepared and purified via chromatography for a homogeneous approach of the visible light-driven dehalogenation reaction. The ICP measurements showed very low Pd and Cu traces (< 1 ppm). The dehalogenation reaction using the linear polymer (Figure 5.67, for synthesis see chapter 6.3) as homogeneous photocatalyst was carried out also in an almost quantitative manner (Figure 5.68). This indicates that the photocatalytic activity of the conjugated polymers does not stem from the minimal metal traces, but from the energetic level of the conjugated system. However,

the drawback of using the soluble linear polymer is that photobleaching occurred during the dehalogenation reaction, shown by the decrease in the absorption maximum of the polymer by 27% (Figure 5.69). In comparison, the crosslinked porous polymer B₂-FL₂-BBT exhibited better stability.

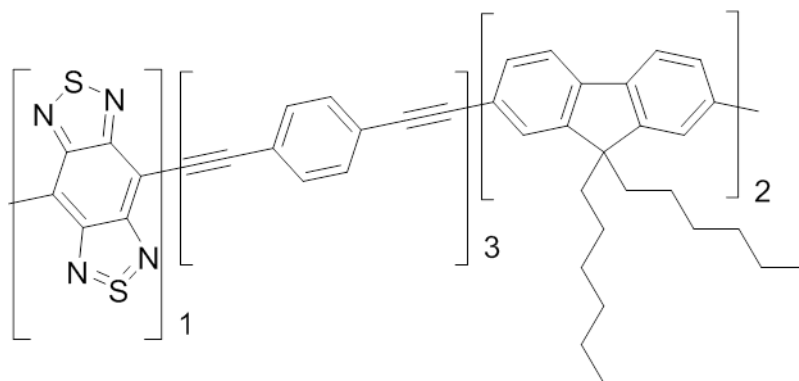


Figure 5.67 Structure of linear polymer used as photocatalyst.

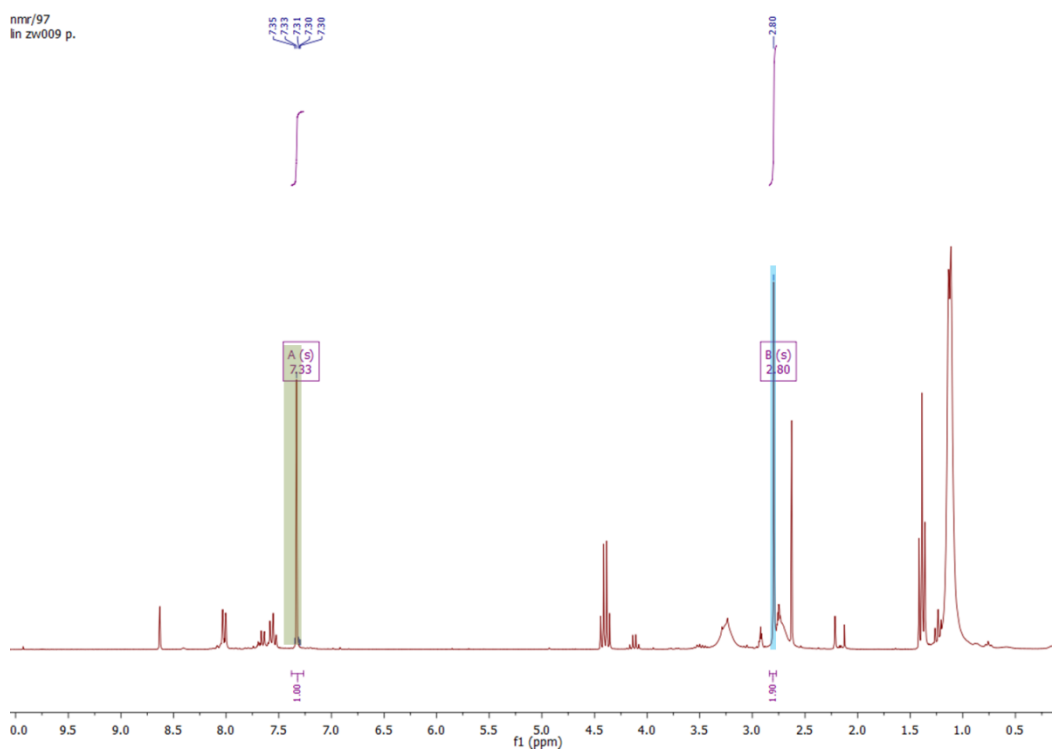


Figure 5.68 ¹H NMR spectrum of the reaction mixture using linear polymer after light irradiation. $\delta = 7.35$ ppm (s, 1H, **trichloroethylene**), 2.80 ppm (s, 3H, C(O)-CH₃, **product**).

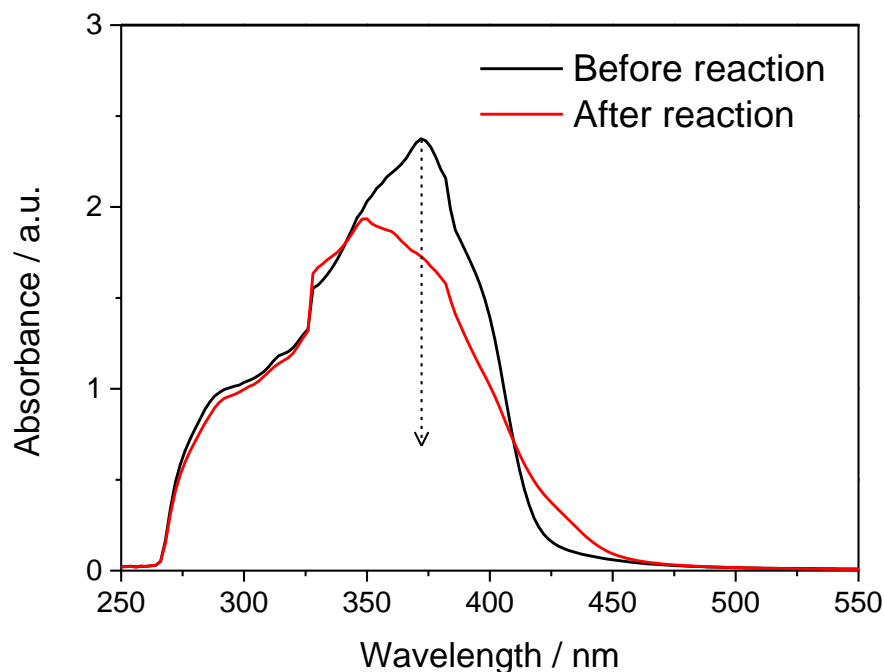


Figure 5.69 UV/vis spectra of the linear polymer before and after the photo dehalogenation reaction.

Furthermore, the overall apparent quantum yield (AQY)²³⁰ of the reaction using B₂-FL₂-BBT as photocatalyst was estimated to gain more information on its efficiency by using a single wavelength LED lamp (460 nm). The details are described in Chapter 6.3. For this heterogeneous photocatalytic reaction, an overall AQY of 1.2 % could be calculated according to the dehalogenation conversion.

5.3.4 Conclusion

In this chapter, a π -conjugated porous polymer via Sonogashira-coupling using high internal phase emulsion technique as heterogeneous, visible light-driven photocatalyst for the reductive dehalogenation of haloketones was developed. The benzobisthiadiazole-based porous polymer offers a new class of robust visible light-driven heterogeneous catalyst systems, with strong and broad absorption from visible to near infra-red range. A household energy saving light bulb was used as the light source, which provides an environmentally sustainable and financially affordable solution for future catalytic processes. The heterogeneous photocatalyst can be easily recycled and reused without significant loss in photoactivity. Further studies of this

highly versatile heterogeneous visible light driven photocatalyst system are expected to find more applications in more demanding catalytic processes.

5.4 Conjugated Porous PolyHIPE as Visible Light Photoinitiator

This chapter is based on the paper “Hierarchically Porous Π -Conjugated PolyHIPE as Heterogeneous Photoinitiator for Free Radical Polymerization under Visible Light”, *Polym. Chem.*, 2014, **5**, 3559-3562 with copyright (2014) from Royal Society of Chemistry.

5.4.1 Introduction

The previous chapters focus on using the CPP photocatalysts for various visible light induced organic transformations. In this chapter, a hierarchically porous π -conjugated polyHIPE was prepared and used as heterogeneous visible light photoinitiator for the radical polymerization of methyl methacrylate (MMA) under a household energy saving light bulb at room temperature. The heterogeneous nature of the porous polymer ensures easy separation and reusability.

Photopolymerization has demonstrated its advantages and played an important role in various industrial applications such as coatings, adhesives, optical waveguides, microelectronics, dental fillings, and other biomaterials for bone and tissue engineering.²³¹⁻²³⁴ In the past, numerous efficient photoinitiators with different absorption ranges for free radical polymerization were developed. However, they mainly absorb in the UV range.²³⁵ Taking nature as a role model, researchers have put tremendous effort in developing new photocatalysts which absorb mainly in the visible range of light. Many of the photocatalysts have established notable prominence in applications such as water splitting, solar energy storage, and photovoltaics.^{60,67,236} Among the visible light photocatalysts, rare metal complexes, especially ruthenium complexes have found large use due to their synthesis, stability and photoredox properties.

However, the high cost and toxicity of those rare metals, as well as their limited availability, present a huge challenge in their sustainability. Therefore there has seen a growing interest in developing metal-free photocatalysts in the field of visible light photocatalysis. In recent year, a number of organic chromophores and dyes were employed successfully in photoredox catalysis.^{66,237,238} Examples of some well-studied photoinitiators acting in the visible

range include titanocene, camphorquinone, organic ketones containing germanium, iridium complexes, and organic dyes.²³⁹⁻²⁴⁶ Despite their high initiation efficiency, strong odor, toxicity, and high migration are often observed with these low-molar-mass photoinitiators and the homogeneous nature makes them difficult to remove. One method to tackle such problems is to use macromolecular photoinitiators.²⁴⁷⁻²⁵⁰ Recently, Kiskan *et al.* reported the use of a phenolphthalein-based microporous polymer network²⁵¹ and a mesoporous graphitic carbon nitride as a metal-free heterogeneous visible light photoinitiator.²⁵²

5.4.2 Synthesis and Characterization of B-(Boc-CB)₂-BO

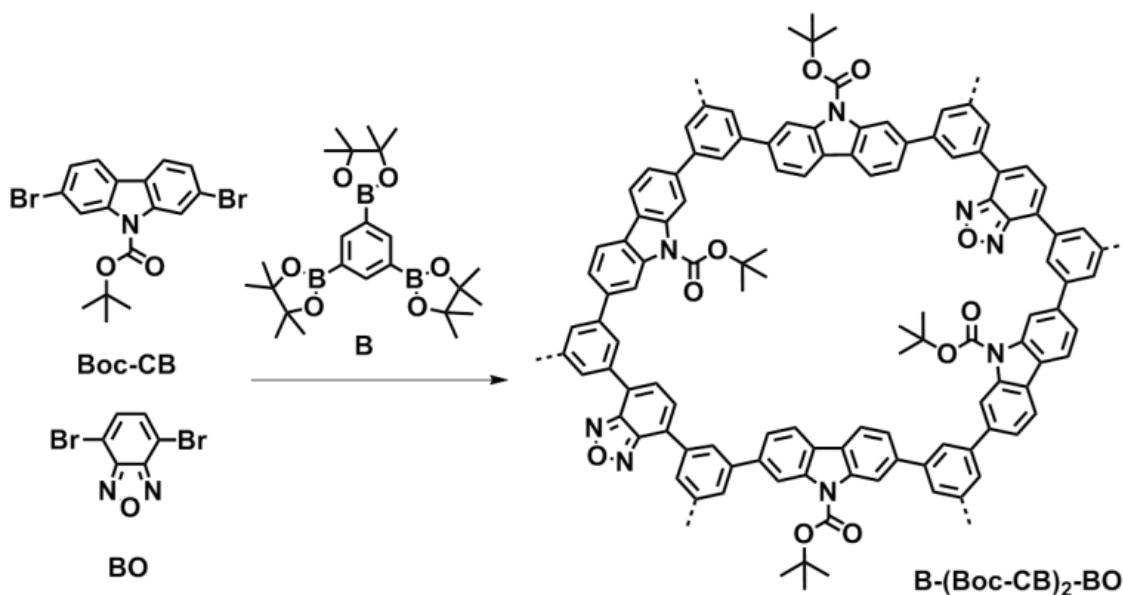


Figure 5.70 Synthetic route and idealized structure of B-(Boc-CB)₂-BO using palladium catalyzed Suzuki-Miyaura cross-coupling reaction via high internal phase emulsion (HIPE) polymerization. Reaction conditions: Pd(PPh₃)₄, K₂CO₃, Span[®] 80, H₂O/toluene, 80 °C, 12 h.

This chapter reports the first use of a π -conjugated polyHIPE B-(Boc-CB)₂-BO (Figure 5.70) as a heterogeneous, visible light photoinitiator in the free radical polymerization of methyl methacrylate (MMA). Via high internal phase emulsion (HIPE) polymerization, the π -conjugated polymer B-(Boc-CB)₂-BO was synthesized via palladium-catalyzed Suzuki-Miyaura cross-coupling reactions using *tert*-butylcarbonate functionalized dibromocarbazole (Boc-CB) with 1,3,5-benzenetriboronic acid tris(pinacol) ester (B) as the cross-linker combined with a strong electron acceptor dibromobenzoxadiazole (BO). The chemical structure, morphology, and optical

properties of the porous polymer were characterized by Fourier transform-infrared (FT-IR) spectroscopy, scanning electron microscopy (SEM), diffusive reflectance (DR) UV/Vis spectroscopy, solid-state ^{13}C magic angle spinning (MAS) nuclear magnetic resonance (NMR) spectroscopy, and N_2 gas sorption measurements.

The system formed stable emulsions that resulted in a monolithic polymer with an interconnected pore structure (Figure 5.72a and b). The polymer was insoluble in all common organic solvents tested. The SEM images showed that the conjugated polyHIPE has a hierarchical pore structure, consisting of micrometer scale cavities, submicron scale interconnected pores, as well as nanometer scale micropores measured by the N_2 gas sorption experiment (Figure 5.73 and Figure 5.74). The Brunauer-Emmett-Teller (BET) surface area, micropore size, and total pore volume measured are $82 \text{ m}^2 \text{ g}^{-1}$, 1.5 nm and $0.128 \text{ cm}^3 \text{ g}^{-1}$, respectively.

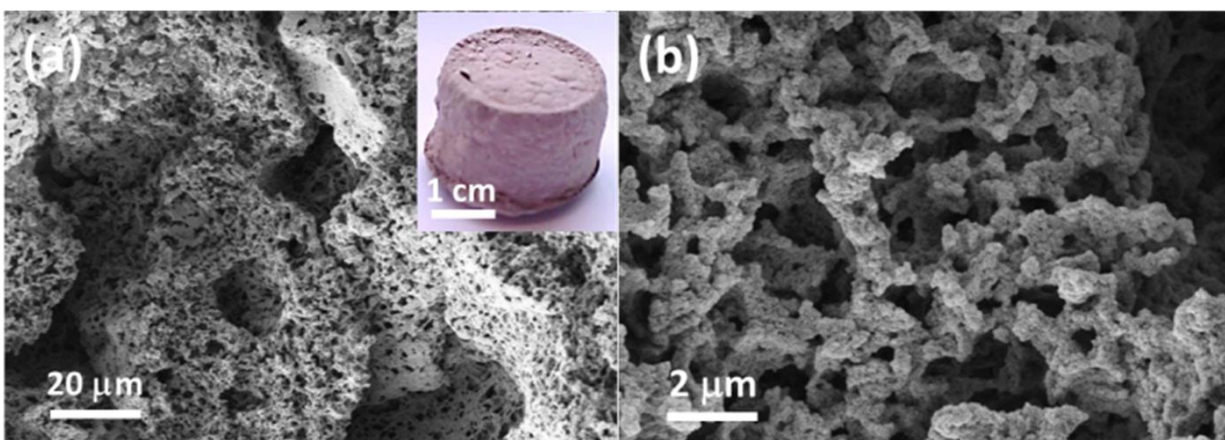


Figure 5.71 (a) and (b) SEM images of B-(Boc-CB) $_2$ -BO, the insert is a photograph of the monolithic polymer.

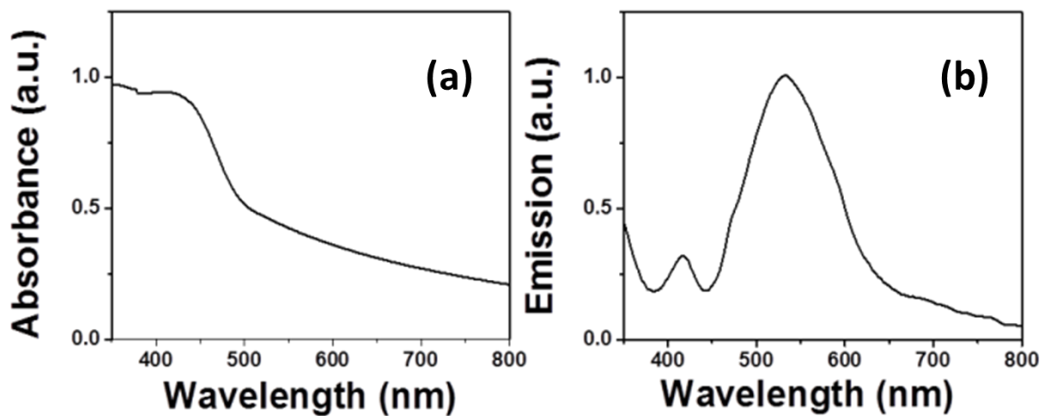


Figure 5.72 (a) DRS UV/Vis, and (b) photoluminescence spectra.

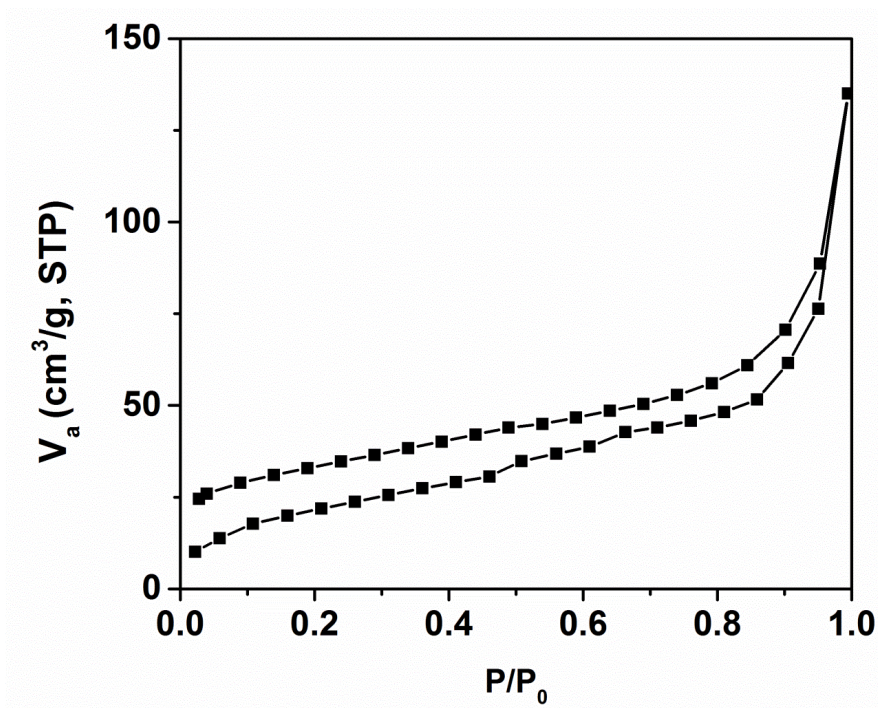


Figure 5.73 N₂ sorption isotherms of BET surface area measurement.

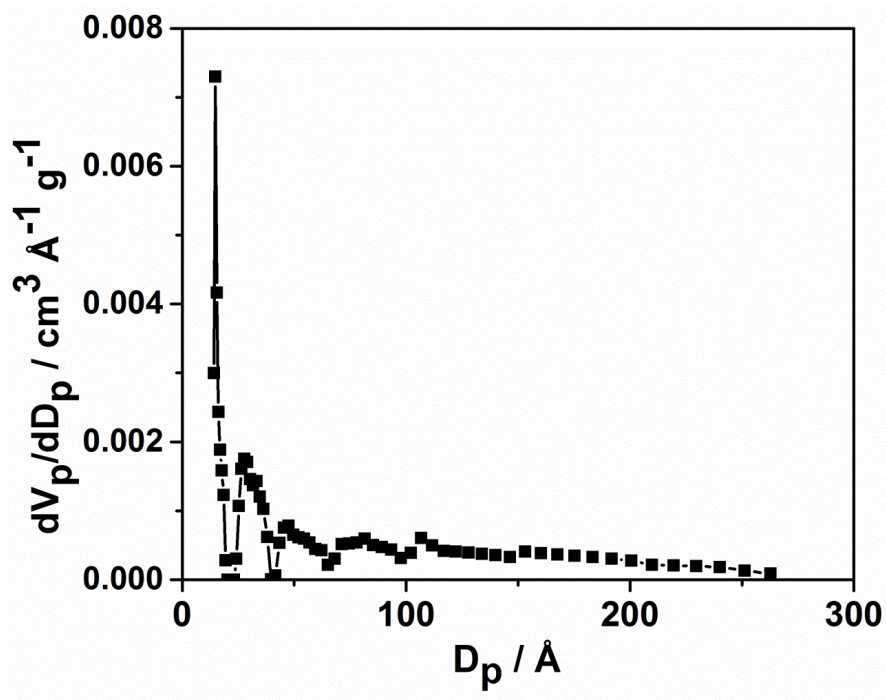


Figure 5.74 Pore size distribution of BET measurement.

The solid state $^{13}\text{C}/\text{MAS}$ NMR spectrum showed chemical shifts at $\delta = 30$ and 85 and 155 ppm, which are assigned to the $-\text{CH}_3$, *quart.*-C and $>\text{C}=\text{O}$ groups of the Boc moiety. The signals between 110 and 150 ppm can be assigned to the aromatic rings in the polymer backbone (Figure 5.75). Thermal gravimetric analysis (TGA) measurements showed that the conjugated network remained intact up to 700 °C, the weight loss at around 200 °C can be attributed to the Boc functional group (Figure 5.76).

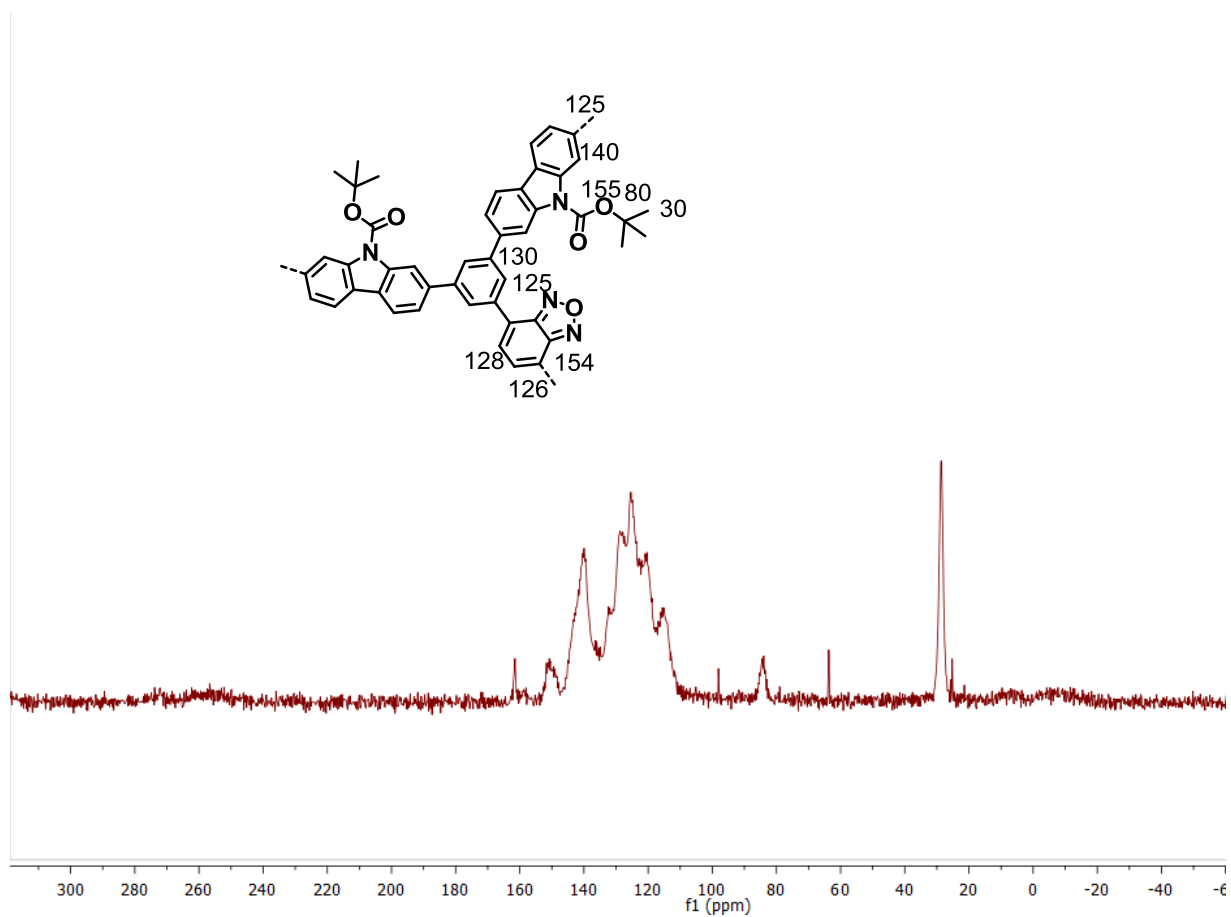


Figure 5.75 Solid-state ^{13}C NMR spectrum of $\text{B}-(\text{BOC-CB})_2\text{-BO}$.

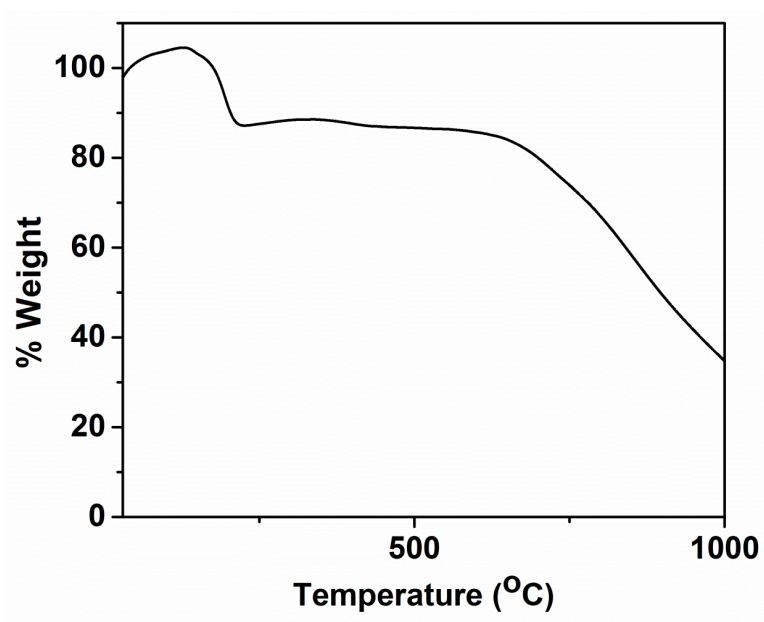


Figure 5.76 Thermogravimetry analysis (TGA) of $\text{B}-(\text{BOC-CB})_2\text{-BO}$.

Figure 5.72c displays very broad absorption band in the visible light range, an optical band gap of 2.16 eV can be derived from the absorption edge. The exhibited baseline increases with decreasing wavelength. This is an indication of light scattering inside the porous structure with sizes in the range of the visible wavelengths. B-(Boc-CB)₂-BO exhibited weak emission with a maximum at about 540 nm (Figure 5.72d), a large Stokes shift occurred, which indicates a better $\pi-\pi^*$ transition in the excited state of the polymer.

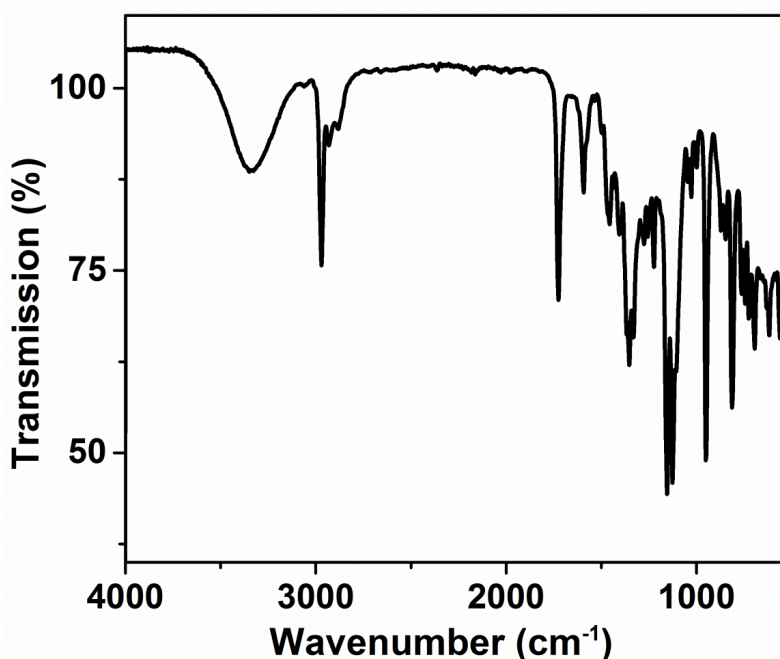
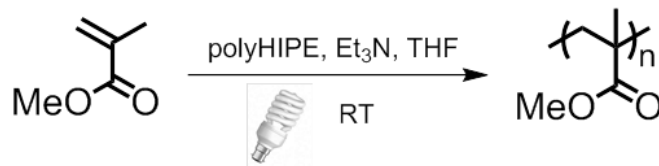


Figure 5.77 FTIR spectrum of conjugated poly(HIPE) B-(Boc-CB)₂-BO.

5.4.3 Photoinitiation of Free Radical Polymerization of Methyl Methacrylate

To demonstrate the photocatalytic activity under visible light, B-(BOC-CB)₂-BO was employed to initiate the free radical photopolymerization of methyl methacrylate (MMA) in 50 wt% THF solution using a 23 W household energy saving light bulb at room temperature. Et₃N was used as a co-initiator. The set-up is showed in Figure 6.22. A kinetic plot of the radical polymerization of methyl methacrylate (MMA) (Figure 5.78) initiated by B-(Boc-CB)₂-BO under visible light at room temperature is shown in Figure 5.79.

Table 5.13 Visible light initiated free radical polymerization using B-(Boc-CB)₂-BO as photoinitiator at room temperature.



Sample	$h\nu$	Conv. (%)	M_n (g mol ⁻¹)	M_w/M_n
Blank ^a	-	-	-	-
Blank ^b	+	-	-	-
Blank ^c	+	-	-	-
B-(Boc-CB) ₂ -BO	+	82	34300	2.67
B-(Boc-CB) ₂ -BO	+	35	12700	2.18
B-(Boc-CB) ₂ -BO	+	35	8300	1.92

^a no light with polyHIPE and coinitiator; ^b no coinitiator with polyHIPE and light; ^c no polyHIPE with light and coinitiator. Conditions: MMA (1 mL, 9.39 mmol), B-(Boc-CB)₂-BO (25 mg) and Et₃N (30 mg) in 50 wt% THF.

Control experiments conducted without light irradiation resulted in no polymer formation. In Figure 5.80, we suggest a similar initiation mechanism as reported in the literature.²⁵² Under visible light irradiation, a charge separation inside the conjugated polyHIPE occurred,²⁵³ which likely could be stabilized within the nanometer-sized pores. Et₃N was oxidized by the hole inside the conjugated polyHIPE into the corresponding radical cation. Another Et₃N molecule formed consequently a free radical after giving away one proton to radical cation. The radical polymerization of MAA was initiated. And the electron followed by the photoinitiation could reaction with the amine cation, forming neutral amine and hydrogen radical.

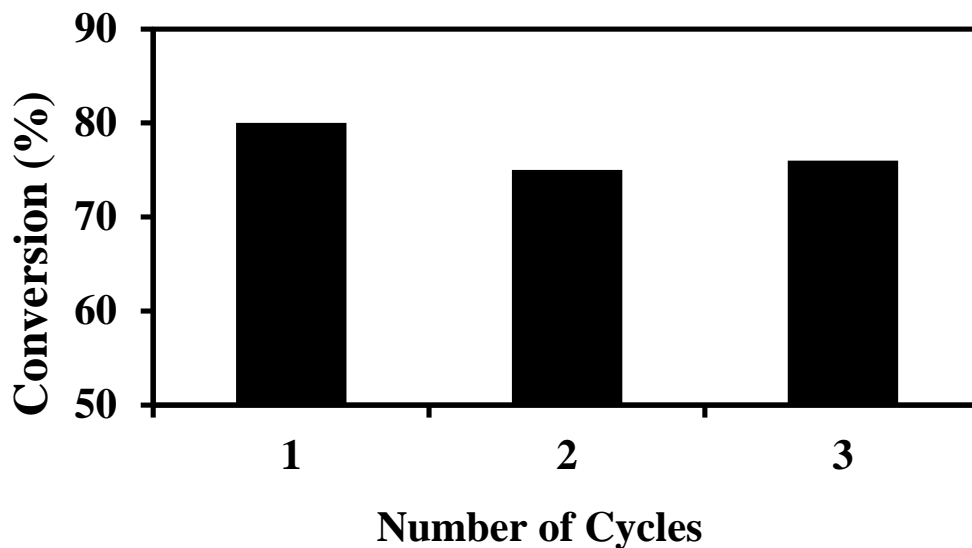


Figure 5.81 Additional repeating experiments of the photopolymerization of methyl methacrylate in 50 wt% THF solution in the presence of Et₃N at room temperature with visible light.

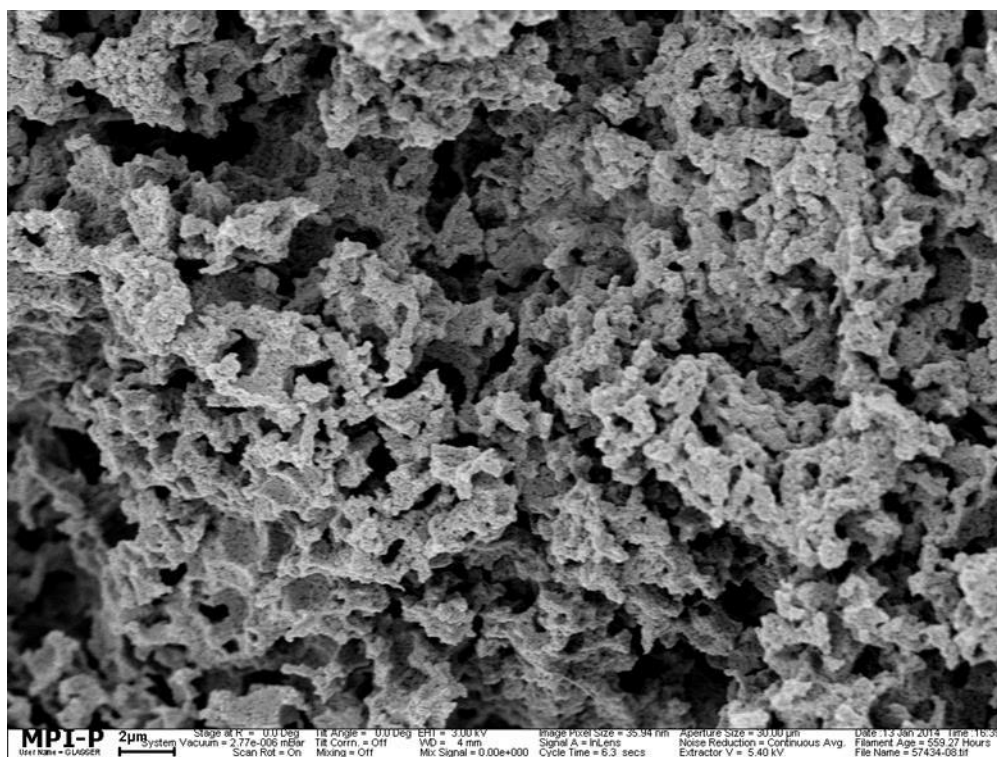


Figure 5.82 SEM image of B-(Boc-CB)₂-BO after the photoinitiation under visible light.

5.4.4 Conclusion

In this chapter, the photopolymerization of MMA using π -conjugated porous polyHIPE as heterogeneous photoinitiator was achieved under visible light. A household energy saving light bulb was used as light source, which provides an economically low-cost solution. The hierarchical porosity of the conjugated polyHIPE could be advantageous in attaining efficient mass transfer in the catalytic reactions. The heterogeneous nature and stable 3D structure of polyHIPE allow its facile removal from the polymerization mixture and reusability without a significant loss of activity. Moreover, the π -conjugated polyHIPE-based photoinitiator minimizes odor, toxicity and migration problems, which usually accompany the low molar mass photoinitiators.

5.5 Hybrid Conjugated Porous Polymer with Pd Nanocrystals

This chapter is based on the paper “Photocatalytic Suzuki Coupling Reaction using Conjugated Microporous Polymer with Immobilized Palladium Nanoparticles under Visible Light”, *Chem. Mater.*, 2015, **27**, 1921-1924 with copyright (2015) from American Chemical Society.

5.5.1 Introduction

This chapter looks beyond the realm of using conjugated porous polymer as metal-free heterogeneous visible light photocatalysts and investigated the hybrid system combining palladium nanocrystals and conjugated porous polymer, which was found to be effective heterogeneous photocatalyst for visible light induced Suzuki cross-coupling reaction at room temperature.

First discovered in the late 1970s, palladium (Pd)-catalyzed Suzuki cross-coupling reaction is one of the most powerful one-step pathway for the formation of carbon-carbon bonds in organic synthesis.^{120,254} Typically, Suzuki coupling reactions are performed under homogenous conditions using a variety of phosphine ligand/palladium catalytic complexes.²⁵⁵⁻²⁵⁷ Despite the relatively high efficiency of these homogeneous systems, the recovery of the costly and potentially toxic palladium catalysts remain as a pressing issue in the development towards a greener, more sustainable chemical industry. Heterogeneous catalysts are favored over homogeneous catalysts because of their facile recyclability and easy compatibility with continuous flow systems.²⁵⁸⁻²⁶³ Extensive research has been done to develop heterogeneous Pd catalysts for Suzuki coupling reactions,²⁶⁴ such as the immobilization or stabilization of Pd nanoparticles (NPs) on silica,²⁶⁵⁻²⁶⁷ carbon nanotubes,²⁶⁸ polymers,²⁶⁹⁻²⁷¹ metal oxides,^{272,273} dendrimers,^{274,275} graphene layers.²⁷⁶ However, due to the high activation barrier of substrates associated with the rate-limiting steps, the majority of these systems with heterogeneous catalysts require elevated temperature (≥ 100 °C or under reflux conditions), intensive heating and prolonged reaction time, which may lead to undesired side reactions and compromise the stability of the catalysts.^{264,277}

Current research in the field of heterogeneous visible light photocatalysis is predominantly focused on the photoredox reactions²⁷⁸ such as the oxidation of alcohols, amines

or the hydroxylation of aromatic compounds,^{279,280} C-H activation reaction,²⁸¹ hydrogen generation,²⁸² oxygen activation,²⁸³ whereas there has been very few reports on classic cross-coupling reactions, such as Suzuki coupling reactions. Recently, Wang *et al.* reported the harvesting of visible light with plasmonic Au-Pd nanostructures and their use as photocatalysts for Suzuki coupling reactions.⁹¹ Zhu *et al.* demonstrated also that Au-Pd alloy NPs can strongly absorb visible light and efficiently catalyze several cross-coupling reactions at ambient temperature.²⁸⁴⁻²⁸⁶ Apart from plasmonic metals, Li *et al.* reported that mesoporous g-C₃N₄, a well-established visible light non-metal photocatalyst, can be used as photoactive anchoring support for Pd nanoparticles to form a Mott-Schottky heterojunction and increase the electron density surrounding Pd NPs via light-amplified effect.²⁸⁷⁻²⁹⁰

Conjugated microporous polymers (CMPs), combining semiconductive π -conjugated skeletons with permanent nanopores, have been applied as organic, heterogeneous visible light photocatalysts for a number of photoredox reactions.^{152,157,199,291,292} With their broad light absorption and tunable semiconductor-range band gaps, we envision the formation of a hybrid heterojunction, *i.e.* a metal-semiconductor contact between Pd NPs and CMP, would result in a positively charged region on the CMP and a negatively charged site on the Pd NPs at the interface due to the Schottky effect. Upon photo-irradiation, both the average energy and the effective flow of free electrons towards the Pd NPs would be amplified, which can be exploited and harvested to catalyze reactions.

In this chapter, it is the aim to utilize the photo-amplified heterojunction effect at the interface between a semiconductive conjugated microporous polymer and Pd NPs. The use of conjugated microporous polymer supported Pd NPs (Pd@CMP) as an efficient heterogeneous, visible light photocatalyst for Suzuki coupling at room temperature is demonstrated.

5.5.2 Synthesis and Characterization of Hybrid Photocatalyst Pd@B-BO₃

A conjugated microporous poly(benzoxadiazole) network (B-BO₃) was chosen as the semiconductive polymer support (Figure 5.83a), on which Pd NPs with sizes between 5 and 10 nm were subsequently immobilized, resulting into the hybrid material Pd@B-BO₃ (Figure 5.83b). To note, the functional groups inside B-BO₃ were end-capped in order to avoid undesired side reactions during the light-induced Suzuki coupling later. About 3 wt% of Pd content in Pd@B-

BO_3 was determined via inductively coupled plasma (ICP). The synthetic and characteristic details of the materials are described in Section 6.4.

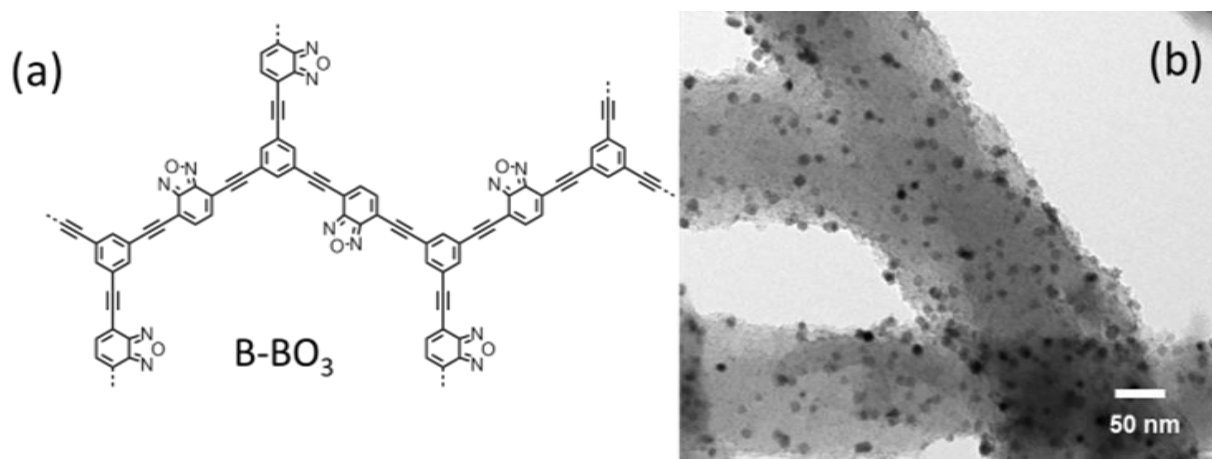


Figure 5.83 (a) Polymer backbone structure of B- BO_3 . (b) TEM image of B- BO_3 immobilized with Pd NPs with sizes between 5 and 10 nm.

The Brunauer-Emmett-Teller (BET) surface area of B- BO_3 was $612 \text{ m}^2/\text{g}$ with a total pore volume of $0.37 \text{ cm}^3/\text{g}$, whereas the BET surface area of Pd@B- BO_3 was $176 \text{ m}^2/\text{g}$ the pore volume of $0.11 \text{ cm}^3/\text{g}$ (Table 5.14 and Figure 5.84 and Figure 5.85). This is likely due to the weight increase after immobilization with Pd NPs. The pore size of ca. 1.4 nm remained.

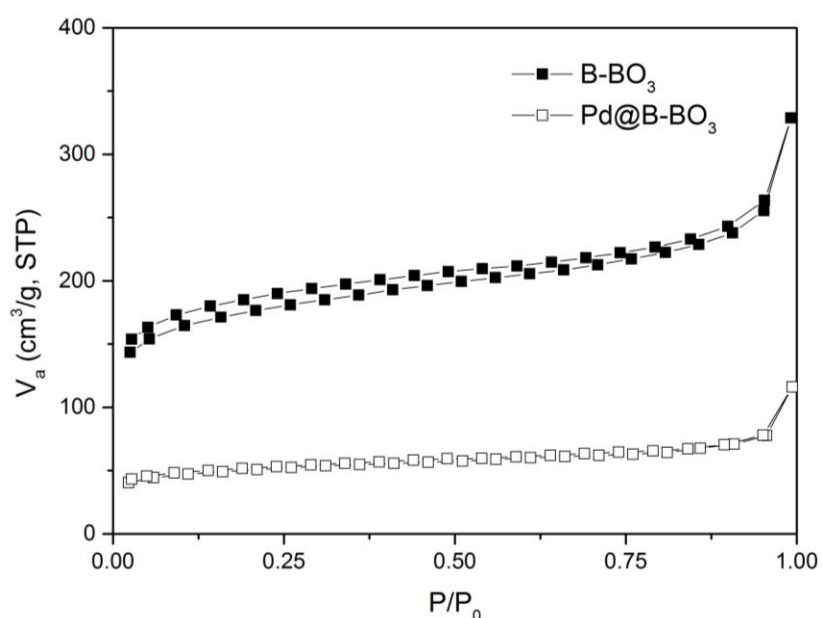


Figure 5.84 N_2 sorption isotherms B- BO_3 and Pd@B- BO_3 .

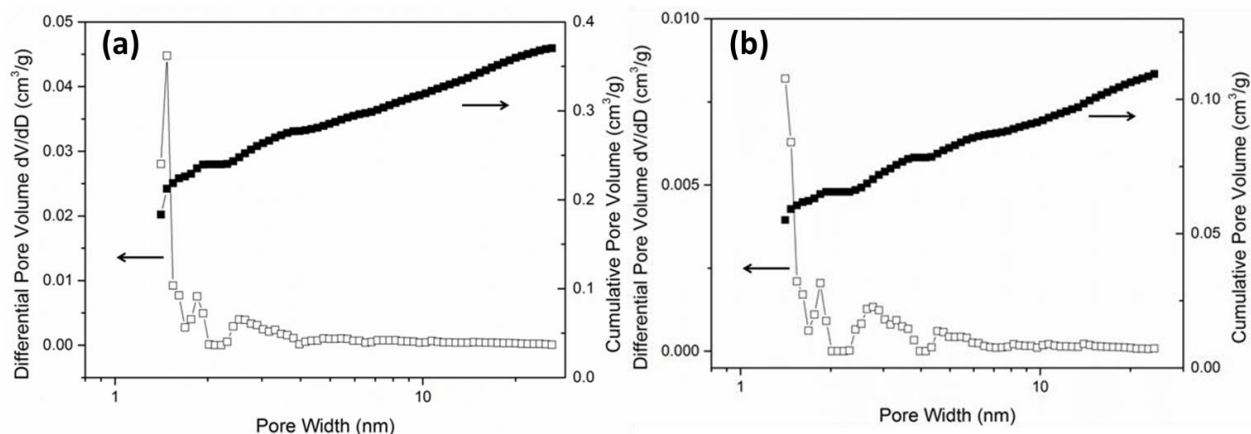


Figure 5.85 Pore size distribution of (a) B-BO₃ and (b) Pd@B-BO₃.

Table 5.14 Porosity data of B-BO₃ and Pd@B-BO₃.

Material	Surface area S_{BET} [m ² /g]	Pore size [nm]	Pore volume [m ³ /g]
B-BO ₃	613	1.4	0.37
Pd@B-BO ₃	176	1.4	0.11

The UV/Vis DR spectrum of Pd@B-BO₃ showed a broader absorption than that of B-BO₃ (Figure 5.86c). This could be attributed to the immobilization of Pd NPs, which also absorb in the visible range due to the inter-band transition and plasmonic effects.

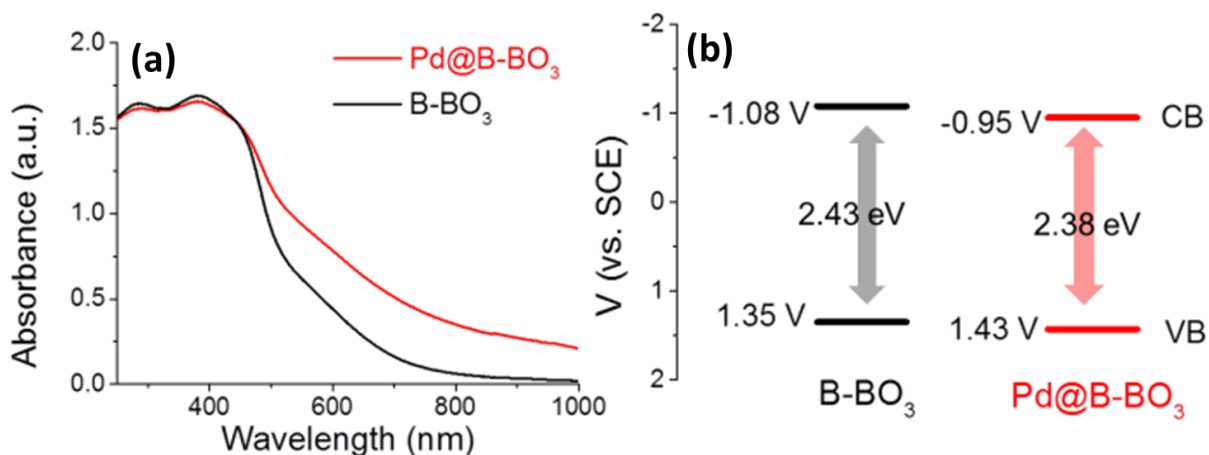


Figure 5.86 (a) UV/vis DR spectra of Pd@B-BO₃ and B-BO₃. (d) VB (HOMO) and CB (LUMO) band positions of Pd@B-BO₃ and B-BO₃ (vs SCE) measured by CV.

Cyclic voltammetry measurements (Figure 5.86b) showed that Pd@B-BO₃ exhibited lower valence band (VB) (-1.43 eV vs SCE) and conduction band (CB) (-0.95 eV vs SCE) than B-BO₃ with a VB of -1.35 eV (vs SCE) and CB of -1.08 eV (vs SCE), respectively. The electron paramagnetic resonance (EPR) showed a large increase of the intensity of Pd@B-BO₃ in dark and under light irradiation compared to B-BO₃ (Figure 5.87). This could also be caused by the plasmonic effects on the Pd NPs. On the other hand, the intensive signal also indicates a longer living electron-hole pair inside Pd@B-BO₃ than in B-BO₃.

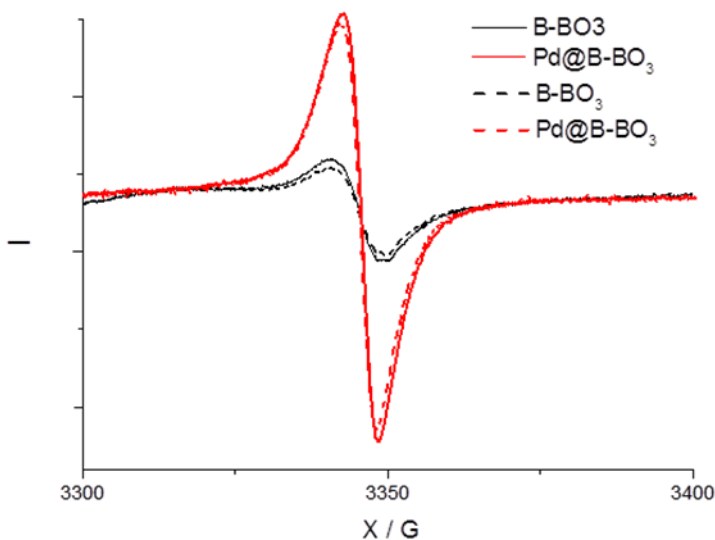


Figure 5.87 Electron paramagnetic resonance (EPR) spectra of B-BO₃ and Pd@B-BO₃ in dark (dash line) and under light irradiation (straight line).

Wang_140805/2
13C CP-MAS NMR 10kHz
Sample: ZW010 CMP
CP 1 ms

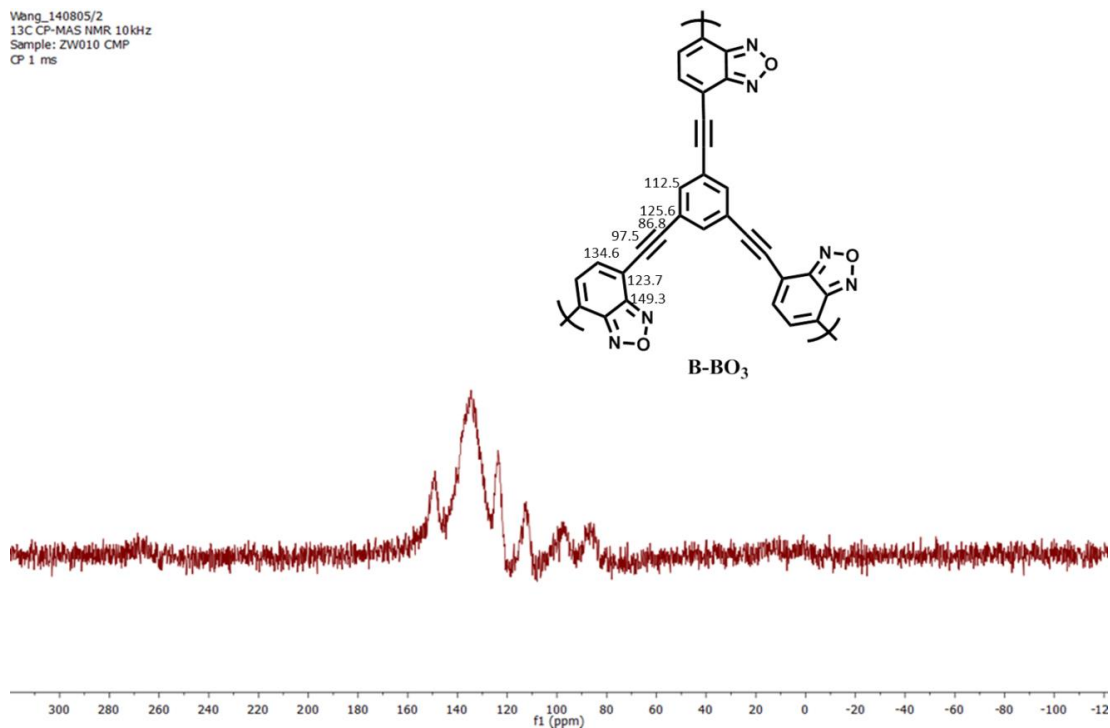


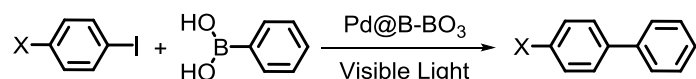
Figure 5.88 Solid-State ^{13}C Magic Angle Spinning Nuclear Magnetic Resonance (MAS-NMR) of B-BO₃.

5.5.3 Photocatalytic Suzuki Cross-coupling at Room Temperature by Pd@B-BO₃

The coupling of iodobenzene with phenylboronic acid was chosen as a model reaction to study the catalytic activity of Pd@B-BO₃ under visible light irradiation. To avoid the photoheating effect, the reaction vial was submerged in a water bath (Figure 6.28). The screening and control experiments are listed in Table 5.15. The reaction gave the desired product in an almost quantitative yield at room temperature in 2 hours (entry 1). An identical reaction system, which was conducted in dark, resulted only in trace conversion, by extending the reaction time to 5 h, a conversion of 13% was observed (entry 2). This is similar to previous report on reactivity of Pd NPs at room temperature in dark.²⁹³ No conversion was also observed without base (entry 3), which is essential to activate boronic acid and facilitate transmetalation.²⁵⁶ Bare B-BO₃ without immobilization of Pd NPs as a control experiment only led to trace yield of the product, which is likely obtained due to the residual amount of Pd (~50 ppm) present in B-BO₃ after its preparation. Using Pd@C as photocatalyst led to a conversion of 16%, indicating a minor contribution of the

Pd plasmonic effect compared to the photocatalytic activity afforded by the hybrid heterojunction between Pd and B-BO₃.

Table 5.15 Screening and mechanism study of the photocatalytic Suzuki coupling reaction using Pd@B-BO₃.^a



Entry	X	Reaction condition variations	Light	Yield ^b (%)
1	H	-	+	98
2	H	-	-	13 ^c
3	H	No K ₂ CO ₃	+	-
4	H	No Pd@B-BO ₃	+	-
5	H	B-BO ₃ as photocatalyst	+	trace
6	H	Pd@C as photocatalyst	+	16 ^d
7	F	-	+	94
8	F	Hole scavenger	+	21 ^e
9	F	Radical scavenger	+	30
10	F	Radical and hole scavengers	+	trace ^f

^aReaction conditions: iodobenzene (1 mmol), phenylboronic acid (1.1 mmol), K₂CO₃ (1.5 mmol), Pd@B-BO₃ (10 mg, 3 wt% Pd content), DMF/H₂O (1.5 mL/1.5 mL), white LED lamp (1.2 W/m²), water bath, room temperature, 2 h. ^bIsolated yields after chromatography. ^cIn dark, 5 h. ^d6 mg of Pd@C (5 wt% Pd content). ^e21% yield of 4-fluorobiphenyl and 17% yield of 4,4'-difluorobiphenyl. ^fTrace amount of 4-fluorobiphenyl and 8% yield of 4,4'-difluorobiphenyl.

To understand the specific role of the photogenerated electron-hole pairs during the photocatalytic Suzuki coupling reaction, a hole (diisopropylethylamine (DIPEA)) and a radical

scavenger (benzoquinone) were added to the reaction mixture respectively. In the same time, the occurrence of a possible homo-coupling of both aryl reactants was also investigated. 4-Fluoriodobenzene was taken as the model aryl halogenide in order to differentiate the homo-coupled products. Under the same reaction condition as entry 1, 4-fluorobiphenyl, as product was obtained in a yield of 94% (entry 6). By adding DIPEA, i.e. when the hole was blocked, 4-fluorobiphenyl was obtained with a yield of 21%, as well as yielding the homo-coupled side product 4,4'-difluorobiphenyl with a conversion of 17% (entry 8). Via addition of benzoquinone, where the generated electron was blocked, 4-fluorobiphenyl was still obtained in a yield of 30% without any observation of homo-coupled side product (entry 9). By blocking both hole and electron upon addition of both scavengers, only traces of 4-fluorobiphenyl were obtained, along with 8% of the homo-coupled 4,4'-difluorobiphenyl (entry 10). It can be observed that both generated hole and electron pair were essential for the light-induced Suzuki coupling reaction. And by only blocking one of the photogenerated electron-hole pair, Pd@B-BO₃ was still active enough to precede the coupling reaction with one activated aryl species under lowered reaction rate.

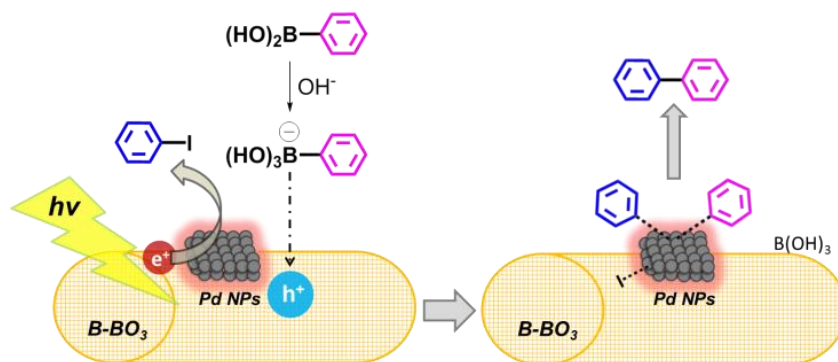


Figure 5.89 Suggested reaction mechanism of the photocatalytic Suzuki coupling via the light-induced heterojunction at the interface of B-BO₃ and Pd NPs.

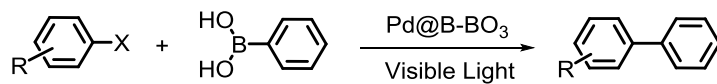
Based on the observations during the screening and control experiments, we propose a possible reaction mechanism as displayed in Figure 5.89. Upon light irradiation, charge separations in form of electron-hole pairs can be generated within the semiconductive polymer B-BO₃. The photoexcited energetic electrons further amplify the Schottky effect by migrating towards the noble metal center (i.e. Pd NPs in this case). With the Pd NPs functioning as active center, the C-I bond of iodobenzene is attacked by the photogenerated electrons. Xiao *et al.* showed via the density functional theory (DFT) calculation, when an electron enters an

unoccupied orbital of the iodobenzene molecule, the C-I bond elongates from 0.214 nm to 0.300 nm,²⁸⁵ facilitating the cleavage of the C-I bond and yielding a transient radical anion, which initially forms an aryl complex with Pd. In the same time, the hole inside the semiconductive polymer B-BO₃ activates the C-B bond of phenylboronic acid, which is transferred into an electronically negative B(OH)₃⁻ species by catching a OH⁻ from the basic reaction medium, forming another aryl Pd complex. The remaining steps, the reductive elimination and transmetalation, should not be affected by the photoactivation, are followed by the formation of the final product.^{294,295}

We then further tested the feasibility of Pd@B-BO₃ as photocatalysts for a series of Suzuki coupling reactions of phenylboronic acids with various aryl halides. As listed in Table 5.16, aryl iodides (for example entry 6 and 10), as expected, were converted more readily than their bromide counterparts (entry 14 and 15), which also showed good to excellent yields. Iodobenzene with electron-donating groups (CH₃, OH, see entry 12 and 13) showed lower conversion rates when compared to those with electron-withdrawing groups such as F, Br or NO₂. *Ortho*-substituted substrates showed lower reactivity compared to other substituted positions on the substrates (entry 11 and 16), which could be caused by steric hindrance during the coupling reaction.

The coupling of iodobenzene and phenylboronic acid were carried out repeatedly under the same reaction condition as entry 1 in Table 5.15. Biphenyl was obtained without significant loss in yield, demonstrated the stability and reusability of Pd-BO₃ as photocatalyst (Figure 5.90). TEM images of the used Pd@B-BO₃ showed a similar structure as the unused one, while a slightly weight loss of Pd was determined via ICP (Figure 5.91).

Table 5.16 Scope of the photocatalytic Suzuki coupling reaction with various substituents using Pd@B-BO₃ as photocatalyst.^a



Entry	Aryl halide	Product	Time (h)	Yield ^b (%)
10			2	98
11			6	84
12			6	75
13			6	90
14			4	96
15			4	95
16			16	76

^aReaction conditions: arylhalide (1 mmol), phenylboronic acid (1.1 mmol), K₂CO₃ (1.5 mmol), Pd@B-BO₃ (10 mg, 3 wt% Pd content), DMF/H₂O (1.5 mL/1.5 mL), white LED lamp (1.2 W/m²), water bath, room temperature. ^bIsolated yields after chromatography.

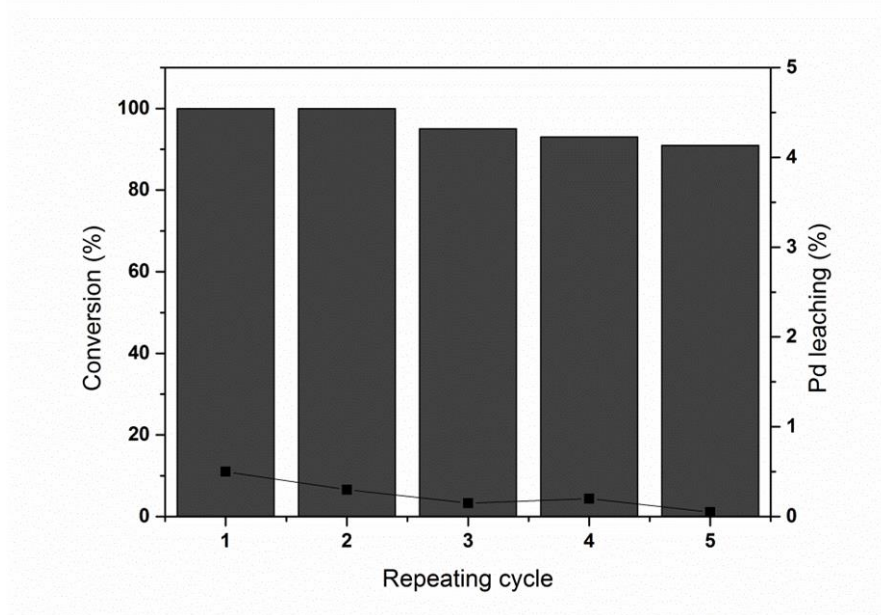


Figure 5.90 Repeating experiment of the photocatalytic Suzuki coupling of iodobenzene and phenylboronic acid. The lost weight percentage of Pd after the repeating cycles is also displayed.

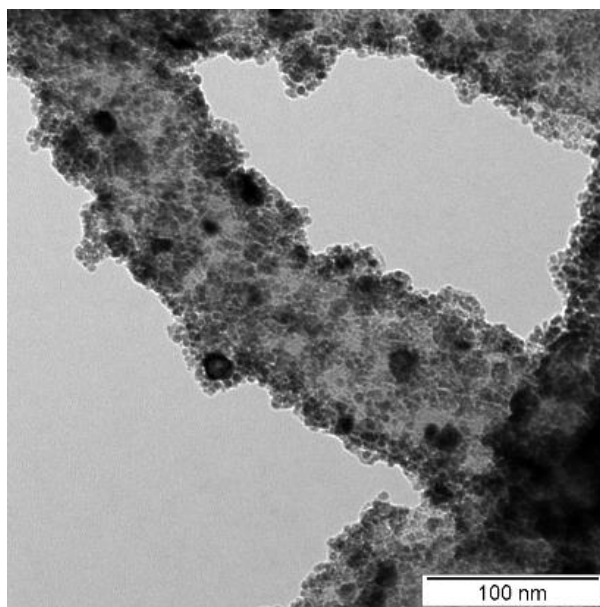


Figure 5.91 TEM image of a used Pd@B-BO₃ sample after the catalytic reactions.

5.5.4 Conclusion

In conclusion, this chapter demonstrated that Pd@B-BO₃, a type of metal-immobilized microporous polymer semiconductor photocatalysts, can be used as efficient, heterogeneous

photocatalysts for the Suzuki coupling reactions via the photo-amplified Schottky effect at the metal-semiconductor interface. The coupling reactions of aryl halides with arylboronic acid yielded excellent conversions in best cases under visible light irradiation at room temperature. Given the heterogeneous nature, the photocatalyst could be easily separated and recycled for further coupling reactions without significant loss in activity. It is envisioned that this novel genre of photocatalysts could be applied to other classic cross-coupling reactions, such as Sonogashira, Stille, Hiyama and other catalytic reactions.

6 Experimental Details and Supplemental Information

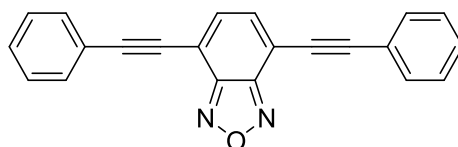
6.1 Molecular Structural Control of Conjugated Porous Polymers

6.1.1 Molecular Structural Design of Conjugated Microporous Poly(benzooxadiazole) Networks for Enhanced Photocatalytic Activity with Visible Light

6.1.1.1 Materials

Tetrakis(triphenylphosphine) palladium(0) (99%), copper (I) iodide (CuI), 1,3,5-triethynylbenzene (97%) and all other solvents were purchased from Aldrich. 4,7-dibromobenzo[c][1,2,5]oxadiazole (Br-BO), 1,2,4-triethynylbenzene and 1,2,4,5-tetraethynylbenzene were synthesized according to literature.^{24,296} All chemicals and solvents were used as received unless otherwise specified.

6.1.1.2 Synthesis of B-BO-B



To 3 mmol (306 mg) of phenylacetylene, 1 mmol (278 mg) BO, 0.05 mmol (58 mg) of tetrakis(triphenylphosphine) palladium(0), 0.05 mmol (9 mg) of CuI were dissolved in 30 mL of

DMF and Et₃N (vol/vol 50/50). The mixture was degassed for 20 min with N₂ and then was heated to 80 °C for 12 h. The cooled mixture was extracted with DCM and diethyl ether from saturated NaHCO₃ solution. The solvent was then evaporated and the crude product was chromatographed with ether/hexane (1:4), affording the final product (262 mg, 82%).

¹H NMR (CDCl₃): δ ppm 7.89, 7.79-7.68, 7.35-7.27

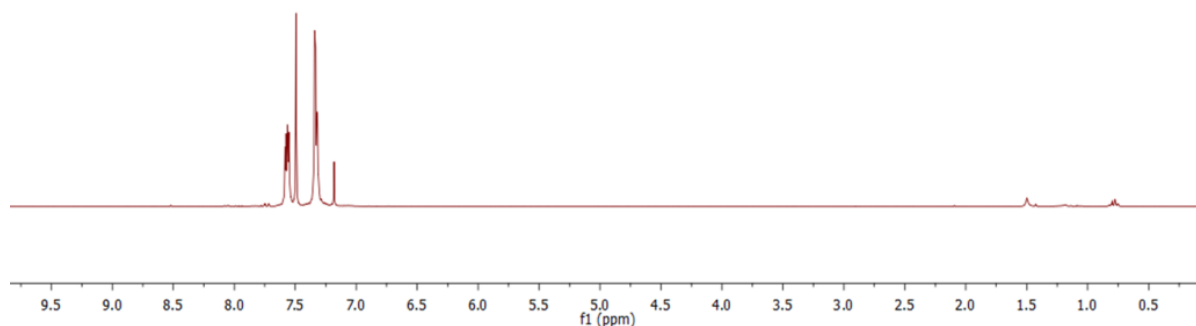
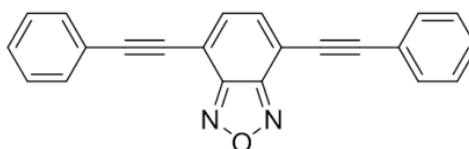
¹³C NMR (CDCl₃): δ ppm 149.6, 134.3, 132.9, 129.1, 128.4, 122.4, 114.1, 98.4, 83.8

6.1.1.3 General Procedure for the Light-Promoted Electron Transfer from Tetramethylphenylenediamine (TMPD) to Dioxygen

10 mg of CMP was added to a solution of tetramethylphenylenediamine (TMPD) (100 mM in 3 mL CH₃CN) and irradiated with a blue LED for 1 h. The resulting reaction mixture was analyzed qualitatively by UV/Vis.

6.1.1.4 NMR spectra of B-BO-B

wangzjun.2160.fid
B-BO-B



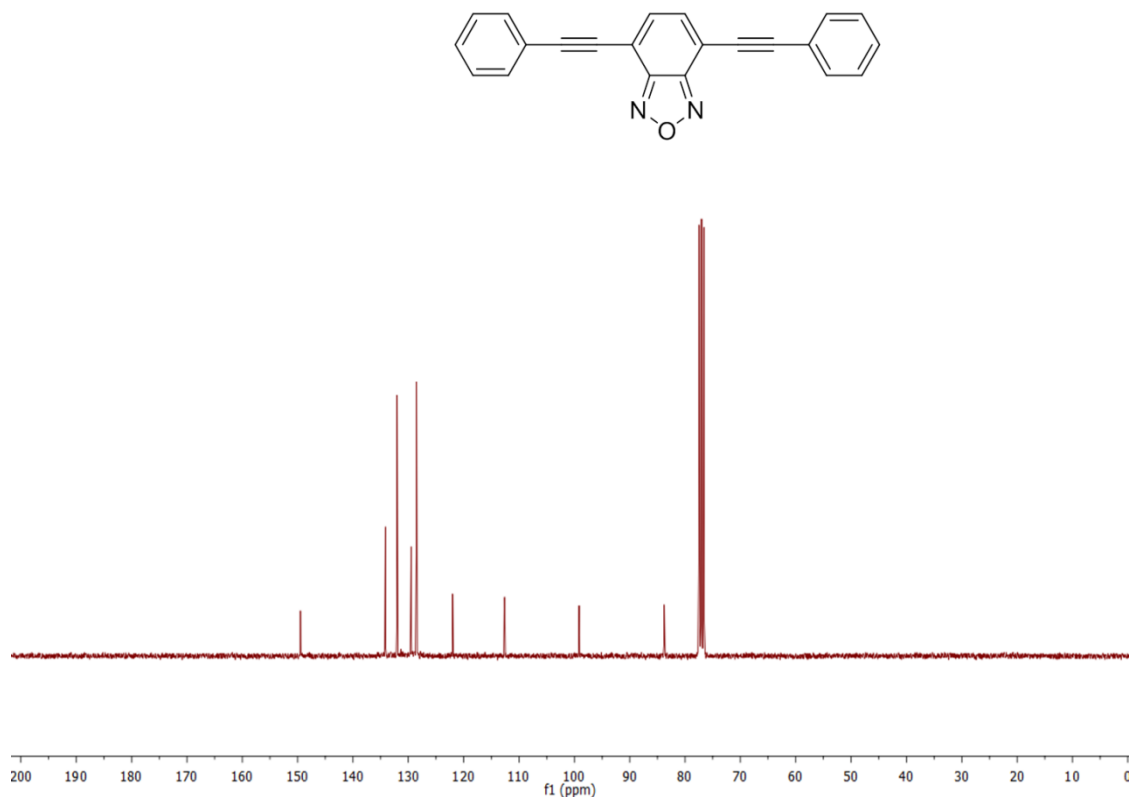


Figure 6.1 ¹H NMR and ¹³C NMR spectrum of B-BO-B.

6.1.2 Conjugated Microporous Poly(Benzochalcogenadiazole)s for Photocatalytic Oxidative Coupling of Amines under Visible Light

6.1.2.1 Materials

Tetrakis(triphenylphosphine) palladium(0) (99%), copper iodide (CuI), 1,3,5-triethynylbenzene, 4,7-dibromo-2,1,3-benzothiadiazole (Br-BT), 4,7-dibromo-2,1,3-benzoselenadiazole (Br-BS) and all the benzyl amine derivatives were purchased. 4,7-Dibromobenzofurazan (Br-BO) was synthesized according to literature.²⁹⁷ All chemicals and solvents were used as received unless otherwise specified.

6.1.2.2 Synthesis of B-BO, B-BT and B-BS via Sonogashira coupling

In a general procedure, the cross-linker 1,3,5-triethynylbenzene (100 mg, 0.67 mmol, 1 eq.) and the dibromides, 4,7-dibromobenzofurazan, 4,7-dibromo-2,1,3-benzothiadiazole or 4,7-dibromo-2,1,3-benzoselenadiazole (BS) (1 mmol each, 1.5 eq. to 1,3,5-triethynylbenzene),

copper(I) iodide (0.03 eq.), tetrakis(triphenylphosphine) palladium(0) (0.03 eq.) were dissolved in 10 mL DMF and the solution was degassed for 5 min. 10 mL dry triethylamine were added and the reaction mixture was heated at 80 °C overnight under nitrogen atmosphere. After cooling, methanol was added and the precipitated powder was filtered and washed with water. The crude product was washed in a Soxhlet-extractor with methanol and dichloromethane for 24 h. The final product was obtained after drying for at least 24 h at room temperature under vacuum. (Reaction scheme see Figure 5.21)

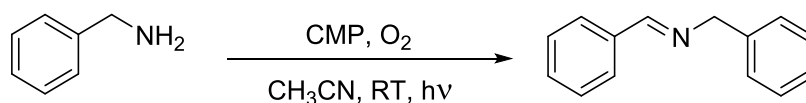
6.1.2.3 Photocatalytic Oxidative Coupling of Benzylamines

Benzylamine and its derivatives (1 mmol), the microporous polymer (3 mg) and 3 mL acetonitrile were mixed together in a 10 mL glass vial. The vial was sealed under O₂ atmosphere by equipping with an O₂ balloon. The reaction mixture was irradiated with a blue LED lamp (460 nm, 1.2 W/cm²) for 3 h under with stirring. To determine the conversion, ¹H-NMR samples of the crude mixture were taken after the CMP was filtered off.

6.1.2.4 Light on-off Experiment

To conduct the light-dependent kinetic study, the LED lamp was switched on and off every hour. Other reaction conditions remain the same as above-mentioned. The conversions were determined by ¹H NMR (Results obtained from diploma thesis of Kim Garth).

6.1.2.5 Monitoring the photocatalytic oxidative coupling of benzylamine using B-BT as photocatalyst



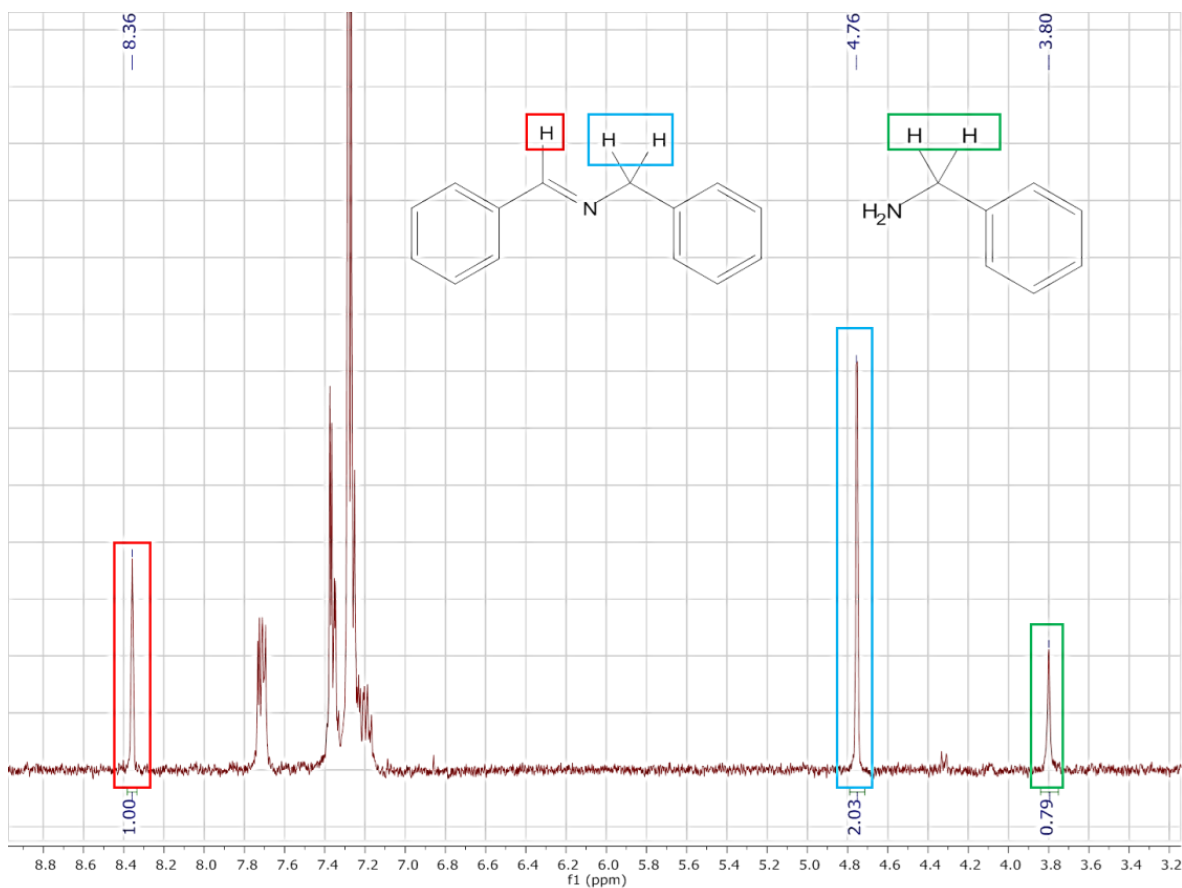


Figure 6.2 ^1H NMR spectrum of the crude mixture of the photo-oxidation of benzylamine with B-BT as photocatalyst. Reaction time 2 h, conversion ~55%.

6.2 Surface Area Control of Conjugated Porous Polymer Photocatalysts

6.2.1 Preparation of Conjugated Porous Polymers by HIPE Polymerization

6.2.1.1 Materials

Bis(4-bromophenyl)amine (NPh_2), 4,7-dibromobenzo[c]-1,2,5-thiadiazole (BT), 2,7-dibromo-9H-carbazole (CB), tetrakis(triphenylphosphine) palladium(0) (99%), potassium carbonate (K_2CO_3), Span® 80 nonionic surfactant, chloroform-d (CDCl_3 , 99.8%), methyl phenyl sulfide, dimethylaminopyridine (DMAP) and all other solvents were purchased from Aldrich. 1,3,5-Tribromobenzene and di-tert-butyl dicarbonate (di-BOC) were obtained from Alfa Aesar and 1,3,5-Phenyltriboronic acid (PB) (98%) was purchased from Combi-Blocks Inc. All chemicals and solvents were used as received unless otherwise specified.

6.2.1.2 Monomer Synthesis

The Boc-functionalized monomers were synthesized according literature²⁹⁸ and the procedure is described as following.

6.2.1.3 Synthesis of Boc-NPh₂

0.991 g NPh₂ (3.05 mmol), 1.334 g di-Boc (6.11 mmol) and 0.373 g DMAP (3.05 mmol) were dissolved in 50 mL dried THF. The reaction mixture was stirred at room temperature under nitrogen for 12 h. After completion, the reaction mixture was poured into 500 mL of Milli-Q water. The precipitate was then washed with cold methanol and dried under vacuum, yielding 1.15 g (89%) product.

¹H NMR (Figure 6.3): 7.35 (d, 2H), 6.98 (d, 2H), 1.37 (s, 9H)

¹³C NMR (Figure 6.4): 153.1, 141.7, 131.9, 128.5, 119.3, 82.0, 28.2

FTIR (Figure 6.7)

6.2.1.4 Synthesis of Boc-CB

0.991 g CB (3.06 mmol), 1.334 g di-BOC (6.11 mmol) and 0.373 g DMAP (3.05 mmol) were dissolved in 50 mL dried THF. The reaction mixture was stirred at room temperature under nitrogen for 12 h. After completion, the reaction mixture was poured into 500 mL of Milli-Q water. The precipitate was then washed with cold methanol and dried under vacuum, yielding 1.18 g (91%) product.

¹H NMR (Figure 6.5): 8.37 (d, 2H), 7.64 (d, 2H), 7.37 (d, 2H), 1.69 (s, 9H)

¹³C NMR (Figure 6.6): 150.3, 139.1, 126.5, 123.8, 121.0, 120.5, 119.6, 85.2, 28.3

FTIR (Figure 6.8)

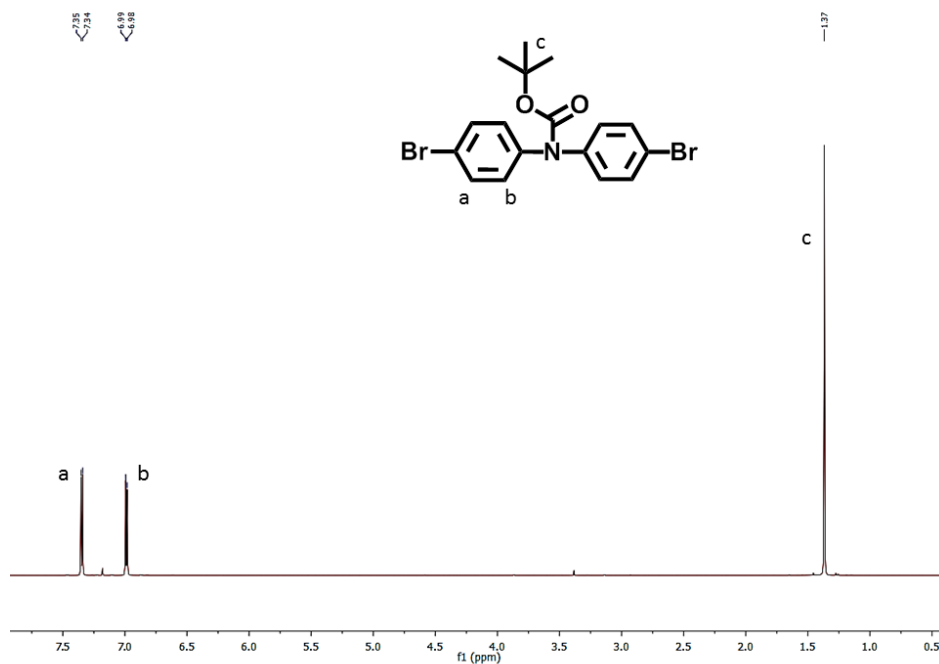


Figure 6.3 ¹H NMR spectrum of Boc-NPh₂.

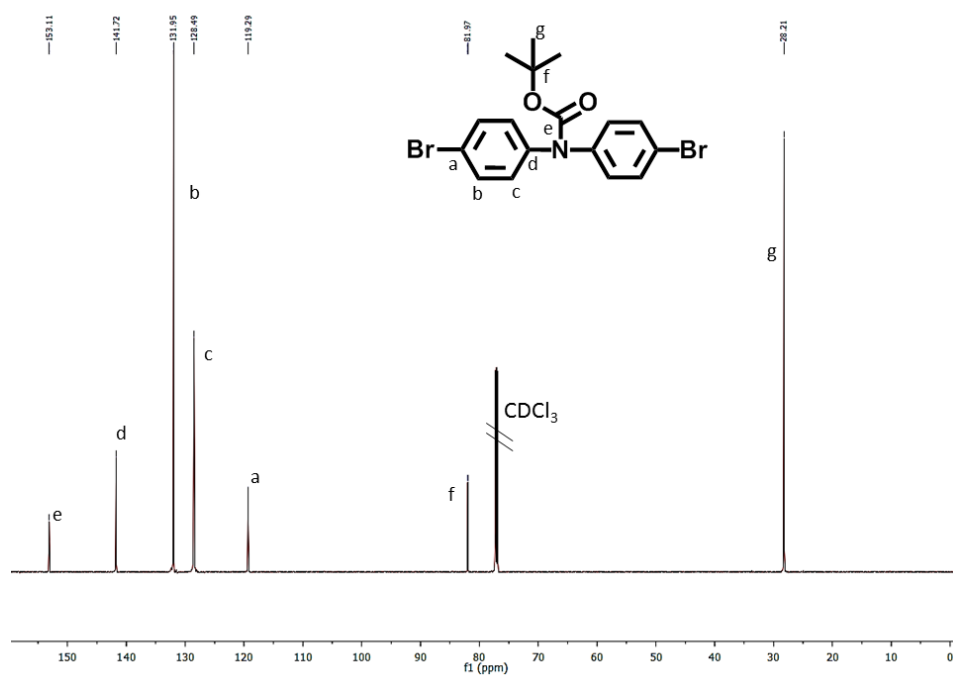


Figure 6.4 ¹³C NMR spectrum of Boc-NPh₂.

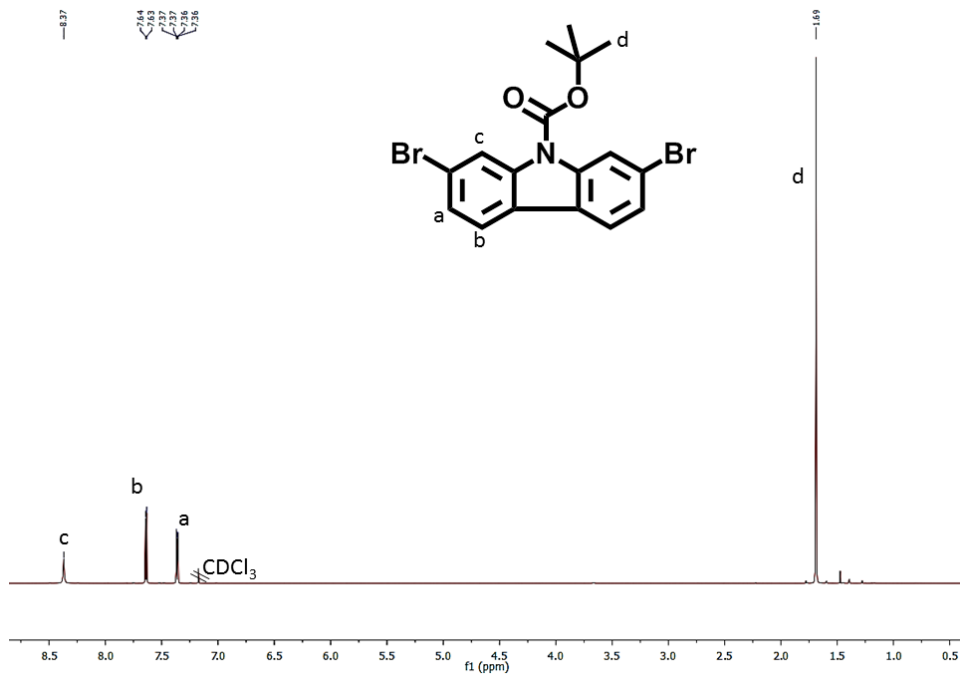


Figure 6.5 ¹H NMR spectrum of Boc-CB.

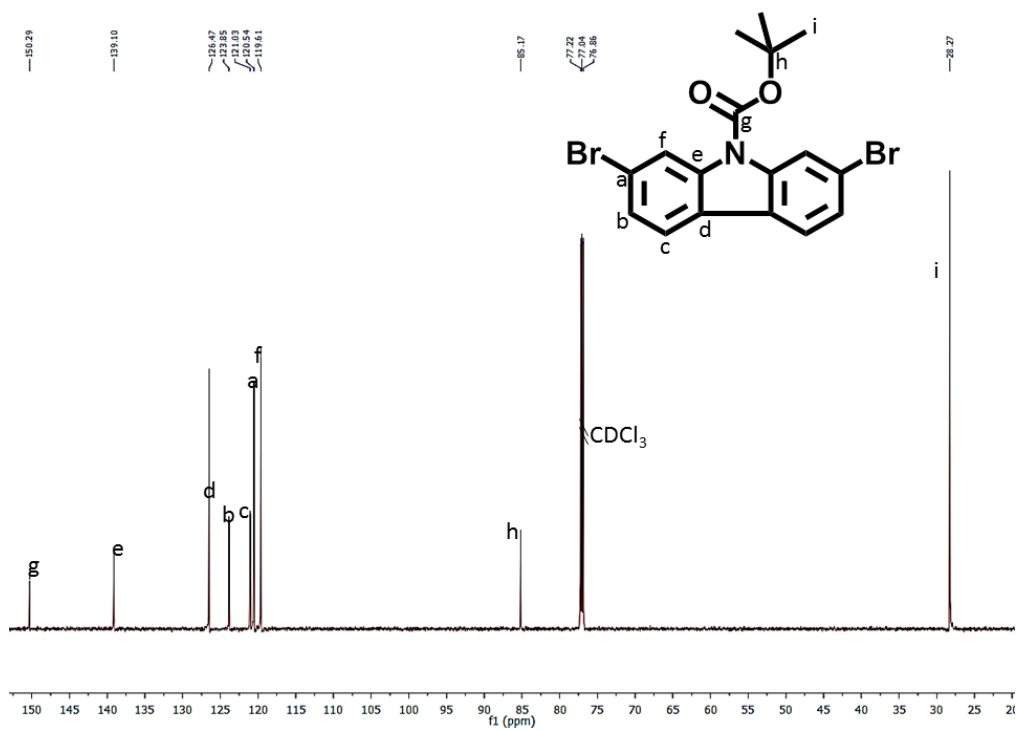


Figure 6.6 ¹³C NMR spectrum of Boc-CB.

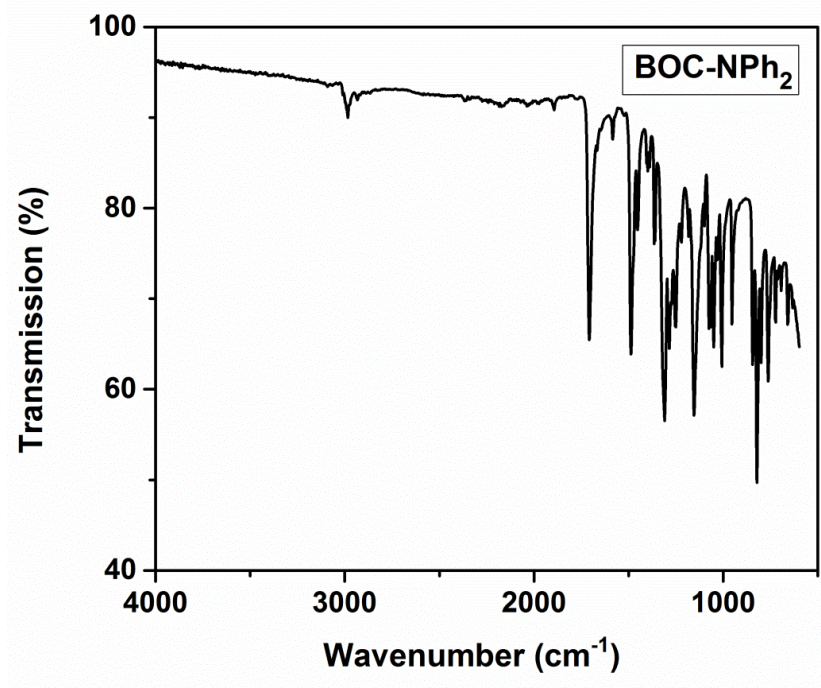


Figure 6.7 FTIR spectrum of BOC-NPh₂.

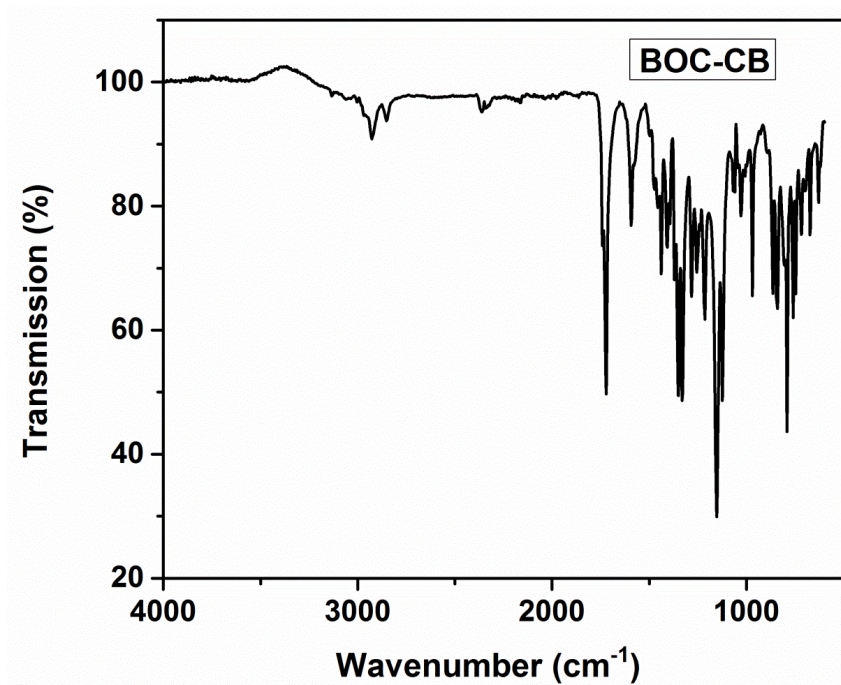


Figure 6.8 FTIR spectrum of BOC-CB.

6.2.1.5 General Procedure for Conjugated Porous Polymer Synthesis via HIPE Polymerization

To 1 equivalent of 1,3,5-Phenyltriboronic acid (PB), 1.5 equivalent of dibromo-compound (CB, NPh₂ or BT), 5 mol% of tetrakis (triphenylphosphine) palladium(0) and 100 mg of Span® 80 were dissolved in 1 mL of toluene. 6 equivalent of K₂CO₃ was dissolved in 9 mL of Milli-Q water. Then, the aqueous phase was slowly added to the organic phase under vigorous stirring using an Ultra Turrax® IKA T18 mechanical stirrer at 14000 RPM. After 30 min, the homogeneous mixture became viscous and was heated to 80 °C for 12 h. The resulted polyHIPE monolith was then washed with Milli-Q water several times and extracted with methanol and then dichloromethane in a soxhlet extractor for 24 h. Drying of the polyHIPE was then performed using supercritical CO₂ on a CPD 300 critical point dryer. (Reaction scheme see Figure 5.37).

6.2.2 General Experimental Procedures in the Continuous Flow System

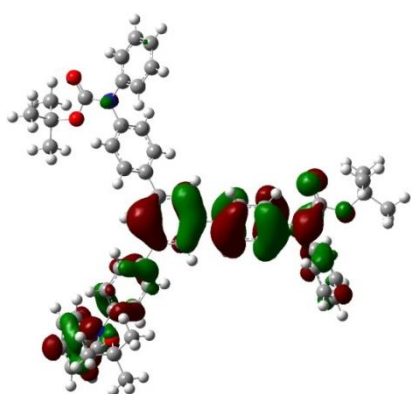
10 mg of conjugated polyHIPE was packed into a transparent glass column (Omnifit, r = 0.35 cm, L = 7 cm) end-capped with two frits, equipped with PTFE-tubing. At a flowrate of 1 mL min⁻¹, 250 mg (2 mmol) of thioanisole (or other derivatives) in 20 mL acetonitrile was pumped through the column continuously for a predetermined time period using a POSTNOVA PN 1610 pump. The column was irradiated with blue light LED lamp (4.5 W cm²) at 460 nm with 1 cm distance to the lamp (OSA Opto Lights). Samples were taken and conversion was determined by ¹H NMR spectroscopy.

6.2.3 Density function theory (DFT) calculations

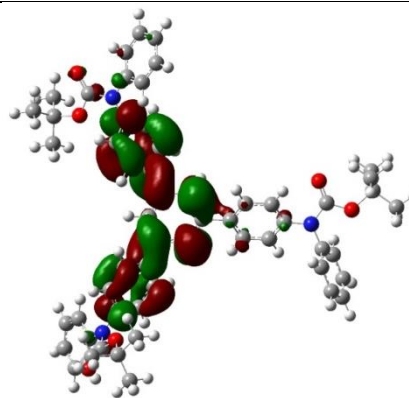
Table 6.1 HOMO-LUMO levels of the polymers calculated with Gaussian 09 using the density function theory RB3LYP/6311G method.

Polymer	HOMO / eV		LUMO / eV		Band gap / eV	
	Star-shaped repeating unit	Ring structure	Star-shaped repeating unit	Ring structure	Star-shaped repeating unit	Ring structure
B-(Boc-NPh ₂) ₃	-5.94	-5.95	-1.28	-1.26	4.66	4.67

B-(NPh₂)₃	-5.22	-5.39	-0.96	-1.16	4.27	4.22
B-(Boc-CB)₃	-5.80	-5.65	-1.38	-1.65	4.43	4.00
B-CB₃	-5.74	-5.63	-1.28	-1.47	4.46	4.17
B-(Boc-CB)₂-BT	-5.83	-5.76	-2.89	-3.10	2.94	2.66
B-CB₂-BT	-5.74	-5.69	-2.99	-3.07	2.76	2.62



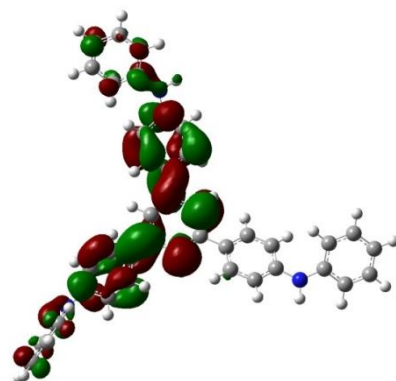
HOMO



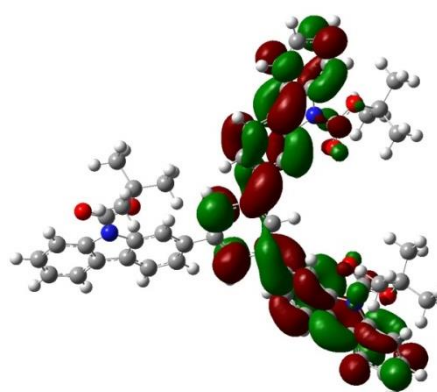
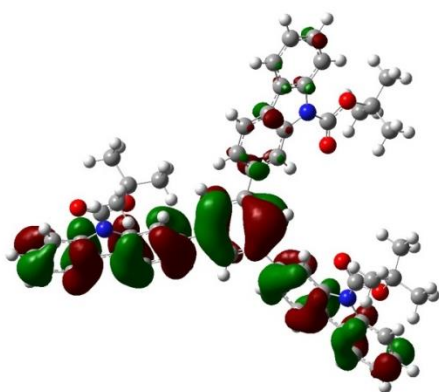
LUMO

B-(Boc-NPh₂)₃

HOMO



LUMO

B-(NPh₂)₃

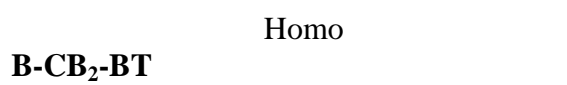
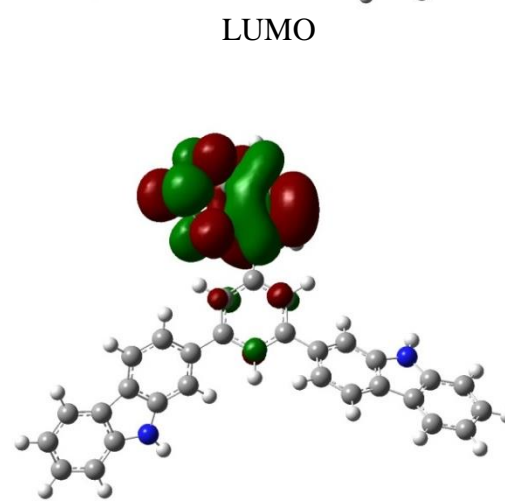
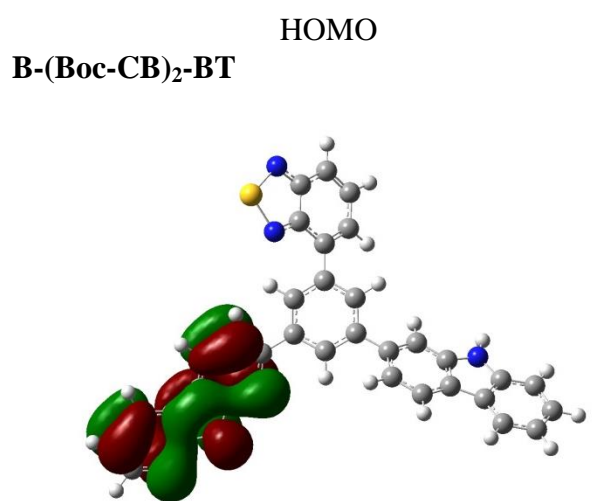
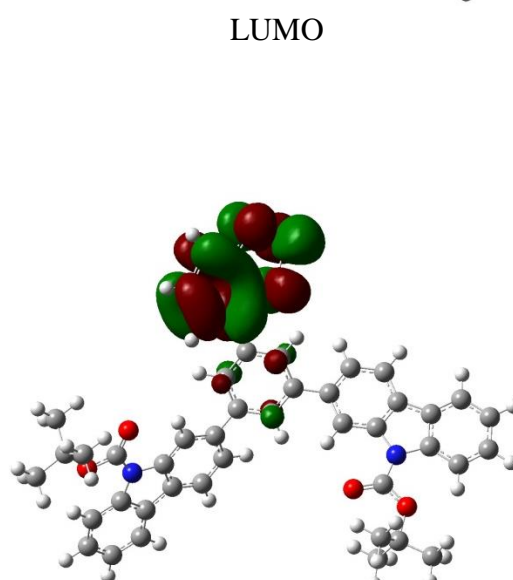
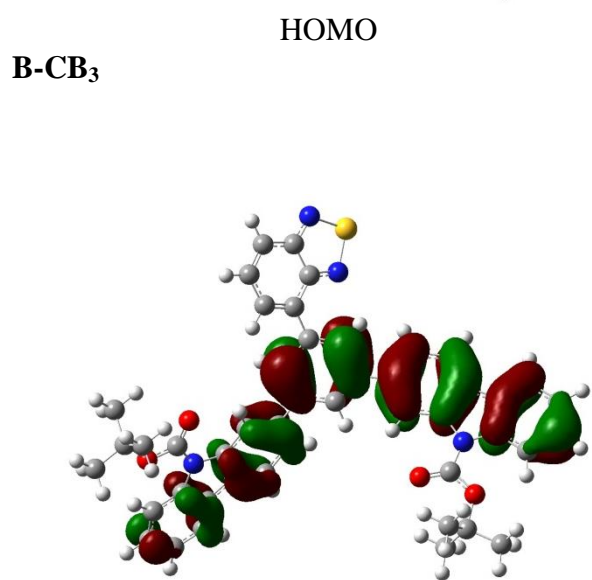
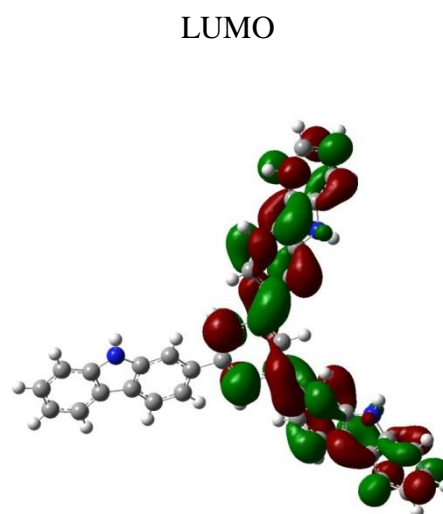
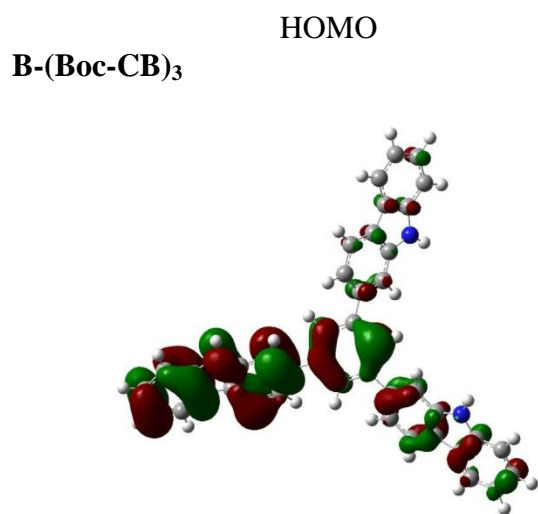
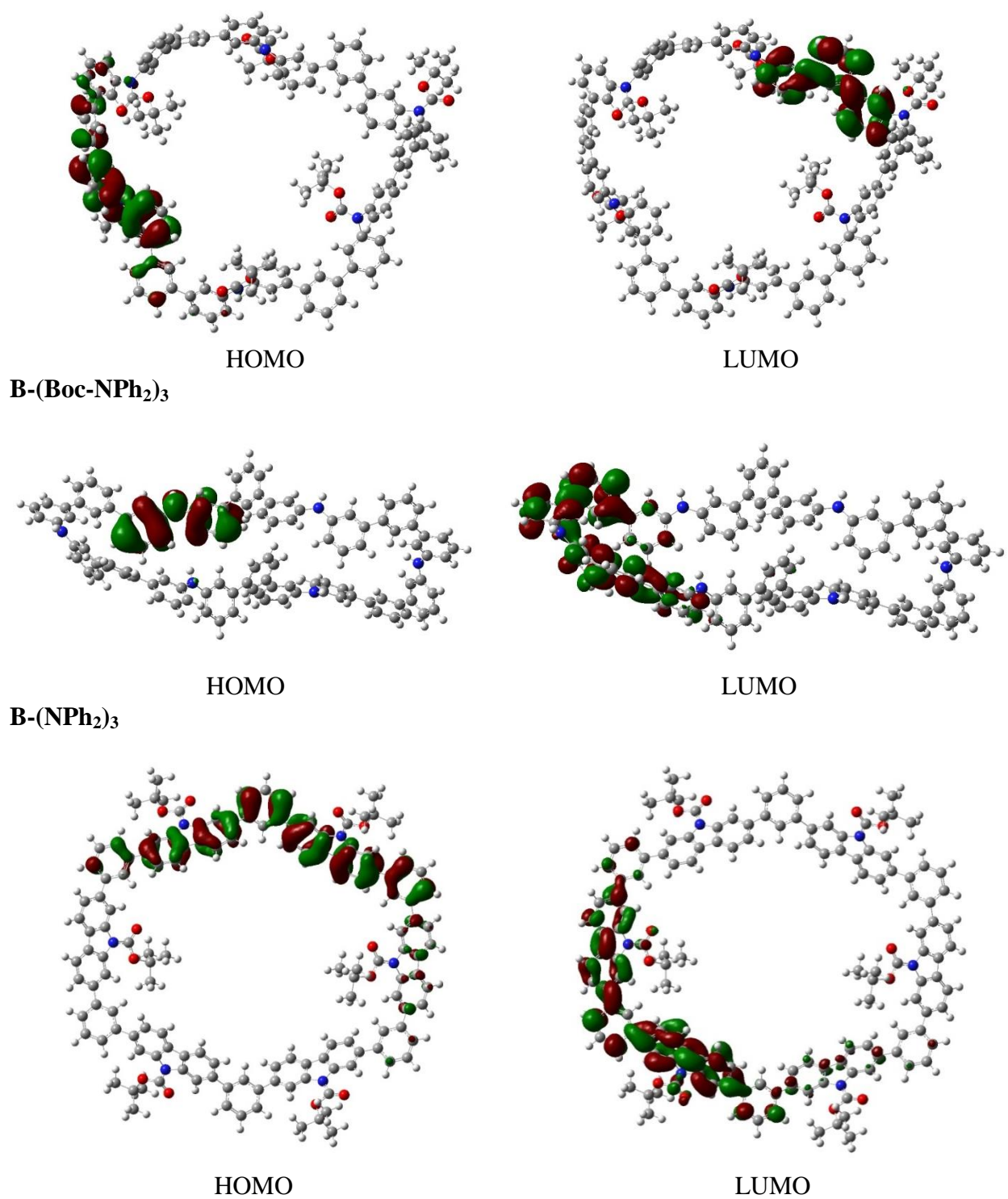
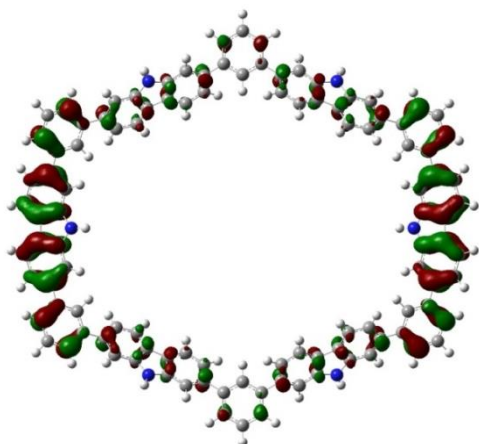


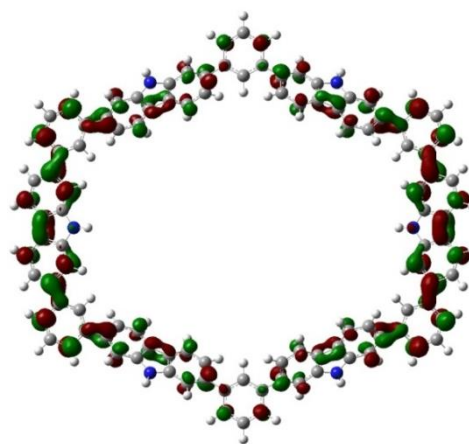
Figure 6.9 HOMO-LUMO band structures of the star-shaped repeating units.



B-(Boc-CB)₃

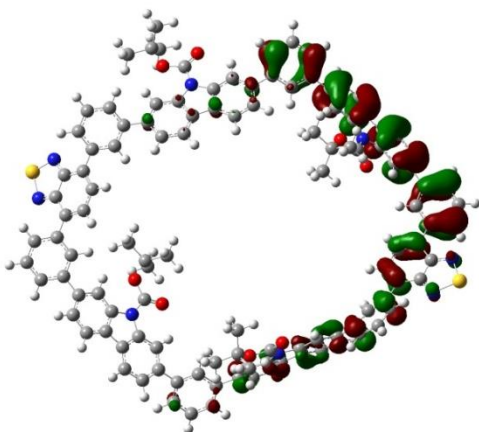


HOMO

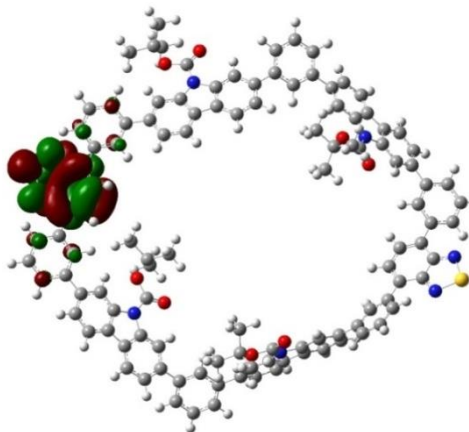


LUMO

B-CB₃

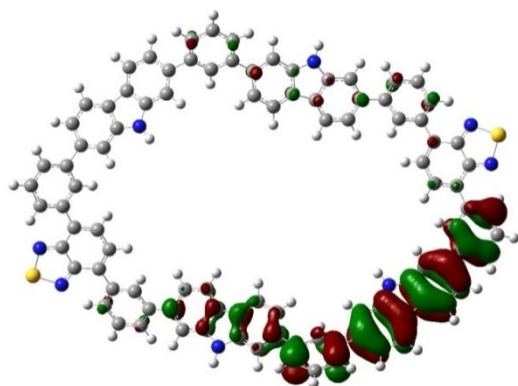


HOMO

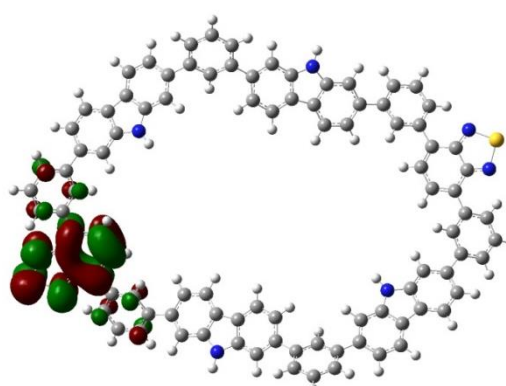


LUMO

B-(Boc-CB)₂-BT



HOMO



LUMO

B-CB₂-BT

Figure 6.10 HOMO-LUMO band structures of the idealized ring structures.

6.2.4 Additional SEM Images of PolyHIPEs

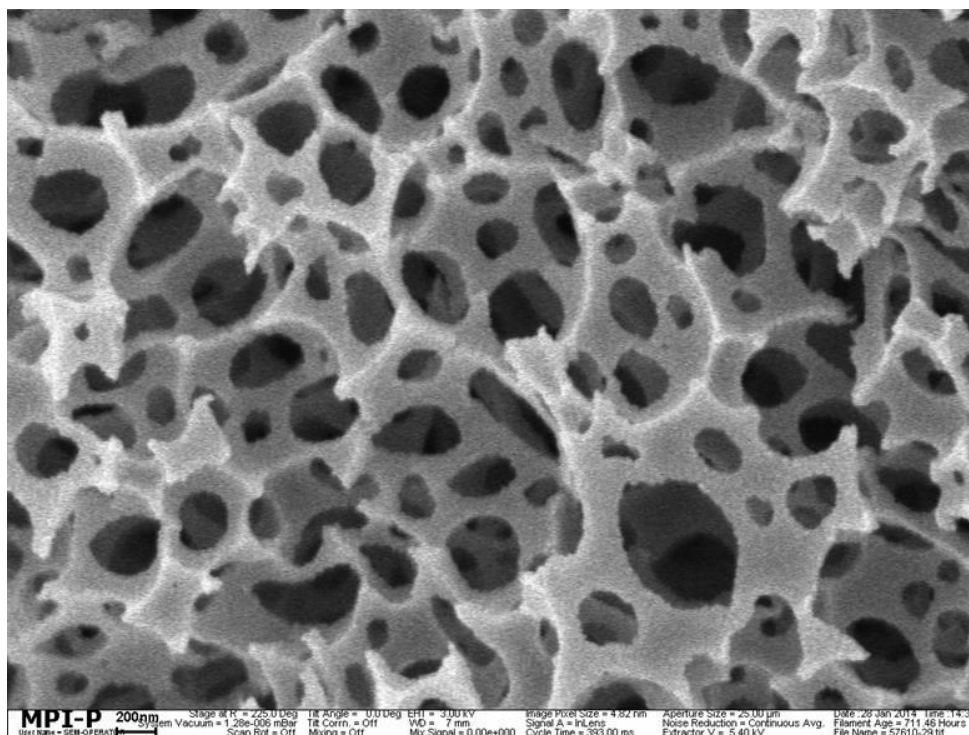
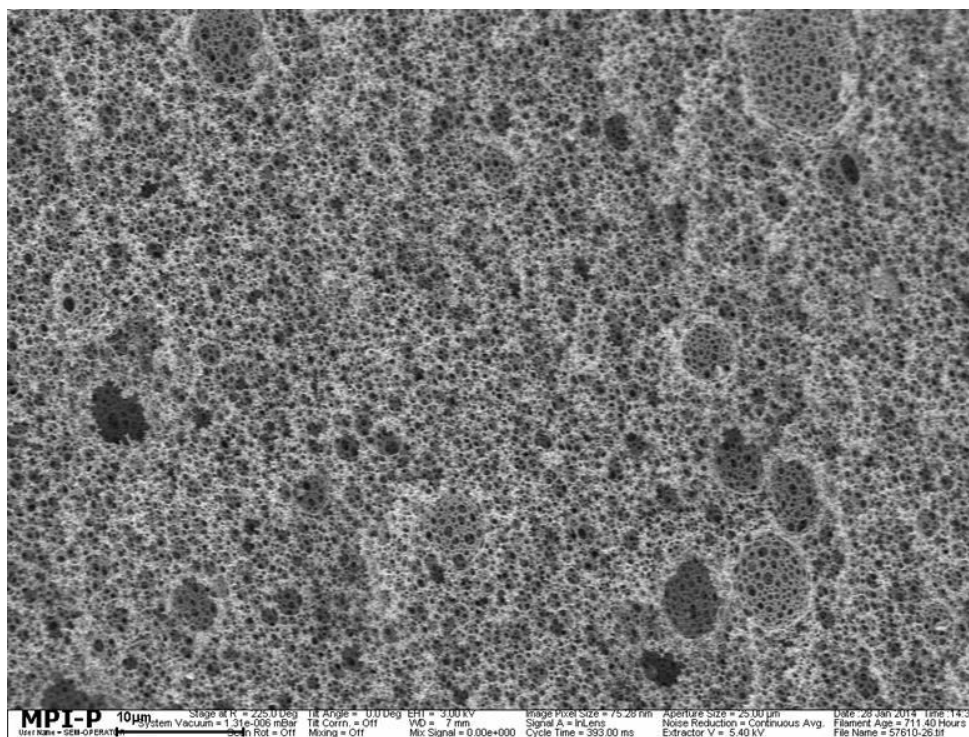


Figure 6.11 SEM images of B-(Boc-NPh₂)₃.

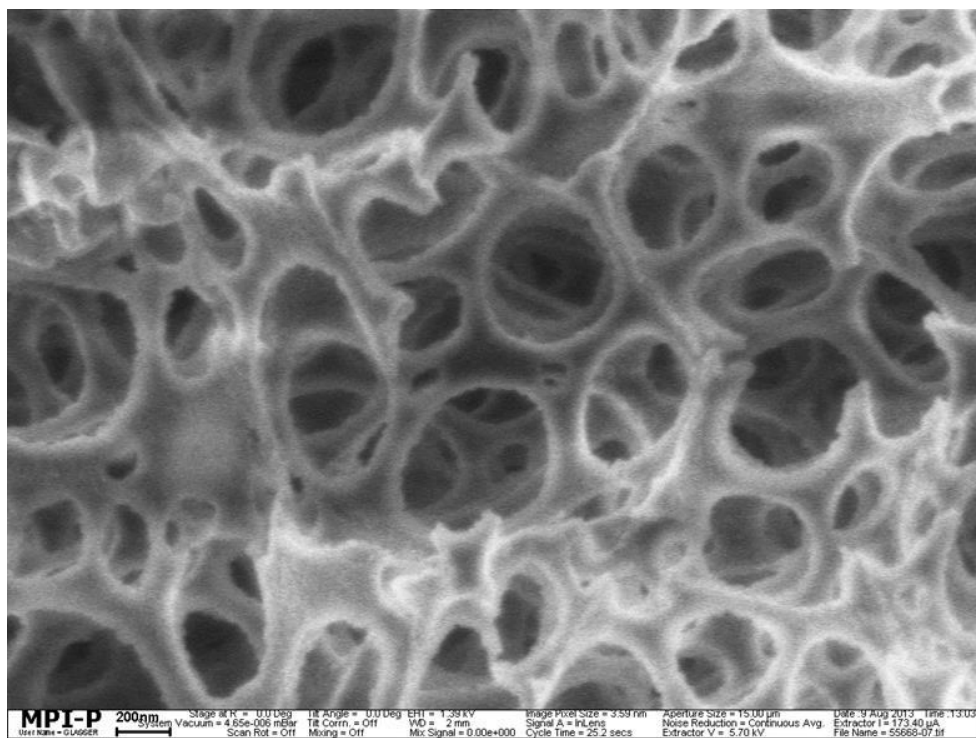
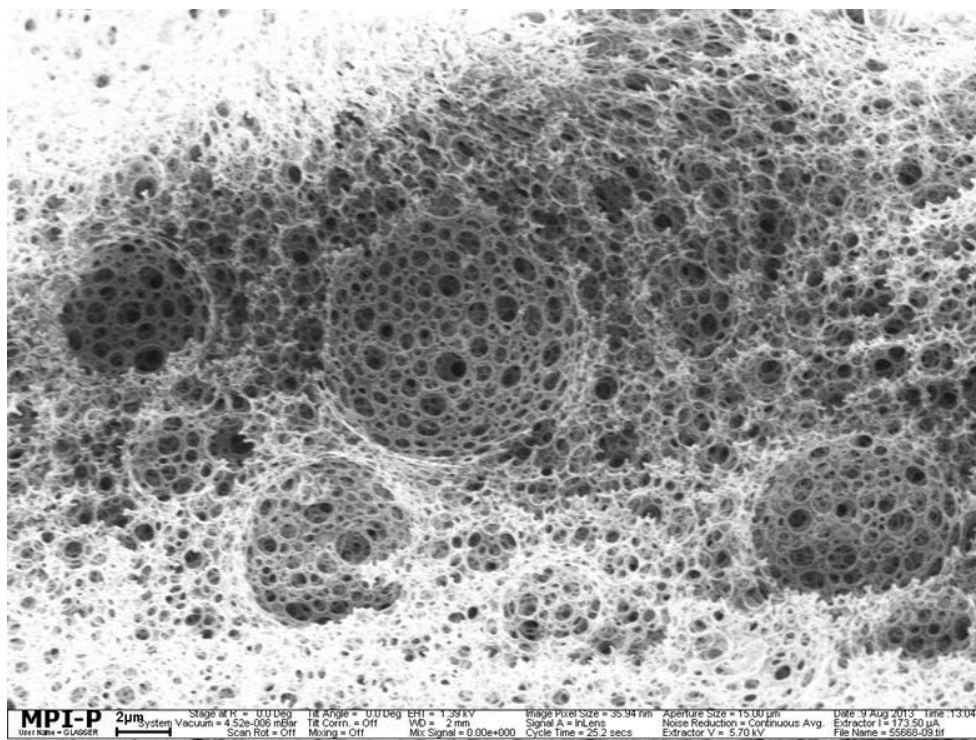


Figure 6.12 SEM images of B-(NPh₂)₃.

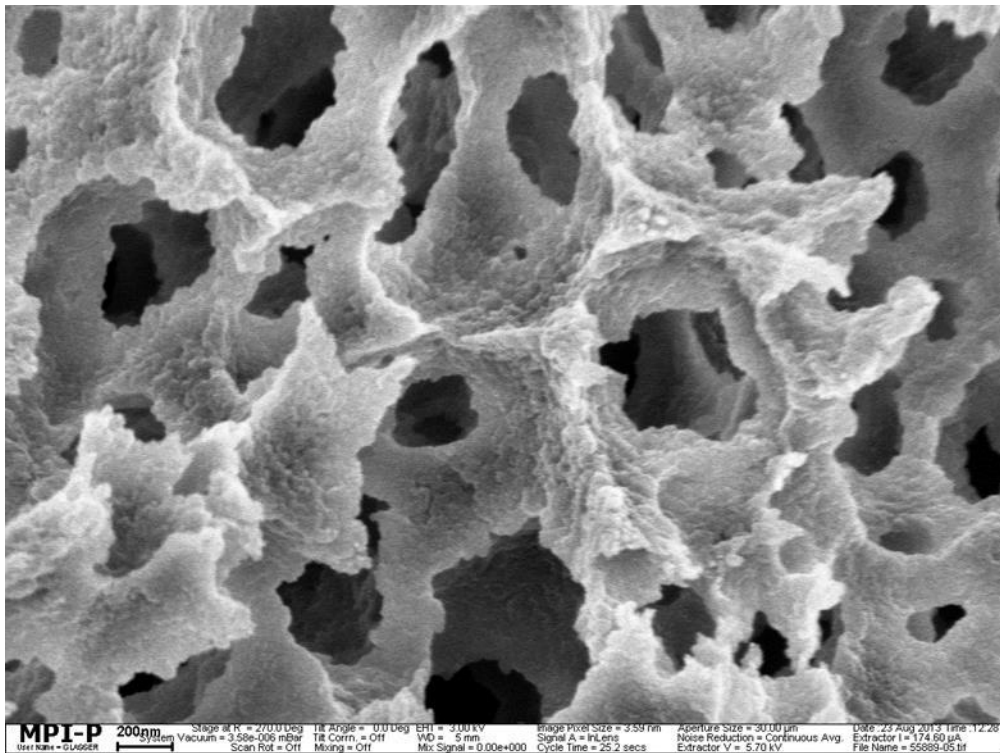
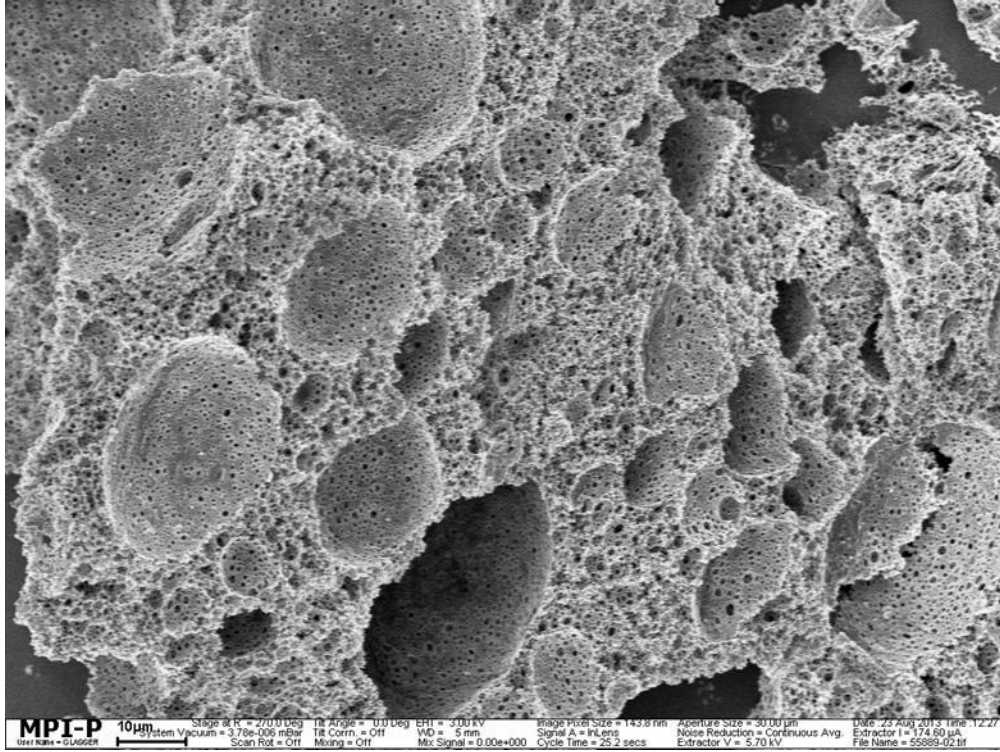


Figure 6.13 SEM images of B-(BOC-CB)₃.

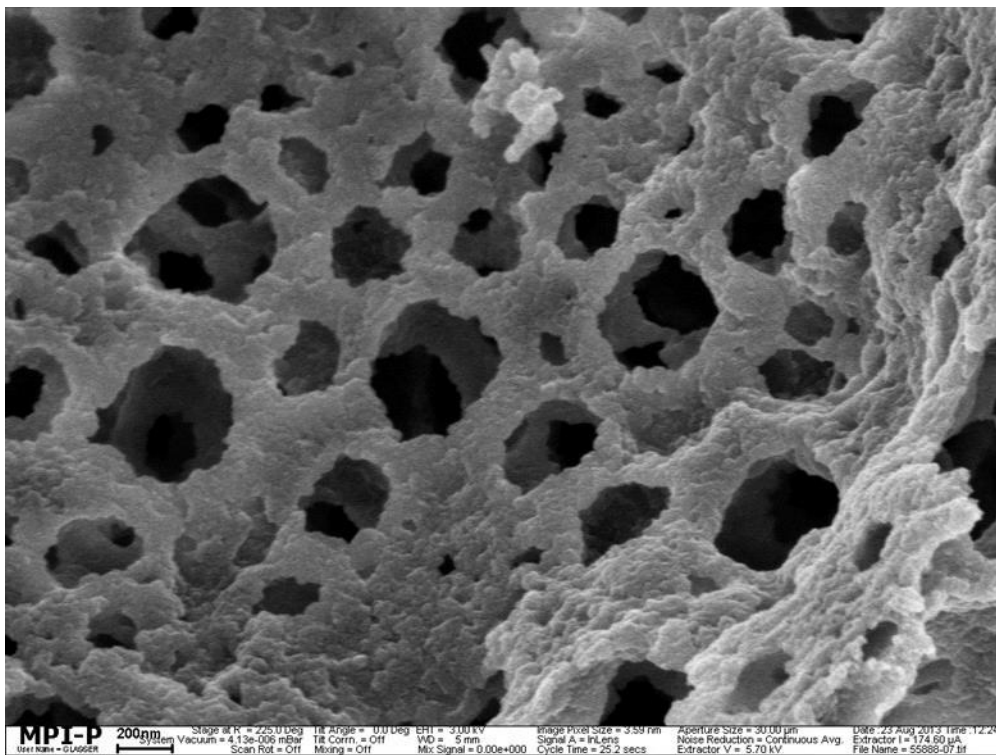
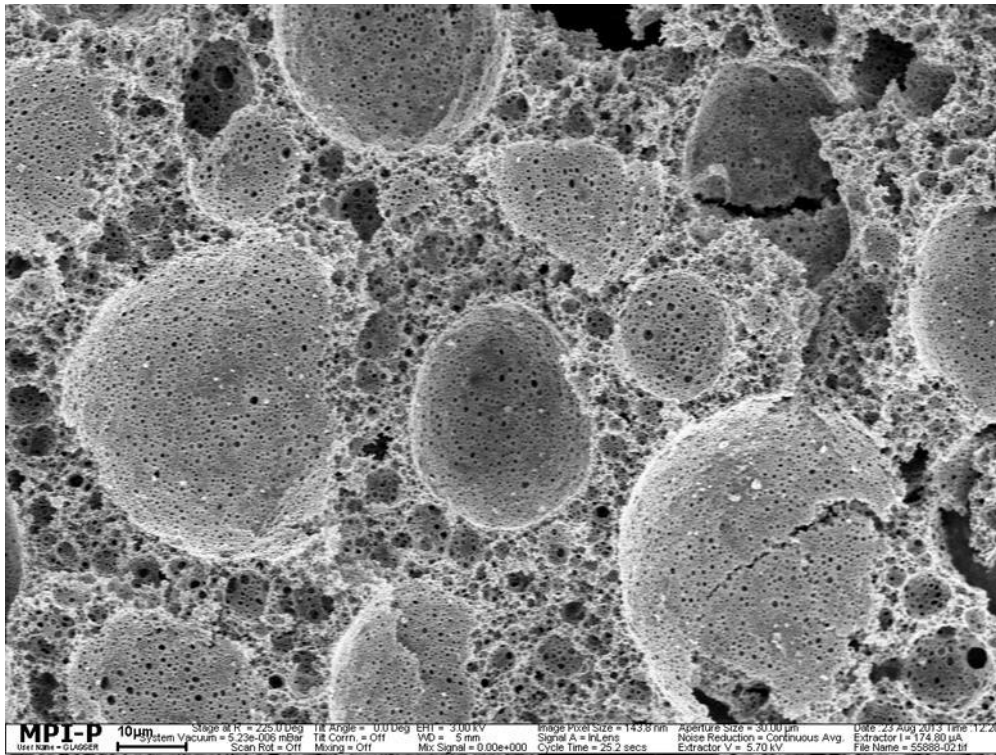


Figure 6.14 SEM images of B-CB₃.

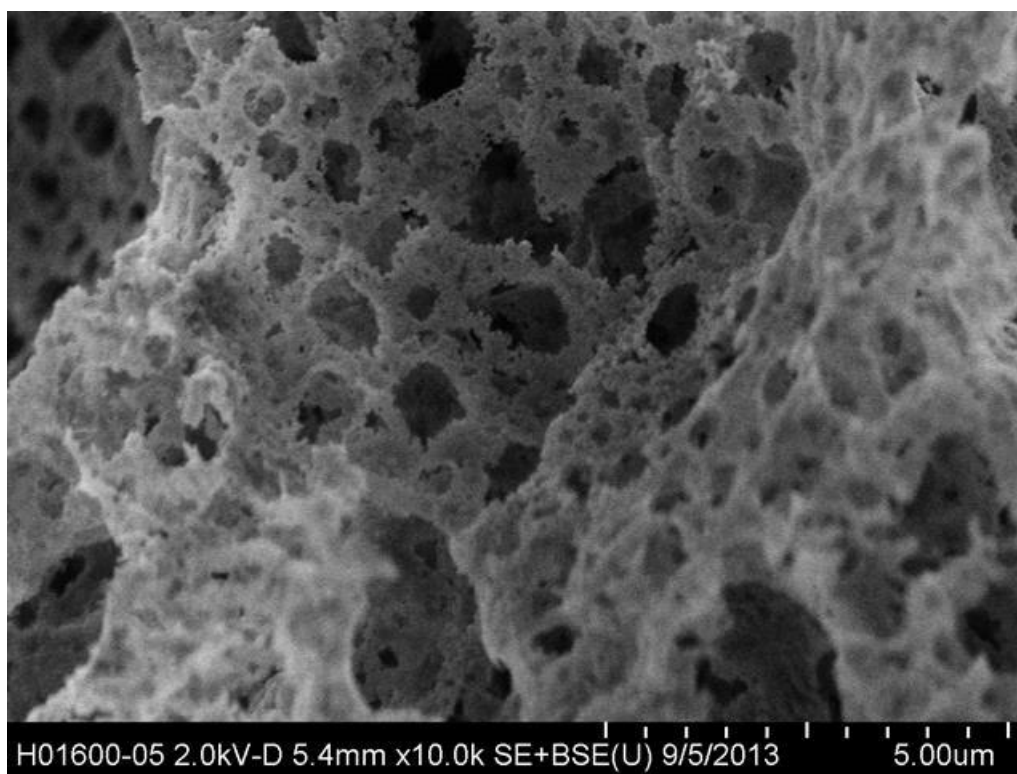
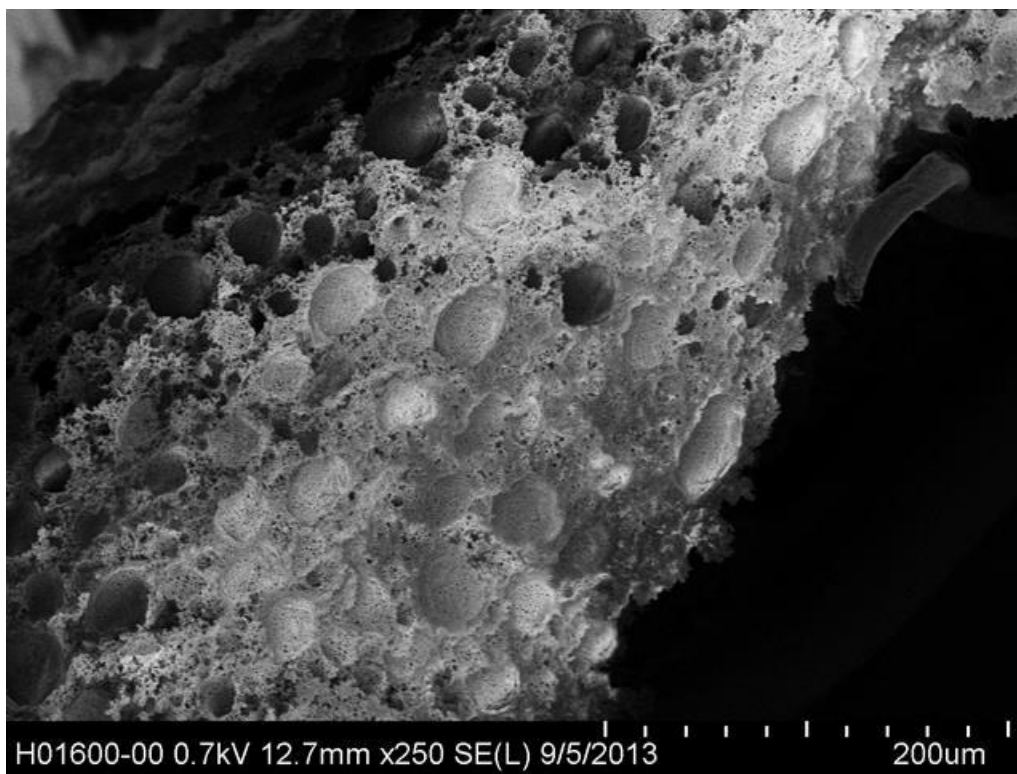


Figure 6.15 SEM images of B-(BOC-CB)₂-BT.

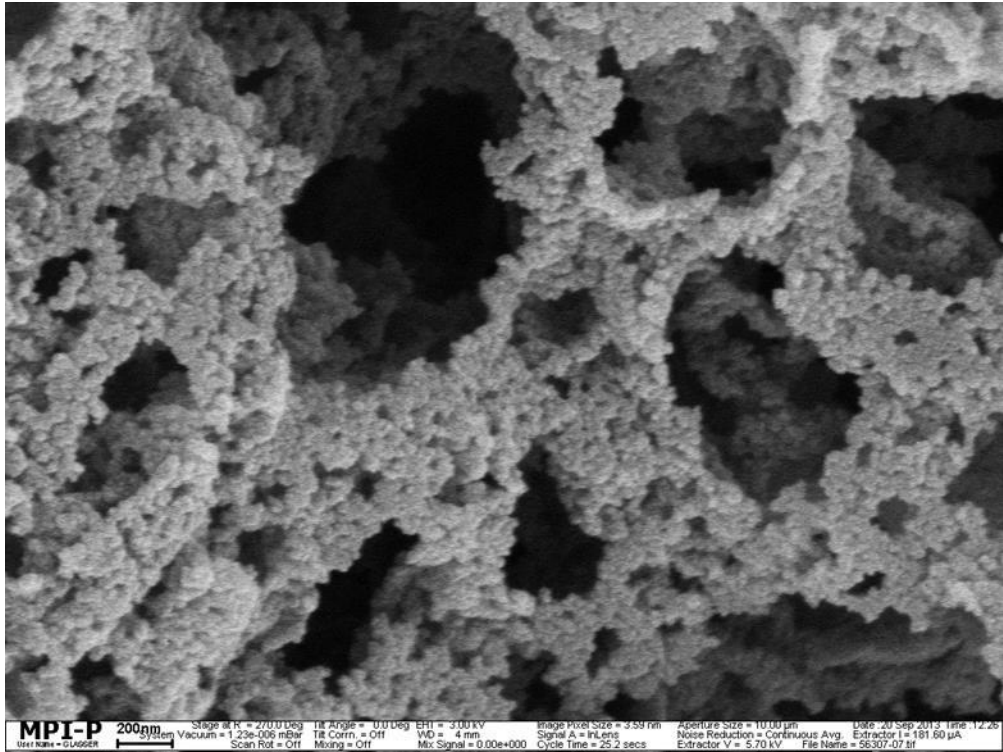
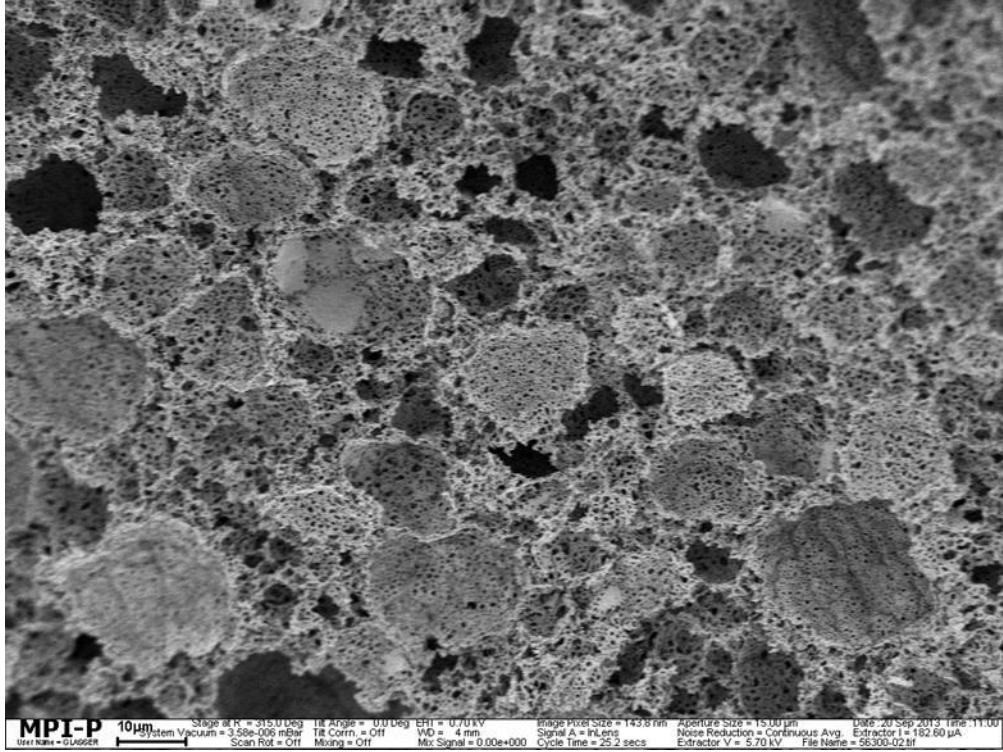


Figure 6.16 SEM images of B-CB₂-BT.

6.3 Chemical Composition Control of Conjugated Porous Polymers

6.3.1 Materials

Di-hexyl-dibromofluorene (99%), tetrakis(triphenylphosphine) palladium(0) (99%), copper (I) iodide (CuI), potassium carbonate (K_2CO_3), Span® 80 nonionic surfactant, 1,3,5-triethynylbenzene (97%), Hantzsch ester, diisopropylethylamine (DIPEA), 2-bromoacetophenone, 2-bromo-4'-fluoroacetophenone, 2-bromo-4'-bromoacetophenone, 2-bromo-4'-cyanoacetophenone, 2-bromo-4'-methylacetophenone, 2-bromo-4'-methoxyacetophenone, 2-bromo-4'-nitroacetophenone and all other solvents were purchased from Aldrich. Dibromo-benzo-bis-thiodiazole (99%) was purchased from Solarmer Materials, Inc. All chemicals and solvents were used as received unless otherwise specified.

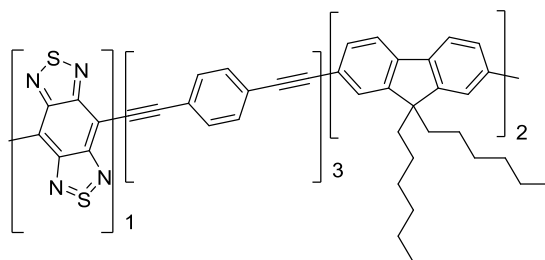
6.3.2 Procedure for the Sonogashira Cross-Coupling Reaction via High Internal Phase Emulsion (HIPE) Polymerization

B₂-FL₂-BBT. To 0.5 mmol (75 mg) of triethynylbenzene, 0.5 mmol (246 mg) di-hexyl-dibromofluorene, 0.25 mmol (88 mg) dibromo-benzo-bis-thiodiazole, 0.025 mmol (29 mg) of tetrakis(triphenylphosphine) palladium(0), 0.02 mmol (5 mg) of CuI and 100 mg of Span® 80 were dissolved in 1 mL of toluene. 414 mg of K_2CO_3 was dissolved in 9 mL of Milli-Q water. Then, the aqueous phase was slowly added to the organic phase under vigorous stirring using an Ultra Turrax® IKA T18 mechanical stirrer at 14000 RPM. After 30 min, the homogeneous mixture became viscous and was heated to 80 °C for 12 h. The resulted monolithic polymer was then washed with Milli-Q water several times and extracted with 50/50 dichloromethane and methanol solution in soxhlet for 24 h. Drying of the polymer was then performed using supercritical CO_2 on a CPD 300 critical point dryer. Elemental analysis: Calculated (based on two repeating units). C, 79.53; H, 6.13; N, 6.68; S, 7.65. Found: C, 66.14; H, 5.24; N, 3.91; S, 5.04. ICP: Cu: 20 ppm, Pd: 15 ppm. (Reaction scheme see Figure 5.53)

B₂-FL₃. To 0.5 mmol (75 mg) of triethynylbenzene, 0.75 mmol (369 mg) di-hexyl-dibromofluorene, 0.025 mmol (29 mg) of tetrakis(triphenylphosphine) palladium(0), 0.02 mmol (5 mg) of CuI and 100 mg of Span® 80 were dissolved in 1 mL of toluene. 414 mg of K_2CO_3 was dissolved in 9 mL of Milli-Q water. Purification of B-FL3 was carried out in the same

procedure as for B-FL2-BBT as described above. Elemental analysis: Calculated: C, 91.45; H, 8.55. Found: C, 89.90; H, 8.13; N, 0.11; S, 0.19. ICP: Cu: 25 ppm, Pd: 20 ppm. (Reaction scheme see Figure 5.53)

6.3.3 Synthesis of the Short Linear Polymer B-FL2-BBT-L



A 25 ml Schlenk tube was filled under nitrogen atmosphere with 70 mg (0.2 mmol, 1eq) dibromobenzothiadiazole, 196 mg(0.4 mmol, 2 eq) 9,9-di-n-hexyl-2,7-dibromofluorene, 76 mg (0.6 mg, 3 eq) 1,4-diethynylbenzene. The starting material was dissolved in a mixture of 2.5 ml dimethylformamid and 2.5 ml triethylamine. Additionally 12 mg (0.01 mmol, 5 mol%) tetrakis(triphenylphosphine)palladium(0) and 9 mg (0.05 mmol, 24 mol%) CuI were added. The mixture was heated for 24 h at 85 °C under constantly stirring. The crude product was dissolved in dichlormethane and washed several times with brine and water. The organic phase was filtered through cellite. The product was concentrated in a rotatory evaporator and precipitated in methanol. Overall the yield for the polymer was 36 mg (15 %). Mn: 2600 Da, PDI: 1.27. ^1H NMR (300 MHz, CDCl_3 , 25 °C): δ 7.66-7.43 (aromatic-H), 1.94-0.78(alkyl-H). Elemental analysis: Cal. C, 84.00; H, 6.23; N, 4.56; S, 5.21. Found: C, 67.14; H, 6.66; N, 0.67; S, 1.53. ICP: Cu: 0.4 ppm, Pd: 0.13 ppm.

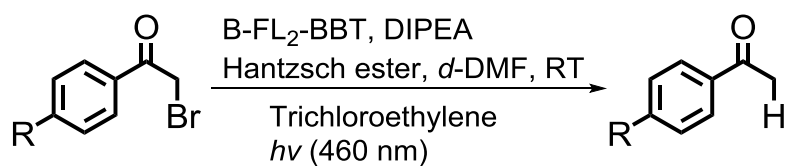
6.3.4 General Procedure for the Photodehalogenation Reaction of α -Bromo acetophene Derivatives

10 mg of B₂-FL₂-BBT, 0.2 mmol of substrate, 0.22 mmol (56 mg) of Hantzsch ester and 0.4 mmol (70 μL) of DIPEA and 0.4 mmol (36 μL) of trichloroethylene (internal standard) were added to 1 mL of deuterated DMF, which was degassed with nitrogen for 5 min. The reaction vial was placed in front of a 23 W household energy saving fluorescent light bulb. Samples were taken and conversions were determined by ^1H NMR using the calibrated internal standard.

6.3.5 Dehalogenation Reaction of α -Bromo-acetophenone using the Linear Polymer as Photocatalyst

5 mg of conjugated linear polymer B-FL₂-BBT-L, 0.1 mmol (20 mg) of α -bromoacetophenone, 0.11 mmol (28 mg) of Hantzsch ester and 0.2 mmol (35 μ L) of DIPEA and 0.2 mmol (18 μ L) of trichloroethylene (internal standard) were added to 0.5 mL of deuterated DMF and then degassed with nitrogen for 2 min. The reaction vial was placed 5 cm in front of a 23 W household energy saving fluorescent light bulb overnight. Samples were taken before and after the reaction for ¹H NMR and UV/Vis measurements.

6.3.6 Apparent Quantum Yield (AQY) Estimation



The apparent quantum yield (AQY) for the dehalogenation of 2-bromoacetophenone was measured using a single wavelength blue LED light source (4.5 W/cm², 460 nm) (OSA Opto Lights). 0.2 mmol of 2-bromoacetophenone, 0.22 mmol of Hantzsch ester, 0.2 mmol of DIPEA and 0.4 mmol of trichloroethylene dissolved in 1 mL of *d*-DMF were added to a glass vial and the irradiation area was controlled at 5.63 cm². After 3 hours, ¹H NMR analysis was conducted (Figure 6.17) and the conversion was calculated by comparing the signal intensity of protons of starting compound (5.0 ppm, 2H, s) and the protons of product (2.82 ppm, 3H, s). A conversion of the dehalogenation reaction of 60% was obtained, which corresponds to an apparent quantum yield (AQY) of 1.2%.

The apparent quantum yield (AQY) was estimated according to the so-called “tried-and-trusted methodology” as the following:²³⁰

$$\text{AQY (\%)} = \frac{\text{number of moles of product obtained}}{\text{number of moles of incident photons}} \times 100$$

wangzijun/95
3h #1 deha

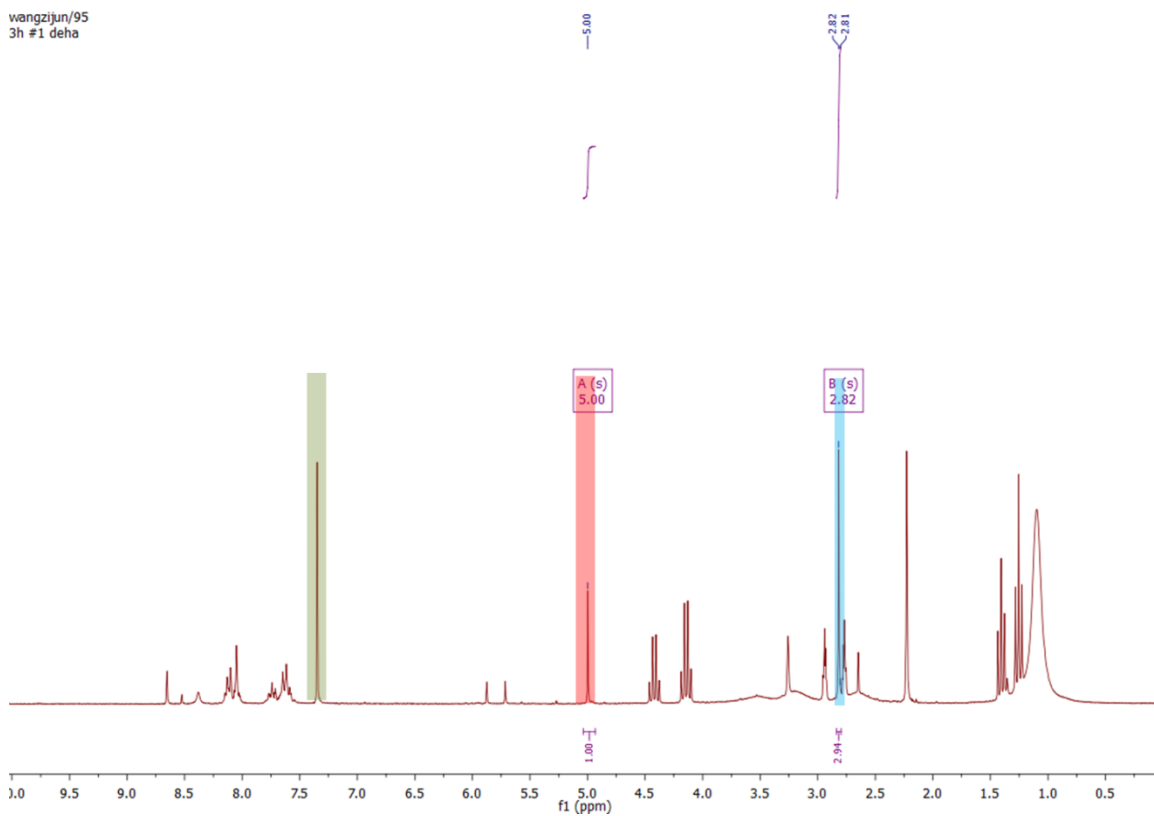


Figure 6.17 ¹H-NMR spectrum for estimation of the apparent quantum yield (AQY) of B₂-FL₂-BBT after a reaction time of 3 h. $\delta = 7.35$ ppm (s, 1H, trichloroethylene), 4.98 ppm (s, 2H, C(O)-CH₂-Br, starting material), 2.80 ppm (s, 3H, C(O)-CH₃, product).

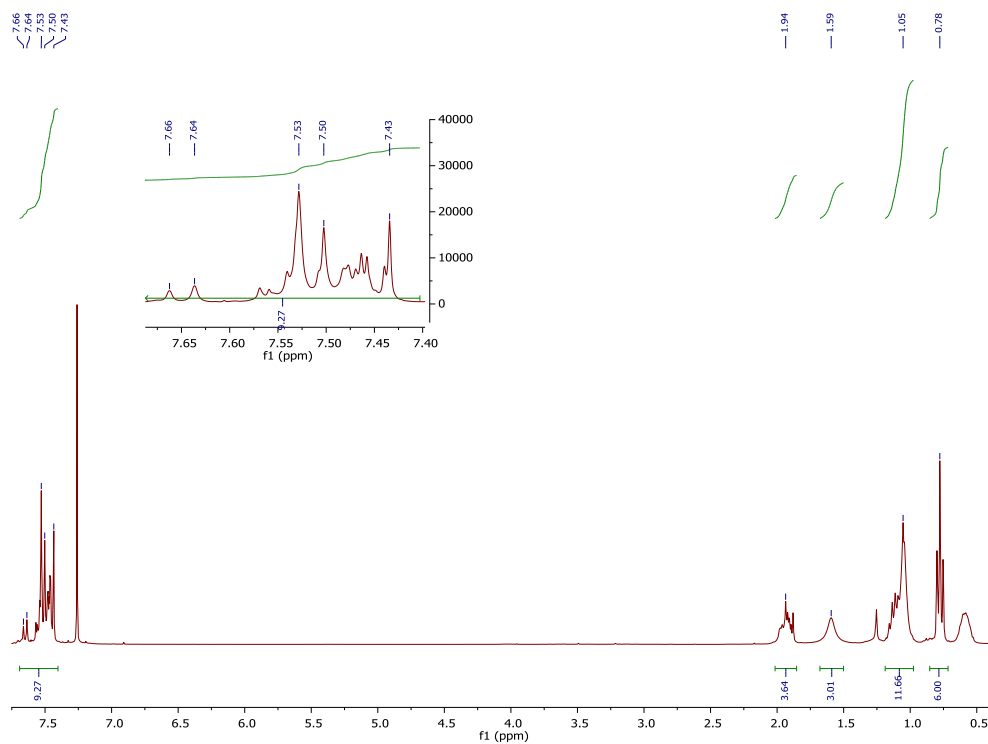


Figure 6.18 ^1H NMR spectrum of the linear polymer $\text{B}_2\text{-FL}_2\text{-BBT-L}$.

6.3.7 Repeating Experiments of Dehalogenation of 2-Bromoacetophenone



Figure 6.19 Simple set-up of the dehalogenation of haloketones a 23 W household energy saving light bulb.

6.4 Conjugated Porous Polymer as Free Radical Photoinitiator

6.4.1 Materials

Benzoxadiazole, 2,7-dibromo-9H-carbazole (CB), tetrakis(triphenylphosphine) palladium(0) (99%), potassium carbonate (K_2CO_3), Span® 80 nonionic surfactant, chloroform-d ($CDCl_3$, 99.8%), dimethylaminopyridine (DMAP) and all other solvents were purchased from Aldrich. 1,3,5-Tribromobenzene and di-*tert*-butyl dicarbonate (di-BOC) were obtained from Alfa Aesar and 1,3,5-Phenyltriboronic acid (PB) (98%) was purchased from Combi-Blocks Inc. Dibromobenzadiazole (BO) was synthesized according to literature.²⁹⁹ All chemicals and solvents were used as received unless otherwise specified.

6.4.2 Synthesis of Boc-CB

0.991 g CB (3.06 mmol), 1.334 g di-BOC (6.11 mmol) and 0.373 g DMAP (3.05 mmol) were dissolved in 50 mL dried THF. The reaction mixture was stirred at room temperature under nitrogen for 12 h. After completion, the reaction mixture was poured into 500 mL of Milli-Q water. The precipitate was then washed with cold methanol and dried under vacuum, yielding 1.18 g (91%) product. (Chemical structure see Figure 6.20).

1H NMR (Figure 6.20): 8.37 (d, 2H), 7.64 (d, 2H), 7.37 (d, 2H), 1.69 (s, 9H)

^{13}C NMR (Figure 6.21): 150.3, 139.1, 126.5, 123.8, 121.0, 120.5, 119.6, 85.2, 28.3

6.4.3 Synthesis of B-(Boc-CB)₂-BO

To 100 mg (0.22 mmol) of PB, 94 mg (0.22 mmol) of BOC-CB, 32 mg (0.11 mmol) of BO, 13 mg (0.011 mmol) of tetrakis(triphenylphosphine) palladium(0) and 100 mg of Span® 80 were dissolved in 1 mL of toluene. 182 mg (1.32 mmol) of K_2CO_3 was dissolved in 9 mL of Milli-Q water. Then, the aqueous phase was slowly added to the organic phase under vigorous stirring using an Ultra Turrax® IKA T18 mechanical stirrer at 14000 RPM. After 30 min, the homogeneous mixture became viscous and was heated to 80 °C for 12 h. The resulted poly(HIPE) was then rinsed with Milli-Q water several times and extracted with 50/50 dichloromethane and methanol solution in a soxhlet for 24 h. Drying of the poly(HIPE) was then performed using supercritical CO_2 (CPD 300 critical point dryer).

6.4.4 Photopolymerization of MMA with B-(BOC-CB)₂-BO

Typical polymerization procedure: In a glass vial, a mixture of MMA (1 mL, 9,39 mmol), B-(BOC-CB)₂-BO (25 mg) and Et₃N (20 mg) were added. The mixture was purged with N₂ for 5 min and the vial was sealed from air. The mixture was then irradiated with a 23 W household energy saving lamp (Osram) for 24 h. After the irradiation, the mixture was dissolved in more THF, the PolyHIPE was filtered off and the product precipitated in methanol. The polymers were collected by filtration and dried under vacuum at 40 °C overnight. The conversions were determined by comparing the integrated peaks corresponding to the vinyl protons ($\delta = 6.09$ and 5.55 ppm) of MMA to the methoxy and methyl group ($\delta = 3.75$ and 1.95) corresponding to the monomers and polymers.

6.4.5 Supplementary Characterization Information

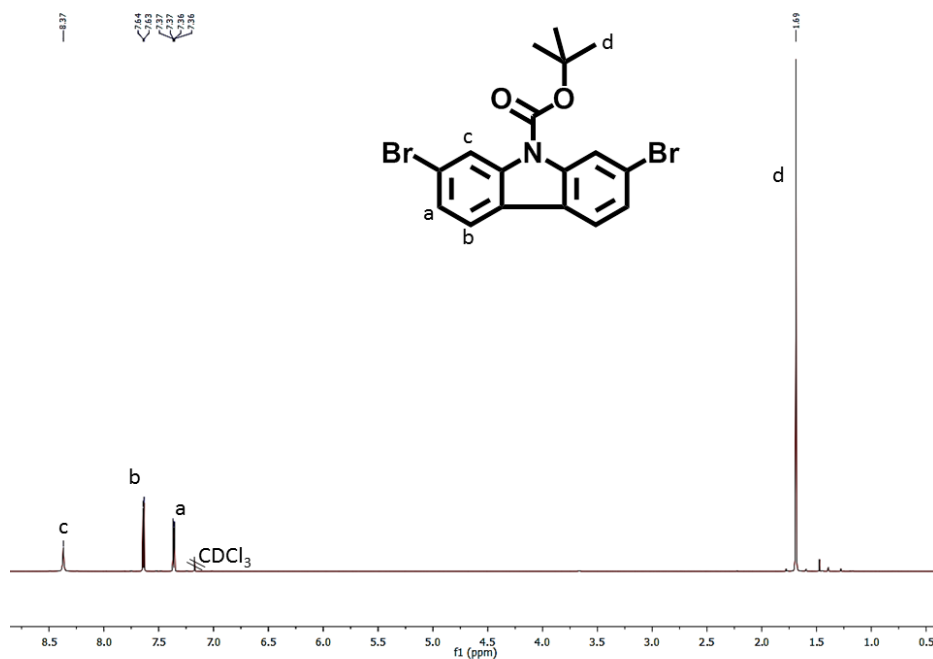


Figure 6.20 ¹H NMR spectrum of BOC-CB.

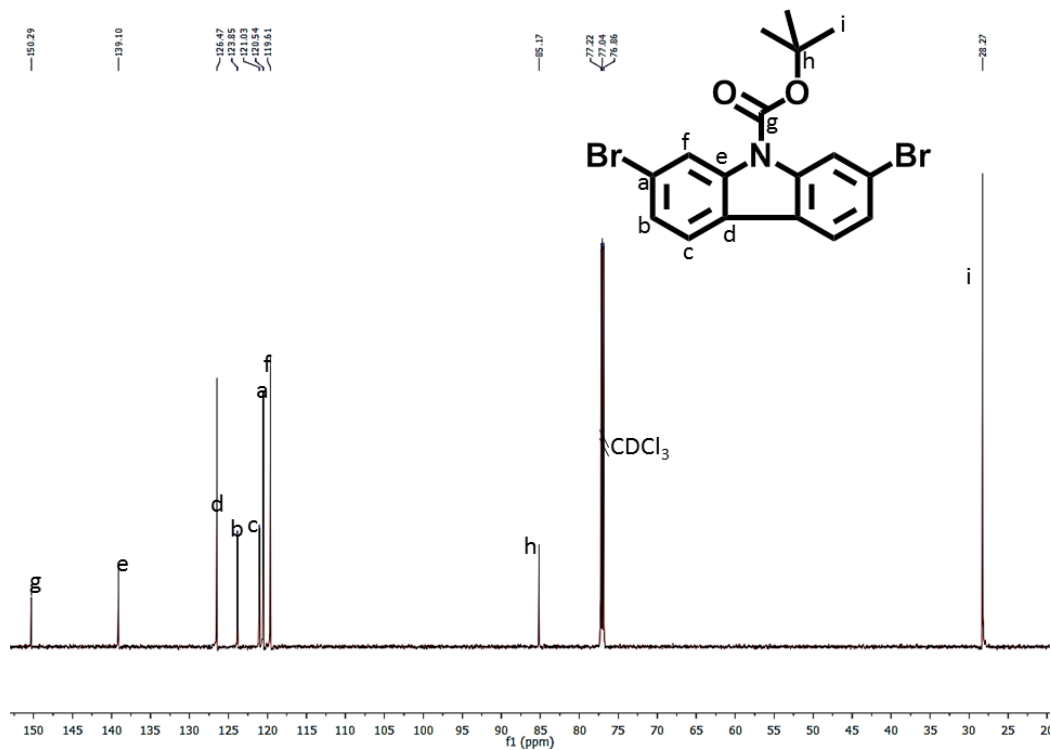


Figure 6.21 ^{13}C NMR spectrum of BOC-CB.



Figure 6.22 A simple photoinitiation set-up using a 23 W household energy saving light bulb.

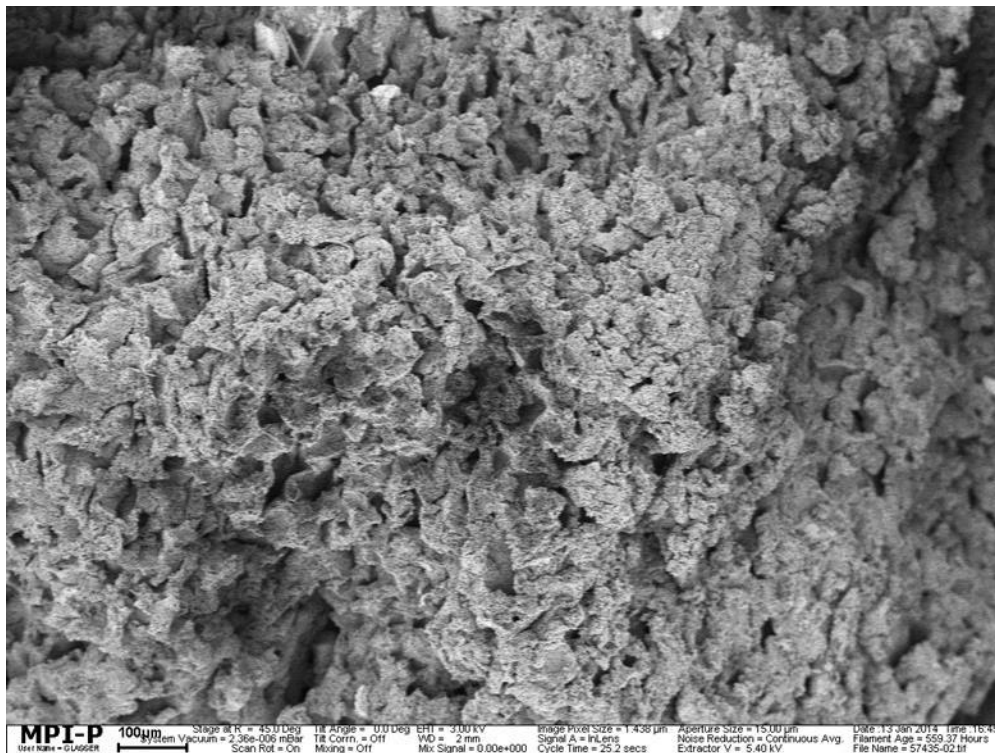


Figure 6.23 SEM image of B-(Boc-CB)₂BO.

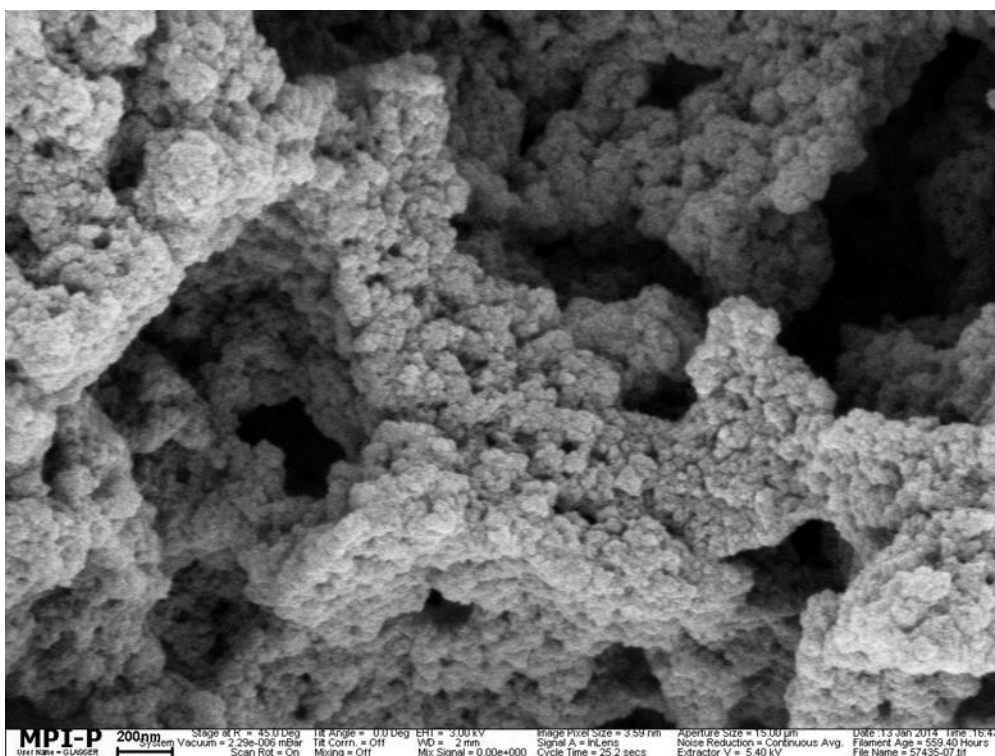


Figure 6.24 SEM image of B-(Boc-CB)₂BO.

6.5 Hybrid Conjugated Porous Polymer with Pd Nanocrystals

6.5.1 Materials

All chemicals and solvents were used as received unless otherwise specified. dibromobenzoxadiazole (dibromo-BO) was synthesized according to literature.²⁹⁷

6.5.2 General procedure for synthesis of end-capped B-BO₃ by Sonogashira cross-coupling reaction

To 1 mmol (150 mg) of triethynylbenzene, 1 mmol (278 mg) dibromo-BO, 0.02 mmol (23 mg) of tetrakis(triphenylphosphine) palladium(0), 0.02 mmol (4 mg) of CuI and 10 mL of Et₃N were dissolved in 10 mL of DMF. After the mixture was degassed with N₂, it was heated to 80 °C for 12 h. The resulted polymer network was then washed with Milli-Q water several times and extracted with 50/50 dichloromethane and methanol solution in soxhlet for 24 h and dried at 50°C under vacuum. A yellowish power was obtained. ICP: Cu: 20 ppm, Pd: 50 ppm. (Chemical structure see Figure 5.83)

Iodobenzene was used as end-capper to react with the residual alkyne bonds. The dried powder of B-BO₃ (200 mg) was redispersed in a mixture of 10 mL DMF and 10 mL Et₃N, and mixed with tetrakis(triphenylphosphine) palladium(0) (25 mg), CuI (4 mg) and excess amount of iodobenzene (204 mg). The reaction was allowed to proceed for 12 h at 80 °C under N₂. After cooling to room temperature, the precipitates were filtered off, washed with DCM and methanol in soxhlet for 24 h and dried in vacuum.

6.5.3 Synthesis of Pd@B-BO₃

The end-capped B-BO₃ (200 mg) was dispersed in water (20 mL) and mixed with acetone solution (5 mL) of Pd(OAc)₂ (70 mg). After stirring at 90 °C for 1 h, the reaction mixture was filtered off, washed with hot water and acetone, dried in vacuum. ICP: Pd: 3 wt%, Cu: 15 ppm

6.5.4 General Procedure for the Suzuki Coupling Reaction by Pd@B-BO₃

Iodobenzene (0.5 mmol), phenylboronic acid (0.55 mmol), K₂CO₃ (0.75 mmol) and 10 mg Pd@B-BO₃ (3 wt% Pd content) were added to 3 mL of DMF/H₂O mixture with a volume ratio of 1:1. The reaction mixture was degassed with N₂ for 5 min and placed 5 cm in front of a white

LED lamp (OSA Opto Lights, 1.2 W/cm²) for a certain period of time. After the reaction, the mixture was filtered to collect the catalyst and the organic phase of the filtrate was extracted twice with DCM and dried over MgSO₄. The pure product was then isolated by silica chromatography. The Pd contents of the photocatalyst after reactions were also monitored by ICP.

6.5.5 Repeating Experiments

After the photocatalysis of Suzuki reaction was performed, the catalyst was filtered, washed, dried and reused for the next cycle. Each cycle followed the general procedure mentioned above.

After the photocatalysis of Suzuki reaction or repeating experiments were performed, the catalyst was filtered, washed, dried and the Pd content was determined by ICP-AES.

6.5.6 Additional SEM and TEM images of Pd@B-BO₃

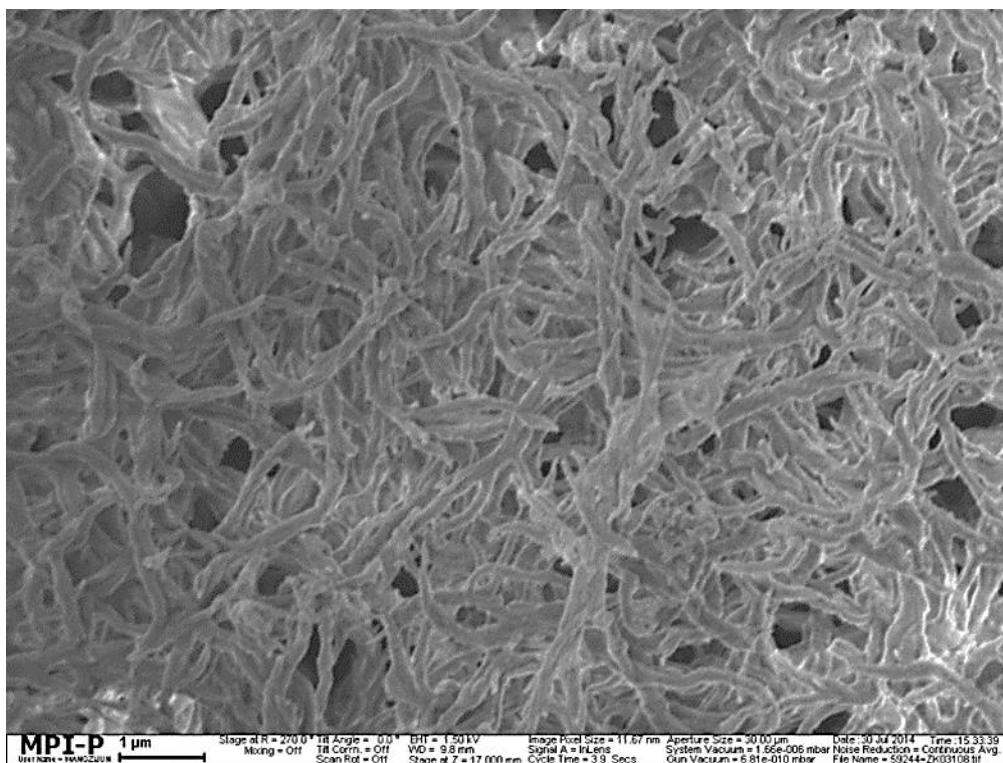


Figure 6.25 SEM image of B-BO₃.

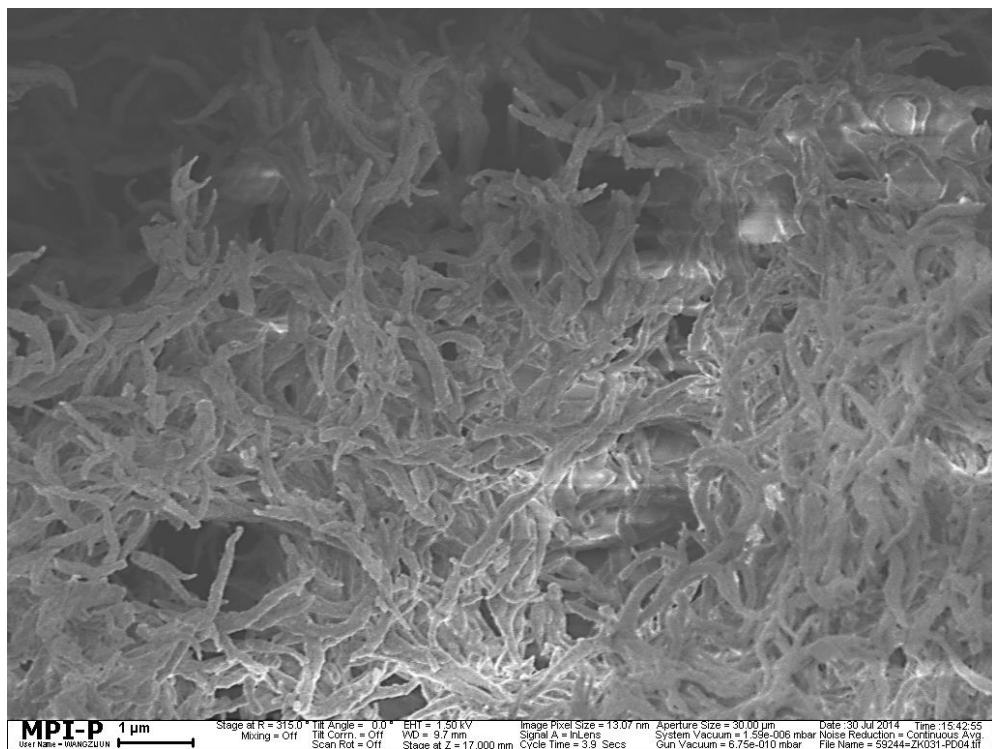


Figure 6.26 SEM image of Pd@B-BO₃.

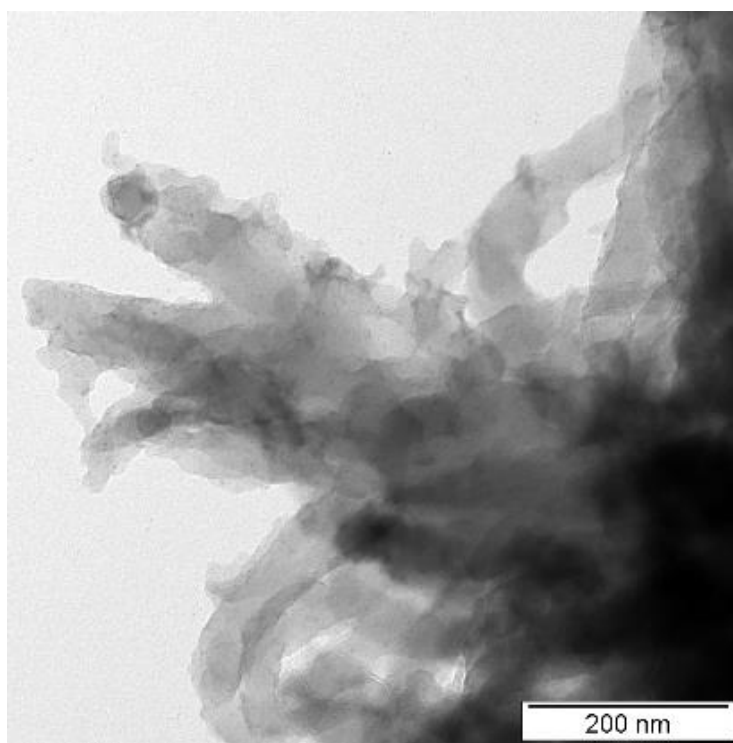


Figure 6.27 TEM images of B-BO₃.

6.5.7 Photocatalytic Reaction Set-up

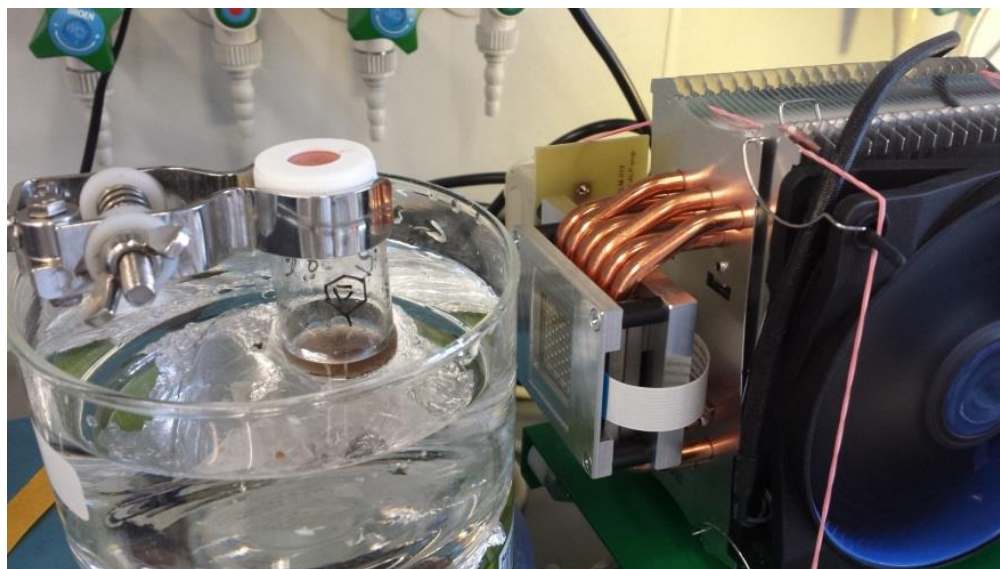


Figure 6.28 The photocatalytic reaction set-up. A water bath was used to avoid the photoheating effect by monitoring the temperature during the reaction.

7 Conclusions

In this thesis, conjugated porous polymers were synthesized and their applications for heterogeneous visible light photocatalysis were explored in depth.

First, conjugated microporous polymer photocatalysts were prepared and the conduction and valance band levels of the polymer series were carefully controlled and fine-adjusted by using different geometric structural design or by altering the chalcogen moieties in the acceptor unit. It was shown that the photocatalyst designed with 1,3,5-substitution positions of the centered phenyl ring and the benzothiadiazole-containing photocatalyst demonstrated the superior photocatalytic activities in the photooxidative coupling of benzylamine and its derivatives.

Next, conjugated polymers with hierachically porous structures were prepared via the high internal phase emulsion polymerization and micropore surface engineering. The thermally cleavable tert-butyl carboxylate group was introduced as spacer into the micropores of the crosslinked polymer network and then subsequently removed by simple heat treatment. The BET surface areas were found to have increased up to eight times and conjugated porous polymers with both micropores and macropores were obtained. Unfortunately, the increased surface area did not lead to enhanced photocatalytic efficiencies in the photooxidation of organic sulfides. This is probably due to the fact that the micropores (~ 1.5 nm) are too small to allow efficient difusion of substrates. Apart from energy level and surface area controls, chemical composition control was also achieved by synthesizing conjugated porous polymers with and without electron-withdrawing acceptor moiety in the conjugated backbones. It was demonstrated that the photocatalyst with incorporated acceptor unit resulted in higher photocatalytic efficiencies of the photoreductive dehalogenation of α -bromoacetophenones. Other than catalyzing organic photoredox reactions, conjugated porous polymer was also shown to be efficient heterogeneous visible light macromolecular photoinitiator for the free radical polymerization of methyl methacrylate at room temperature using a household energy saving light bulb as the light source.

Standing alone, conjugated porous polymers are effective and robust metal free visible light photocatalyst. With immobilized palladium nanocrystals it was found that the hybrid photocatalyst was able to enable the visible light induced Suzuki-Miyaura cross-coupling

reaction at room temperature thanks to the Schottky effect at the metal-semiconductor interface. In addition, the hybrid photocatalyst can be recycled and reused for up to 5 times without significant loss in efficiency.

8 References

- (1) Hornsey, I. S.; Royal Society of Chemistry (Great Britain). *A history of beer and brewing*; Royal Society of Chemistry: Cambridge, UK, 2003.
- (2) Kibria, M. G.; Chowdhury, F. A.; Zhao, S.; AlOtaibi, B.; Trudeau, M. L.; Guo, H.; Mi, Z. *Nat Commun* **2015**, *6*.
- (3) Sun, J.; Zhang, J.; Zhang, M.; Antonietti, M.; Fu, X.; Wang, X. *Nat Commun* **2012**, 1139.
- (4) Wang, X. C.; Maeda, K.; Thomas, A.; Takanabe, K.; Xin, G.; Carlsson, J. M.; Domen, K.; Antonietti, M. *Nat Mater* **2009**, *8*, 76.
- (5) Liu, J.; Liu, Y.; Liu, N. Y.; Han, Y. Z.; Zhang, X.; Huang, H.; Lifshitz, Y.; Lee, S. T.; Zhong, J.; Kang, Z. H. *Science* **2015**, *347*, 970.
- (6) Kudo, A.; Miseki, Y. *Chem Soc Rev* **2009**, *38*, 253.
- (7) Khan, S. U. M.; Al-Shahry, M.; Ingler, W. B. *Science* **2002**, *297*, 2243.
- (8) Chen, X. B.; Shen, S. H.; Guo, L. J.; Mao, S. S. *Chem Rev* **2010**, *110*, 6503.
- (9) Zou, Z. G.; Ye, J. H.; Sayama, K.; Arakawa, H. *Nature* **2001**, *414*, 625.
- (10) Chen, X. B.; Liu, L.; Yu, P. Y.; Mao, S. S. *Science* **2011**, *331*, 746.
- (11) Maeda, K.; Teramura, K.; Lu, D. L.; Takata, T.; Saito, N.; Inoue, Y.; Domen, K. *Nature* **2006**, *440*, 295.
- (12) Gao, X. H.; Bin Wu, H. B.; Zheng, L. X.; Zhong, Y. J.; Hu, Y.; Lou, X. W. *Angew Chem Int Edit* **2014**, *53*, 5917.
- (13) Ghosh, S.; Kouame, N.; Ramos, L.; Remita, S.; Dazzi, A.; Bessearu, A.; Beaunier, P.; Goubard, F.; Aubert, P.; Remita, H. *Nat Mater* **2015**.
- (14) Chen, X. F.; Zhang, J. S.; Fu, X. Z.; Antonietti, M.; Wang, X. C. *J Am Chem Soc* **2009**, *131*, 11658.
- (15) Fukuzumi, S.; Koumitsu, S.; Hironaka, K.; Tanaka, T. *J Am Chem Soc* **1987**, *109*, 305.
- (16) Hirao, T.; Shiori, J.; Okahata, N. *B Chem Soc Jpn* **2004**, *77*, 1763.
- (17) Zhu, M. Z.; Zheng, N. *Synthesis-Stuttgart* **2011**, 2223.
- (18) Tucker, J. W.; Stephenson, C. R. J. *Org Lett* **2011**, *13*, 5468.
- (19) Tucker, J. W.; Nguyen, J. D.; Narayanam, J. M. R.; Krabbe, S. W.; Stephenson, C. R. J. *Chem Commun* **2010**, *46*, 4985.
- (20) Zou, Y. Q.; Chen, J. R.; Liu, X. P.; Lu, L. Q.; Davis, R. L.; Jorgensen, K. A.; Xiao, W. J. *Angew Chem Int Edit* **2012**, *51*, 784.
- (21) Cheng, Y. N.; Yang, J.; Qu, Y.; Li, P. X. *Org Lett* **2012**, *14*, 98.
- (22) Condie, A. G.; Gonzalez-Gomez, J. C.; Stephenson, C. R. J. *J Am Chem Soc* **2010**, *132*, 1464.
- (23) Jiang, J. X.; Su, F.; Trewin, A.; Wood, C. D.; Campbell, N. L.; Niu, H.; Dickinson, C.; Ganin, A. Y.; Rosseinsky, M. J.; Khimyak, Y. Z.; Cooper, A. I. *Angew Chem Int Edit* **2007**, *46*, 8574.
- (24) Yuan, S. W.; Dorney, B.; White, D.; Kirklín, S.; Zapol, P.; Yu, L. P.; Liu, D. J. *Chem Commun* **2010**, *46*, 4547.
- (25) Kuhn, P.; Antonietti, M.; Thomas, A. *Angew Chem Int Edit* **2008**, *47*, 3450.
- (26) Chen, Q.; Luo, M.; Wang, T.; Wang, J. X.; Zhou, D.; Han, Y.; Zhang, C. S.; Yan, C. G.; Han, B. H. *Macromolecules* **2011**, *44*, 5573.
- (27) Li, A.; Lu, R. F.; Wang, Y.; Wang, X.; Han, K. L.; Deng, W. Q. *Angew Chem Int Edit* **2010**, *49*, 3330.
- (28) Xu, C.; Hedin, N. *J Mater Chem A* **2013**, *1*, 3406.
- (29) Pandey, P.; Katsoulidis, A. P.; Eryazici, I.; Wu, Y. Y.; Kanatzidis, M. G.; Nguyen, S. T. *Chem Mater* **2010**, *22*, 4974.

- (30) Ren, S. J.; Bojdys, M. J.; Dawson, R.; Laybourn, A.; Khimyak, Y. Z.; Adams, D. J.; Cooper, A. I. *Adv Mater* **2012**, *24*, 2357.
- (31) Kuhn, P.; Forget, A.; Su, D. S.; Thomas, A.; Antonietti, M. *J Am Chem Soc* **2008**, *130*, 13333.
- (32) Mondal, S. S.; Bhunia, A.; Baburin, I. A.; Jager, C.; Kelling, A.; Schilde, U.; Seifert, G.; Janiak, C.; Holdt, H. J. *Chem Commun* **2013**, *49*, 7599.
- (33) Xu, Y. H.; Chen, L.; Guo, Z. Q.; Nagai, A.; Jiang, D. L. *J Am Chem Soc* **2011**, *133*, 17622.
- (34) Xu, Y. H.; Nagai, A.; Jiang, D. L. *Chem Commun* **2013**, *49*, 1591.
- (35) Gu, C.; Chen, Y. C.; Zhang, Z. B.; Xue, S. F.; Sun, S. H.; Zhang, K.; Zhong, C. M.; Zhang, H. H.; Pan, Y. Y.; Lv, Y.; Yang, Y. Q.; Li, F. H.; Zhang, S. B.; Huang, F.; Ma, Y. G. *Adv Mater* **2013**, *25*, 3443.
- (36) Chen, L.; Honsho, Y.; Seki, S.; Jiang, D. L. *J Am Chem Soc* **2010**, *132*, 6742.
- (37) Kou, Y.; Xu, Y. H.; Guo, Z. Q.; Jiang, D. L. *Angew Chem Int Edit* **2011**, *50*, 8753.
- (38) Sevilla, M.; Alvarez, S.; Centeno, T. A.; Fuertes, A. B.; Stoeckli, F. *Electrochim Acta* **2007**, *52*, 3207.
- (39) Feng, X. L.; Liang, Y. Y.; Zhi, L. J.; Thomas, A.; Wu, D. Q.; Lieberwirth, I.; Kolb, U.; Mullen, K. *Adv Funct Mater* **2009**, *19*, 2125.
- (40) Li, A.; Sun, H. X.; Tan, D. Z.; Fan, W. J.; Wen, S. H.; Qing, X. J.; Li, G. X.; Li, S. Y.; Deng, W. Q. *Energ Environ Sci* **2011**, *4*, 2062.
- (41) Wang, X. S.; Liu, J.; Bonfont, J. M.; Yuan, D. Q.; Thallapally, P. K.; Ma, S. Q. *Chem Commun* **2013**, *49*, 1533.
- (42) Rao, K. V.; Mohapatra, S.; Maji, T. K.; George, S. J. *Chem-Eur J* **2012**, *18*, 4505.
- (43) Zhang, P.; Guo, J.; Wang, C. C. *J Mater Chem* **2012**, *22*, 21426.
- (44) Liu, X. M.; Xu, Y. H.; Jiang, D. L. *J Am Chem Soc* **2012**, *134*, 8738.
- (45) Xiang, Z. H.; Cao, D. P. *Macromol Rapid Comm* **2012**, *33*, 1184.
- (46) Xu, Y. H.; Jin, S. B.; Xu, H.; Nagai, A.; Jiang, D. L. *Chem Soc Rev* **2013**, *42*, 8012.
- (47) Chen, L.; Yang, Y.; Jiang, D. L. *J Am Chem Soc* **2010**, *132*, 9138.
- (48) Chen, L.; Yang, Y.; Guo, Z. Q.; Jiang, D. L. *Adv Mater* **2011**, *23*, 3149.
- (49) Ma, L. Q.; Wanderley, M. M.; Lin, W. B. *Acs Catal* **2011**, *1*, 691.
- (50) Zhang, Y.; Zhang, Y.; Sun, Y. L.; Du, X.; Shi, J. Y.; Wang, W. D.; Wang, W. *Chem-Eur J* **2012**, *18*, 6328.
- (51) Ciamician, G. *Science* **1912**, *36*, 385.
- (52) Plotnikov, I. S. *Photochemie*; W. Knapp: Berlin, 1910.
- (53) Braslavsky, S. E.; Braun, A. M.; Cassano, A. E.; Emeline, A. V.; Litter, M. I.; Palmisano, L.; Parmon, V. N.; Serpone, N.; Alfano, O. M.; Anpo, M.; Augugliaro, V.; Bohne, C.; Esplugas, S.; Oliveros, E.; von Sonntag, C.; Weiss, R. G.; Schiavello, M. *Pure Appl Chem* **2011**, *83*, 931.
- (54) Xuan, J.; Xiao, W. J. *Angew Chem Int Edit* **2012**, *51*, 6828.
- (55) Yoon, T. P. *Acs Catal* **2013**, *3*, 895.
- (56) Yoon, T. P.; Ischay, M. A.; Du, J. N. *Nat Chem* **2010**, *2*, 527.
- (57) Zhang, G.; Kim, G.; Choi, W. *Energ Environ Sci* **2014**, *7*, 954.
- (58) Schultz, D. M.; Yoon, T. P. *Science* **2014**, *343*, 985.
- (59) Prier, C. K.; Rankic, D. A.; MacMillan, D. W. C. *Chem Rev* **2013**, *113*, 5322.
- (60) Narayanam, J. M. R.; Stephenson, C. R. J. *Chem Soc Rev* **2011**, *40*, 102.
- (61) Lang, X. J.; Chen, X. D.; Zhao, J. C. *Chem Soc Rev* **2014**, *43*, 473.
- (62) Kisch, H.; Macyk, W. *Chemphyschem* **2002**, *3*, 399.
- (63) Dagherir, R.; Drogui, P.; Robert, D. *Ind Eng Chem Res* **2013**, *52*, 3581.
- (64) Bingham, S.; Daoud, W. A. *J Mater Chem* **2011**, *21*, 2041.
- (65) Ravelli, D.; Fagnoni, M. *Chemcatchem* **2012**, *4*, 169.
- (66) Neumann, M.; Fuldner, S.; Konig, B.; Zeitler, K. *Angew Chem Int Edit* **2011**, *50*, 951.

- (67) Kalyanasundaram, K. *Coord Chem Rev* **1982**, *46*, 159.
- (68) Campagna, S.; Puntoriero, F.; Nastasi, F.; Bergamini, G.; Balzani, V. *Top Curr Chem* **2007**, *280*, 117.
- (69) McCusker, J. K. *Accounts Chem Res* **2003**, *36*, 876.
- (70) Bock, C. R.; Connor, J. A.; Gutierrez, A. R.; Meyer, T. J.; Whitten, D. G.; Sullivan, B. P.; Nagle, J. K. *J Am Chem Soc* **1979**, *101*, 4815.
- (71) Kim, G.; Choi, W. *Appl Catal B-Environ* **2010**, *100*, 77.
- (72) Parrino, F.; Augugliaro, V.; Camera-Roda, G.; Loddo, V.; Lopez-Munoz, M. J.; Marquez-Alvarez, C.; Palmisano, G.; Palmisano, L.; Puma, M. A. *J Catal* **2012**, *295*, 254.
- (73) Park, Y.; Singh, N. J.; Kim, K. S.; Tachikawa, T.; Majima, T.; Choi, W. *Chem-Eur J* **2009**, *15*, 10843.
- (74) Shishido, T.; Miyatake, T.; Teramura, K.; Hitomi, Y.; Yamashita, H.; Tanaka, T. *J Phys Chem C* **2009**, *113*, 18713.
- (75) Lang, X. J.; Ji, H. W.; Chen, C. C.; Ma, W. H.; Zhao, J. C. *Angew Chem Int Edit* **2011**, *50*, 3934.
- (76) Lang, X. J.; Ma, W. H.; Zhao, Y. B.; Chen, C. C.; Ji, H. W.; Zhao, J. C. *Chem-Eur J* **2012**, *18*, 2624.
- (77) Furukawa, S.; Ohno, Y.; Shishido, T.; Teramura, K.; Tanaka, T. *Acs Catal* **2011**, *1*, 1150.
- (78) Rueping, M.; Zoller, J.; Fabry, D. C.; Poscharny, K.; Koenigs, R. M.; Weirich, T. E.; Mayer, J. *Chem-Eur J* **2012**, *18*, 3478.
- (79) Higashimoto, S.; Kitao, N.; Yoshida, N.; Sakura, T.; Azuma, M.; Ohue, H.; Sakata, Y. *J Catal* **2009**, *266*, 279.
- (80) Li, C. J.; Xu, G. R.; Zhang, B. H.; Gong, J. R. *Appl Catal B-Environ* **2012**, *115*, 201.
- (81) Sarina, S.; Zhu, H. Y.; Zheng, Z. F.; Bottle, S.; Chang, J.; Ke, X. B.; Zhao, J. C.; Huang, Y. N.; Sutrisno, A.; Willans, M.; Li, G. R. *Chem Sci* **2012**, *3*, 2138.
- (82) Linic, S.; Christopher, P.; Ingram, D. B. *Nat Mater* **2011**, *10*, 911.
- (83) Tanaka, A.; Hashimoto, K.; Kominami, H. *Chem Commun* **2011**, *47*, 10446.
- (84) Tanaka, A.; Hashimoto, K.; Kominami, H. *J Am Chem Soc* **2012**, *134*, 14526.
- (85) Sarina, S.; Zhu, H. Y.; Jaatinen, E.; Xiao, Q.; Liu, H. W.; Jia, J. F.; Chen, C.; Zhao, J. *J Am Chem Soc* **2013**, *135*, 5793.
- (86) Sugano, Y.; Shiraishi, Y.; Tsukamoto, D.; Ichikawa, S.; Tanaka, S.; Hirai, T. *Angew Chem Int Edit* **2013**, *52*, 5295.
- (87) Naya, S.; Kimura, K.; Tada, H. *Acs Catal* **2013**, *3*, 10.
- (88) Zhao, J.; Zheng, Z. F.; Bottle, S.; Chou, A.; Sarina, S.; Zhu, H. Y. *Chem Commun* **2013**, *49*, 2676.
- (89) Gonzalez-Bejar, M.; Peters, K.; Hallett-Tapley, G. L.; Grenier, M.; Scaiano, J. C. *Chem Commun* **2013**, *49*, 1732.
- (90) Pineda, A.; Gomez, L.; Balu, A. M.; Sebastian, V.; Ojeda, M.; Arruebo, M.; Romero, A. A.; Santamaria, J.; Luque, R. *Green Chem* **2013**, *15*, 2043.
- (91) Wang, F.; Li, C. H.; Chen, H. J.; Jiang, R. B.; Sun, L. D.; Li, Q.; Wang, J. F.; Yu, J. C.; Yan, C. H. *J Am Chem Soc* **2013**, *135*, 5588.
- (92) Su, F. Z.; Mathew, S. C.; Lipner, G.; Fu, X. Z.; Antonietti, M.; Blechert, S.; Wang, X. C. *J Am Chem Soc* **2010**, *132*, 16299.
- (93) Zheng, Z. S.; Zhou, X. S. *Chinese J Chem* **2012**, *30*, 1683.
- (94) Zhang, P. F.; Wang, Y.; Li, H. R.; Antonietti, M. *Green Chem* **2012**, *14*, 1904.
- (95) Mohlmann, L.; Baar, M.; Riess, J.; Antonietti, M.; Wang, X. C.; Blechert, S. *Adv Synth Catal* **2012**, *354*, 1909.
- (96) Zhu, J. J.; Xiao, P.; Li, H. L.; Carabineiro, S. A. C. *Acs Appl Mater Inter* **2014**, *6*, 16449.

- (97) Zhao, Z. W.; Sun, Y. J.; Dong, F. *Nanoscale* **2015**, *7*, 15.
- (98) Cao, S. W.; Low, J. X.; Yu, J. G.; Jaroniec, M. *Adv Mater* **2015**, *27*, 2150.
- (99) Reineke, S.; Lindner, F.; Schwartz, G.; Seidler, N.; Walzer, K.; Lussem, B.; Leo, K. *Nature* **2009**, *459*, 234.
- (100) Burroughes, J. H.; Bradley, D. D. C.; Brown, A. R.; Marks, R. N.; Mackay, K.; Friend, R. H.; Burn, P. L.; Holmes, A. B. *Nature* **1990**, *347*, 539.
- (101) Sekitani, T.; Nakajima, H.; Maeda, H.; Fukushima, T.; Aida, T.; Hata, K.; Someya, T. *Nat Mater* **2009**, *8*, 494.
- (102) Katz, H. E.; Singer, K. D.; Sohn, J. E.; Dirk, C. W.; King, L. A.; Gordon, H. M. *J Am Chem Soc* **1987**, *109*, 6561.
- (103) Kajzar, F.; Lee, K. S.; Jen, A. K. Y. *Adv Polym Sci* **2003**, *161*, 1.
- (104) Li, G.; Shrotriya, V.; Huang, J. S.; Yao, Y.; Moriarty, T.; Emery, K.; Yang, Y. *Nat Mater* **2005**, *4*, 864.
- (105) Bronstein, H.; Chen, Z. Y.; Ashraf, R. S.; Zhang, W. M.; Du, J. P.; Durrant, J. R.; Tuladhar, P. S.; Song, K.; Watkins, S. E.; Geerts, Y.; Wienk, M. M.; Janssen, R. A. J.; Anthopoulos, T.; Siringhaus, H.; Heeney, M.; McCulloch, I. *J Am Chem Soc* **2011**, *133*, 3272.
- (106) Siringhaus, H. *Adv Mater* **2005**, *17*, 2411.
- (107) Muccini, M. *Nat Mater* **2006**, *5*, 605.
- (108) Wang, Y. Y.; Jing, X. L. *Polym Advan Technol* **2005**, *16*, 344.
- (109) Kim, B. R.; Lee, H. K.; Park, S. H.; Kim, H. K. *Thin Solid Films* **2011**, *519*, 3492.
- (110) Strobl, G. R. *The Physics of Polymers*; Springer, 2007.
- (111) Zhan, X. W.; Zhu, D. B. *Polym Chem-Uk* **2010**, *1*, 409.
- (112) Park, D. H.; Kim, M. S.; Joo, J. *Chem Soc Rev* **2010**, *39*, 2439.
- (113) Tuncel, D. *Nanoscale* **2011**, *3*, 3545.
- (114) He, M.; Qiu, F.; Lin, Z. Q. *J Mater Chem* **2011**, *21*, 17039.
- (115) Waltman, R. J.; Bargon, J. *Can J Chem* **1986**, *64*, 76.
- (116) Yamamoto, T. *J Organomet Chem* **2002**, *653*, 195.
- (117) Cheng, Y. J.; Luh, T. Y. *J Organomet Chem* **2004**, *689*, 4137.
- (118) Osaka, I.; McCullough, R. D. *Accounts Chem Res* **2008**, *41*, 1202.
- (119) Miyaura, N.; Suzuki, A. *J Chem Soc Chem Comm* **1979**, 866.
- (120) Miyaura, N.; Yamada, K.; Suzuki, A. *Tetrahedron Lett* **1979**, *20*, 3437.
- (121) Matos, K.; Soderquist, J. A. *J Org Chem* **1998**, *63*, 461.
- (122) Kurti, L. C., Barbara *Strategic Applications of Named Reactions in Organic Synthesis*; Elsevier, 2005.
- (123) Sonogashira, K.; Tohda, Y.; Hagihara, N. *Tetrahedron Lett* **1975**, 4467.
- (124) Sonogashira, K.; Yatake, T.; Tohda, Y.; Takahashi, S.; Hagihara, N. *J Chem Soc Chem Comm* **1977**, 291.
- (125) Sonogashira, K.; Takahashi, S.; Hagihara, N. *Macromolecules* **1977**, *10*, 879.
- (126) Sonogashira, K. *J Organomet Chem* **2002**, *653*, 46.
- (127) Pirgulyev, N. S.; Brel, V. K.; Zefirov, N. S.; Stang, P. J. *Tetrahedron* **1999**, *55*, 12377.
- (128) Bohm, V. P. W.; Herrmann, W. A. *Eur J Org Chem* **2000**, 3679.
- (129) Osakada, K.; Yamamoto, T. *Coordin Chem Rev* **2000**, *198*, 379.
- (130) Suzuki, A. *Chem Commun* **2005**, 4759.
- (131) Suzuki, A. *Angew Chem Int Edit* **2011**, *50*, 6722.
- (132) Chen, S. H.; Horvath, R. F.; Joglar, J.; Fisher, M. J.; Danishefsky, S. J. *J Org Chem* **1991**, *56*, 5834.
- (133) Langecker, J.; Rehahn, M. *Macromol Chem Phys* **2008**, *209*, 258.
- (134) Wang, Y. F.; Deng, W.; Liu, L.; Guo, Q. X. *Chinese J Org Chem* **2005**, *25*, 8.

- (135) Chinchilla, R.; Najera, C. *Chem Soc Rev* **2011**, *40*, 5084.
- (136) Liu, C.; Zhang, H.; Shi, W.; Lei, A. W. *Chem Rev* **2011**, *111*, 1780.
- (137) Shi, W.; Liu, C.; Lei, A. W. *Chem Soc Rev* **2011**, *40*, 2761.
- (138) Jin, Y. H.; Zhu, Y. L.; Zhang, W. *Crystengcomm* **2013**, *15*, 1484.
- (139) Cordes, E. H.; Jencks, W. P. *J Am Chem Soc* **1962**, *84*, 832.
- (140) Kotha, S.; Brahmachary, E.; Lahiri, K. *Eur J Org Chem* **2005**, 4741.
- (141) Gevorgyan, V.; Yamamoto, Y. *J Organomet Chem* **1999**, *576*, 232.
- (142) Karami, B.; Khodabakhshi, S. *J Serb Chem Soc* **2011**, *76*, 1191.
- (143) Yamada, M.; Tanaka, Y.; Yoshimoto, Y.; Kuroda, S.; Shimao, I. *B Chem Soc Jpn* **1992**, *65*, 1006.
- (144) McCubbin, J. A.; Krokhin, O. V. *Tetrahedron Lett* **2010**, *51*, 2447.
- (145) Hayashi, M.; Nakayama, S.; Kawabata, H. *Chem Commun* **2000**, 1329.
- (146) Tan, D. Z.; Fan, W. J.; Xiong, W. N.; Sun, H. X.; Cheng, Y. Q.; Liu, X. Y.; Meng, C. G.; Li, A.; Deng, W. Q. *Macromol Chem Phys* **2012**, *213*, 1435.
- (147) Jiang, J. X.; Su, F.; Trewin, A.; Wood, C. D.; Niu, H.; Jones, J. T. A.; Khimyak, Y. Z.; Cooper, A. I. *J Am Chem Soc* **2008**, *130*, 7710.
- (148) Schmidt, J.; Werner, M.; Thomas, A. *Macromolecules* **2009**, *42*, 4426.
- (149) Vilela, F.; Zhang, K.; Antonietti, M. *Energ Environ Sci* **2012**, *5*, 7819.
- (150) Zhang, K.; Kopetzki, D.; Seeberger, P. H.; Antonietti, M.; Vilela, F. *Angew Chem Int Edit* **2013**, *52*, 1432.
- (151) Urakami, H.; Zhang, K.; Vilela, F. *Chem Commun* **2013**, *49*, 2353.
- (152) Zhang, K.; Vobecka, Z.; Tauer, K.; Antonietti, M.; Vilela, F. *Chem. Commun.* **2013**, *49*, 11158.
- (153) Wang, C. C.; Guo, Y.; Yang, Y.; Chu, S.; Zhou, C. K.; Wang, Y.; Zou, Z. G. *Acs Appl Mater Inter* **2014**, *6*, 4321.
- (154) Zhang, G., Ni, C. Liu, L., Zhao, G., Fina, F., Irvine, J. *J Mater Chem A* **2015**.
- (155) Sprick, R., Jiang, J., Bonillo, B., Ren, S., Ratvijitvech, T., Guiglion, P., Zwijnenburg, M. Adams, D., Cooper, A. *J Am Chem Soc* **2015**.
- (156) Jiang, X.; Wang, P.; Zhao, J. *J Mater Chem A* **2015**, *3*, 7750.
- (157) Jiang, J. X.; Li, Y. Y.; Wu, X. F.; Xiao, J. L.; Adams, D. J.; Cooper, A. I. *Macromolecules* **2013**, *46*, 8779.
- (158) Kang, N.; Park, J. H.; Ko, K. C.; Chun, J.; Kim, E.; Shin, H. W.; Lee, S. M.; Kim, H. J.; Ahn, T. K.; Lee, J. Y.; Son, S. U. *Angew Chem Int Edit* **2013**, *52*, 6228.
- (159) Xiang, Z. H.; Cao, D. P.; Wang, W. C.; Yang, W. T.; Han, B. Y.; Lu, J. M. *J Phys Chem C* **2012**, *116*, 5974.
- (160) El-Kaderi, H. M.; Hunt, J. R.; Mendoza-Cortes, J. L.; Cote, A. P.; Taylor, R. E.; O'Keeffe, M.; Yaghi, O. M. *Science* **2007**, *316*, 268.
- (161) Furukawa, H.; Ko, N.; Go, Y. B.; Aratani, N.; Choi, S. B.; Choi, E.; Yazaydin, A. O.; Snurr, R. Q.; O'Keeffe, M.; Kim, J.; Yaghi, O. M. *Science* **2010**, *329*, 424.
- (162) Liu, X. M.; Xu, Y. H.; Guo, Z. Q.; Nagai, A.; Jiang, D. L. *Chem Commun* **2013**, *49*, 3233.
- (163) Verwey, E. J. W., Overbeek, J. *Theory of Stability of Lyophobic Colloids*; Elsevier: Amsterdam, 1948.
- (164) Derjaguin, B. V., Landau, L. *Acta Physicochim (URSS)* **1941**, *14*.
- (165) Napper, D. H. *Ind Eng Chem Prod Rd* **1970**, *9*, 467.
- (166) Napper, D. H. *J Colloid Interf Sci* **1977**, *58*, 390.
- (167) Horie, K.; Mita, I.; Kambe, H. *J Appl Polym Sci* **1967**, *11*, 57.
- (168) Lissant, K. J. *J Colloid Interf Sci* **1966**, *22*, 462.
- (169) Lissant, K. J.; Mayhan, K. G. *J Colloid Interf Sci* **1973**, *42*, 201.

- (170) Lissant, K. J.; Peace, B. W.; Wu, S. H.; Mayhan, K. G. *J Colloid Interf Sci* **1974**, *47*, 416.
- (171) Yao, C. H.; Qi, L.; Jia, H. Y.; Xin, P. Y.; Yang, G. L.; Chen, Y. *J Mater Chem* **2009**, *19*, 767.
- (172) Mert, E. H.; Kaya, M. A.; Yildirim, H. *Des Monomers Polym* **2012**, *15*, 113.
- (173) Moglia, R. S.; Holm, J. L.; Sears, N. A.; Wilson, C. J.; Harrison, D. M.; Cosgriff-Hernandez, E. *Biomacromolecules* **2011**, *12*, 3621.
- (174) Wang, D.; Smith, N. L.; Budd, P. M. *Polym Int* **2005**, *54*, 297.
- (175) Sergienko, A. Y.; Tai, H. W.; Narkis, M.; Silverstein, M. S. *J Appl Polym Sci* **2002**, *84*, 2018.
- (176) Gao, X. T.; Wachs, I. E. *J Phys Chem B* **2000**, *104*, 1261.
- (177) Rossel, R. A. V.; McGlynn, R. N.; McBratney, A. B. *Geoderma* **2006**, *137*, 70.
- (178) Brunauer, S.; Deming, L. S.; Deming, W. E.; Teller, E. *J Am Chem Soc* **1940**, *62*, 1723.
- (179) Sing, K. S. W.; Everett, D. H.; Haul, R. A. W.; Moscou, L.; Pierotti, R. A.; Rouquerol, J.; Siemieniewska, T. *Pure Appl Chem* **1985**, *57*, 603.
- (180) Altschuler, S. A.; Kozyrev, B. M. *Electron Paramagnetic Resonance*; Academic Press: New York, 1964.
- (181) Scholz, F. *Electroanalytical Methods* Springer, 2010.
- (182) Lang, X.; Chen, X.; Zhao, J. *Chem. Soc. Rev.* **2014**, *43*, 473.
- (183) Cuthbertson, J. D.; MacMillan, D. W. *Nature* **2015**, *519*, 74.
- (184) Zuo, Z.; Ahneman, D. T.; Chu, L.; Terrett, J. A.; Doyle, A. G.; MacMillan, D. W. *Science* **2014**, *345*, 437.
- (185) Pirnot, M. T.; Rankic, D. A.; Martin, D. B.; MacMillan, D. W. *Science* **2013**, *339*, 1593.
- (186) Nagib, D. A.; MacMillan, D. W. C. *Nature* **2011**, *480*, 224.
- (187) McNally, A.; Prier, C. K.; MacMillan, D. W. *Science* **2011**, *334*, 1114.
- (188) Du, J. N.; Skubi, K. L.; Schultz, D. M.; Yoon, T. P. *Science* **2014**, *344*, 392.
- (189) Skubi, K. L.; Yoon, T. P. *Nature* **2014**, *515*, 45.
- (190) Nguyen, J. D.; D'Amato, E. M.; Narayanam, J. M. R.; Stephenson, C. R. J. *Nature Chem.* **2012**, *4*, 854.
- (191) Dai, C. H.; Narayanam, J. M. R.; Stephenson, C. R. J. *Nature Chem.* **2011**, *3*, 140.
- (192) Condie, A. G.; Gonzalez-Gomez, J. C.; Stephenson, C. R. J. *Am. Chem. Soc.* **2010**, *132*, 1464.
- (193) Nguyen, T. M.; Nicewicz, D. A. *J. Am. Chem. Soc.* **2013**, *135*, 9588.
- (194) Nicewicz, D. A.; Nguyen, T. M. *ACS Catal.* **2014**, *4*, 355.
- (195) Neumann, M.; Földner, S.; König, B.; Zeitler, K. *Angewandte Chemie International Edition* **2011**, *50*, 951.
- (196) Yang, W. L.; Zhang, L.; Hu, Y.; Zhong, Y. J.; Wu, H. B.; Lou, X. W. *Angew Chem Int Edit* **2012**, *51*, 11501.
- (197) Yang, J. H.; Wang, D. G.; Han, H. X.; Li, C. *Accounts Chem Res* **2013**, *46*, 1900.
- (198) Choi, J. R.; Tachikawa, T.; Fujitsuka, M.; Majima, T. *Langmuir* **2010**, *26*, 10437.
- (199) Zhang, K.; Kopetzki, D.; Seeberger, P. H.; Antonietti, M.; Vilela, F. *Angew. Chem. Int. Ed.* **2013**, *52*, 1432.
- (200) Terao, J.; Wadahama, A.; Matono, A.; Tada, T.; Watanabe, S.; Seki, S.; Fujihara, T.; Tsuji, Y. *Nature Commun.* **2013**, *4*.
- (201) Su, C.; Acik, M.; Takai, K.; Lu, J.; Hao, S.-j.; Zheng, Y.; Wu, P.; Bao, Q.; Enoki, T.; Chabal, Y. J.; Ping Loh, K. *Nat Commun* **2012**, *3*, 1298.
- (202) Schmidt, J.; Kundu, D. S.; Blechert, S.; Thomas, A. *Chem. Commun.* **2014**, *50*, 3347.
- (203) Su, F.; Mathew, S. C.; Möhlmann, L.; Antonietti, M.; Wang, X.; Blechert, S. *Angew. Chem. Int. Ed.* **2011**, *50*, 657.
- (204) Kang, N.; Park, J. H.; Ko, K. C.; Chun, J.; Kim, E.; Shin, H. W.; Lee, S. M.; Kim, H. J.; Ahn, T. K.; Lee, J. Y.; Son, S. U. *Angew. Chem. Int. Ed.* **2013**, *52*, 6228.

- (205) Bokhari, M.; Carnachan, R. J.; Cameron, N. R.; Przyborski, S. A. *Biochem. Biophys. Res. Commun.* **2007**, *354*, 1095.
- (206) Dizge, N.; Keskinler, B.; Tanriseven, A. *Colloid Surface B* **2008**, *66*, 34.
- (207) Pierre, S. J.; Thies, J. C.; Dureault, A.; Cameron, N. R.; van Hest, J. C. M.; Carette, N.; Michon, T.; Weberskirch, R. *Adv Mater* **2006**, *18*, 1822.
- (208) Su, F.; Bray, C. L.; Tan, B.; Cooper, A. I. *Adv. Mater.* **2008**, *20*, 2663.
- (209) Mert, E. H.; Yildirim, H.; Üzümcü, A. T.; Kavas, H. *React. Funct. Polym.* **2013**, *73*, 175.
- (210) Ottens, M.; Leene, G.; Beenackers, A. A. C. M.; Cameron, N.; Sherrington, D. C. *Industrial & Engineering Chemistry Research* **2000**, *39*, 259.
- (211) Li, W. L.; Zhang, W. J.; Dong, X. Q.; Yan, L. S.; Qi, R. G.; Wang, W. C.; Xie, Z. G.; Jing, X. B. *J Mater Chem* **2012**, *22*, 17445.
- (212) Zhang, K.; Vobecka, Z.; Tauer, K.; Antonietti, M.; Vilela, F. *Chem. Commun.* **2013**, *49*, 11158.
- (213) Saint-Cricq, P.; Pigot, T.; Nicole, L.; Sanchez, C.; Lacombe, S. *Chem. Commun.* **2009**, 5281.
- (214) Sanjuan, A.; Aguirre, G.; Alvaro, M.; Garcia, H. *Appl Catal B-Environ* **1998**, *15*, 247.
- (215) Pulko, I.; Krajnc, P. *Macromol. Rapid Commun.* **2012**, *33*, 1731.
- (216) Kimmins, S. D.; Cameron, N. R. *Adv. Funct. Mater.* **2011**, *21*, 211.
- (217) Barbetta, A.; Dentini, M.; Leandri, L.; Ferraris, G.; Coletta, A.; Bernabei, M. *Reactive & Functional Polymers* **2009**, *69*, 724.
- (218) Schwab, M. G.; Senkovska, I.; Rose, M.; Klein, N.; Koch, M.; Pahnke, J.; Jonschker, G.; Schmitz, B.; Hirscher, M.; Kaskel, S. *Soft Matter* **2009**, *5*, 1055.
- (219) Padwa, A.; Bullock, W. H.; Dyszlewski, A. D. *J. Org. Chem.* **1990**, *55*, 955.
- (220) Fernandez, I.; Khair, N. *Chem. Rev.* **2003**, *103*, 3651.
- (221) Bäckvall, J.-E. *Modern oxidation methods*; 2nd, completely rev. and enlarged ed.; Wiley-VCH: Weinheim, Germany, 2010.
- (222) Kaczorowska, K.; Kolarska, Z.; Mitka, K.; Kowalski, P. *Tetrahedron* **2005**, *61*, 8315.
- (223) Perles, J.; Iglesias, M.; Ruiz-Valero, C.; Snejko, N. *J. Mater. Chem.* **2004**, *14*, 2683.
- (224) Perles, J.; Iglesias, M.; Martin-Luengo, M. A.; Monge, M. A.; Ruiz-Valero, C.; Snejko, N. *Chem. Mater.* **2005**, *17*, 5837.
- (225) Dybtsev, D. N.; Nuzhdin, A. L.; Chun, H.; Bryliakov, K. P.; Talsi, E. P.; Fedin, V. P.; Kim, K. *Angewandte Chemie-International Edition* **2006**, *45*, 916.
- (226) Wang, X. C.; Maeda, K.; Chen, X. F.; Takanabe, K.; Domen, K.; Hou, Y. D.; Fu, X. Z.; Antonietti, M. *J. Am. Chem. Soc.* **2009**, *131*, 1680.
- (227) Chen, Y.; Zhang, J. S.; Zhang, M. W.; Wang, X. C. *Chem Sci* **2013**, *4*, 3244.
- (228) Wang, Z. J.; Ghasimi, S.; Landfester, K.; Zhang, K. A. I. *Chem. Commun.* **2014**, *50*, 8177.
- (229) Wang, Z. J.; Ghasimi, S.; Landfester, K.; Zhang, K. A. I. *Chem. Commun.* **2014**, *50*, 8177.
- (230) Maschmeyer, T.; Che, M. *Angew. Chem. Int. Ed.* **2010**, *49*, 1536.
- (231) Anseth, K. S.; Newman, S. M.; Bowman, C. N. *Biopolymers li* **1995**, *122*, 177.
- (232) Fisher, J. P.; Dean, D.; Engel, P. S.; Mikos, A. G. *Ann Rev Mater Res* **2001**, *31*, 171.
- (233) Kloosterboer, J. G. *Adv. Polym. Sci.* **1988**, *84*, 1.
- (234) Yagci, Y.; Jockusch, S.; Turro, N. J. *Macromolecules* **2010**, *43*, 6245.
- (235) Roffey, C. G. *Photogeneration of Reactive Species for UV Curing*, 1997.
- (236) Juris, A.; Balzani, V.; Barigelletti, F.; Campagna, S.; Belser, P.; Vonzelewsky, A. *Coord. Chem. Rev.* **1988**, *84*, 85.
- (237) Marin, M. L.; Santos-Juanes, L.; Arques, A.; Amat, A. M.; Miranda, M. A. *Chem. Rev.* **2012**, *112*, 1710.
- (238) Liu, H. J.; Feng, W.; Kee, C. W.; Zhao, Y. J.; Leow, D.; Pan, Y. H.; Tan, C. H. *Green Chemistry* **2010**, *12*, 953.

- (239) Lalevee, J.; Tehfe, M. A.; Dumur, F.; Gigmès, D.; Blanchard, N.; Morlet-Savary, F.; Fouassier, J. P. *Acs Macro Letters* **2012**, *1*, 286.
- (240) Jockusch, S.; Timpe, H. J.; Schnabel, W.; Turro, N. J. *J. Phys. Chem. A* **1997**, *101*, 440.
- (241) Ganster, B.; Fischer, U. K.; Moszner, N.; Liska, R. *Macromolecules* **2008**, *41*, 2394.
- (242) Moszner, N.; Fischer, U. K.; Ganster, B.; Liska, R.; Rheinberger, V. *Dent. Mater.* **2008**, *24*, 901.
- (243) Jakubiak, J.; Allonas, X.; Fouassier, J. P.; Sionkowska, A.; Andrzejewska, E.; Linden, L. A.; Rabek, J. F. *Polymer* **2003**, *44*, 5219.
- (244) Degirmenci, M.; Onen, A.; Yagci, Y.; Pappas, S. P. *Polym. Bull.* **2001**, *46*, 443.
- (245) Jakubiak, J.; Rabek, J. F. *Polimery-W* **1999**, *44*, 447.
- (246) Davidenko, N.; Garcia, O.; Sastre, R. *J Biomat Sci-Polym E* **2003**, *14*, 733.
- (247) Gacal, B.; Akat, H.; Balta, D. K.; Arsu, N.; Yagci, Y. *Macromolecules* **2008**, *41*, 2401.
- (248) Temel, G.; Aydogan, B.; Arsu, N.; Yagci, Y. *Macromolecules* **2009**, *42*, 6098.
- (249) Yagci, Y.; Onen, A. *J Macromol Sci Chem* **1991**, *A28*, 25.
- (250) Akat, H.; Gacal, B.; Balta, D. K.; Arsu, N.; Yagci, Y. *J Polym Sci Pol Chem* **2010**, *48*, 2109.
- (251) Kiskan, B.; Antonietti, M.; Weber, J. *Macromolecules* **2012**, *45*, 1356.
- (252) Kiskan, B.; Zhang, J. S.; Wang, X. C.; Antonietti, M.; Yagci, Y. *Acs Macro Letters* **2012**, *1*, 546.
- (253) Kohler, A.; dos Santos, D. A.; Beljonne, D.; Shuai, Z.; Bredas, J. L.; Holmes, A. B.; Kraus, A.; Mullen, K.; Friend, R. H. *Nature* **1998**, *392*, 903.
- (254) Miyaura, N.; Suzuki, A. *J. Chem. Soc., Chem. Commun.* **1979**, 866.
- (255) Miyaura, N.; Suzuki, A. *Chem Rev* **1995**, *95*, 2457.
- (256) Buchwald, S. L. *Accounts Chem Res* **2008**, *41*, 1439.
- (257) Yin, L. X.; Liebscher, J. *Chem Rev* **2007**, *107*, 133.
- (258) Kesavan, L.; Tiruvalam, R.; Ab Rahim, M. H.; bin Saiman, M. I.; Enache, D. I.; Jenkins, R. L.; Dimitratos, N.; Lopez-Sanchez, J. A.; Taylor, S. H.; Knight, D. W.; Kiely, C. J.; Hutchings, G. J. *Science* **2011**, *331*, 195.
- (259) Grirrane, A.; Corma, A.; Garcia, H. *Science* **2008**, *322*, 1661.
- (260) Gallon, B. J.; Kojima, R. W.; Kaner, R. B.; Diaconescu, P. L. *Angew. Chem. Int. Ed.* **2007**, *46*, 7251.
- (261) Datta, K. K.; Reddy, B. V.; Ariga, K.; Vinu, A. *Angew. Chem. Int. Ed.* **2010**, *49*, 5961.
- (262) Kim, S. W.; Kim, M.; Lee, W. Y.; Hyeon, T. *J. Am. Chem. Soc.* **2002**, *124*, 7642.
- (263) Wan, Y.; Wang, H. Y.; Zhao, Q. F.; Klingstedt, M.; Terasaki, O.; Zhao, D. Y. *J. Am. Chem. Soc.* **2009**, *131*, 4541.
- (264) Fihri, A.; Bouhrara, M.; Nekoueishahraki, B.; Basset, J. M.; Polshettiwar, V. *Chem Soc Rev* **2011**, *40*, 5181.
- (265) Han, P.; Wang, X. M.; Qiu, X. P.; Ji, X. L.; Gao, L. X. *J. Mol. Catal. A: Chem.* **2007**, *272*, 136.
- (266) Zheng, Z. L.; Li, H. F.; Liu, T. F.; Cao, R. *J Catal* **2010**, *270*, 268.
- (267) Das, D. D.; Sayari, A. *J Catal* **2007**, *246*, 60.
- (268) Sokolov, V. I.; Rakov, E. G.; Bumagin, N. A.; Vinogradov, M. G. *Fullerenes Nanotubes and Carbon Nanostructures* **2010**, *18*, 558.
- (269) Najman, R.; Cho, J. K.; Coffey, A. F.; Davies, J. W.; Bradley, M. *Chem Commun* **2007**, 5031.
- (270) Beletskaya, I. P.; Kashin, A. N.; Khotina, I. A.; Khokhlov, A. R. *Synlett* **2008**, 1547.
- (271) Wei, G. W.; Zhang, W. Q.; Wen, F.; Wang, Y.; Zhang, M. C. *J Phys Chem C* **2008**, *112*, 10827.
- (272) Kantam, M. L.; Roy, S.; Roy, M.; Sreedhar, B.; Choudary, B. M. *Adv. Synth. Catal.* **2005**, *347*, 2002.

- (273) Gniewek, A.; Ziolkowski, J. J.; Trzeciak, A. M.; Zawadzki, M.; Grabowska, H.; Wrzyszczyk, J. J. *Catal.* **2008**, *254*, 121.
- (274) Gopidas, K. R.; Whitesell, J. K.; Fox, M. A. *Nano Lett.* **2003**, *3*, 1757.
- (275) Wu, L.; Li, B. L.; Huang, Y. Y.; Zhou, H. F.; He, Y. M.; Fan, Q. H. *Org. Lett.* **2006**, *8*, 3605.
- (276) Scheuermann, G. M.; Rumi, L.; Steurer, P.; Bannwarth, W.; Mulhaupt, R. *J Am Chem Soc* **2009**, *131*, 8262.
- (277) Wang, F.; Mielby, J.; Richter, F. H.; Wang, G.; Prieto, G.; Kasama, T.; Weidenthaler, C.; Bongard, H.-J.; Kegnæs, S.; Fürstner, A.; Schüth, F. *Angew. Chem. Int. Ed.* **2014**, *53*, 8645.
- (278) Lang, X.; Chen, X.; Zhao, J. *Chem Soc Rev* **2014**, *43*, 473.
- (279) Tsukamoto, D.; Shiraishi, Y.; Sugano, Y.; Ichikawa, S.; Tanaka, S.; Hirai, T. *J Am Chem Soc* **2012**, *134*, 6309.
- (280) Su, F. Z.; Mathew, S. C.; Mohlmann, L.; Antonietti, M.; Wang, X. C.; Blechert, S. *Angew Chem Int Edit* **2011**, *50*, 657.
- (281) Rueping, M.; Zoller, J.; Fabry, D. C.; Poscharny, K.; Koenigs, R. M.; Weirich, T. E.; Mayer, J. *Chemistry – A European Journal* **2012**, *18*, 3478.
- (282) Wang, X. C.; Maeda, K.; Thomas, A.; Takanebe, K.; Xin, G.; Carlsson, J. M.; Domen, K.; Antonietti, M. *Nat. Mater.* **2009**, *8*, 76.
- (283) Christopher, P.; Xin, H.; Linic, S. *Nat Chem* **2011**, *3*, 467.
- (284) Sarina, S.; Zhu, H. Y.; Xiao, Q.; Jaatinen, E.; Jia, J. F.; Huang, Y. M.; Zheng, Z. F.; Wu, H. S. *Angew. Chem. Int. Ed.* **2014**, *53*, 2935.
- (285) Xiao, Q.; Sarina, S.; Jaatinen, E.; Jia, J., Arnold, D., Liu, H., Zhu, H. *Green Chem.* **2014**, *16*, 4272.
- (286) Xiao, Q.; Sarina, S.; Bo, A. X.; Jia, J. F.; Liu, H. W.; Arnold, D. P.; Huang, Y. M.; Wu, H. S.; Zhu, H. Y. *ACS Catal.* **2014**, *4*, 1725.
- (287) Rikken, G. L. J. A.; Braun, D.; Staring, E. G. J.; Demandt, R. *Appl. Phys. Lett.* **1994**, *65*, 219.
- (288) Subramanian, V.; Wolf, E.; Kamat, P. V. *J. Phys. Chem. B* **2001**, *105*, 11439.
- (289) Li, X. H.; Baar, M.; Blechert, S.; Antonietti, M. *Scientific Reports* **2013**, *3*.
- (290) Li, X.-H.; Antonietti, M. *Chem Soc Rev* **2013**, *42*, 6593.
- (291) Wang, Z. J.; Landfester, K.; Zhang, K. A. I. *Polym. Chem.* **2014**, *5*, 3559.
- (292) Wang, Z. J.; Ghasimi, S.; Landfester, K.; Zhang, K. A. I. *Chem. Commun.* **2014**, *50*, 8177.
- (293) Wang, F.; Li, C.; Sun, L.-D.; Xu, C.-H.; Wang, J.; Yu, J. C.; Yan, C.-H. *Angew. Chem. Int. Ed.* **2012**, *51*, 4872.
- (294) Thathagar, M. B.; ten Elshof, J. E.; Rothenberg, G. *Angew. Chem. Int. Ed.* **2006**, *45*, 2886.
- (295) MacQuarrie, S.; Horton, J. H.; Barnes, J.; McEleney, K.; Looock, H. P.; Crudden, C. M. *Angew. Chem. Int. Ed.* **2008**, *47*, 3279.
- (296) Blouin, N.; Michaud, A.; Gendron, D.; Wakim, S.; Blair, E.; Neagu-Plesu, R.; Belletête, M.; Durocher, G.; Tao, Y.; Leclerc, M. *J. Am. Chem. Soc.* **2008**, *130*, 732.
- (297) Blouin, N.; Michaud, A.; Gendron, D.; Wakim, S.; Blair, E.; Neagu-Plesu, R.; Belletete, M.; Durocher, G.; Tao, Y.; Leclerc, M. *J Am Chem Soc* **2008**, *130*, 732.
- (298) Zambounis, J. S.; Hao, Z.; Iqbal, A. *Nature* **1997**, *388*, 131.
- (299) Bijleveld, J. C.; Shahid, M.; Gilot, J.; Wienk, M. M.; Janssen, R. A. J. *Adv Funct Mater* **2009**, *19*, 3262.

9 List of Related Publications

Z. J. Wang, K. Landfester, K. A. I. Zhang, Hierarchically Porous π -Conjugated PolyHIPE as a Heterogeneous Photoinitiator for Free Radical Polymerization under Visible Light, *Polym. Chem.*, 2014, 5, 3559-3562

Z. J. Wang, S. Ghasimi, K. Landfester, K. A. I. Zhang, Highly Porous Conjugated Polymers for Selective Oxidation of Organic Sulfides under Visible Light, *Chem. Comm.*, 2014, 50, 8177-8180

Z. J. Wang, S. Ghasimi, K. Landfester, K. A. I. Zhang, A Conjugated Porous Polybenzobisthiadiazole Network for a Visible Light-Driven Photoredox Reaction, *J. Mater. Chem. A*, 2014, 2, 18720-18724

Z. J. Wang, S. Ghasimi, K. Landfester, K. A. I. Zhang, Photocatalytic Suzuki Coupling Reaction Using Conjugated Microporous Polymer with Immobilized Palladium Nanoparticles under Visible Light, *Chem. Mater.*, 2015, 27, 1921-1924

Z. J. Wang, K. Garth, S. Ghasimi, K. Landfester, K. A. I. Zhang, Conjugated Microporous Poly(Benzochalcogenadiazole)s for Photocatalytic Oxidative Coupling of Amines under Visible Light, *ChemSusChem*, 2015, 8, 3459-3464

Z. J. Wang, S. Ghasimi, K. Landfester, K. A. I. Zhang, Molecular Structural Design of Conjugated Microporous Poly(Benzooxadiazole) Networks for Enhanced Photocatalytic Activity with Visible Light, *Adv. Mater.*, 2015, 27, 6265-6270

S. Ghasimi, S. Prescher, Z. J. Wang, K. Landfester, J. Yuan, K. A. I. Zhang, Heterophase Photocatalysts from Water-Soluble Conjugated Polyelectrolytes: An Example of Self-Initiation under Visible Light, *Angew. Chem. Int. Ed.*, 2015, DOI: 10.1002/anie.201505325

Z. J. Wang, S. Ghasimi, K. Landfester, K. A. I. Zhang, 2015, Conjugated Nanoporous Polymer via Metal-Free Synthesis for Visible Light-Promoted Oxidative Hydroxylation of Arylboronic Acids, submitted

Z. J. Wang, S. Ghasimi, K. Landfester, K. A. I. Zhang, 2015, Bandgap Engineering of Conjugated Nanoporous Poly-benzobisthiadiazoles via Copolymerization for Enhanced Photocatalytic 1,2,3,4-Tetrahydroquinoline Synthesis under Visible Light, submitted

R. Li, Z. J. Wang, L. Wang, B. C. Ma, S. Ghasimi, H. Lu, K. Landfester, K. A. I. Zhang, 2015, Photocatalytic Selective Bromination of Aromatic Compounds using Microporous Organic Polymers with Visible Light, submitted

W. Huang, Z. J. Wang, B. C. Ma, S. Ghasimi, K. Landfester, K. A. I. Zhang, 2015, Hierarchically Porous Polytriazine Networks via Solid Vapor Synthesis with Enhanced Visible Light Photocatalytic Activity, submitted